Universitat Autònoma de Barcelona

0.5 0.5 2

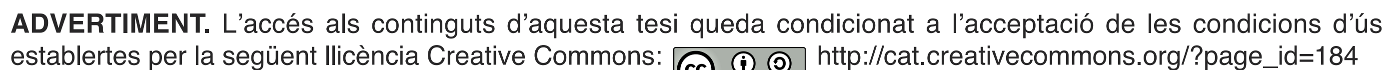

ADVERTIMENT. L'accés als continguts d'aquesta tesi queda condicionat a l'acceptació de les condicions d'ús establertes per la següent llicència Creative Commons: http://cat.creativecommons.org/?page_id=184

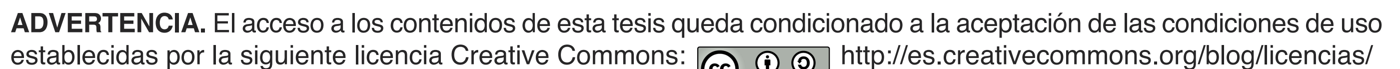

ADVERTENCIA. El acceso a los contenidos de esta tesis queda condicionado a la aceptación de las condiciones de uso establecidas por la siguiente licencia Creative Commons: http://es.creativecommons.org/blog/licencias/

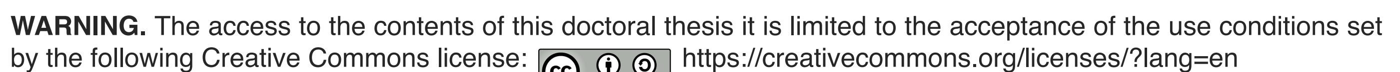

WARNING. The access to the contents of this doctoral thesis it is limited to the acceptance of the use conditions set by the following Creative Commons license: https://creativecommons.org/licenses/?lang=en

Resistive Switching in $Hf_{0.5}Zr_{0.5}O_2$ ferroelectric tunnel junctions

Milena Cervo Sulzbach

April 2021

Doctoral Thesis

SUPERVISOR

Prof. Josep Fontcuberta Grinó

TUTOR

Prof. Jordi Sort Viñas

Institut de Ciència de Materials de Barcelona ICMAB-CSIC

Laboratory of Multifunctional Oxides and Complex Structures

Universitat Autònoma de Barcelona

Department of Physics, Faculty of Science

Doctoral program: Physics

Prof. Josep Fontcuberta Griñó, research professor at the Institut de Ciència de Materials de Barcelona – Consejo Superior de Investigaciones Científicas, and **Prof. Jordi Sort Viñas**, ICREA Research Professor at the Universitat Autònoma de Barcelona

CERTIFY

that **Milena Cervo Sulzbach** carried out under his direction the research work entitled "Resistive Switching in $Hf_{0.5}Zr_{0.5}O_2$ ferroelectric tunnel junction memristors". This work has been developed within the Ph.D. program in Physics at the Universitat Autònoma de Barcelona at the Department of Physics.

For that record, he signs the certificate.

Bellaterra, April 2021

Prof. Josep Fontcuberta Griñó Prof. Jordi Sort Viñas

Acknowledgments

The conclusion of this thesis could not have been possible without the support of many people that walked with me during these years. First of all, I am greatly thankful for Prof. Josep Fontcuberta and for supervising my work and encouraging me. Your deep knowledge in fundamental and applied physics and patience were fundamental for the conclusion of this research. Thanks to Dr. Ignasi Fina for the assistance in methodology, experiment preparation, analysis of data, and publication preparations. Thank you both for your time, effort and motivation.

Thank you to La Caixa foundation for financial support during my Ph.D.

I am deeply thankful for the time and attention of Dr. Florencio Sánchez, Raul Solanas, Raúl Pérez, and Dr. Mengdi Qian in the sample fabrication process in ICMAB and ICN2.

Special thanks to Dr. Jaume Gazques and Saúl Estandía for the time and effort to obtain great STEM images and the valuable discussions for understanding our results.

Thank you to Anna Crespi, Joan B. Esquius, Javier Campos, Maite Simón, Andrés Gómez, Luigi Morrone, Neus Romà, Anna Esther Carrillo and Judith Oró for the technical support and attention. Your work was essential for this thesis.

Thank you for the bottom of my heart to the team of Polifab – Polimi for your support during my international stay. Even though it was a short period of time and maybe not incredible scientific results arouse from that, I have learned a lot and your attention was really important. Special thanks for Prof. Riccardo Bertacco, Dr. Marco Asa, Dr. Daniella Petti, Dr. Alessia Romeo, Dr. Christian Rinaldi, Claudio Somaschini and Lorenzo Livietti for your hospitality, time and caring.

Thank you to Prof. Francesca Campdabal and Dr. Mireia Bargallo Gonzalez for opening your laboratory for me, the great assistance, and patience.

I wish to express my special thank you to prof. Vassil Skumryev. Without your effort and receptiveness, this Ph.D. would never have happened.

I want to extend my gratitude to Huan Tan, Jike Lyu, Xiao Long for your effort and assistance with experimental data acquisition and analysis during these years. Also, to Dr. Gervasi Herranz, Yunwei Sheng, Mathieu Mirjolet, Yu Chen, Dr. Ferrán Macià, and Pedro Barusco for support and valuable discussions.

This thesis could have never been concluded without the constant support, friendship, and caring of my family and friends. To my family, I will be forever grateful for the endless support and understanding. I wish I could have been more present in the last years, but your constant support for me pursuing my dreams is beyond words. To my dear friends, words cannot express how thankful I am. Albert, Sarah, Nikos, Jairo, Katie, Victor, Cecile, Anna, Neus, and Laura, we met in extreme situations, and your relentless happiness, understanding, love, and motivation made these years possible and changed my life forever. To my friends from Brasil, Giulia, Rodrigo, Everton, Luis Gustavo, Vinicius, and Grazielle, thank you for your support, friendship, and love. To Barbara, my forever thank you; you have no idea how much you helped me and how deeply thankful I am for your support and friendship. To all La Caixa fellows, thank you. To dear Fatima, thank you for your patience and fantastic work. This thesis is also yours!

The project that gave rise to these results received the support of a fellowship from **”la Caixa” Foundation** (ID **100010434**). The **fellowship code** is **LCF/BQ/IN17/11620051**.

This project has received funding from the European Union´s Horizon 2020 research and innovation program under the Marie Skłodowska-Curie grant agreement No. 713673

To all women

Abstract

The requirement for high-performance data storage and computing systems in the Internet of Things (IoT) era reaches the limits of the current technology. DRAM and NAND flash memories show significant drawbacks as data volatility and limitations of speed. On the other hand, *Von Neumann* bottleneck limits computing performance by imposing a physical limitation for communication between parts of the computer. New memory technologies, like resistive random-access memory (ReRAM), have been proposed as alternative devices that combine high performance, low price, and high density.

One promising type of ReRAM is a ferroelectric tunnel junction (FTJ), which is composed of an ultrathin layer of ferroelectric material sandwiched between two metallic electrodes. The ferroelectric polarization (P) direction modulates the barrier properties at the interface with the electrodes, changing electrons' conductivity. A high and low resistance states (HRS and LRS, respectively) can be stabilized in a device by reversing P. Therefore, information can be written by applying an external voltage pulse to polarize the sample in one particular direction and store in its resistance. Nevertheless, other electric field-driven effects can also cause resistive switching in FTJ. This thesis aims to explore the resistive switching phenomena in $Hf_{0.5}Zr_{0.5}O_2$ ferroelectric tunnel junctions that could be used in highly efficient data storage.

HfO_2-based oxides have been explored as ReRAM elements due to their resistance change caused by redox reactions. However, the discovery of ferroelectricity in doped-HfO_2 opens doors to use polarization reversal as a phenomenon to control the resistance and, therefore, to writing information. Here, epitaxial HZO films with a thickness smaller than 5 nm are used. Electrical and structural analyses have allowed identifying the coexistence of genuine ferroelectric switching and ionic-like motion as mechanisms to induce resistance change in the same junction. It was found that ionic-motion-driven resistive switching takes advantage of incoherent grain boundaries between orthorhombic (ferroelectric) phase and monoclinic (paraelectric) phase grains. By engineering the film's microstructure, using a substrate with a different in-plane lattice parameter, the ferroelectric switching was optimized, and the ionic motion was suppressed. Also, sealing the grain boundaries with an extra dielectric layer increased the writing voltage window for purely ferroelectric switching and significantly impacted device performance.

Ultrathin (2 nm) HZO films grown on scandate substrates were used to demonstrate robust memristive properties associated with polarization reversal. Reproducible potentiation/depression cycles and spike-timing-dependent plasticity (STDP) measurements were demonstrated. These results, combined with HZO films' compatibility with current CMOS technology, environmentally friendly production, and good performance, show HZO tunnel junctions are feasible alternatives for application in non-volatile memories. Also, memristive properties of modulation of conduction show they can be used in neuromorphic inspired devices.

Resumen

El requisito de sistemas informáticos y de almacenamiento de datos de alto rendimiento en la era del Internet de las cosas (IoT) alcanza los límites de la tecnología actual. Las memorias flash DRAM y NAND presentan importantes desventajas como la volatilidad de los datos y limitaciones de velocidad. Por otro lado, el cuello de botella de v*on Neumann* limita el rendimiento informático al imponer una limitación física para la comunicación entre las partes del ordenador. Se han propuesto nuevas tecnologías de memoria, como ReRAM, en dispositivos alternativos que combinan alto rendimiento, bajo precio y alta densidad.

Un tipo prometedor de ReRAM es una unión de túnel ferroeléctrico (FTJ), que és compuesta por una capa ultrafina de material ferroeléctrico intercalado entre dos electrodos metálicos. La dirección de la polarización (P) modula las propiedades de barrera en la interfaz con los electrodes, cambiando la conductividad de los electrones. Los estados de alta y baja resistencia (HRS y LRS, respectivamente) se pueden estabilizar en el dispositivo invirtiendo P. Por lo tanto, la información se puede escribir aplicando un pulso externo de voltaje para polarizar la muestra en una dirección particular y almacenarla en su resistencia. Sin embargo, otros efectos impulsados por el campo eléctrico también pueden causar conmutación resistiva en FTJ. Esta tesis tiene como objetivo explorar los fenómenos de variación resistiva en uniones de túneles ferroeléctricos de $Hf_{0.5}Zr_{0.5}O_2$ que se pueden utilizar en el almacenamiento de datos de alta eficiencia.

Óxidos basados en HfO_2 han sido utilizados durante décadas como elementos en ReRAM debido a su cambio de resistencia causado por reacciones redox. Sin embargo, el descubrimiento de la ferroelectricidad en el HfO_2 dopado abre las puertas para utilizar la inversión de polarización como fenómeno para controlar la resistencia y, por lo tanto, para escribir información. Aquí, se utilizan capas epitaxiales de HZO con un grosor inferior a 5 nm. Análisis eléctricos y estructurales han permitido identificar la coexistencia de la inversión ferroeléctrica genuina y movimiento iónico como mecanismos para inducir cambios de resistencia en el mismo electrodo. Se encontró que la variación de resistencia causada por movimiento iónico se aprovecha de las fronteras de grano incoherentes entre las fases de grano ortorrómbica (ferroeléctrica) y monoclínica (paraeléctrica). Al diseñar la microestructura de la capa, utilizando un sustrato con un parámetro de red diferente, se optimiza la variación de resistencia por inversión ferroeléctrica y se suprime el movimiento iónico. Además, al sellar las fronteras de grano con una capa dieléctrica adicional aumentó la

ventana de voltaje de escritura para la variación resistiva puramente ferroeléctrica y afectó significativamente el rendimiento del dispositivo.

Capas ultrafinas (2 nm) de HZO fueron crecidas en sustratos scandate para demostrar robustas propiedades memristivas. Se demuestran ciclos de potenciación/depresión reproducibles y mediciones de *spike-timing-dependent plasticity* (STDP). Estos resultados, combinados con la compatibilidad de las capas de HZO con la tecnología CMOS actual, la producción amigable con el medio ambiente y el buen rendimiento, muestran que las uniones de túnel ferroeléctricas de HZO son alternativas viables para su aplicación en memorias no volátiles. Además, las propiedades memristivas fundamentales de la modulación de la conducción muestran que pueden usarse en dispositivos con inspiración neuromórfica.

Objective and structure of the thesis

A deep understanding of resistive switching (RS) in epitaxial $Hf_{0.5}Zr_{0.5}O_2$ ferroelectric tunnel junctions is studied. Structural and electrical characterization allows the identification of two main mechanisms responsible for RS. By optimizing the measurement conditions, memristive abilities due to genuine ferroelectric switching are explored and show a promising future for neuromorphic application.

Chapter 1

This chapter introduces the field of memory devices, memristors, and ferroelectric tunnel junctions. A description of the structure and ferroelectricity in HfO_2-based oxides is done. The coexistence of ferroelectric and non-ferroelectric resistive switching in classic perovskite oxides and doped-HfO_2 ferroelectrics is discussed.

Chapter 2

This chapter contains a description of the experimental methods used to characterize ferroelectric tunnel junctions. It contains sections devoted to sample fabrication, electrical and structural characterization.

Chapter 3

This chapter demonstrates electroresistance (ER) results in epitaxial $Hf_{0.5}Zr_{0.5}O_2$ ferroelectric tunnel junctions. Electrical measurements show the coexistence of ferroelectric and non-ferroelectric resistive switching mechanisms causing ER. Structural characterization techniques are used to investigate the appearance of non-ferroelectric switching and the importance of grain boundaries. This chapter is extensively based on the manuscript Sulzbach, M. C., Estandía, S., Long, X., Lyu, J., Dix, N., Gàzquez, J., Chisholm, M. F., Sánchez, F., Fina, I., Fontcuberta, J., Unraveling Ferroelectric Polarization and Ionic Contributions to Electroresistance in Epitaxial $Hf_{0.5}Zr_{0.5}O_2$ Tunnel Junctions. *Adv. Electron. Mater.* 2020, 6, 1900852.

Chapter 4

An approach for suppression of the ionic-related motion resistive switching is proposed. A detailed study of the performance of FTJ is presented. This chapter is extensively based on the manuscript

Sulzbach, M. C., Estandía, S., Gàzquez, J., Sánchez, F., Fina, I., Fontcuberta, J., Blocking of Conducting Channels Widens Window for Ferroelectric Resistive Switching in Interface-Engineered $Hf_{0.5}Zr_{0.5}O_2$ Tunnel Devices. *Adv. Funct. Mater.* 2020, 30, 2002638.

Chapter 5

A genuine ferroelectric switching effect is observed in the epitaxial ultrathin HZO ferroelectric junction. Memristive behavior is explored for neuromorphic applications. This chapter is extensively based on the manuscript M. C. Sulzbach, H. Tan, S. Estandía, J. Gàzquez, F. Sánchez, I. Fina, J. Fontcuberta, Ferroelectric and resistive switching in epitaxial 2 nm $Hf_{0.5}Zr_{0.5}O_2$ tunnel junctions submitted in March 2021 to ACS Applied Electronic Materials and it is currently under revision.

Annex

Patterning of ferroelectric tunnel junctions using optical lithography and electrical characterization. Fabrication steps were performed in Polifab, Politecnica Milano – Italy.

Contents

Chapter 1. Introduction 1
1.1. Motivation 1
1.1.1. Limitation of the current memory devices technology 1
1.2. ReRAM 3
1.2.1. Memristors 5
1.2.2. Ferroelectric Memristor 6
1.3. Ferroelectric tunnel junctions 11
1.3.1. Electrical transport mechanisms through ultrathin insulators 12
1.3.2. Resistive switching mechanisms in ferroelectric tunnel junctions 14
1.4. HfO_2-based oxides 18
1.4.1. Ferroelectricity in HfO_2 oxide 19
1.4.2. $Hf_{0.5}Zr_{0.5}O_2$ phase composition 20
1.4.3. Ferroelectric properties of HZO 24
1.5. Coexistence of FE switching and non-FE switching 27
1.5.1. Perovskite oxides 28
1.5.2. HfO_2-based films 31
Chapter 2. Experimental Methods 34
2.1. Sample fabrication 34
2.1.1. Pulsed laser deposition (PLD) 35
2.1.2. Top electrode fabrication 37
2.2. Electric characterization 37
2.2.1. Measurement configuration 38
2.2.2. Experimental setup 38
2.2.3. Ferroelectric properties 42
2.3. Structural characterization 58
2.3.1. Atomic force microscopy (AFM) 58
2.3.2. Piezo Force Microscopy (PFM) 59
2.3.3. X-ray Diffraction (XRD) 60
2.3.4. Scanning Transmission Electron Microscopy (STEM) 64
Chapter 3. Ferroelectric and Ionic-based Contributions to Electroresistance in HZO 67
3.1. Introduction 68

3.2. Samples ... 70
3.3. Junctions grown on STO (001) substrates ... 70
3.4. $Hf_{0.5}Zr_{0.5}O_2$ film microstructure dependence on the substrate ... 76
3.5. Ferroelectric tunnel junctions grown on GSO (001) and LSAT (001) substrates ... 78
3.6. Conclusion ... 79
3.7. Appendix ... 80
Chapter 4. Suppression of Conduction Channels and Enlargement of FE Switching Window ... 87
4.1. Introduction ... 88
4.2. Samples ... 91
4.3. Capping junctions grown on STO (001) substrates ... 91
4.3.1. X-ray Diffraction ... 92
4.3.2 Electrical characterization ... 93
4.3.3. Electroresistance ... 94
4.4. Capping junctions grown on GSO (001) substrates ... 97
4.5. Endurance ... 99
4.6. Scanning Tunneling Electron Microscopy ... 101
4.7. Conclusion ... 105
4.8. Appendix ... 105
Chapter 5. Ferroelectric and Resistive Switching in Ultrathin Tunnel Junctions ... 107
5.1. Introduction ... 108
5.2. Samples ... 109
5.3. Structural characterization ... 109
5.3.1. Topography ... 110
5.3.2. X-ray Diffraction ... 110
5.4. HZO (2 nm) tunnel junction ... 111
5.4.1. Scanning Transmission Electron Microscopy ... 112
5.4.2 Electrical characterization ... 113
5.4.3 Memristive ... 121
5.5. Thicker HZO junctions ... 124
5.6. Conclusion ... 127
5.7. Appendix ... 128
Chapter 6. Conclusion ... 135

Annex. Patterning of Ferroelectric Tunnel Junctions using Optical Lithography 137
I. One-step lithography 138
II. Three-step lithography and patterning FTJ 142
a. Step 1 – MESA patterning 142
b. Pillar / junction area definition 144
c. Contact deposition 145
III. FTJ characterization 147
a. Structural / Optical microscopy 147
b. Electrical characterization 148
Bibliography 158
List of Figures 176
List of Tables 187
List of Abbreviations 188
List of Acronyms 191
List of Publications 193
Author contributions 194

Chapter 1. Introduction

1.1. Motivation

This thesis aims to investigate resistive switching in ferroelectric tunnel junctions composed of $Hf_{0.5}Zr_{0.5}O_2$ (HZO) thin films. The memristive character of these devices offers a good prospect for application in storage devices and neuromorphic-inspired systems. This chapter will present the current technology scenario and how ferroelectric tunnel junctions are compared to other types of resistive switching devices. A review of the basic structure, conduction mechanisms, and functionalities of FTJ will be presented as well as a brief introduction of HfO_2-based oxides. Finally, examples of resistive and ferroelectric switching's coexistence will be made for classic perovskites and HfO_2-based ferroelectrics.

1.1.1. Limitation of the current memory devices technology

The race for high-performance data storage devices and processing units has been boosted by the recent needs in large computing systems and the Internet of Things (IoT). The state-of-the-art fast-access data is stored in charge-based elements with node sizes around 15 to 18 nm. However, at this scale, heat, and leakage current start to compromise the storage, and the technology becomes limited. Moreover, 5G and machine learning technologies demand faster and lower energy consumption devices, opening the door for intensive research for a new generation of memories.

At this moment, two basic types of devices are used for this particular purpose: dynamic random access memory (DRAM) and flash (NAND flash). DRAM is a key building block in main memory systems since it is cheap and fast. Nevertheless, it is a volatile memory, i.e., data are lost when power is shut off, representing a significant drawback.[1] On the other hand, flash memory is nonvolatile and retains data when power is off. Despite its popularity and advantages, issues like speed, endurance, and power consumption limit its applicability.[2] Both types of devices store bits of information in the form of electric charge, and for this reason, as their size shrinks, the amount of stored charge reduces and leaks, compromising its functionality.

In addition to storage units, processing units are crucial for developing highly efficient computing. The increasing amount of data that has to be processed in image and audio recognition, signal

processing, machine learning, and smart sensors require a change in how data is handle in computers. In classical *von Neumann* architecture, the data has to be transferred between computing and memory units typically via a bus system, giving rise to the so-called Von Neumann bottleneck, which restricts the communication due to limited memory and data bus bandwidth.[3] In order to fill the gap between memory and logic units, the concept of physical separation between them has to be modified. This can be achieved by adding logic functionalities into memory units or a fine-grained distribution of memory functionalities into processing units (computing-in-memory, CiM).[4]

Since the studies with biological systems started to highlight how the human brain acquires and processes information,[5,6] the research in neuro-inspired architectures has arisen. This approach intends to combine both logic and memory functionalities in one synaptic device, in the so-called neuromorphic computing. This approach does not limit to mimic the biological brain ability of highly parallel processing, and it intends to enable artificial devices to adapt to complex and unexpected environments with high reaction speed and minimal power consumption.[7] As an example of the superior performance of biological brains over the current supercomputer technology, a human brain can perform complex tasks such as visual recognition or motion control, having a power consumption in the order of 20 W with fast speed and precision.[8,9]

Therefore, the challenge for engineer nonvolatile memory devices that can also integrate processing ability in neuromorphic architecture is launched. Resistive random memories (ReRAM) appear as attractive candidates to overcome performance limitations in the storage data perspective. Besides, some types of ReRAM can display multi-states or multiple resistances that depend on the device's history, i.e., previous voltage-time excursions $V(t)$, thus constituting a memristor element.[10] Memristors can adapt and change their state over time in response to different stimuli as it happens in the human brain. In particular, it has been demonstrated that if stimulated with a train of pulses that simulates the input from spiking neurons, memristors may exhibit biologically-inspired learning rule[11–15] resembling the spike-timing-dependent plasticity (STDP) observed in biological neurons.[5,6] Hence, memristors have been considered artificial inorganic synapses.

The observation of nonvolatile data storage, adaptation, and learning skills are key and essential characteristics for memristors to be further investigated as elements for neuromorphic architecture.

The road for engineer electronic data storage integrated into processing units is long. This thesis's scope is to explore HfO_2-based ferroelectric tunnel junction's electrical properties that can be used as memristors. These characteristics, combined with the fact that this material is compatible with the current CMOS technology,[16,17] can be easily integrated into 3D arrays, [18] shows good retention and endurance properties,[19] and is environmentally friendly, open doors for deeper understanding and exploration of these devices.

1.2. ReRAM

A resistive switching cell is generally a two-terminal device built by a capacitor-like metal-insulator-metal (MIM) structure, composed of an insulating or resistive material sandwiched between two electron conductor electrodes. An external voltage pulse can electrically switch these cells, and the information is stored in its resistance state. An appropriate writing voltage pulse can program the device to a low (ON, LRS) and a high (OFF, HRS) resistance state. In binary logic, these states correspond to "*1*" and "*0*", respectively. In many types of ReRAM, more than two resistance states have been demonstrated.[20–23] The bit or the state is read by applying a read voltage using the same two terminals. The semiconductor industry has been using MIM and metal-insulator-semiconductor (MIS) junctions in CMOS technology for decades, which ensured extensive research in these systems.

Different physical phenomena can lead to the resistance switching (RS) effect. Depending on the physical mechanism, the cell requires particular conditions to function. For example, valence change memories (VCM) are triggered by migration of anions, typically oxygen vacancies, inside the insulator material or active layer due to the electric field-drive motion.[3,24] A change in its stoichiometry leads to a change in the electronic conductivity, and it is possible to establish different resistive states. One particular type of VCM is the so-called soft-dielectric breakdown (sDB) cells, where the region that changes stoichiometry is limited to nanometric filamentary regions inside the insulator matrix. When a specific polarity of the voltage is applied in one electrode, mobile oxygen vacancies create a filament with high electrical conduction that short-circuits the electrodes.[25,26] Currently, current can flow through the filament, and the resistive switching cell assumes a low resistance (ON). By inverting the electric field's polarity, a small filament region close to one of the electrodes breaks, i.e., oxygen vacancies diffuse. The conductivity of the cell increases, and the cell assumes a high resistance state (OFF). The

formation/destruction of the filament is reversible, and, therefore, the ON/OFF states are used for storing information.

Instead of moving oxygen ions, it is also possible to induce the diffusion of metallic ions across the insulator,[27] creating electrochemical memories (ECM). ReRAM functioning is similar to the sBD cell; however, the filament is now formed by metal ions. For this, one of the electrodes must be an electrochemically active metal (M), such as Ag, Cu, or Ni, and the other is an electrochemically inert counter electrode (CE), such as Pt, Ir, W, etc. The insulator is an electrolyte or M^{z+} ion conductor. The external electric field can induce an oxidation reaction at the metal M that becomes M^{z+} and diffuse towards the opposite electrode. There, cations reduce and start to accumulate, creating a metallic filament. When the electric field is inverted, part of the filament is dissolved. Attempts with Ag^{+} and Cu^{+} ions[3,27] were made, and it was found that retention and endurance can be tailored by using different programing voltages. Nevertheless, the random nature of the filament formation and the constant need for mass transport inside the device challenge the large implementation of such ReRAMs.

Phase change memories (PCM), on the other hand, do not depend on the diffusion of ions but make use of chalcogenide alloys that can undergo a rapid and reversible change between ordered crystalline and disordered amorphous atomic structures. The different electrical resistance of these two states is then used to store data. In 1970, Ron Neal and Gordon Moore, co-founder of Intel Corp., published a 256-bit amorphous semiconductor memory.[28] It took more than 30 years until the first commercially available PCM was revealed in 2006. The widest research materials are the germanium-antimony-tellurium (GST) alloys,[3,29] even though simple oxides like VO_2[30] can also show such effect. However, these devices seem to have intrinsic limitations due to temperature-dependent switching and, thus, higher power requirements.

Another type of ReRAM device is based on spin-transfer-torque (STT), in which spin-polarized currents can manipulate the magnetization of a thin film. Besides, magneto-resistive effects provide the possibility of electrical read-out of the magnetization state. These devices offer a fast operation with high endurance for nonvolatile memories. Nevertheless, the complicated multilayer structure has prevented 3D integration until now. This technology does not allow storage of multiple bits in one cell or perform analog switching between multiple resistance states.[3]

An alternative for resistive switching mechanism is ferroelectricity. It is a purely electronic effect,

and it takes advantage of polarization reversal in a ferroelectric material to induce change in the resistance. The spontaneous polarization of the ferroelectric remains even after the electric field used to polarized it is removed, which guarantees nonvolatile storage.[9] Ferroelectric perovskites like $SrBi_2Ta_2O_9$ (SBT) and $Bi_{4-x}La_xTi_3O_{12}$ (BLT) have been implemented as capacitors in FeRAM.[9,31,32] In these devices, a large electric field is used to polarize the cell in one direction, which stores either *1* or *0* (binary logic). However, in the reading step, a transistor associated with the ferroelectric capacitor forces the polarization to be reversed towards one particular direction, for example, *0*. If the FeRAM already was in the *0* state, no change occurs. Nonetheless, if the cell was in state *1*, polarization switching induces a current pulse in the device's output. If this pulse is detected, the cell state is associated with state *1*. Since the process overwrites the cell, the reading step in FeRAM is destructive and requires the cell to be rewritten. On a different configuration of the device, thick ferroelectric films have been introduced in Schottky diodes, where the polarization modulates the Schottky barrier height formed between ferroelectric/electrode.[33] The reading voltage is smaller than the coercive field of the ferroelectric. Capacitors composed of $BiFeO_3$ (BFO),[34] $BaTiO_3$ (BTO)[35], and PZT[36] films have been built, and the stored state can be measured without erasing it. Still, thick capacitors have a limitation in scalability and require large voltage in the write step, requiring large power.

An alternative to ferroelectric resistive switching cells is ferroelectric tunnel junctions (FTJ). An ultrathin layer of ferroelectric material composes these devices, and the polarization direction of the ferroelectric film controls the tunneling barrier height and tunneling resistance of electrons.[37–40] The ratio between the maximum (OFF) and minimum (ON) resistance states is often called tunneling electroresistance (TER). These devices show great scalability, do not require large power, and have non-destructive reading steps. Moreover, a partial polarization reversal of the ferroelectric, which is possible due to the formation of ferroelectric domains, allows stabilization of multi-resistance states. As mentioned in section 1.1.1, ReRAMs that show multiple resistance states can be used as memristive elements. In this thesis, ferroelectric tunnel junctions will be explored, and further details of their functionalities will be discussed in section 1.2.2.3. The next section will focus on a brief introduction about memristors and ferroelectric memristors.

1.2.1. Memristors

Memristors are resistive-switching devices characterized by a continuous change in resistance with

the amount of current flown across the device. L. Chua predicted this element in 1971 as a result of symmetry considerations in theoretical electronics.[10] This element is commonly called a resistor with memory. In is a non-linear resistor whose resistance or conductance depends on input signals' history and can also depend explicitly on time t. In 2008, the experimental observation of such elements was found in $Pt/TiO_2/Pt$ junctions.[41] Since then, several other physical systems have been designated as memristors. In particular, VCM and ferroelectric resistive-switching devices show memristive abilities, as mentioned in the previous sections.

1.2.2. Ferroelectric Memristor

In this section, the ferroelectric memristor concept is explored, starting from ferroelectric materials' fundamental physics. In the sequence, the importance of the ferroelectric thickness will be discussed, and, finally, the memristive properties in ferroelectric thin films are considered.

1.2.2.1. Ferroelectrics

As mentioned previously, ferroelectric materials display a spontaneous electric polarization that can be switched by applying an external electric field. They make part of a broad class of dielectric and insulator solids (Figure 1.1) that exhibit polarization when submitted to an external electric field, which is obtained by breaking the material's symmetry. Within dielectrics, some have non-centrosymmetric crystal structures and, because of this, exhibit piezoelectricity, which is the separation of opposite charges inside the solid caused by mechanical stress. The inverse effect is also valid, i.e., an external electric field induces these materials' deformation. A subgroup of piezoelectrics that becomes polar and leads to spontaneous polarization (P). A variation of temperature modifies the position of atoms inside the crystal structure slightly, causing a polarization change. This effect is denominated pyroelectricity. Finally, the spontaneous polarization of certain pyroelectrics can be switched under an external field and remains non-zero when it is removed, which is the case of ferroelectrics. The first experimental evidence of ferroelectricity was discovered in 1920 by Joseph Valasek during experiments on Rochelle salt.[42] Figure 1.1 shows a sketch with the hierarchy of dielectrics.

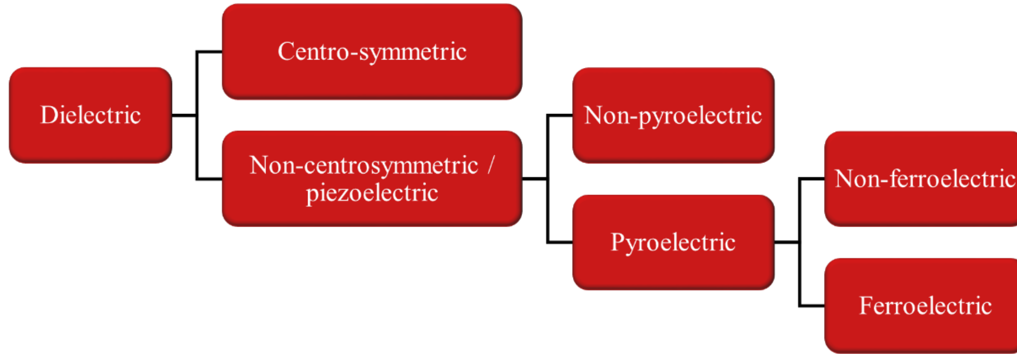

Figure 1. 1. Hierarchy of dielectric materials.

The non-centrosymmetric structure of the crystal leads to a non-symmetric distribution of charges inside the unit cell and, therefore, the appearance of a dipole moment *p*. The macroscopic polarization *P* of the solid is then given by the sum over all unit cell moments p_i normalized by the unit cell volume v_i, which can be described as $P = \sum_i p_i/v_i$. This results in a net charge at the material surface, whereas charges are still compensated in the bulk solid. Thus, the polarization can also be understood in terms of surface charge. Its unit is the same as for charge density, $[P] = C \cdot m^{-2}$. In $BaTiO_3$, for example, the polarization originates from the displacement of Ti ions in the *c* axis of a perovskite structure. In Hf-based oxides, the origin of ferroelectricity is different and it will be discussed in section 1.4.1.

A ferroelectric material can have all its dipole moments align, constituting a single-domain structure. Nevertheless, a typical phenomenon is the formation of ferroelectric domains. Each domain has a macroscopic spontaneous electric polarization along one crystallographic direction. The splitting into domains lowers the free energy of the crystal by reducing the electrostatic energy. However, a finite amount of energy is required to form the physical region between two domains, i.e., domain walls. [43]

The direction of polarization can be altered through the application of an external electric field. The polarization dependence on the external electric field has a hysteretic shape. The *P*(*E*) loop for polydomain samples is shown in Figure 1.2. Starting from the origin, the material is polarized under the electric field (*E*), and the polarization *P* increases (black curve). When enough field is applied, P saturates, reaching its maximum value (+ P_s). Once the electric field is reduced to zero, most domains remain polarized in that direction, but some do not, resulting in a decrease of the polarization to a remnant polarization (+ P_R). In single-domain samples, the remnant polarization

is the maximum polarization achievable. As the electric field inverts polarity, the polarization decreases until it reaches zero. The electric field value in which this happens is called the coercive field ($-E_c$). If the field continues to decrease, the ferroelectric saturates in the opposite direction ($-P_R$) the same way as the positive field. The electric field goes back to its initial positive value to complete the loop, as Figure 1.2 indicates. Ferroelectricity is detected in materials only if the temperature is below the Curie temperature (T_C), in which a phase transition to a paraelectric state happens.

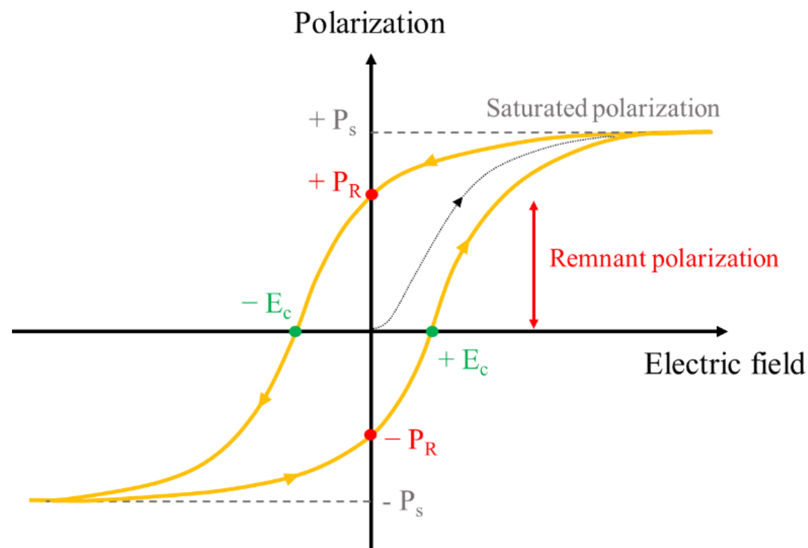

Figure 1. 2. Evolution of polarization in the function of the external electric field. The remnant polarization (P_R), coercive field (E_C), and saturated polarization (P_S) for both electric field polarities can be extracted.

1.2.2.2. Ferroelectric dependence on thickness

As described in the previous section, the ferroelectric polarization state can be probed by applying an electric field, i.e., a voltage to the material. To apply the voltage homogeneously, is it common to bring a metallic electrode in contact with the ferroelectric in both extremities, creating a capacitor. As mentioned before, the polarization will induce surface charges (σ_S) to be accumulated at the interface FE/electrode. In thin ferroelectric films, these interfaces' electrostatic conditions become increasingly important as these surface charges will be compensated by screening charges in the metal. An ideal metal would screen σ_S completely in an infinitesimal thin plane directly at the interface (Figure 1.3(a)). In a non-ideal metal, the screening charges will be distributed over a finite depth or screening length (λ_{eff}), as sketched in Figure 1.3(b). According to Thomas Fermi

theory,[44] this length is in the order of interatomic distances. The better conductor is the metal, the smaller is the screening length.

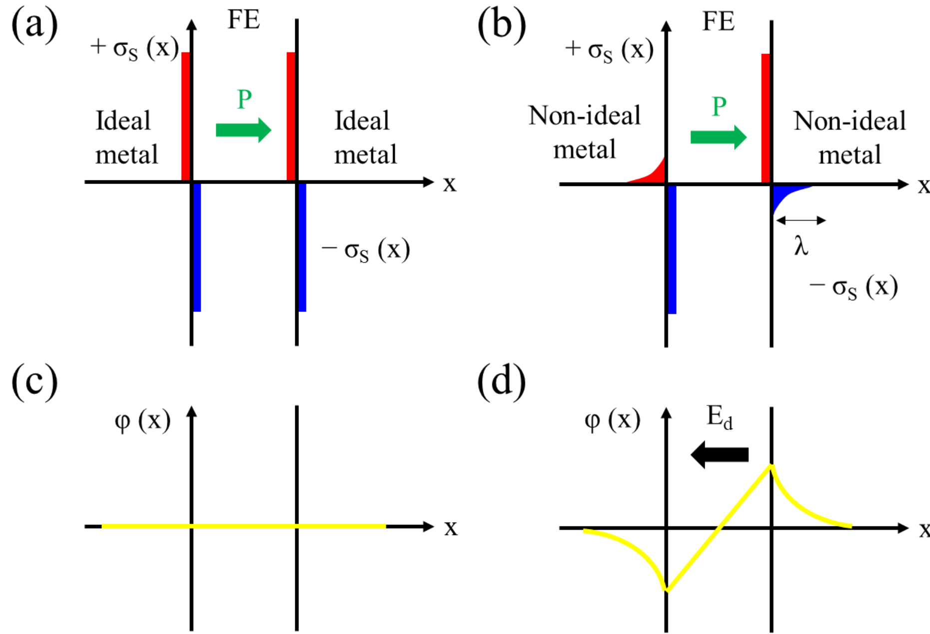

Figure 1. 3. Sketch of charge distribution σ(x) at the interfaces of the ferroelectric layer with (a) ideal metal or (b) non-ideal metal electrodes. In (b), the metal screening charges are spread over a finite screening length λ_{eff}. In non-ideal metals, not all surface charges are compensated by the metal. Electrostatic potential profile φ(x) in the case of (c) ideal metal and (d) non-ideal metal electrodes. The incomplete compensation of charges at the interface gives rise to an internal depolarizing field E_d in the ferroelectric layer.

Perfect compensation of charges by an ideal metal causes no electrostatic potential to be generated inside the FE film (Figure 1.3(c)). However, in the case of non-ideal metals, the accumulation of charges at the interfaces generates a non-zero electrostatic potential (φ(x)), resulting in a finite depolarization field E_d (Figure 1.3(d)).[45] This field tends to destabilize the ferroelectric polarization and, in the case of very thin films, drives the formation of domains with opposite polarization directions.[46,47] The minimum thickness in which a finite polarization could be measured was called critical thickness.[48,49] However, surface modifications at the atomic level can contribute to the stabilization of ferroelectric polarization in ultrathin films. A vast method used to increase ferroelectricity in small dimensions is to grow FE films on a substrate that exerts epitaxial strain.[50–53] The strain can also stabilize a polar crystal phase in thin films that are not stable in bulk; for example, depositing a classical perovskite ferroelectric on a substrate with smaller in-plane lattice parameters results in a compressive strain. The ferroelectric unit cell

compensates for the in-plane compression by expanding perpendicularly, which can stabilize a phase with enhanced out-of-plane polarization.[50–52]

1.2.2.3. Memristive characteristics

As mentioned previously, the ratio between the maximum (OFF) and minimum (ON) resistance states is often called tunneling electroresistance (TER). The study with different ferroelectric materials, like BTO,[54–56] BFO,[57,58], and PZT[59] in FTJ, has shown large TER values, which encourage the use of such materials in binary memories.[37] However, a non-uniform ferroelectric domain configuration can be exploited to build a multi-state logic or memristors.[60] In principle, any intermediate state of the macroscopic polarization between the two saturation values, i.e., $+P_s$ and $-P_s$, can be obtained in a ferroelectric device by adjusting the ratio of up and down polarization domains. However, the stochastic and complex nature of polarization switching appears as a challenge to stabilize these intermediate states and assess them in a deterministic way.[60,61] In 2012, Chanthbouala et al.[62] have shown that intermediate resistance states in Co/$BaTiO_3$ (2nm) /LSMO ferroelectric tunnel junctions could be observed depending on the history of write voltage pulses. By mapping the evolution of ferroelectric domain distribution by piezoresponse force microscopy (PFM), the authors correlate the progression of the device's resistance with the ferroelectric polarization switching from up to down. A similar observation was made in Co/BFO/CCMO tunnel devices in the following year,[57] where the final resistance could be modulated by the amplitude of a writing voltage pulse (Figure 1.4(a)). The PFM images collected in one electrode show that a minimum resistance is obtained for a large majority of domains pointing up (towards the Co). As these domains are switched down by an external voltage, the resistance increases. A simple model of parallel conduction correlates the resistance and ferroelectric domain population (Figure 1.4(c)). The final resistance of a junction depends on the fraction of domains with polarization pointing down (towards the CCMO), indicated by the variable s. The maximum and minimum values of resistance, $R_{\downarrow}$ and $R_{\uparrow}$, respectively, must be extracted from previous measurements as Figure 1.4(b).

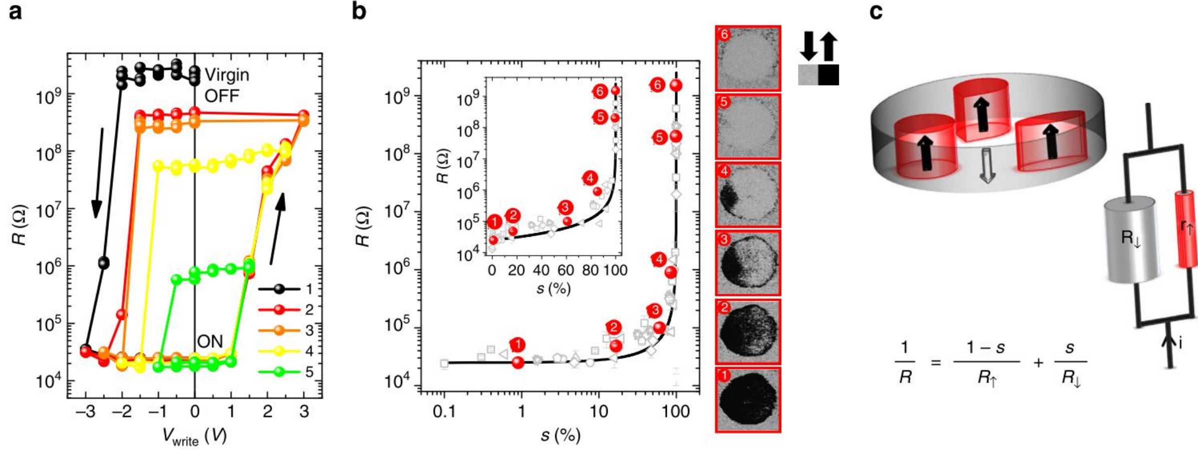

Figure 1. 4. Non-uniform ferroelectric domain distribution and memristive behavior. Measurements performed in Co/BiFeO$_3$ (4.5 nm)/Ca$_{0.96}$Ce$_{0.04}$MnO$_3$ tunnel junctions. (a) Resistance dependence on the writing voltage for 100 ns pulses. Intermediate resistance states are stabilized by decreasing the maximum amplitude. (b) Correlation of resistance state and fraction of domains with polarization pointing down (s) obtained by PFM images from 10 different junctions. PFM image for six resistance states in the same junction is shown on the side. The black line is a calculation from the parallel resistance model sketched in (c). Image taken from [37].

Therefore, an appropriate writing voltage pulse switches the polarization direction of a group of domains in the ferroelectric film, which causes variation in the junction's total resistance. This partial switch allows stabilization of intermediate states in a ferroelectric tunnel junction and observation of memristive behavior.[37,57]

1.3. Ferroelectric tunnel junctions

As introduced in the previous sections, ferroelectric tunnel junctions (FTJ) have a simple capacitor structure in which an ultrathin ferroelectric layer is sandwiched between two electrodes, as Figure 1.5 shows. The ferroelectric domain polarization direction points either to one or the other electrode and can be switched by an external electric field. The tunneling current crossing the device is modulated by the barrier height between ferroelectric/interface, which is affected by the polarization direction. The high-quality deposition of ultrathin material layers boosted the research with ferroelectric tunnel junctions since 2000.[49,63–65] These devices have presented fast switching,[66] large OFF/ON ratio,[57] good retention properties,[19,67] low fatigue,[68] and memristive properties.[69,70] Even though the aim of using ultrathin layers is to enable the direct tunneling of electrons, other conduction mechanisms can contribute to the electrical transport in FTJ.

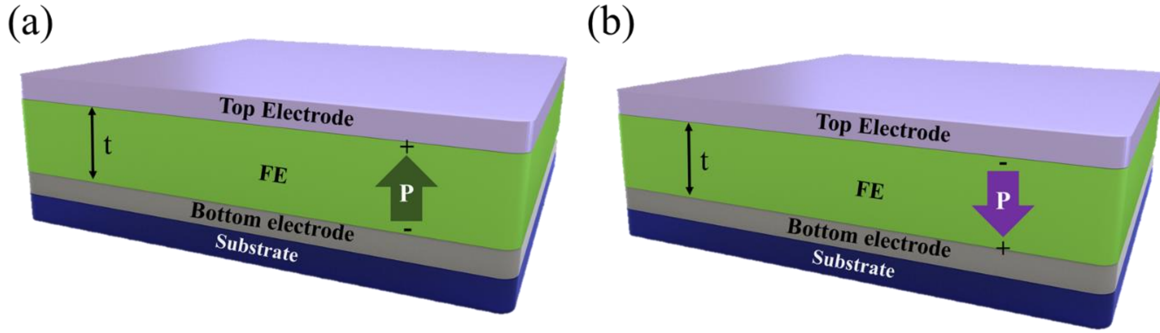

Figure 1. 5. Sketch of the capacitor-like structure of a ferroelectric tunnel junction. The ferroelectric grains' polarization points towards the (a) top or the (b) bottom electrode.

1.3.1. Electrical transport mechanisms through ultrathin insulators

Independently on the ferroelectric character of the ultrathin insulator film used in FTJ, different conduction mechanisms can contribute to the current across the barrier. When a voltage V is applied in the tunnel junction, direct tunneling (DT), Fowler-Nordheim tunneling (FNT), and thermionic injection (TI) can happen. This section focuses on electrical transport mechanisms through ultrathin insulators. In the next section, the physical phenomena that may cause resistance change in ferroelectric tunnel junctions are explored. Figure 1.6 sketches the three mechanisms. Each mechanism will be more relevant depending on the conditions implied by the energy barrier formed at the metal and the insulator interface.

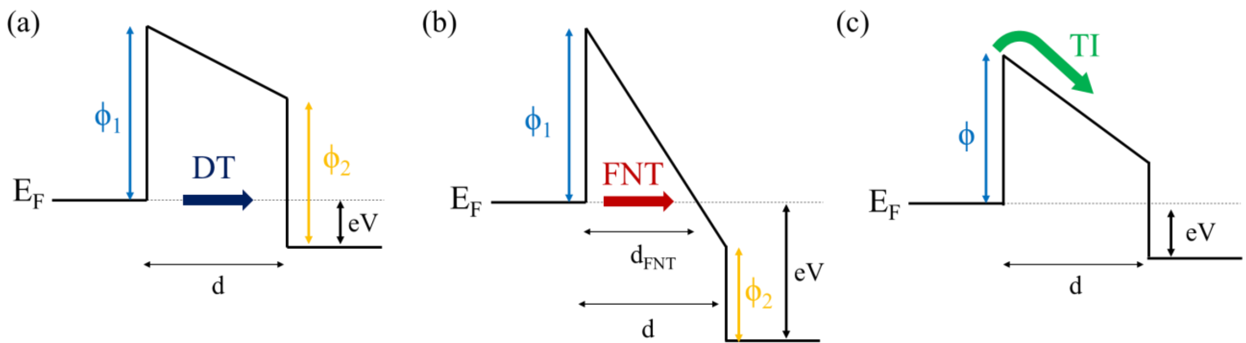

Figure 1. 6. Sketch for electrical transport mechanisms in ferroelectric tunnel junctions. (a) Direct tunneling (DT), (b) Fowler-Nordheim tunneling (FNT), and (c) thermionic injection (TI).

Direct tunneling

The energy barrier at the interface prevents charge carriers from moving freely through the system. In the case the insulator thickness is only a few nanometers, quantum tunneling becomes

possible.[40,71,72] In ferroelectric barriers, the polarization charges of the thin barrier at the interface with the electrode are screened by free electrons in the metal, changing the interfacial energy barrier. In the case of asymmetric interfaces, i.e., the electrodes are composed of different metals, the screening lengths are distinct and the associated barrier heights ϕ_1 and ϕ_2, are modified differently. This results in an asymmetric barrier profile commonly denominated trapezoidal, as Figure 1.6(a) displays. Based on the Brinkman model ,[73] Gruverman et al.[39] used the Wentzel-Kramers-Brillouin (WKB) approximation and determined an applied voltage V results in the following tunnel current density:

$$j_{DT}(V) \cong C \cdot \frac{\exp\left\{\alpha(V)\left[\left(\phi_2 - \frac{eV}{2}\right)^{3/2} - \left(\phi_1 + \frac{eV}{2}\right)^{3/2}\right]\right\}}{\alpha^2(V)\left[\left(\phi_2 - \frac{eV}{2}\right)^{1/2} - \left(\phi_1 + \frac{eV}{2}\right)^{1/2}\right]} \times \sinh\left\{\frac{3eV}{4}\alpha(V)\left[\left(\phi_2 - \frac{eV}{2}\right)^{\frac{1}{2}} - \left(\phi_1 + \frac{eV}{2}\right)^{\frac{1}{2}}\right]\right\} \qquad \textit{Eq. 1. 1}$$

Where $C = -4em^*m_e/[9\pi^2\hbar^3]$, $\alpha(V) = 4d\sqrt{2m^*m_e}/\ [3\hbar(\phi_1 + eV - \phi_2)]$, m^* is the relative effective mass of tunneling charge carries, and d is the thickness of the barrier. The constants used are m_e (electron mass), e (the electron charge), and $\hbar$ (reduced Planck constant).[39,73] At low voltages, i.e., $eV << \phi_1$ and $eV << \phi_2$, the current is nearly linear with the voltage following Ohm`s law. However, when increasing the voltage, the current density becomes exponential with voltage.

Fowler-Nordheim Tunneling

At higher voltages, Fowler-Nordheim tunneling overcomes the contribution of direct tunneling and dominates the conduction. When the voltage in one electrode exceeds the barrier height at the interface ($V > \phi_1/e$), the effective tunneling barrier width decreases from d to d_{FNT}, increasing tunneling probability. This happens because part of the ferroelectric energy barrier profile lies beneath the electrode's Fermi energy (E_F), as sketched in Figure 1.6(b). A simplified and widely used expression for the current density in this regime when an electric field E is applied is given by Eq. 1.2.

$$j_{FNT}(E) = \frac{e^3 m_e}{8\pi h m^* \phi_i} E^2 exp\left[-\frac{8\pi\sqrt{2m^*}}{3he} \cdot \frac{\phi_i^{\frac{3}{2}}}{E}\right] \qquad Eq.\ 1.\ 2$$

Note that in this equation, the electric field is considered as a parameter and not the voltage. This happens because the electric field E is a superposition of the applied field $E_{ap} = -V/d$, the depolarization field E_{dep} and the field due to band alignment $E_{band} = \frac{\phi_2 - \phi_1}{ed}$. Also, only one potential barrier height is taken into account (ϕ_i), the energy barrier that electrons must overcome during transport. Therefore, for $V > 0$, $\phi_i = \phi_1$ and for $V < 0$, $\phi_i = \phi_2$.[74]

Thermionic injection

At non-zero temperatures, charge carriers have a finite probability of overcoming the interface barrier simply by thermal excitation (Figure 1.6(c)). This mechanism is described by thermionic injection and becomes important for relatively high temperature or high applied voltages ($V \geq 3k_B T/e$). In thicker ferroelectric films, TI and FNT are the main conduction mechanisms. The current density is described by Eq. 1.3.

$$j_{TI}(E) = A^{**} T^2 exp\left[-\frac{1}{k_B T}\left(\phi_i - \sqrt{\frac{e^3 E}{4\pi\epsilon_0\epsilon_{ifl}}}\right)\right] \qquad Eq.\ 1.\ 3$$

Where the potential barrier ϕ_i is the energy barrier electrons, ϵ_{ifl} is the relative permittivity of the ferroelectric responsible for image force lowering, A^{**} is the effective Richardson constant for the material, but its value normally approaches the unmodified Richardson constant $A^* = \frac{4\pi m_e k_B^2 e}{h^3} \approx 1.2 \times 10^6 A \cdot m^{-2} K^{-2}$.[74] Here, the electric field E is also a superposition of the applied field, the depolarization field E_{dep} and the field due to band alignment.

1.3.2. Resistive switching mechanisms in ferroelectric tunnel junctions

It is very common to associate the resistance variation on ferroelectric capacitors solely to polarization reversal. However, other microscopic effects can cause a similar effect. In this section, four mechanisms that can induce resistive switching in ferroelectric tunnel junctions will be discussed: electrostatic, interface, strain effect, or ionic motion. Independently on the microscopic reason, ferroelectric tunnel junctions show a resistance dependence on the applied external voltage

or writing voltage pulse. The ratio between the maximum (OFF) and minimum (ON) resistances of a tunnel junction is given by the tunneling electroresistance (*TER* or simply *ER*), where

$$TER = \frac{R_{OFF} - R_{ON}}{R_{ON}} \times 100\ \%$$

By definition, $R_{ON} < R_{OFF}$, so $TER > 0$. For comparison with previous work on FTJ, the ratio R_{OFF}/R_{ON} is also used.

Electrostatic effect

As described in section 1.2.2.2, the surface charges induced by the polarization ($\sigma_s = P$) are screened at the interface by free charge carriers from the metallic electrodes (M_1, M_2). A sketch similar to Figure 1.3 will be used next to obtain the barrier height changes caused by polarization switching in a ferroelectric junction. Accordingly, the distribution of charges at the interfaces varies depending on the polarization direction, as sketched in Figure 1.7(a, b).

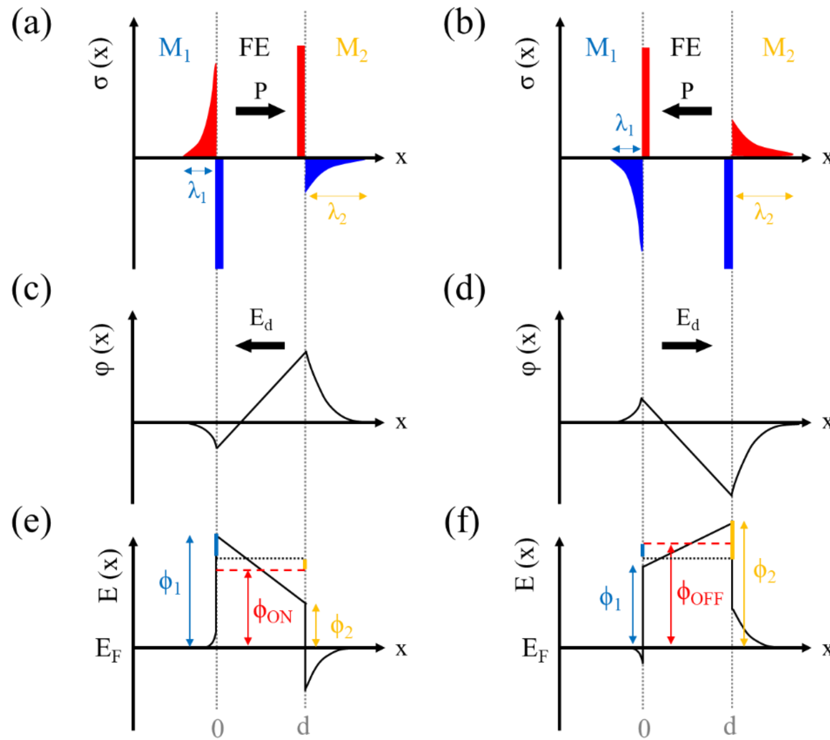

Figure 1. 7. Electrostatic changes in asymmetric FTJ. The metallic electrodes M_1 and M_2 have screening lengths λ_1 and λ_2, respectively. Charge distribution at the interfaces of electrode/ferroelectrics for polarization (a) $P\rightarrow$ and (b) $P\leftarrow$. Due to an incomplete screening of the polarization charges, a finite depolarization field E_d emerges with direction-dependent on P.

Electrical potential profile for (c) P→ and (d) P←. (e, f) Energy profile, where ϕ_{ON} and ϕ_{OFF} average barrier heights are related to the polarization direction and lead to different tunneling resistances. Adapted from [75].

The electrical potential inside the metal caused by charge accumulation or depletion as a function of the distance x is given by Eq. 1.4. The Thomas-Fermi screening model[44] assumed $\varphi_1(\infty) = \varphi_2(\infty)$, and the surface charge density σ_s is equal in both electrodes.

$$\varphi_{1,2}(x) = \begin{Bmatrix} \mp \frac{\sigma_s \lambda_1}{\epsilon_0 \epsilon_1} e^{\frac{x}{\lambda_1}}, for\ x \leq 0 \\ \pm \frac{\sigma_s \lambda_2}{\epsilon_0 \epsilon_2} e^{\frac{(d-x)}{\lambda_2}}, for\ x \geq d \end{Bmatrix} \qquad \textit{Eq. 1. 4}$$

Where $\lambda_{1,\ 2,}$ and $\epsilon_{1,\ 2}$ are the Thomas-Fermi screening lengths and the electrodes' ionic permittivities, respectively. Also, $\pm \sigma_s$ is the screening charge surface densities. The surface charge density calculated by continuity conditions of potential at the interfaces is given by Eq. 1.5.[74]

$$\sigma_S = \frac{Pd}{\epsilon_{stat}\left(\frac{\lambda_1}{\epsilon_1} + \frac{\lambda_2}{\epsilon_2}\right) + d} \qquad \textit{Eq. 1. 5}$$

Where ϵ_{stat} is the static relative permittivity of the barrier. The depolarizing field inside the ferroelectric can be calculated by Eq. 1.6.

$$E_d = -\frac{P - \sigma_s}{\epsilon_0 \epsilon_{stat}} \qquad \textit{Eq. 1. 6}$$

Figure 1.7(c, d) shows the resulting potential profile for both polarization directions. As a consequence of the polarization reversal, the barrier heights at the interfaces changes by $\Delta\phi$, which can be estimated by Eq. 1.7. Therefore, the barrier heights at each interface are given by Eq. 1.8.[74]

$$\Delta\phi = \frac{\lambda_i \sigma_s}{\epsilon_0 \epsilon_i} e, \qquad i = 1, 2 \qquad \textit{Eq. 1. 7}$$

$$\phi_i^{\rightarrow,\leftarrow} = \phi_i \pm \Delta\phi \qquad i = 1, 2 \qquad \textit{Eq. 1. 8}$$

Where $\phi^{\rightarrow,\leftarrow}$ is the barrier height depending on the polarization and ϕ_i is the initial barrier height, which can be estimated by the difference of the metal work function of each electrode (W_i) and the electron affinity (χ) of the ferroelectric $\phi_i = W_i - \chi$.[76] Note that this value is a simple estimation,

and the correct value must be experimentally measured. When the electrical transport through the ferroelectric barrier is dominated by direct tunneling, the barrier height plays a critical role. Also, at low bias, the current density depends on the average barrier height and the thickness d (Eq. 1.9).

$$j_{DT} \propto \frac{\sqrt{\phi}}{d} \exp[-d\sqrt{\phi}]V \qquad \text{Eq. 1. 9}$$

Therefore, a small change in the barrier height results in very large changes in the tunneling resistance. Pantel and Alexe[74] have calculated the effect of polarization reversal on the current density not only for direct tunneling but also for Fowler-Nordheim and thermionic emission in a ferroelectric tunnel junction. BTO layers with different thicknesses were taken into account, as shown in Figure 1.8(a). Note that by increasing the barrier thickness, thermionic injection becomes more relevant than DT and FNT. Indeed, Yoong et al.[18] considered only thermionic emission as a conduction mechanism in ≈ 10 nm thick HZO junctions. Figure 1.8(b) indicates that direct tunneling dominates at a small voltage region for a 3.2 nm FTJ, whereas FNT becomes more relevant at higher voltages. In conclusion, the purely electrostatic effect is supposed to be the main cause for high OFF/ON ratios measured in FTJ of different thicknesses.

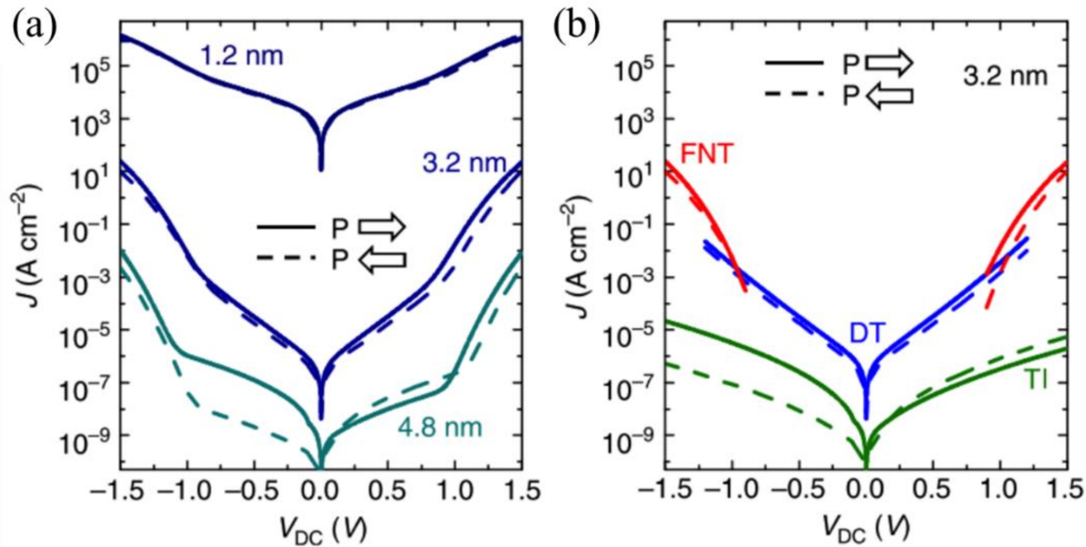

Figure 1. 8. Theoretical current densities considering direct tunneling (DT), thermionic emission (TI), and Fowler-Nordheim tunneling (FNT). (a) Current density (J) versus voltage (V) for 1.2, 3.2, and 4.8 nm BTO tunnel junction. (b) J versus V for 3.2 nm junction, showing the contribution of each conduction mechanism. The solid and dashed lines represent polarization P pointing right and left, respectively. Adapted from [37,74].

Atomistic interface effects

Previous studies have reported that the ferroelectric barrier can be modified due to electronic state change at ferroelectric/electrode interfaces. These researches were conducted by combining first principle calculations[77] and experimental results.[78] The ionic displacement induced in the ferroelectric material upon switching was responsible for resistive switching due to the bonding distance variation.

Piezoelectric strain effects

Under the application of an electric field, ferroelectric materials exhibit an inverse piezoelectric effect, causing a change in thickness and a change in the tunneling width.[79] Depending on the electric field's direction, the strain caused can be either compressive or tensile, i.e., increasing or decreasing the barrier thickness. As thickness is considered in the expression of tunneling conductance (Eq. 1.9), an exponential dependence of the resistance is expected. Kohlstedt et al.[72] have predicted resistance variations up to 70%. Ab-initio based calculations on symmetric FTJ suggested that the inverse piezoelectric effect could lead to resistance changes up to a factor of two.[80]

Ionic motion

In ferroelectric capacitors with thicknesses larger than 20 nm, the tunneling current is strongly suppressed. Nevertheless, they still present resistance changes when an external voltage is applied. It is believed that, in certain cases, the resistive switching could be due to the electric-field-driven motion charged defects through the ferroelectric. This motion could lead to the formation of conducting filaments[81,82] or changes at the Schottky barrier at the interface.[35,83] The coexistence of this effect and electrostatic switching in HZO ferroelectric capacitors[82] is essential, and it will be more discussed in section 1.5.

1.4. HfO_2-based oxides

The filament-based metal-oxides VCM implemented with various transition metal-oxides (HfO_2, ZrO_2, Ta_2O_5, TiO_2, etc.) has received considerable attention due to low power consumption, nanosecond switching, large endurance, and retention. HfO_2 has become one of the favorites in advanced transistor gate stack applications within this group, considering its high permittivity and bandgap, stability on silicon[84–87], and CMOS fabrication process compatibility. Also, HfO_2 has

one of the stronger oxygen affinities for transition metals and is relatively stable and compatible with most metals used in a clean room environment (TiN, TaN, W).[88–90]

The filament formation in HfO_2-based devices is discussed in terms of dielectric breakdown, i.e., an abrupt formation of an oxygen-deficient filament that is more conductive than the surrounding insulator matrix. After the forming step, the filament can be ruptured by inversion of voltage polarity. It has been reported that crystalline films' grain boundaries might play a critical role in forming conductive filaments. Grain boundaries are characterized by the mismatch angle created between crystal faces, and because of this, bonds between atoms can be broken, and atomic positions can move, leaving the possibility for the average charge of the electron clouds to vary in the area of the grain boundary. This is precisely what happens in high-temperature superconductors like $YBa_2Cu_3O_{7-\delta}$.[91] In yttria-stabilized zirconia (YSZ)[92] and $LaSrMnO_3$,[93–95] the presence of dislocations in the crystal structure often strongly affects the conduction properties of thin films due to the large ionic conductivity in these regions.

In HfO_2, the study with conductive atomic force microscopy (C-AFM) has allowed characterizing with nanometric resolution the conductivity of nano-crystals and grain boundaries (GB) in polycrystalline films.[96,97] It was found that the current preferably flows along with GB, which is also the preferential region for dielectric breakdown and filament formation. *Ab initio* calculations of the GB structure in monoclinic HfO_2 were employed, and it was found that segregation of vacancies is thermodynamically favorable.[98] At low vacancy concentration, individual defect states are introduced into the HfO_2 band gap. However, higher vacancy density leads to a conductive sub-band confined to the GB region due to overlapping of the localized Hf d-state in the HfO_2 band gap. This sub-band effectively constitutes a percolation path for the current flow, consistent with the C-AFM maps of leakage current and topography.[97,98]

1.4.1. Ferroelectricity in HfO_2 oxide

In 2011, Böscke et al. reported ferroelectric behavior in Si-doped HfO_2 oxide.[99] The bulk stable monoclinic HfO_2 phase was inhibited by deposition of a TiN top electrode, which caused mechanical encapsulation of the film and stabilized the orthorhombic phase. It was observed that the annealing step after top electrode deposition caused a non-linearity on the capacitance-voltage measurements. The $P(V)$ curves collected on samples with increasing Si content show a gradual transition from ferroelectric to an antiferroelectric character. Grazing Incidence X-ray diffraction

(GI-XRD) pattern of the structure matched an orthorhombic phase. Up to that moment, all reported HfO_2 bulk phases, including orthorhombic (space groups $p4_2/nmc$, $Fm\overline{3};m$, $P2_1/c$, Pbca, Pbcm) were centrosymmetric and, therefore, could not show ferroelectricity. A rare orthorhombic with space group $2bc2_1$, which is not centrosymmetric, has been reported in Mg stabilized ZrO_2.[100,101] Since the chemistry of HfO_2 and ZrO_2 are alike, similar crystalline phases are expected for both compounds. Sang et al.[102] have experimentally proved the existence of o-phase in Gd-doped HfO_2 thin film based on transmission electron diffraction (TEM) studies. By comparing the images collected with five orthorhombic space groups projected along four major zone axis, the authors concluded that, apart from eventual monoclinic grains, the o-phase present belongs to the non-centrosymmetric $Pca2_1$ space group.

Since then, HfO_2 has been doped with different elements such as Al,[103] Y, Zr,[104] Gd,[102] La, etc.[105] Even in undoped HfO_2, it is possible to achieve ferroelectricity by further reducing the film thickness and choosing proper processing conditions.[106] Specifically, Mueller et al.[103] explored the possibility of stabilizing the ferroelectric phase in Y-doped HfO_2 without the support of a mechanically confining top electrode. From the application point of view, these findings open avenues for this material to be applied in ferroelectric-base memories. Indeed, ferroelectric field transistors (FeFET) based on HfO_2 are now implemented in CMOS technology.[107–110] In these devices, the ON and OFF states originate from the metal-insulator-metal structure's different conductance associated with the ferroelectric polarization direction.

1.4.2. $Hf_{0.5}Zr_{0.5}O_2$ phase composition

Among the elements used as dopants, Zr is especially interesting to form $Hf_{1-x}Zr_xO_2$. The wide range of doping concentrating allows tunability of the material properties from dielectric with high dielectric constant ($x \approx 0$, HfO_2) to ferroelectric ($x \approx 0.5$) and antiferroelectric ($x \approx 0.8$), which performances are also dependent on the film thickness.[111] The ferroelectric behavior can be finely tuned by varying x around 0.5, but $Hf_{0.5}Zr_{0.5}O_2$ (HZO) seems to be the optimal composition.[104,112–114] The origin of ferroelectricity in the HZO fluorite structure has been largely investigated experimentally[102,114] and theoretically.[115] Its appearance is not a trivial problem, considering the intricate phase diagram of HfO_2 thin films. As a matter of fact, it is well known that these materials can organize in different phases depending on the temperature and pressure in which they are submitted. At atmospheric temperature and pressure, bulk HfO_2 adopts a monoclinic structure (m-

phase) with space group $P2_1/c$ (Figure 1.9(b)). Thus, this structure is centrosymmetric and does not support spontaneous polarization necessary. With increasing temperature, tetragonal (t-phase, space group $P4_2/nmc$, above 2050 K, Figure 1.9(a)) and cubic phase (c-phase, space group Fm-3m, above 2803K) can be stabilized.

When doped and confined, polycrystalline HfO_2 thin films transition to a non-centrosymmetric orthorhombic structure (o-phase). Figure 1.9(c,d) shows its crystal structure. Materlik et al.[115] suggested that o-phase can also be thermodynamically stabilized in $Hf_{0.5}Zr_{0.5}O_2$ atomic layer deposition (ALD) grown films. It was suggested that the bulk free energy and the surface energy of the o-phase have intermediate values between those of m- and t-phases, so the o-phase can be stabilized in a particular thickness and grain size. Park et al.[111] have suggested that, during a post-deposition annealing step, the HZO ALD grown films are mainly composed by t-phase. This phase transition to the bulk-stable monoclinic is highly unlikely due to a high kinetic barrier (t→m). However, the transition from t→o could occur during cooling due to the transition's negligible energy barrier. Under these particular conditions, the o-phase becomes stable at room temperature. Even though a full understanding of the ferroelectric phase stabilization in HfO_2-based films is still under investigation, it is clear that size effects (surface energies favors higher symmetry) and confinement strain (distortions favors lower symmetry) are essential in the evolution of the m-phase to the high-symmetry t-phase and polar o-phase. Ultimately, intrinsic (surface energies) and extrinsic (confinement strain) mechanisms can favor stabilizing the orthorhombic polar phase in fluorite structures.[116]

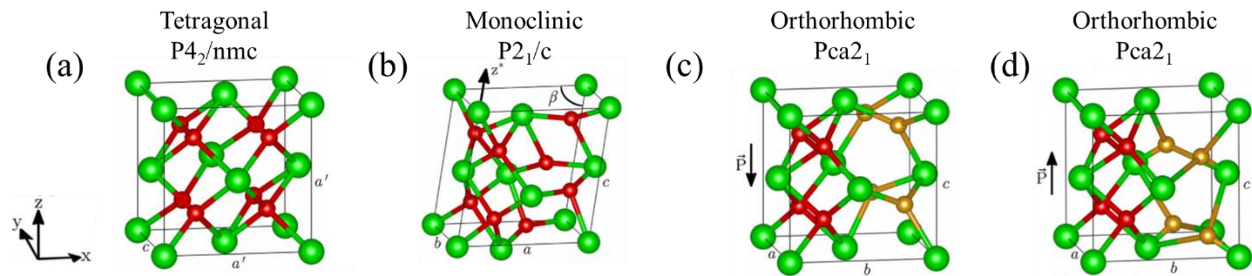

Figure 1. 9. Crystal phases are illustrated for ZrO_2, where Zr atoms are represented in green and O atoms in red. (a) Tetragonal structure with space group $P4_2/nmc$. (b) Monoclinic phase with space group $P2_1/c$, where $\beta = 80º$. (c, d) Non-centrosymmetric orthorhombic phase with space group $Pca2_1$ in which polarization is observed for [001] and [00$\bar{1}$] directions, respectively. The O atoms believed to be responsible for the polarization are highlighted in gold. Adapted from [115].

Polycrystalline HZO films can contain a mixture of different phases, making it difficult to explore

ferroelectricity's fundamental mechanisms.[117] Furthermore, strong "wake-up" and fatigue effects are observed in these films and can affect FE-based memory devices' performance.[118,119] In this scenario, epitaxially grown HZO films rise as a great opportunity to control the ferroelectric and dielectric properties for memory applications. Indeed, ferroelectric HZO films have been successfully epitaxially grown in yttria-stabilized zirconia (YSZ),[117,120–122] $LaAlO_3$,[18] $SrTiO_3$,[123–125] and Si substrates.[116,126] However, Lyu et al. have demonstrated that HZO films grown on STO substrates exhibit XRD peaks corresponding to monoclinic (002) and (-111) reflections as well as the (111) reflections of o-HZO.[123]

Subsequently, Estandía et al.[53] have pointed out that the microstructure of epitaxial HZO film is composed of m- and o- grains that could be modulated by the appropriate choice of the substrate. Thin HZO epitaxial films have been grown on a $La_{2/3}Sr_{1/3}MnO_3$ buffered substrate in which a set of single-crystalline oxide substrates with a wide range of lattice parameters. It was found that the substrate exerts a compressive or tensile strain in the $La_{2/3}Sr_{1/3}MnO_3$ (LSMO) bottom electrode film. This strain state strongly influences the formation of the orthorhombic and monoclinic phases in the HZO because the electrode is the epitaxial template on which HZO grows. Figure 1.10(a) shows a sketch with the single crystalline (001)-oriented substrates used. The lattice mismatch corresponds to the mismatch between LSMO and the substrate calculated by $f = 100 \cdot (a_s - a_{LSMO})/a_{LSMO}$, where the a_{LSMO} and a_S are the lattice parameters of bulk LSMO and substrate, respectively. A structural investigation of the HZO film by X-ray diffraction (XRD) and scanning transmission electron microscopy (STEM) demonstrated that the orthorhombic phase is strongly favored with respect to the monoclinic for increasing substrate lattice parameter as long as the fully strained state of the LSMO is maintained.

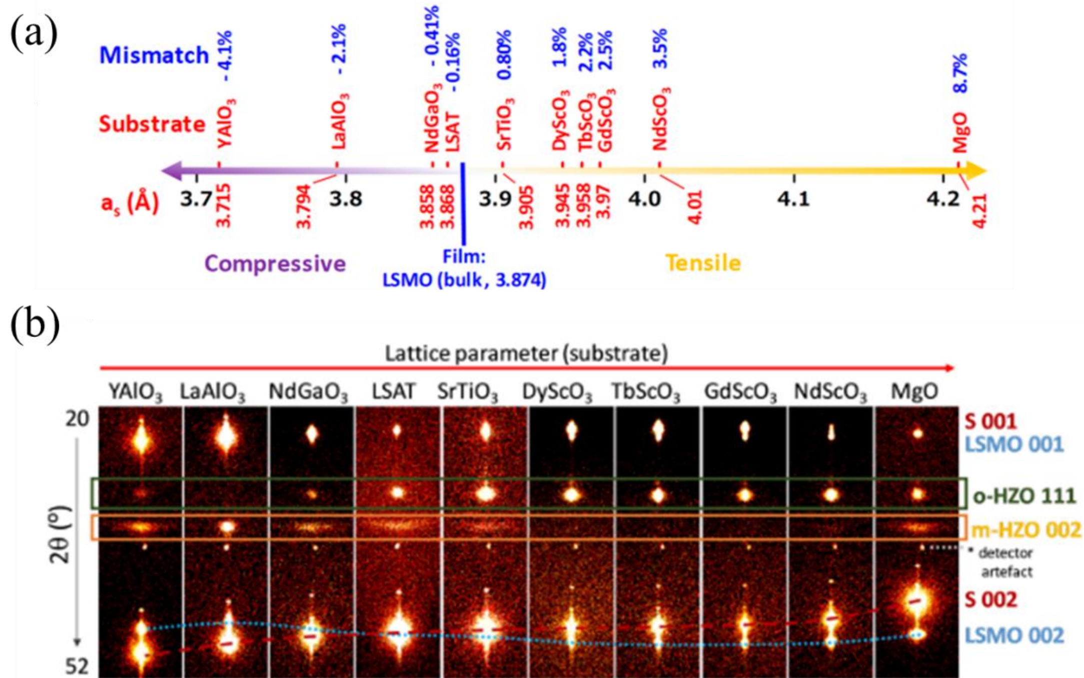

Figure 1. 10. (a) Sketch showing the lattice mismatch between the LSMO electrode and the substrates. (b) X-ray diffraction 2θ-χ frames of the HZO/LSMO bilayers. Intense diffraction peaks from the substrate and LSMO can be identified. The o-HZO (111) peak is a bright circular spot in the films grown in most substrates, whereas the m-HZO (002) reflection is generally elongated along χ, signaling higher mosaicity. Adapted from [53].

Figure 1.10(b) displays XRD 2θ-χ frames collected on HZO/LSMO grown on different substrates. The (001) and (002) strong reflections of the substrate (S) and LSMO electrode can be identified. The bright circular spot from the o-HZO (111) reflection can be observed, whereas the m-HZO (002) is generally elongated in χ, signaling higher mosaicity. This analysis indicates that the orthorhombic phase is favored on substrates with a large lattice parameter, while the monoclinic increases when the lattice parameter of the substrate is smaller. The films on substrates with very large (MgO) or very small ($YAlO_3$) lattice parameters do not follow this tendency, which is probably related to plastic relaxation of the LSMO and no transfer of strained template to the HZO film. Therefore, it was possible to conclude that the ratio of o-/m-HZO phase composition is dependent on the substrate in which the film is deposited. Also, XRD pole figures around asymmetrical o-HZO (-111) and m-HZO (-111) reflections indicate the existence of four crystal variants with 90º rotation in the plane for both phases. Therefore, in a thin film, grains with different orientations in the plane are visible.[53]

1.4.3. Ferroelectric properties of HZO

Understanding how the HZO microstructure impacts the ferroelectric properties is pivotal for optimizing HfO_2-based memory performance. Indeed, it has been shown that the remnant polarization (P_R) of HZO films increases for lower thickness in epitaxial[125,127] and polycrystalline films.[128,129] Lyu et al.[127] reported that P_R decreases from ≈ 25 μC·cm^{-2} to ≈ 14 μC·cm^{-2} when increasing the thickness from 6.9 to 13.8 nm in epitaxial HZO films grown on LSMO/STO buffer, as shown in Figure 1.11(a). Figure 1.11(b) demonstrates that the epitaxial HZO layers with 9 nm thick grown on different substrates display very different remnant polarization even though the coercive voltages are similar (V_c ≈ 2 – 3 V). Also, in epitaxial HZO, Wei et al.[125] observed a reduction from 34 μC·cm^{-2} to 18 μC·cm^{-2} in the remnant polarization by increasing the thickness from 5 to 9 nm. In the last case, the epitaxial films are claimed to be composed of a rhombohedral polar HZO phase.

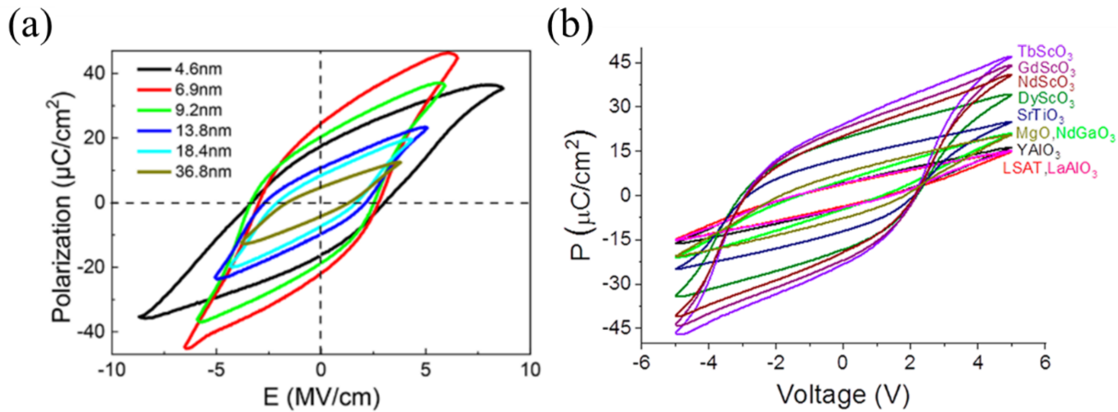

Figure 1. 11. (a) Polarization curves dependent on the external electric field recorded at 1 kHz in Pt/HZO/LSMO//STO epitaxially grown films. Taken from [127]. (b) Polarization-voltage curves collected in Pt/HZO (9.5 nm)/LSMO heterostructures epitaxially grown on different substrates as indicated. Taken from [53].

A major issue for the application of HZO in memory devices is related to poor endurance and possible wake-up effect. Poor endurance is usually related to two phenomena: fatigue effect or hard breakdown of the dielectric. The first one consists of the gradual decrease of the ferroelectric remnant polarization with the number of cycles,[105,130] resulting in loss of the information recorded. The second is related to a dramatic increase of leakage current with field cycling, suppressing the film's ferroelectric properties.[19,131] Recently, Lyu et al.[19] have reported optimized endurance properties of epitaxial HZO integrated into Si substrates, proving HfO_2-based

memories are promising.

On the other hand, the wake-up effect can be described by a remnant polarization increase with the increasing cycling number. This effect corresponds to an opening or de-pinching of the pristine hysteresis loop with field cycling.[130] For the sake of illustration of these effects, Figure 1.12(a) shows the current-voltage curves in Sr-doped HfO_2 thin films in three different stages (pristine, woken-up, and fatigued), while Figure 1.12(b) displays the changes in P_R due to fatigue and wake-up. The switching current curve has two peaks in the pristine state in both negative and positive electric fields (blue curve). During the field-cycling, these switching peaks merge (wake-up, black curve), increasing the P_R in Figure 1.12(b). With further cycling, the switchable polarization decreases (red curve), which corresponds to the fatigue effect typical in many ferroelectrics.

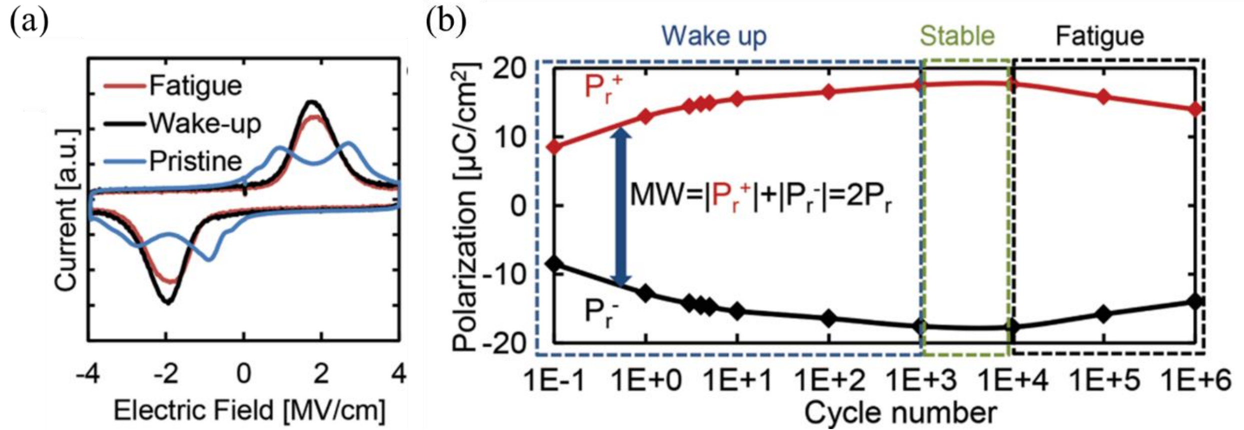

Figure 1. 12. (a) Current-voltage curve collected in Sr:HfO_2 for pristine, woken-up, and fatigued states. (b) Extracted dependence of positive and negative remnant polarization with the number of cycles. Adapted from [130].

Investigations conducted with first-order reversal curve (FORC) measurements indicated an inhomogeneous internal electric field could lead to a split pristine switching peak.[130] The microscopic origin is related to charged defects, such as oxygen vacancies, that are asymmetrically distributed through the film.[105] Indeed, a high oxygen vacancy concentration is expected near the electrodes due to HfO_2 reduction by the metallic electrodes. During the electric field cycling, the oxygen vacancies are redistributed within the device, and the electric field can be distributed evenly, accompanied by the merging of the switching current peaks.[130] Another possible mechanism of the wake-up effect is a field-cycling-induced phase transition. Lomenzo et al.[132] first suggested a phase transition from tetragonal to orthorhombic phase as the origin of observable

wake-up effect in ferroelectric HfO_2. Indeed, Pešić et al.[130] observed a phase transition from the monoclinic to the orthorhombic phase using STEM. Figure 1.13(a, b, c) shows cross-sectional TEM images of the pristine, waken-up, and fatigued, respectively, of polycrystalline Gd:HfO_2 film neat the TiN top electrode. In the pristine state, the interfacial region is highly defective, and the crystalline structure was identified to be tetragonal, whereas the dominant crystalline phase in the bulk region was monoclinic. After electric cycling, the thickness of the highly defective interface decreased, and the dominant crystalline phase of the bulk transitioned to orthorhombic, even though there was still a track of tetragonal phase at the interface. The fatigued sample shows no tetragonal phase.

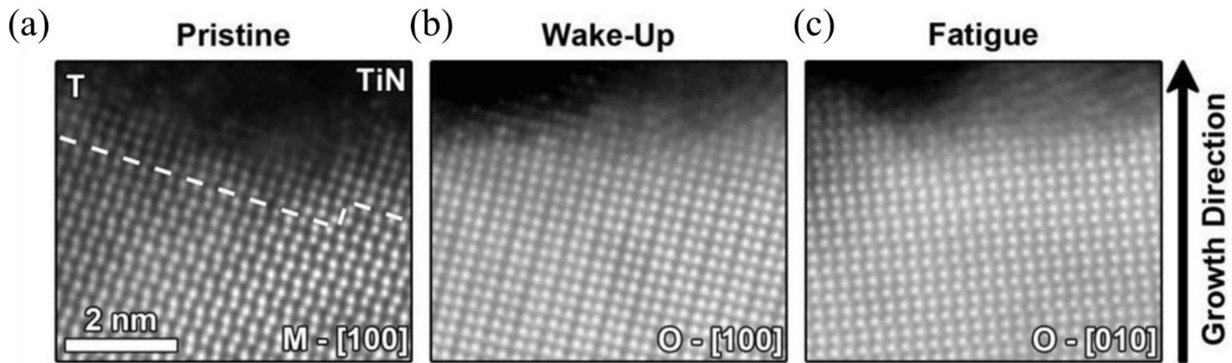

Figure 1. 13. Cross-section STEM images on Gd:HfO_2 in the (a) pristine, (b) wake-up, and (c) fatigued states showing the transition of the bulk monoclinic and the tetragonal at the interface with the electrode to orthorhombic. Taken from [130].

It has been suggested that oxygen vacancies might play a critical role in the HfO_2-based phase transition. Hoffmann et al.[133] have investigated the free energies of crystalline phases of HfO_2 computationally and found out that they are affected by oxygen vacancy concentration. The high concentration taken into account is unreasonable for the entire thin film, but it might be possible at interfacial regions that generally contain more defects than the bulk.[105] Park et al.[134,135] reported that the cycle numbers required for waking up polycrystalline HZO thin films decrease with increasing annealing temperature and concluded that a phase change from tetragonal to orthorhombic phase takes place in HZO. Ultimately, evidence of the wake-up effect for different doping elements in polycrystalline HfO_2 indicates that the wake-up effect can be attributed to the redistribution of oxygen vacancies or phase transformation from non-FE to FE phase by repetitive electrical field cycling.[105,135–138]

The wake-up effect in epitaxial HfO_2-based films is hardly reported. Lyu et al.[19] have observed wake-up only in 4.6 nm HZO film integrated epitaxially in Si (001) substrate. Yoong et al.[18] has shown that 10 nm HZO grown on LSMO/LAO buffered substrates required around 100 cycles to achieve maximum remnant polarization, which was associated with oxygen vacancy redistribution. In order to identify possible causes for wake-up STEM cross-section images can be used, as in the report from Pešić et al.,[130] to monitor possible phase transition in epitaxial HZO films that could lead to a wake-up effect. Regarding wake-up driven by redistribution of oxygen vacancies, a careful analysis must be performed. As mentioned previously, ionic motion is enhanced in HfO_2-based oxides grain boundaries, and not even epitaxial films can avoid grain boundary formation. Therefore, they may act as active sites for ionic motion and possible wake-up. A detailed discussion about this effect will be explored in Chapter 5.

1.5. Coexistence of FE switching and non-FE switching

Several studies in asymmetric junctions composed of $BaTiO_3$, $PbTiO_3$, $PbZr_xTi_{1-x}O_3$, and $BiFeO_3$ barriers associated the resistive switching with the incomplete screening of polarization charges at the barrier/electrode interfaces.[54,55] The electrode asymmetry ensures a different screening length, and the asymmetric deformation of the barrier potential leads to electroresistance associated with polarization reversal. However, other purely electronic effects like electrostatic charge modulation in manganite electrodes or defects motion could lead to resistive switching in ferroelectric capacitors. Indeed, it is well established that voltage-driven oxygen vacancy migration results in resistive switching in complex oxides with perovskite structures, such as $Nb:SrTiO_3$ and $BiFeO_3$,[139,140] and transition metal oxides like HfO_2, TiO_2, TaO_2, CuO.[24] The formation energy for charged oxygen vacancies is generally low,[141–143] making it difficult to avoid their presence in oxide films, which increases the sensitivity to redox-related resistive switching. Moreover, Strukov and Williams[144] have suggested that an exponential enhancement of oxygen vacancy drift velocity in large electric fields can induce switching in the nanosecond range, even though thermally activated diffusion at room temperature is negligible. This mechanism is particularly relevant in tunnel junctions, as the used electric fields can easily exceed 10 $MV{\cdot}cm^{-1}$.[145]

Because of the nearly identical features of electronic and ionic switching processes, it is challenging to distinguish them. Coincident polarization and resistive switching in ferroelectric capacitors, for example, are not sufficient proof of a purely electronic effect since the screening of

polarization charges by redistribution of oxygen vacancies can be effective too.[146–148] Besides, as investigations in HfO_2-based devices pointed out, the presence of grain boundaries is pivotal in the formation of conductive filaments that can result in sDB resistive switching.

Therefore, a detailed investigation must be executed to evaluate if the electroresistance observed is indeed related to the barrier's modulation due to polarization reversal and not due to ionic motion. During this thesis, this discussion will be done in the context of ferroelectric HZO tunnel junctions. However, in this section, some examples of the coexistence of genuine ferroelectric switching and ionic-related switching will be discussed in classical perovskite oxides as well as in doped-HfO_2 thin films.

1.5.1. Perovskite oxides

Perovskite oxides have a general formula of ABO_3 where A and B designate electropositive elements forming cations that transfer electrons to the oxygen. In undistorted highly-symmetric cubic unit cells, the A-cations occupy the cube corners, and the B-cations are located in the cube center. The oxygen anions are face-centers so that they form an octahedron around the B-cation. Distortions of the ideal cubic structure and orbital hybridization between oxygen atoms and the A- or B-site cations can lead to ferroelectric properties in $BaTiO_3$, $BiFeO_3$, and $PbZr_xTi_{1-x}O_3$.[75] In this section, the resistive switching mechanism reported in paraelectric (LSMO, STO) and ferroelectric perovskites (BTO, BFO, PZT) will be detailed. In the latter, the coexistence of FE and non-FE resistive switching will be summarized.

LSMO

The chemical formula of LSMO can be expressed as $La_{1-x}Sr_xMnO_3$. The mixed occupancy of A site in perovskite structure by La^{3+} and Sr^{2+} cations induces a mixed-valence state in the Mn cation with Mn^{3+} and Mn^{4+}. The oxygen content influences the magnetic and electrical properties by changing the Mn^{4+}/Mn^{3+} ratio.[149–151] For instance, oxygen vacancies decrease the effective hole concentration, leading to higher electrical resistivity.[145] If the hole concentration change is sufficiently large, a metal-to-insulator phase transition occurs. Moreover, a high concentration of oxygen vacancy in LSMO can trigger a structural phase transition from a perovskite lattice to a Brownmillerite superstructure [152–154], accompanied by a dramatic increase of electrical resistivity. Besides, Gonzalez-Rosillo et al.[151,155] have reported resistive switching in bulk LSMO due to

oxygen exchange with the environment or with a capping CeO_{2-x} layer. These mechanisms can, therefore, cause resistive switching in LSMO thin films.

$SrTiO_3$

Szot et al.[156] have reported that epitaxial STO thin films grown on $SrRuO_3$-buffered STO single crystals display resistive switching characteristics. Local conductive atomic force microscopy images demonstrate the formation of conductive filaments in the whole extension of the film. The authors argue that the high concentration of vacancies induces a current-driven redox process which induces a local metal-to-insulator transition. On the other hand, Qin et al.[145] explored resistive switching properties in LSMO/STO/LSMO tunnel junction and correlated this effect with oxygen vacancy migration across the LSMO/ferroelectric bottom interface.

$BaTiO_3$

In the same work, Qin et al.[145] compared the resistive switching effects in BTO and STO tunnel junctions and found out that the resistance dependence on voltage collected in both oxides shows similar coercive fields and ON/OFF ratio. Moreover, the ON/OFF ratio for increasing barrier thickness decreases monotonically, which is not expected for purely polarization-induced electrostatic charge modulation.[55,157] The similarities were claimed to be due to a field-controlled motion of oxygen within the LSMO layer that produces a hole-depletion barrier, resulting in metal to insulator transition associated with increasing the tunneling barrier. It has been demonstrated that when a large concentration of oxygen vacancies is present in BTO films, redox-related resistive switching can be recognized.[32,158]

Qian et al.[35] have reported the coexistence of electroresistance due to polarization reversal and from ionic motion. The electroresistance response dependence on the writing pulse duration indicated that short writing pulses induce ≈ 100 % electroresistance in Pt/BTO/LSMO heterostructures, whereas longer writing times result in ≈ 4600 % *ER*. Temperature-dependent electrical measurements display a dependence on the critical time scale to observe either one effect or another, suggesting a thermally activated ionic motion process. It was argued that for short writing pulses, the Schottky barrier between ferroelectric/electrode is modulated by the polarization, resulting in a low ER effect. However, for long writing times, a larger modification of the barrier occurs due to the accumulation of oxygen vacancies at the interface and, even though

the ferroelectric character of the film is preserved, the *ER* takes place due to larger modulation of the barrier due to ionic motion.

In the study of memristive effects of Co/BTO/LSMO, Kim et al.[54] have pointed out that oxygen vacancy mobility induces the Co electrode's oxidation creating a CoO_x/BTO interface. In this case, the extra dielectric layer at the interface leads to less effective screening of the ferroelectric depolarizing field, affecting the retention of the ferroelectric-related resistive switching effect. The modulation of the barrier height and CoO_x width caused by the external voltage is discussed, but an independent resistive switching related to ionic motion is not detailed.

$BiFeO_3$

Y.-M. Kim et al.[147] have reported that the accumulation of vacancies at the interface LSMO/BFO strongly affects polarization switching phenomena. The redistribution of vacancies accompanies the switching process either into the LSMO phase or within the BFO matrix. This process is limited by vacancy transport times, and it has impacts on the ferroelectric switching kinetics.

In the study of thick polycrystalline BFO junctions, Cardona Rodríguez et al.[159] observed a resistive switching effect even after the ferroelectric was fully saturated, indicating the coexistence of electroresistance due to FE and non-FE origin. Indeed, it has been suggested by conductive AFM images that redistribution of oxygen vacancies within grain boundaries could play a key role in resistive switching behavior in polycrystalline BFO films.[140]

$PbZr_xTi_{1-x}O_3$

Resistive switching in ferroelectric PZT has been explored for many years in capacitor structures and nanotubes. Nonnenmann et al.[160] reported resistive switching in ferroelectric perovskite PZT nanotubes related to the formation of conductive filaments in the film. Their analyses of current-voltage curves of Pt/$Pb(Zr_{0.52}Ti_{0.48})O_3$/Pt junctions have shown that a higher conduction state is stabilized for samples annealed in a low oxygen partial pressure atmosphere which coincided with the enhancement of resistive switching effect. It was argued that the annealing in an atmosphere with an oxygen deficit promotes the formation of oxygen vacancies, and their voltage-driven motion creates nanometric conductive filaments within grain boundaries of polycrystalline PZT.

On the other hand, Kohlstedt et al.[161] have investigated the coexistence of ferroelectric and non-

ferroelectric resistive switching in epitaxial $Pb(Zr_{0.2}Ti_{0.8})O_3$ capacitors. By simultaneous measurements of the current through the capacitor and its piezoelectric response, it was detected that the coercive field of the ferroelectric was different from the voltage necessary to induce resistive switching with non-FE origin. Also, the results have shown that ferroelectricity is an independent phenomenon from resistive switching.

The work of Qin et al.[145] in LSMO/$Pb(Zr_{0.2}Ti_{0.8})O_3$/LSMO tunnel junctions have concluded that the origin of the resistive switching was a field-controlled motion of oxygen within the LSMO layer and not the polarization reversal of the ferroelectric. The creation of a hole-depletion barrier results in metal-to-insulator transition associated with increasing the tunneling barrier that causes resistive switching.

1.5.2. HfO_2-based films

In the case of ferroelectric HfO_2-base oxides, this discussion has not been largely established as this material's ferroelectric properties have just been recently explored for memory applications. Indeed, tunnel junctions involving ferroelectric polycrystalline and epitaxial HfO_2 barriers have shown electroresistance effects in several reported works.[82,162–165] However, the available data do not allow to indisputably conclude if polarization-related effects directly govern the observed ER or result from electric-field induced charge motion. For example, Ambriz-Vargas et al.[16,162] reported current-voltage curves on 2.8 nm thick polycrystalline HZO barriers. Even though the $I(V)$ curves were dramatically different after a positive and negative writing step, the data did not allow robust extraction of the barrier parameters and possible change due to polarization reversal. Also, Yoong et al.[18] reported $I(V)$ data on HZO epitaxial barriers of about 10 nm thick and corresponding $P(V)$ curves. Transport data were analyzed using thermionic emission over a polarization-modulated barrier since direct tunneling across the barrier is unlikely. It was observed that the properties of the barrier were significantly different depending on the magnitude of the writing voltage, whereas, in the same voltage range, the polarization loop appeared to be saturated. This evidence suggests that the barrier properties are not only dictated by polarization, but other mechanisms may be relevant.

The years of research in non-ferroelectric HfO_2 ReRAM have allowed gathering information about the correlation of structural defects and conduction properties in polycrystalline films. Iglesias et al.[166] have demonstrated that highly conductive and breakdown sites are concentrated mainly at

grain boundaries of polycrystalline HfO_2. Also, Bersuker et al.[97] have shown that, in monoclinic HfO_2, the formation of a conductive filament is responsible for resistive switching, and grain boundaries play a crucial role. These grain boundaries are still present in ferroelectric HfO_2 films, even in epitaxial ones. Fundamental differences in the physical mechanism of resistive switching due to filament formation and ferroelectric switching prohibit a straightforward combination of these two concepts in one memory device. Nevertheless, one can influence the observation of the other, and interpretations of resistive switching in HfO_2-based oxides can be mistakenly attributed to ferroelectricity when RS is responsible.

Starschich et al.[136] shown that ferroelectric and resistive switching within one capacitor structure could be independently observed. Nevertheless, they were not interchangeable, i.e., either ferroelectric switching was achieved by short voltage pulses or filament formation was induced by applying longer voltage pulses. On the other hand, Mikheev et al.[167] reported the coexistence of ferroelectric and non-ferroelectric resistive switching in one polycrystalline 4.5 nm thick HZO capacitor. The external voltage was the control parameter for observing one or other effect in p^+Si/HZO/TiN junctions. For low voltages, mobile charged oxygen vacancies drift and create a depletion/accumulation layer at the Si interface, causing changes in the effective potential barrier height. When larger voltages are applied and coincide with the coercive field of the ferroelectric, electrostatic modulation of the barrier height due to polarization reversal is observed.

Max et al.[82] also demonstrated that both effects could be stabilized in the same HfO_2-based device. The analysis in TiN/Sr:HfO_2 (12 nm)/Pt devices was performed in terms of the current contributions during each effect. It has been found out that the order of appearance of FE or non-FE switching was crucial. If a filament was formed inside the capacitor and resistive switching occurs before, no ferroelectric switching could be measured. The reason is that even in HRS, the current through the partially destroyed filament is much higher than the displacement current of the ferroelectric. However, if ferroelectric switching was stabilized first, then resistive switching could be induced later. Also, the voltage pulses applied have a big impact. A short triangular-shaped pulse induces ferroelectric switching in a pristine capacitor without dielectric breakdown in the first step. A clear wake-up effect was observed, and a large number of cycles needed to be applied (10^5 cycles) to stabilize the remnant polarization ($\approx 12\ \mu C.cm^{-2}$). Next, quasi-static long voltage pulses were employed to induce redox reactions and create conductive filament. At this

point, the ferroelectric switching was substituted by a filament formation/destruction resistive switching. In some devices, the breaking of the filament was accompanied by a dramatic decrease of current that the authors associated with a hard breakdown that homogeneously diffused oxygen vacancies and ensured a complete dissolution of the filament. The authors claimed that this hard breakdown was possible due to the previous cycling to stabilize the remnant polarization that led to a strong oxygen depletion close to the interface, which prohibited the filament's reformation. This ensured a very low conductivity in the HRS, and ferroelectric switching could be induced in the device afterward. In such polycrystalline films, the filaments presumably were formed within grain boundaries, as oxygen and vacancies have lower activation energy to move in this region.[168,169] Ferroelectric characterization obtained after the hard breakdown shows remnant polarization of 5 $\mu C.cm^{-2}$ without significant variations in the coercive field. Also, no relevant wake-up at this stage was observed, and the endurance of P_R value was larger than 10^5 cycles. Ultimately, ferroelectric cycling enabled the redistribution and generation/recombination of oxygen defects, influencing resistive switching properties.

This work ultimately shows that resistive switching due to ferroelectric switching and ionic motion can coexist in ferroelectric HfO_2-based capacitor. Therefore, when investigating electroresistance in $Hf_{0.5}Zr_{0.5}O_2$ epitaxial tunnel junctions, the devices' electrical characterization must be meticulous in identifying the mechanism responsible for changes in resistance indisputably. By correctly addressing the ER effect to either resistive or ferroelectric switching, one can compare the results with similar literature systems and optimize the electrical response parameters due to polarization reversal.

Chapter 2. Experimental Methods

A ferroelectric (FE) material can switch its polarization direction when submitted to an external electric field. In a ferroelectric capacitor, the following sequence probes the amplitude and direction of polarization (*P*): 1) a large voltage (+ V_{max}) is applied in one electrode while the other is grounded, which creates an electric field (*E*) inside the material and aligns FE in this direction. 2) The voltage decreases until it reaches equal voltage but in opposite polarity (- V_{max}), inverting the electric field's direction and causes polarization switching. 3) The voltage returns to its initial value (+ V_{max}), and the FE restores its initial polarization direction. In order to assess the changes in P, one can monitor the current response from the system and measure an *I*(*V*) curve, which contains contributions from polarization reversal, displacement from the capacitor, and leakage current. By integrating this current in time, the polarization dependence on the external voltage can be calculated, i.e., a *P*(*V*) curve. Different measurement techniques to acquire *I*(*V*) curves are described in this chapter.

As described in the Introduction, in a FTJ, the polarization modulates the barrier height at the interface ferroelectric/electrode, which affects the electron tunneling conduction and, thus, the junction's resistance. The technique to measure the resistance dependence on the electric field and electroresistance is described below. Besides, the technique used to grow epitaxial thin films by pulsed laser deposition (PLD) will be detailed. Structural analysis methods used along with the thesis, like atomic force microscope (AFM), piezo force microscope (PFM), X-ray diffraction (XRD), X-ray reflection (XRR), and scanning transmission electron microscopy (STEM) are summarized.

2.1. Sample fabrication

The ferroelectric tunnel junctions studied here have the structure of a plano-parallel capacitor in which a ferroelectric film with thickness *t* is sandwiched between two metal electrodes. The area of the junction is defined by the top electrode extension, as seen in Figure 2.1. This structure allows the measurement of the polarization of the film and the electric transport of the stack. In this thesis, the HZO ferroelectric film is sandwiched between a $La_{2/3}Sr_{1/3}MnO_3$ (LSMO) film bottom electrode and a platinum top electrode.

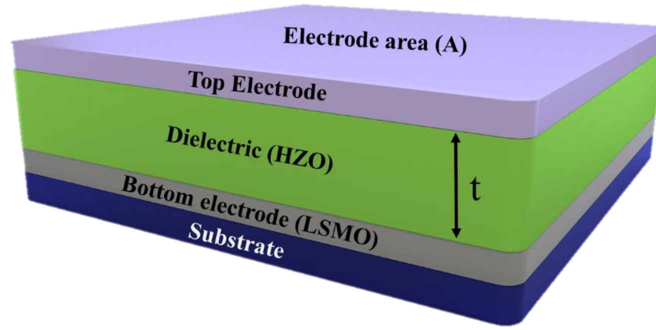

Figure 2.1. Sketch of a plano-parallel capacitor with area A.

Epitaxial layers of LSMO and $Hf_{0.5}Zr_{0.5}O_2$ (HZO) have been grown in a single process by pulsed laser deposition (PLD) using a suitable substrate. The single crystalline substrates used are (001) oriented cubic $SrTiO_3$ (STO), $(LaAlO_3)_{0.3}(Sr_2TaAlO_6)_{0.7}$ (LSAT), (110) oriented $GdScO_3$ (GSO), and $TbScO_3$ (TSO) (pseudocubic setting is used for scandates).

2.1.1. Pulsed laser deposition (PLD)

This physical vapor deposition (PVD) technique employs a high-power KrF excimer laser beam (λ = 248 nm, pulse width ≈ 10 - 40 ns) focused on the ceramic target inside the vacuum chamber. The laser spot area is measured right before entering the chamber, at the UV window, and corresponds to 2 mm^2. The calibration of the system indicates a laser fluence of 2 $J\cdot cm^{-2}$ arriving at the target.

The vacuum chamber is filled with oxygen with determined oxygen partial pressure (P_{O2}) during the film deposition, and the target is connected to a DC motor to create a constant speed rotation to ensure uniform ablation. As the target material is ablated by the lased, it vaporized into a plasma. The generated plume, which composition is the species to be deposited, expands perpendicularly to the target's surface until it arrives at the substrate placed at a certain distance. The oxygen pressure is optimized to achieve the film's correct stoichiometry. The sample holder is kept at a specific temperature to allow atoms rearrangement and nucleation on the substrate's surface. Further details of the technique can be found elsewhere.[170] A sketch of the PLD setup and a photo taken during a deposition at ICMAB is shown in Figure 2.2.

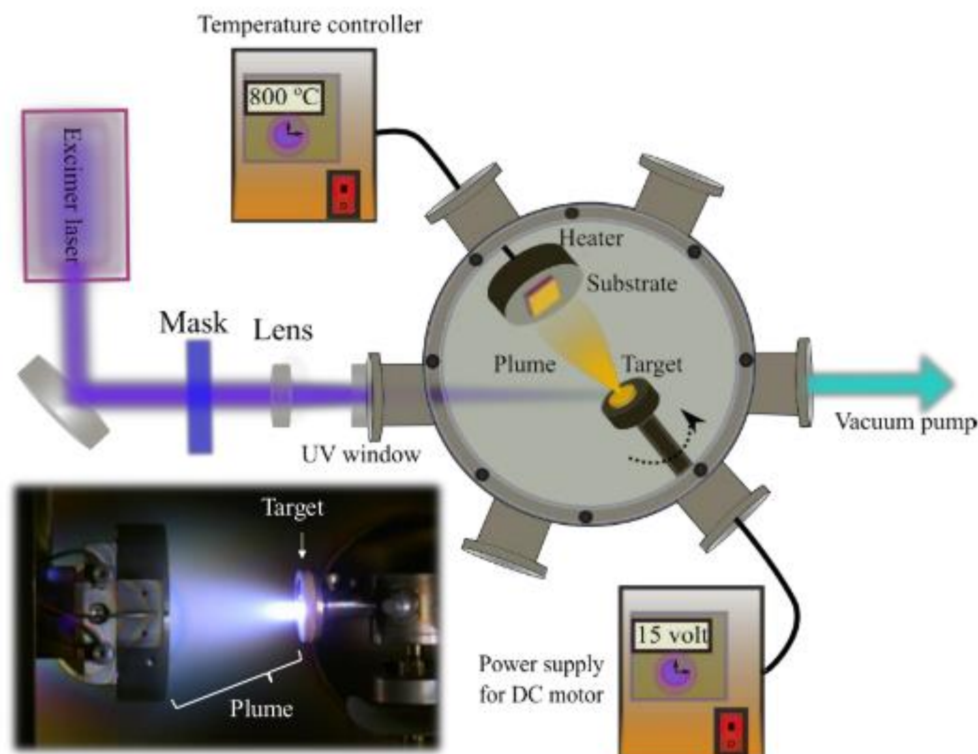

Figure 2. 2. Sketch and photo of PLD setup at ICMAB. Adapted from [76].

The critical parameters for the film growth are substrate temperature, gas pressure, and laser frequency. During this work, films of LSMO, HZO, $SrTiO_3$, and AlO_x layers were grown, and the optimized parameters for deposition are shown in Table 2.1. Further details can be found in references [127,131].

Material	Temperature (ºC)	Oxygen pressure (mbar)	Laser frequency (Hz)
LSMO	700	0.1	5
HZO	800	0.1	2
STO	700	0.02	2
AlO_x	Room Temperature	0.1 * (Ar)	5

*Table 2. 1. Deposition parameters for oxides. The AlO_x layer is amorphous, and the gas inside the chamber was argon, as indicated with an *.*

The number of PLD pulses controls the thickness of the films, and the growth rate (nanometers / PLD pulse) was calculated using XRR measurements. Details of this technique are in section 2.3.3.

2.1.2. Top electrode fabrication

Platinum top electrodes were deposited ex-situ by rf sputtering. XRR was also used to estimate the deposition rate. Platinum, being a noble metal, has good chemical and electric stability and is easy to grow without impurities. It is also appropriate for ferroelectricity and transport measurements.[171] The sputtering deposition is performed inside a vacuum chamber. Therefore, after positioning the substrate inside, the chamber is evacuated. When the pressure reaches ~10^{-6} Torr, argon is injected at constant flux. Then, the shield around the platinum target is charged negatively (cathode), whereas the sample holder is charged positively (anode). The electrically neutral argon gas atoms are ionized in collisions with the shield's surface, which creates a plasma. The ionized atoms are accelerated towards the cathode, ejecting materials from the target. Ions ejected from the target are attracted towards the anode and condensate on the substrate to be coated.

In this thesis, the platinum was deposited on the HZO films through TEM grids that work as a shadow mask. The mask is attached to a metallic holder to avoid bending. This holder is fixed accordingly to the sketch in Figure 2.3(a). The chosen grid allows 400 electrodes to be deposited simultaneously with a diameter of 20 µm, being 10 µm apart from each other. The deposition happens with a sputtering power of 20 W, 10 sccm Argon flux, at room temperature, and distance target-sample equals 5 cm. The resulting platinum thickness is 20 nm for all samples.

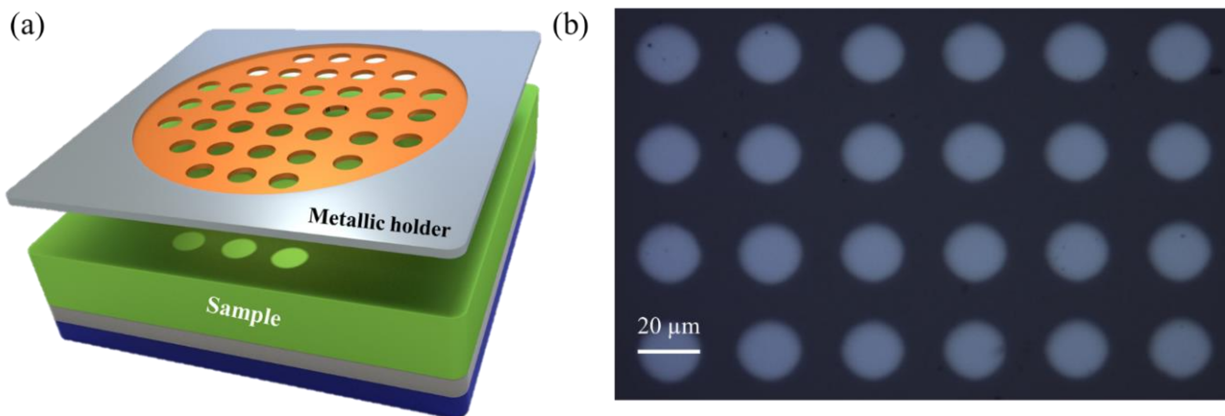

Figure 2. 3. (a) Sketch of deposition arrangement of platinum top electrodes using sputtering. (b) Optical microscopy of Pt circular electrodes with a diameter of 20 µm.

2.2. Electric characterization

This section describes the measurement setup and the electrical characterization techniques employed to study FTJ. The current response of a ferroelectric junction carries ferroelectric and

non-ferroelectric contributions. The ferroelectric term can be used to extract information from polarization switching. The non-ferroelectric term (leakage, charging/discharging of the capacitor) brings information about the dielectric. Nevertheless, if not correctly understood, they can cause the wrong estimation of coercive field and remnant polarization of the ferroelectric.

Resistance measurements in FTJ and its dependence on the external voltage are also disclosed. This technique takes advantage of the tunneling current through the ferroelectric film and is called electrical transport measurements.

2.2.1. Measurement configuration

The way the electrodes of the capacitor are electrically connected is called the measurement configuration. In this thesis, the appropriate configuration is top-bottom, in which the voltage is applied to the top electrode, whereas the bottom one is grounded, as Figure 2.4 indicates. Considering the different metals composing the electrodes, the two interfaces (electrode 1/ferroelectric and ferroelectric/electrode 2) are different.

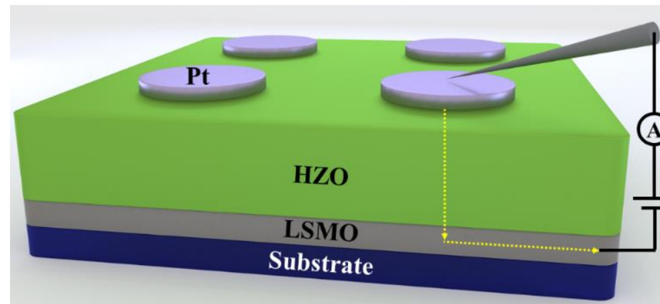

Figure 2. 4. Top-bottom configuration for electric connections used to measure ferroelectric and transport measurements.

2.2.2. Experimental setup

This system consists of two parts: the probe station and the voltage and current source equipment. The probe station is fixed on a mechanical vibration insulating base (CCR Series) from Janis and Lakeshore companies. The sample holder is electrically isolated, and the cable connections are coaxial to allow high sensitivity of current. Moreover, the Faraday cage provided by the vacuum chamber also avoids interference from environment electric fields.

2.2.2.1. Probe station

The system used is a Lakeshore EMPX-HP multifunctional probe station. Samples can be measured in vacuum up to 10^{-6} mbar and in a temperature range from 5 K to 650 K. However, an air atmosphere and room temperature environment were set as standard conditions unless other specific parameters are indicated.

The sample is positioned in the center of the chamber on a sample stage. A standard Zoom 70x (7:1 zoom) microscope is positioned above a glass window in the chamber lid, illuminating the sample by coaxial or ring light controllable through a light source. This setup is useful for positioning probes and the vision of highly reflective samples. The probes are ZN50R-03-W tips made of tungsten with a radius of 3 μm. Up to 4 probes can be used simultaneously. A sketch of the system and pictured from the chamber and probe is shown in Figure 2.5.

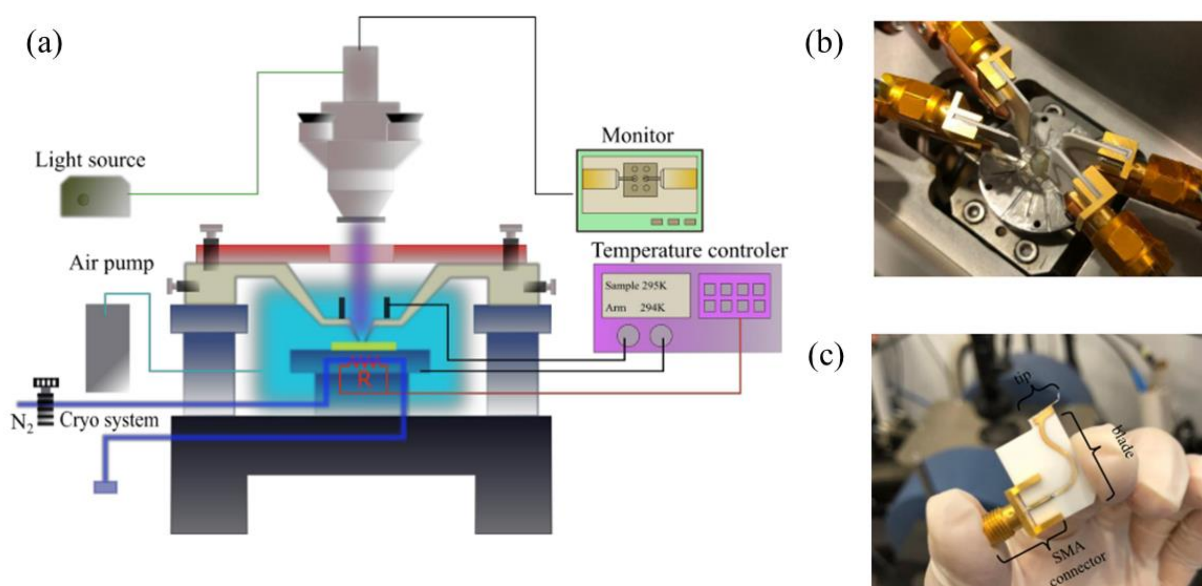

Figure 2. 5. (a) Sketch of Lakeshore EMPX-HF system, including controls of vacuum and temperature. (b) Picture from the sample stage and probes connected to a sample. (c) Details from ZN50R-03-W tip. Taken from [76].

2.2.2.2. AixACCT TFAnalizer 2000

The ferroelectric and transport characterization has been performed using the TFAnalizer 2000 system. Coaxial cables were connected between the equipment and the probe station. This system applies voltages up to 25 V between 500 μHz and 200 kHz and measures current. The $I(V)$ and $P(V)$ measurement modes will be described in section 2.2.3.

In transport measurements, a trapezoidal writing pulse with fixed width ($\tau_W = \tau_{rise} + \tau_{plateau}$) and amplitude ($V_W$) is sent to the sample to polarize the ferroelectric. After a delay time (τ_D), a bipolar voltage triangular pulse is applied for the reading step as the current response is recorded, as shown in Figure 2.7(a). The resistance is calculated at a voltage (V_R). Note that the reading $I(V)$ must have a maximum voltage smaller than the coercive field (V_c) of the ferroelectric. The reading triangular voltage pulse ranges from -1 to 1 V (Figure 2.7(b)). The resistance is calculated for $V_R = 0.9$ V. In the case of FTJ composed of other ferroelectric materials, like $BaTiO_3$[35,55,62,172] and $BiFeO_3$[57,173,174], the reading voltage is lower, taking advantage of the large leakage currents. However, epitaxial HZO films have lower electric conductivity. Besides, the tunneling current drops exponentially with the tunneling barrier thickness. Therefore, the reading voltage must be larger to determine the *ER*. Figure 2.6(c) shows the current in logarithmic scale for a Pt / HZO (4.6 nm) / LSMO // STO (001) device. The current cannot be properly read below ≈ 10 pA, which corresponds to the experimental setup sensitivity.

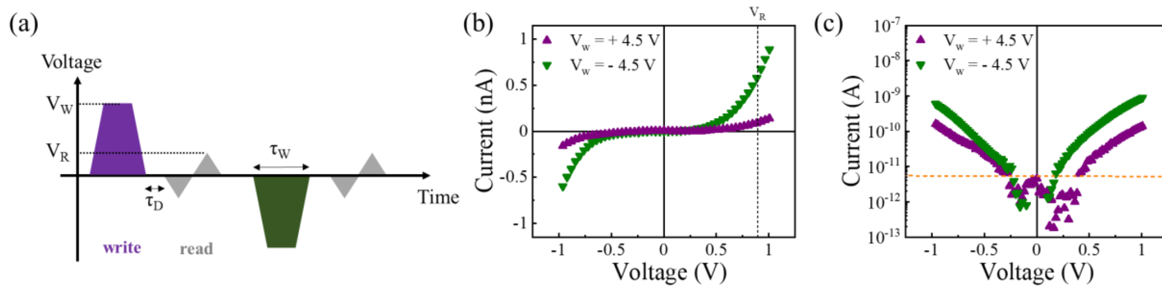

Figure 2. 6. (a) Sketch of pulses applied on the junction for transport characterization. (b) Reading I(V) recorded after polarization (writing) with positive or negative V_w. The junction's resistance is calculated for $V_R = 0.9$ V, indicated with a black vertical line. (c) Logarithmic scale of I(V) current. A horizontal dashed line around 10 pA indicates experimental setup sensitivity.

The sequence of writing pulses employed for the resistance measurements follows the two approaches indicated below. In both cases, the junction's dependence on the external writing voltage is established.

Method 1: V_w varies its amplitude from $V_{max} \rightarrow 0 \rightarrow -V_{max} \rightarrow 0 \rightarrow V_{max}$ (Figure 2.7(a)). The ferroelectric layer is polarized in one direction by applying a large + V_{max}, and the resistance assumes a high resistive state (HRS, red symbol in Figure 2.7(b)). Next, V_w gradually decreases, reaching a value near V_C^- (blue dashed line). At this point, the ferroelectric polarization starts to switch direction, decreasing the junction's average barrier height. Accordingly, the resistance

decreases. When the V_w becomes negative and reaches maximum amplitude (- V_w), the ferroelectric is polarized in the opposite direction. The sample assumes a low resistive state (LRS). Once the ferroelectric is polarized in one direction, the resistance remains constant. Nevertheless, when $V_w \approx V_c^+$ (orange dashed line), the resistance starts to increase, indicating that ferroelectric domains are being switched to their initial direction. Since the polarization switching is reversible, the system returns to its initial value, creating a resistance loop.

Method 2: + V_w and - V_w are applied in sequence. The absolute amplitude gradually increases from $0 \rightarrow |V_{max}|$ (Figure 2.7(c)). Since the junction is not previously polarized, it has a random distribution of domain polarization. V_w starts from a minimum value of 1 V. A pair of pulses with the same amplitude but opposite polarities are applied in sequence (+ V_{w1}, - V_{w1}) as indicated in pink in Figure 2.7(d). The resistance is plotted as a function of the absolute value of V_w. Next, the amplitude increases to V_{w2}, as indicated in blue, and a set of (+ V_{w2}, - V_{w2}) is applied. The amplitude keeps increasing until $|V_w|$ reaches a chosen $|V_{max}|$.

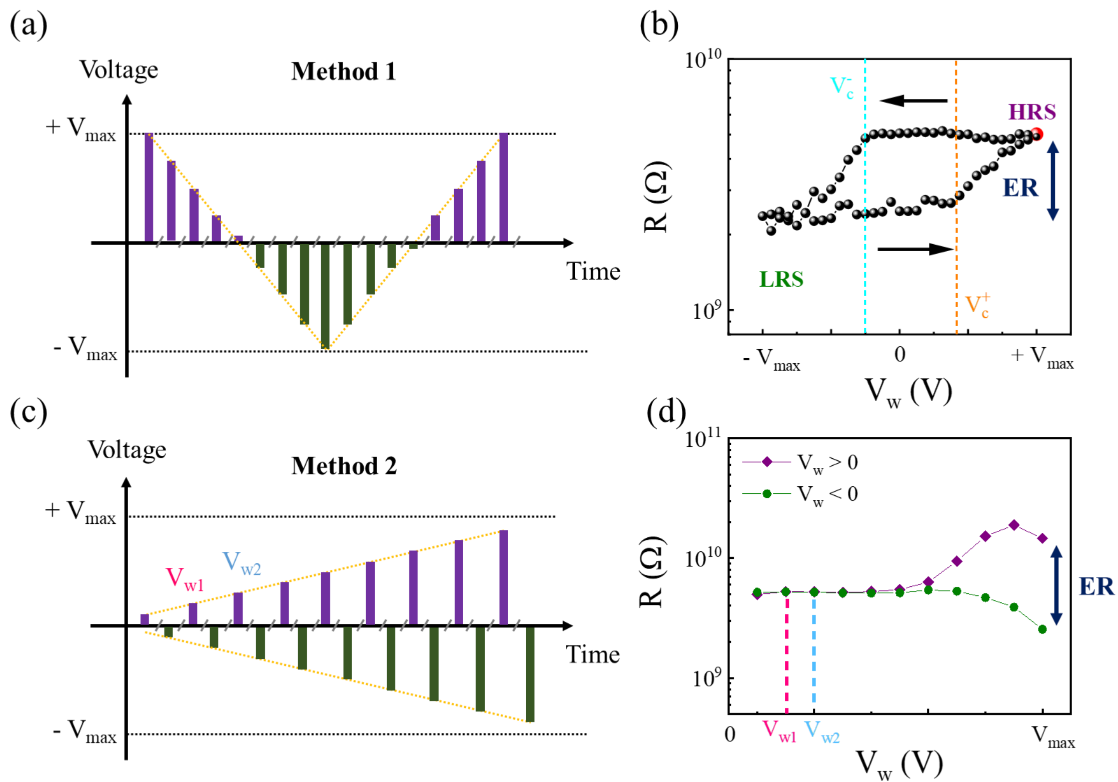

Figure 2. 7. (a) Sketch of Method 1 for ER measurement. (b) Representative resistance loop obtained from the sequence in (a). (c) Sketch of Method 2. (d) Resistance dependence on writing pulse amplitude obtained from the sequence (c).

2.2.3. Ferroelectric properties

Ferroelectric hysteresis loops are recorded using a triangular voltage waveform *V*(*t*) and measuring current *I*(*t*). A virtual ground method is used, and it relies on keeping one node of the circuit at a steady reference potential. The charge is obtained by the integration of current in time. Then, the polarization of the plano-parallel capacitor, with area *A*, is calculated.

$$P = \frac{\int_0^{t_f} I(t) \cdot dt}{A} \qquad \textit{Eq 2. 1.}$$

It is worth noticing that in an ideal ferroelectric, the measured charge value obtained by integrating the current flowing into the circuit does not correspond to the material's polarization but the electric displacement (*D*).

$$D \equiv \epsilon_0 E + P_{total} \qquad \textit{Eq 2. 2}$$

$$D \equiv \epsilon_0 E + (P_{linear} + P_{FE}) \qquad \textit{Eq 2. 3}$$

Where ϵ_0 is the vacuum permittivity, P_{linear} is the linear polarization generated in a dielectric due to an electric field's application, and P_{FE} is the spontaneous polarization from a ferroelectric material. In the case of linear, homogeneous, and isotropic dielectric, the linear polarization of the material is defined as:

$$P_{linear} = \epsilon_0 \chi E \qquad \textit{Eq 2. 4}$$

Where χ is the electric susceptibility. Therefore, combining both equations:

$$D \equiv \epsilon_0 E + \epsilon_0 \chi E + P_{FE} = \epsilon_0 (1 + \chi) E + P_{FE} \qquad \textit{Eq 2. 5}$$

$$D \equiv \epsilon_0 \epsilon_r E + P_{FE} = \epsilon E + P_{FE} \qquad \textit{Eq 2. 6}$$

Ferroelectric materials have a high susceptibility ($\chi >> 1$), which allows approximating $\epsilon = \epsilon_0(1 + \chi) \approx \epsilon_0 \chi$, assuming, thus, $\epsilon_r = \chi$. Then,

$$D \approx \epsilon_0 \chi E + P_{FE} = P_{total} \qquad \textit{Eq 2. 7}$$

$$D \approx P_{total} \qquad \textit{Eq 2. 8}$$

Thin ferroelectric films' characterization is particularly challenging since extrinsic contributions to the current can affect the measured coercive fields and remnant polarization. The main

contributions for the total current recorded in FTJ are the displacement current ($I_{DE} = \frac{\partial D}{\partial t}$) and leakage current ($I_{leakage}$). Using Eq. 2.6, the derived displacement current also contains two contributions:

$$I_{DE} = \frac{\partial D}{\partial t} + I_{leakage} = \frac{\partial(\epsilon E + P_{FE})}{\partial t} + I_{leakage} = I_{\epsilon} + I_{FE} + I_{leakage} \qquad Eq\ 2.\ 9$$

The current I_{FE} is caused by ferroelectric domain switching, and dielectric current I_{ϵ} corresponds to the capacitor's charging current. The leakage current is related to the electron flow through the material, taking advantage of defects in the crystal[175], grain boundaries[97], or injection of current from electrodes[74,174]. Different measuring techniques are used to separate each contribution. The dynamic hysteresis mode (DHM) accounts for $I_{FE} + I_{\epsilon} + I_{leakage}$. In order to remove the leakage, the Dynamic Leakage Current Compensation (DLCC) method can be used. Nevertheless, the $\epsilon_0 \chi E$ contribution (I_{ϵ}) can lead to misleading estimation of ferroelectric parameters, like coercive field and remnant polarization. Alternatively, the PUND method accounts only for I_{FE} and is mostly used in this thesis. These techniques are detailed in the following sections.

Ferroelectric tunnel junctions can be simplified as lossy capacitors, and the equivalent circuit from the (sample + setup) system is indicated in Figure 2.8. The experimental setup has two elements: a series resistance (R_s) and a capacitance (C). They are intrinsic to the system and arise from wiring, shielding, and amplifiers.

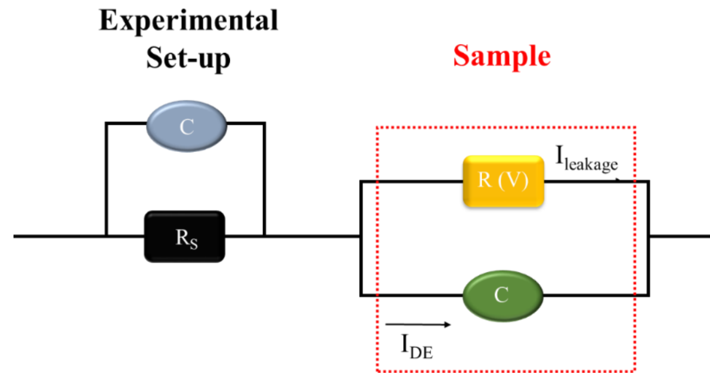

Figure 2. 8. Equivalent circuit from experimental setup and sample.

The combination of the elements presented in Figure 2.8 can delay the electric signal arriving at the sample. A general equation can estimate the time constant of the circuit $\tau_{RC} = R \cdot C$, where R

and C are the equivalent resistance and capacitance, respectively. Their values include contributions from the sample and the experimental setup. During this thesis, the experimental setup does not change, i.e., R_s and C are not modified. Considering each sample has a capacitance, the time constant of the circuit will change for different samples. Therefore, one could estimate the maximum time constant of the circuit for a particular sample.

The chosen sample is the thinnest HZO capacitor (t = 2.3 nm), which have the largest capacitance accordingly to the plano-parallel equation $C = \frac{\epsilon_0 \epsilon_r A}{t}$. Samples with thicker HZO films will have lower capacitance and a shorter time constant. This measurement does not aim to extract the equivalent capacitance and resistance ($\tau_{RC} = R_{eq} \cdot C_{eq}$) of the circuit, but the time constant itself. For this, a triangular bipolar signal with an amplitude of 1 V and 100 kHz is applied to the sample, as Figure 2.9 shows. The black line indicates the expected pure displacement current in Figure 2.9(b). The current measured exponentially can be fitted by an exponential curve $\mathrm{I} = \mathrm{I_0 e^{-t/\tau_{RC}}}$, where I_0 = amplitude and τ_{RC} = time constant. So, the τ_{RC} for the (system + HZO capacitors) is τ_{RC} = 0.5 μs. This value indicates that effects that happen faster cannot be observed.

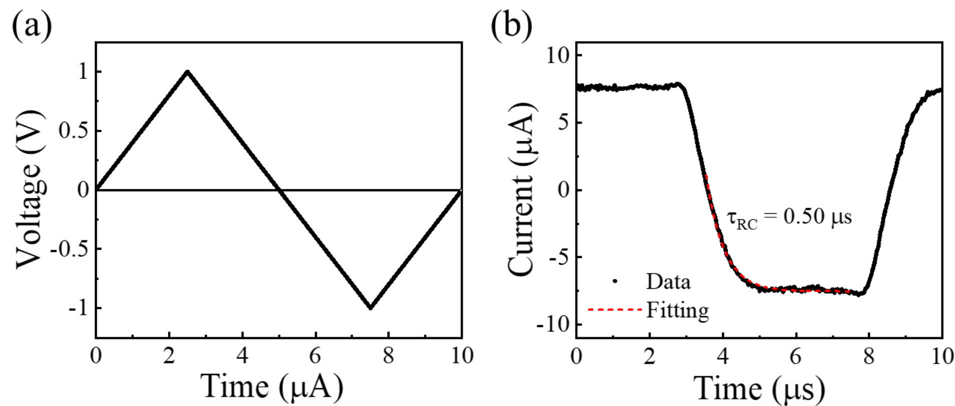

Figure 2. 9. (a) Applied voltage signal to Pt/HZO (2 nm)/LSMO junction and (b) measured current. The fitting indicated by the dashed line calculates a τ_{RC} = 0.5 μs.

2.2.3.1. Dynamic Hysteresis Mode (DHM)

The most common mode for current-voltage measurement is DHM. This method consists of applying four bipolar triangular excitation signals of frequency ν_0 (measurement frequency) separated by a delay time τ_D. A sketch of the pulse sequence, the measured $I(V)$, and its integration into $P(V)$ is shown in Figure 2.10.

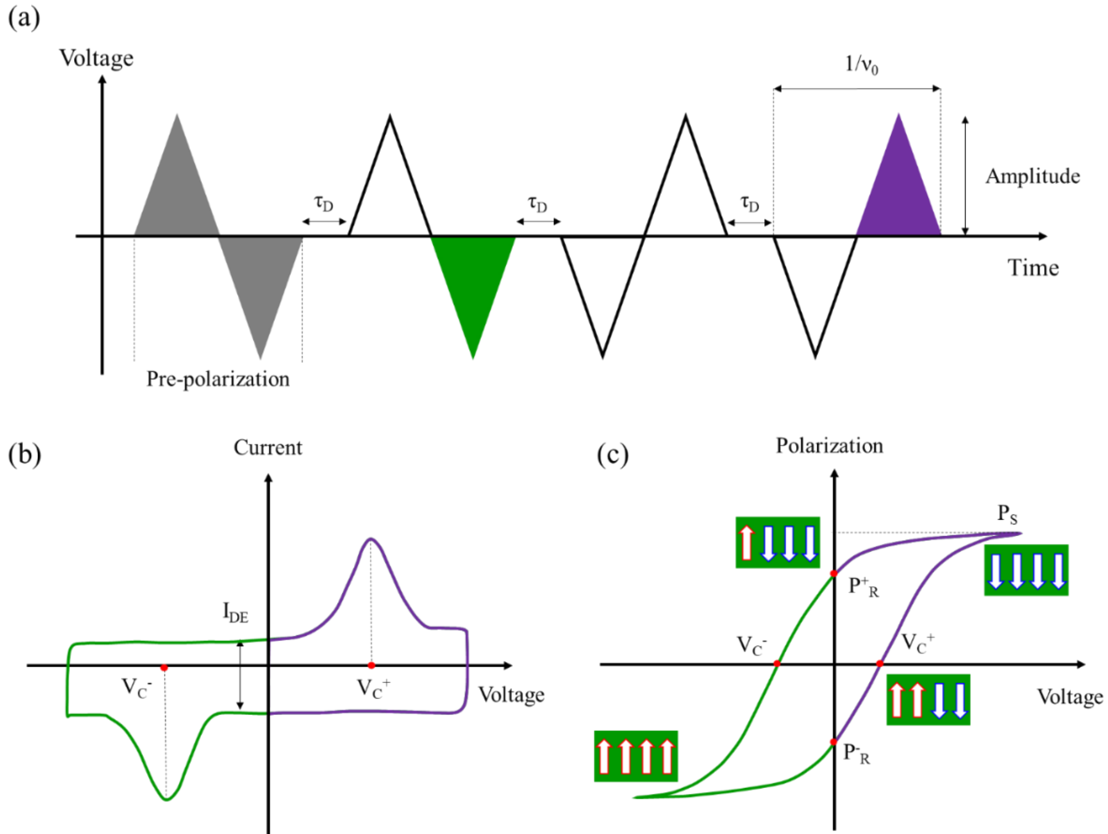

Figure 2. 10. (a) Sketch of the voltage pulse sequence used for measurement with frequency ν_0 using DHM mode. (b) I(V) curve obtained from (a). It is possible to identify coercive voltages (V_c^- ,V_c^+) and displacement current (I_{DE}). (c) The integration of current in time results in the polarization curve P(V).

The first pulse (gray) pre-polarizes the ferroelectric into a negative polarization state. The hysteresis loop is calculated from the current response measured when the second half of the second pulse (green) and the second half of the fourth pulse (purple) are applied. The current integrated in time divided by the electrode area results in the polarization loop (Eq. 2.1). The first and third pulses are necessary to set the same polarization state while recording the positive and negative parts' final loop. This method is convenient because it does not continuously cycle the sample, avoiding fatigue. In leaky samples, however, the polarization switching peak can be distorted as leakage contribution is overlapped, leading to a miscalculation of remnant polarization (P_R) and coercive field (V_C).

2.2.3.2. Dynamic Leakage Current Compensation (DLCC)

Meyer[176] developed this compensation technique associated with the DHM and generally is used to subtract the leakage from an $I(V)$ curve. The procedure takes into consideration two assumptions:

i. The leakage current, I_{leakage}, is independent of the measurement frequency
ii. The displacement current, I_{DE}, and the switching current, I_{FE}, are linearly dependent on the measurement frequency.

Then, two DHM cycles are measured at two frequencies (ν_0 and $\nu_0/2$). Based on the first assumption, the I_{leakage} is the same for both cycles, which allows its subtraction from the total current. Therefore, the current that remains is $I_{DLCC} = I_{DE} + I_{FE}$. The assumptions are only valid for low and middle frequencies since, at high frequency, the series resistance (R_S) affects the loop after compensation due to its frequency-dependent contribution.

Even though this technique gives reliable ferroelectric parameters in general, measurements collected in ultrathin ferroelectric capacitors, i.e., highly leaky junctions, are not fully compensated or are deformed. Thus, $I(V)$ obtained by PUND will also be used to characterize FTJ in particular cases.

2.2.3.3. PUND technique

Positive-Up-Negative-Down (PUND) technique is another method used in this thesis to obtain reliable $I(V)$ characterization.[177–179] In this case, five voltage pulses are applied to the sample, as shown in Figure 2.11.

The first negative pulse (X) pre-polarizes the sample in one direction. While the second (P) pulse is applied, which switches the polarization to the opposite direction, the current is measured. It contains ferroelectric (I_{FE}) and non-ferroelectric contributions (I_{DE}, I_{leakage}). The third positive pulse (U) does not induce any switching since the sample is already polarized in this direction and, thus, the current only non-ferroelectric contributions, as the yellow line in Figure 2.11(b) shows. The same happens for the fourth (U) and fifth (N) negative pulses. Thus, one can subtract the current measured for pulses with the same polarity ($I_P - I_U$, $I_N - I_D$) to observe only the ferroelectric contribution (I_{FE}^+ and I_{FE}^-). The final $I(V)$ is sketched in Figure 2.11(c), and its integration in time gives rise to the polarization curve.

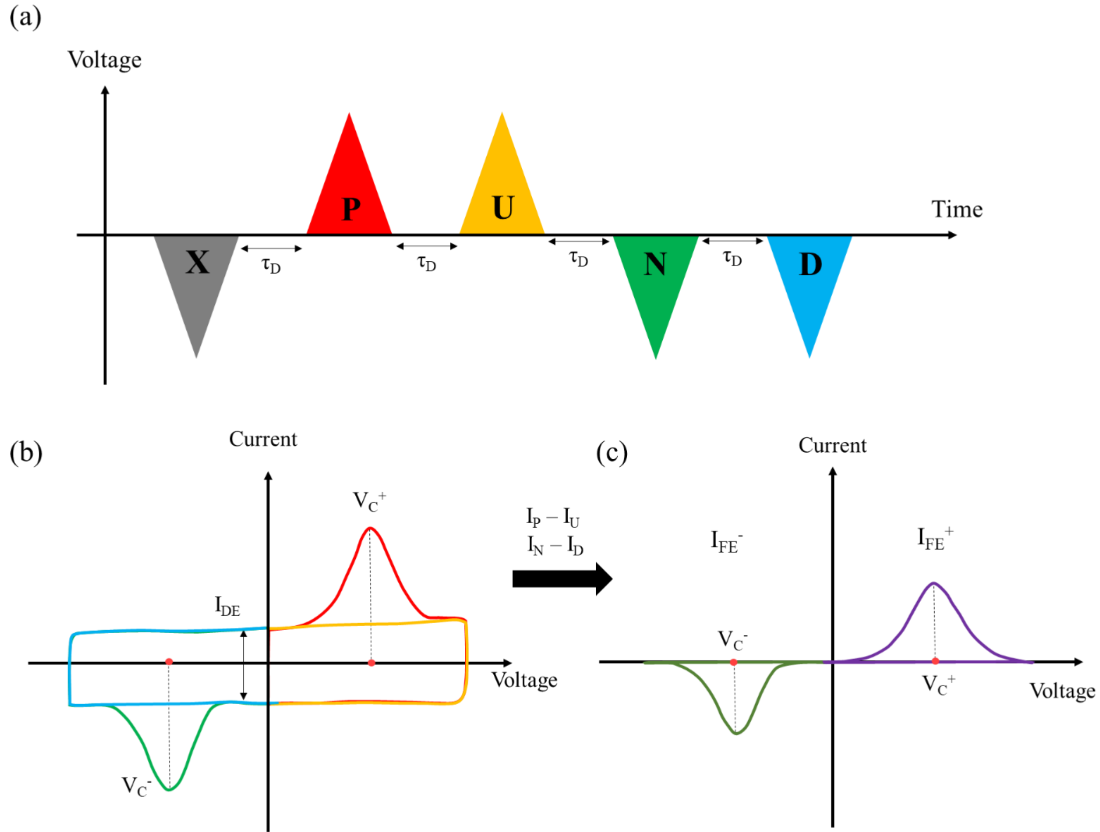

Figure 2. 11. (a) Sequence of pulses applied to the sample using the PUND technique. (b) Representation of current response corresponding to each voltage pulse. (c) Final I(V) obtained by ($I_P - I_U$) and ($I_N - I_D$). The only current contribution visible is related to ferroelectric switching.

In order to compare the characterization of the ferroelectric obtained with the three methods, $I(V)$ and $P(V)$ curves were recorded at 5 kHz in a Pt / HZO (4.6 nm) / LSMO // GSO (001) junction is shown in Figure 2.12. The curves in Figure 2.12(a,b) are obtained with DHM. The peak identified in green indicates the high leakage from the sample, which overlaps with the ferroelectric response and deforms the curve for $V > 3.5$ V. The corresponding $P(V)$, calculated by integration of the current in time, carries this deformation as the leakage contribution is also integrated. Also, the positive coercive field extracted from the $P(V)$ curve ($V_c^+ \approx 2.5$ V) is not located at the same voltage as the switching peak in the $I(V)$ curve. The integration of leakage causes this incorrect value. The remnant polarization is overestimated as $P_R \approx 30$ μC·cm^{-2}.

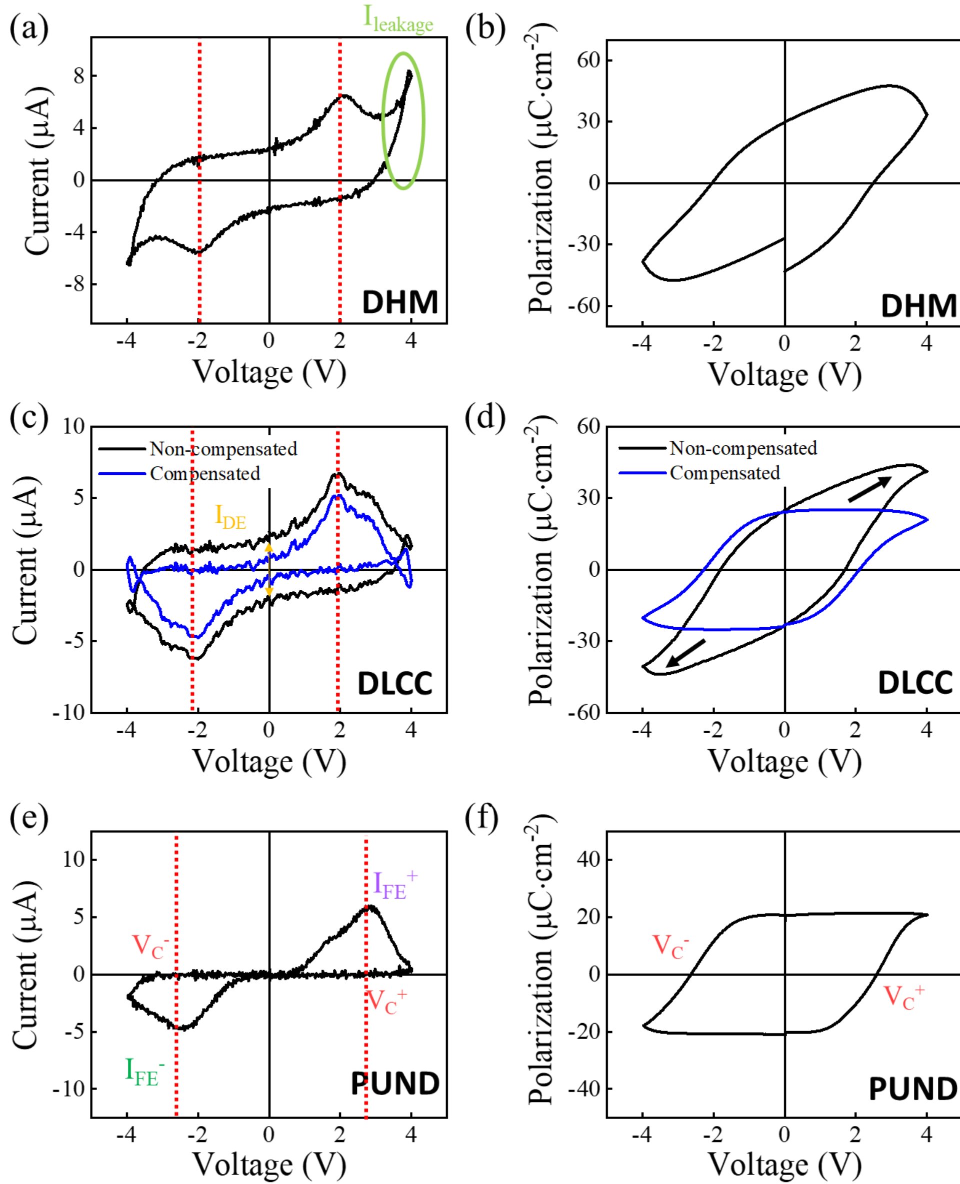

Figure 2. 12. Comparison between I(V) and P(V) curves recorded at 5 kHz with (a, b) DHM, (c, d) DLCC, and (e, f) PUND techniques for a junction with structure Pt / HZO (4.6 nm) / LSMO / GSO (001).

Having observed the large leakage in Figure 2.12(a), the DLCC mode can be used to apply for the compensation. The raw $I(V)$ curve obtained with this mode is shown in Figure 2.12(c), represented in black. A small loop appears close to the maximum voltage associated with the series resistance R_S.[180] Even though the leakage was compensated, this $I(V)$ has a significant contribution from the displacement current (I_{DE}), indicated by the yellow arrow. Direct integration of the current response results into the black $P(V)$ curve in Figure 2.12(d). The ferroelectric parameters extracted

are $P_R \approx 24$ μC·cm^{-2}, $V_c^+ \approx + 1.7$ V, and $V_c^- \approx - 1.8$ V, showing discrepancies with the ones obtained by DHM. The linear contribution from electric susceptibility ($\epsilon_0 \chi E$) (Eq. 2.6) distorts the $P(V)$ curve in the diagonal direction as the arrows indicate. Therefore, the coercive fields extracted from this measurement are underestimated. It is possible to perform a second compensation to remove the electric susceptibility contribution by linear subtracting of a constant slope ($\chi \approx \epsilon_r = 30$). The blue line represents the result in Figure 2.12(c, d). After compensation, the ferroelectric parameters are $P_R \approx 24$ μC·cm^{-2}, $V_c^+ \approx + 2.1$ V, and $V_c^- \approx - 2.3$ V. The compensated $I(V)$ curve stills shows a residual contribution from the displacement current. The switching peaks do not change position, indicating that the subtraction does not affect the material's ferroelectric intrinsic response (coercive field). The compensated $P(V)$ curve shows coercive voltage values exactly where the I(V) switching peaks are located.

Finally, to observe an $I(V)$ curve without any residual leakage or displacement current contributions, the PUND method is tested. The $I(V)$ curve indicates clear ferroelectric switching loops for both voltage polarities. The ferroelectric parameters extracted from Figure 2.12(e, f) are $P_R \approx 21$ μC·cm^{-2}, $V_c^+ \approx + 2.4$ V and $V_c^- \approx - 2.6$ V. As the compensated DLCC and PUND curves show different coercive fields, PFM complementary measurements are performed to confirm their values. The analysis, which will be shown in Chapter 5, indicates the $V_c^{+,-}$ obtained with PUND as more accurate.

The asymmetry between positive and coercive fields is visible independently on the $I(V)$ measuring method, which is attributed to an imprint field (E_{imp}) in the junction. The imprint field is calculated by $E_{imp} = 1/2 \times (E_c^+ + E_C^-)$ and it represents an internal field driving FE polarization towards a preferential direction when external bias is removed. Junctions with similar structure but grown on STO (001) crystalline substrates have displayed an analogous behavior attributed to an E_{imp} = – 150 kV/cm (≈ - 0.07 V) pointing towards the platinum top electrode.[131] Taking into consideration the coercive fields extracted with the PUND measurements, the imprint field is – 220 kV/cm pointing towards the platinum top electrode in a Pt / HZO (4.6 nm) / LSMO / GSO (001) junction. Nevertheless, as detailed in the Introduction, there are differences in the crystalline structure between HZO films grown in STO (001) and GSO (001) substrates, which might be the origin of such different values.

2.2.3.4. Training measurement

Studies with ferroelectric capacitors have shown that two phenomena can affect polarization: wake-up and fatigue. The wake-up effect increases P_R with increasing electric field cycling number[119,130,136], while fatigue or aging causes a decrease in P_R due to bipolar field cycling.[105,181,182] The fatigue happens to every ferroelectric material and is associated with domain pinning and trap generation.[130,181] However, in the study of ultrathin junctions, a third effect was observed, which is referred to as "training" The training effect causes a dramatic decrease of leakage as the device is cycled.

Note that training and wake-up have a key difference. The wake-up is an electrical treatment that redistributes defects inside the ferroelectric layer, allowing previously pinned grains to switch their polarization. Pešic et al.[130] also attributed that monoclinic non-ferroelectric grains suffer phase transition to orthorhombic ferroelectric caused by oxygen vacancies diffusion. However, changes in the electrical conduction between pristine and woken-up devices have not been reported. The training effect also redistributes defects inside the film, but it causes a decrease in the junction's conductivity. In the case of ultrathin ferroelectric junctions, this large conductivity leads to a high leakage current in the pristine junction, in such a way that masks the FE switching peak in $I(V)$ curves. Nevertheless, by cycling the sample a large number of times, the defects are rearranged, the leakage current decreases, and allowing identification of the FE switching peak.

Accordingly, the training effect measurement is done by applying a large number of rectangle voltage pulses and monitoring the $I(V)$ evolution with the number of cycles until the leakage current decreases. A sketch of the measurement is shown in Figure 2.13(a). This mode combines two separated waveforms, triangles and rectangle, with the following intention:

i. ***Triangle pulses*** The current response of the sample is recorded while applying a triangular voltage pulse. It corresponds to a reading $I(V)$ curve. This step is done periodically after a chosen number of square pulses ($N_1, N_2, \ldots, N_i$) to monitor the FTJ $I(V)$ curve.

ii. ***Rectangle pulses*** These pulses cycle the sample. A certain number ($N = \sum_{x=0}^{i} N_x$) of bipolar square pulses (similar to a writing pulse V_w) are applied to train the junction without measuring the current response electronically.

The amplitude of the triangle and rectangle pulses is 3 V, which is similar to the sample's coercive field ($V_c \approx 2.5$ V). However, the field cycling is not related to the switching of the ferroelectric but to redistribute charged defects by voltage-driven motion. Indeed, Max et al.[82] have reported that voltage cycling with low voltage avoids soft dielectric breakdown and allows oxygen vacancies to be redistributed inside the insulator. Since there are two types of waveforms in the measurement, there are two frequencies: ν_{triangle} = time needed to perform bipolar triangular pulse, and $\nu_{\text{rectangle}}$ = frequency of bipolar rectangle pulses. In this thesis, $\nu_{\text{rectangle}}$ = 100 Hz, ν_{triangle} = 1 kHz, and the final number of pulses (N) is indicated in each measurement.

Figure 2.13(b) shows an example of the training measurement in which the number of rectangle pulses applied before each $I(V)$ is indicated in the caption. Figure 2.13(c) shows an $I(V)$ recorded with PUND at 5 kHz before and after the training. The pristine device does not show any switching peak since the large leakage is masking the ferroelectric switching. After $N = 10^4$ cycles and the leakage is reduced, the PUND measurement exhibit the switching peaks I_{FE}^+ and I_{FE}^-.

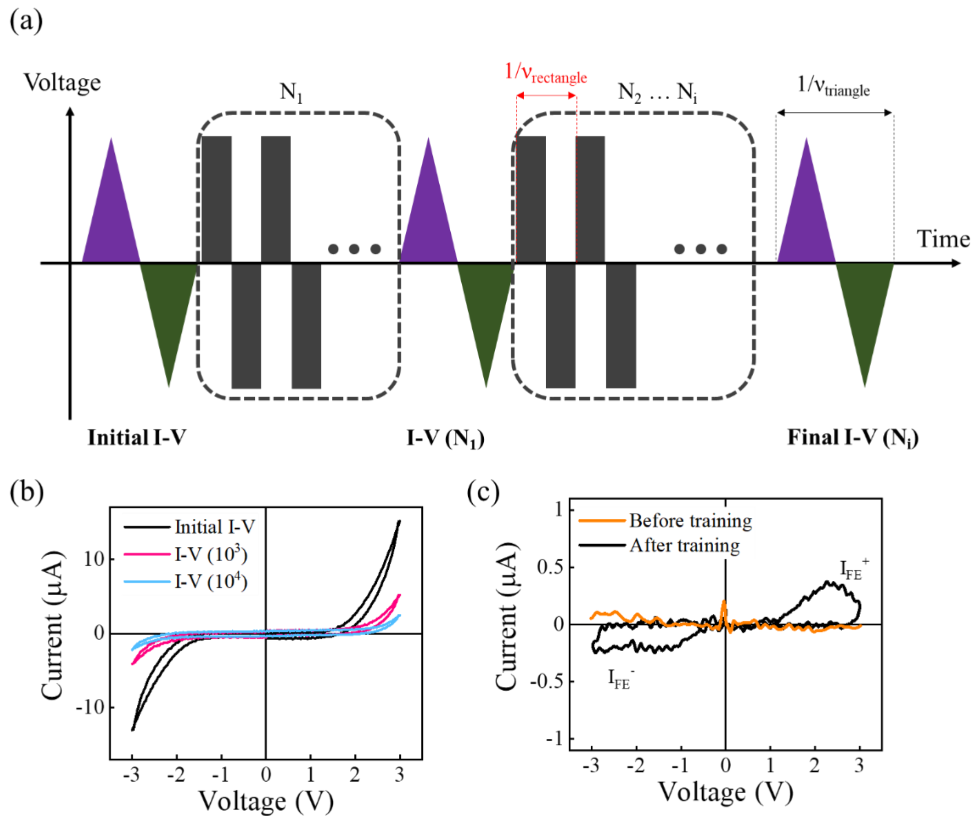

Figure 2. 13. (a) Sketch of pulse train applied for the training measurement. (b) I(V) for $\nu_{triangle}$ = 1 kHz obtained in pristine junction (black line) after $N_1 = 10^3$ cycles (pink line) and after $N_2 = 10^4$

cycles (blue line). (c) I(V) recorded with PUND at 5 kHz before and after junction training shown in (b).

2.2.3.5. Retention

Retention measurements are performed to have information about the decay of polarization in time. Short retention causes memory failure if the polarization drops to a minimum value that cannot be detected. This measurement is done by polarizing the sample with a voltage writing pulse (V_w) the same way as in Figure 2.6(a). After a chosen retention time (t_1, t_2... t_i), a triangular bipolar pulse is applied as reading $I(V)$. In this thesis's case, this reading $I(V)$ is intended to measure the junction's resistance and establish how long the resistive state remains stable. Thus, the reading $I(V)$ is performed from – 1 V to + 1 V, and the resistance is measured at V_R = 0.9 V. A sketch of the measurement is shown in Figure 2.14 with an example of retention measurement. The resistance versus time is plotted for positive and negative writing pulse V_w (Figure 2.14(b)). In this particular case, the resistance did not vary significantly, indicating that the device remains polarized after 1000 s.

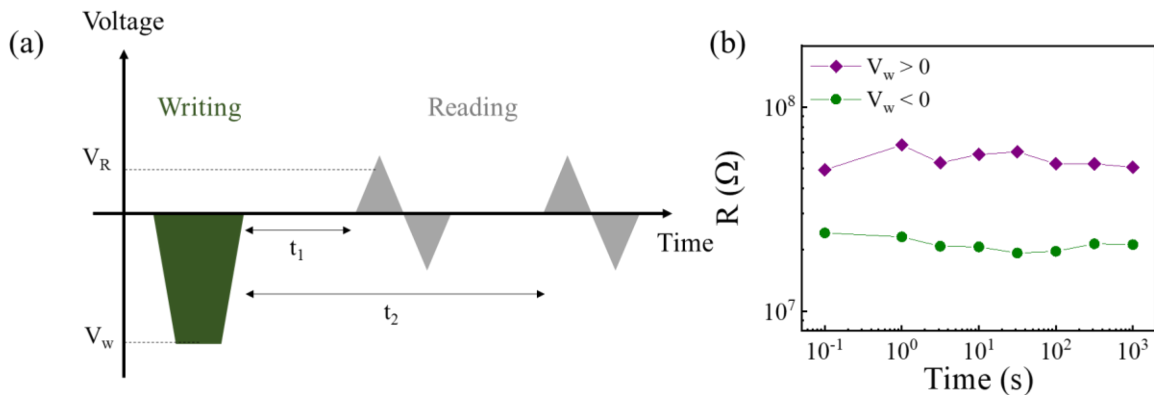

Figure 2. 14. (a) Sketch of measurement. Reading I(V) is recorded after (t_1 and t_2) writing pulse. (b) Example of the evolution of resistance in time in which total retention time = 1000 seconds.

2.2.3.6. Endurance

The ferroelectric material's ability to retain its polarization states through a large number of writing/reading cycles is a critical feature in ferroelectric-based devices. The junction's endurance is investigated by applying a sequence of alternating positive and negative writing pulses with the same amplitude (V_w) and duration (τ_w), as shown in Figure 2.15(a). The resistance is measured after each writing pulse at V_R = 0.9 V from reading $I(V)$, similar to Figure 2.6(a). An example of endurance measurement is exhibited in Figure 2.15(b), which shows the resistance dependence on

the number of writing pulses. Positive writing pulses ($V_w > 0$) defines a high resistive state (OFF). Meanwhile, negative writing pulses ($V_w < 0$) decrease the resistance to a low resistive state (ON). The spread of the ON/OFF resistance values and the *ER* can be extracted from the $R(N_p)$ plot. In Figure 2.15(b), the OFF and ON average resistive states are 2 x 10^{10} and 1.3 x 10^{10} Ω, respectively, with 1.1 x 10^9 and a 1.7 x 10^8 Ω standard deviation. The *ER* calculated from these data indicates a mean value of 58 % with a standard deviation ($\sigma(ER)$) of 10 %. Therefore, this measurement demonstrates the stability of ON and OFF resistance states and reproducibility of the *ER* obtained with these particular conditions of writing pulse (V_w, τ_w).

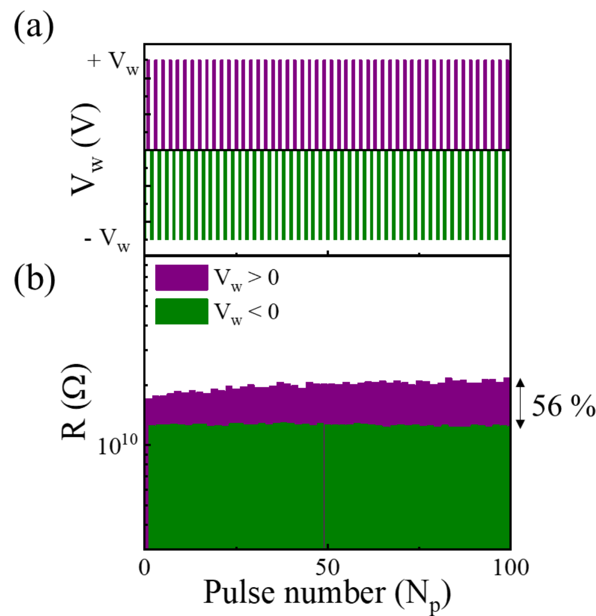

Figure 2. 15. (a) Sequence of writing pulses consists of alternating positive and negative V_w with a fixed duration (τ_D). (b) Example of endurance measurement for 100 pulses obtained with writing pulse sequence in (a).

2.2.3.7. Switching speed

In order to get a deeper insight into the switching speed in HZO films, the transient polarization switching current is probed directly using a fast pulse measurement setup.[183] Figure 2.16(a) shows a typical positive-up-negative-down (PUND) rectangular pulse sequence that is applied to the junction in order to disentangle the polarization switching current (I_{FE}) and the charging current of the capacitor. The first positive pulse (V = + 4 V, τ = 1 μs) sets the polarization to a saturated state, pointing towards the LSMO. Then, two negative voltage pulses (V = - 4 V, τ = 1 μs) in sequence are applied. The current in the first positive pulse is associated with the displacive (charging the

capacitor and driving of polarization) and non-displacive currents (mainly tunneling charges across the barrier). In contrast, the current in the second pulse only corresponds to the charging of the capacitor. In the two negative pulses, the displacive current peak is followed by the tunneling-related current plateau.

The fine details of the current response ($I(t)$) can be better appreciated in Figure 2.16(b), where the $I(t)$ curves collected during the sequential negative pulses are depicted. Note that they were shifted to have coincidental origin in time. The displacive peaks are now appearing at the voltage $V(t)$ onset, followed roughly by the tunnel current plateau. The displacive current's amplitude is somewhat larger in the first pulse (blue line), which corresponds to polarization switching. Integration of the $I(t)$ data leads to the remnant polarization of the HZO film and can be compared with values extracted by PUND. In the case of Figure 2.16, the capacitor has structure Pt/HZO (2 nm)/LSMO//GSO (001), and the integrated polarization signal ≈ 2 $\mu C \cdot cm^{-2}$ is consistent with PUND measurement (Chapter 5). More importantly, the polarization-switching current peak develops in a time scale shorter than 500 ns, which sets an upper limit for the polarization switching time. This time is comparable with the time constant of the (circuit + sample) system, limiting the time scale to 500 ns. Therefore, it is possible to infer that the intrinsic ferroelectric switching time can be faster than 500 ns. Even though this thesis does not intend to investigate the dynamics of ferroelectric switching deeply, in order to have a more precise value of the switching time, the time constant of the circuit must be reduced either by reducing its capacitance or the series resistance (due to bottom electrode or circuit).

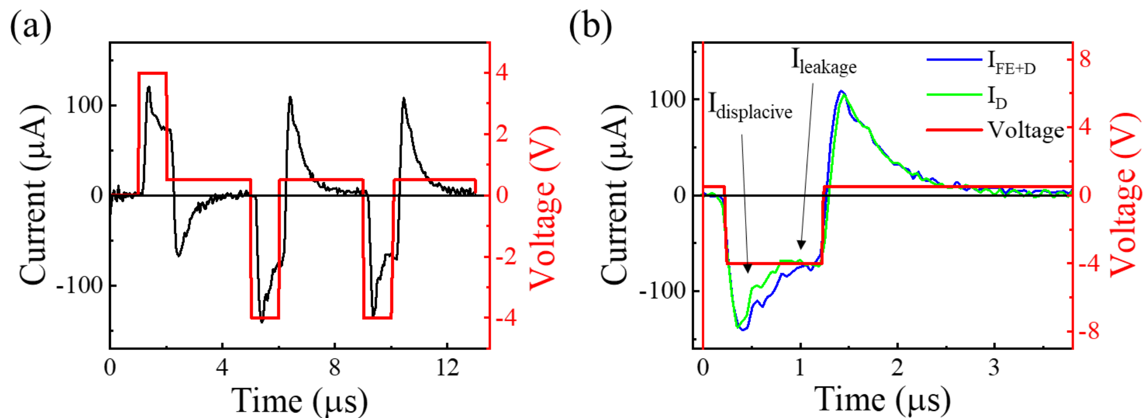

Figure 2. 16. (a) Complete train of voltage pulses applied to the capacitor and measured current response. Junction is pre-polarized with V_w = + 4 V pulse with τ_w = 1μs duration. (b) Overlapped

current peaks and applied voltage for the two consecutive negative pulses with indications of displacive peak and leakage plateau associated with tunneling through the HZO barrier.

2.2.3.8. Potentiation / depression

The memristic abilities of ferroelectric-based devices have been used to mimic some characteristics of biological synapses for neuromorphic application.[70,184,185] A primarily explored behavior is the potentiation/depression ability, where potentiation corresponds to a decrease of the device's resistance and depression is related to an increase. In order to observe this effect, the resistance is continuously modulated by N_p writing pulses with the sequence shown in Figure 2.17(a), mimicking the potentiation/depression processes in neuronal firing. After each writing pulse, the resistance is measured at $V_R = 0.9$ V, as indicated in Figure 2.6(a, b).

Figure 2.17(b) shows the resistance dependence on the number of pulses ($R(N_p)$). It can be appreciated that the resistance of the device changes gradually with N_p. The gradual increase of resistance is achieved by applying $V_w > 0$ (depression), whereas the resistance progressively decreases when $V_w < 0$ (potentiation). The effect's reproducibility and robustness are demonstrated by similar resistance variation in four potentiation/depression cycles.

Resistance data from Figure 2.17(b) can be fitted with an exponential model[20,184] according to the equation $R_{p,d} = R_0^{p,d} + A_{p,d}e^{-\left(N_p - N_0^{p,d}\right)/\tau_{p,d}}$, where p = potentiation, d = depression, R_0 = initial resistance, N_p = number of pulses, N_0 = number of positive (depression) or negative (potentiation) pulse and τ = non-linearity of the effect.[184,186,187] The equation dictates that larger resistance variations can be achieved by an appropriate combination of voltage amplitude and the number of pulses. Considering that the resistance of FTJ also depends on the duration of the writing pulses, this parameter is also critical. As the τ parameter for depression and potentiation becomes similar, the smaller is the non-linearity, indicating that the same number of pulses is necessary for both effects. As a matter of fact, for neuromorphic applications, $\tau_d = \tau_p$ would be the ideal behavior. By fitting the data (green dashed lines) in Figure 2.17(b), the non-linearity for potentiation and depression is calculated as $\tau_p = 1.28 \pm 0.22$ and $\tau_d = 0.41 \pm 0.04$, respectively, indicating that more pulses are necessary to increase R than to decrease.

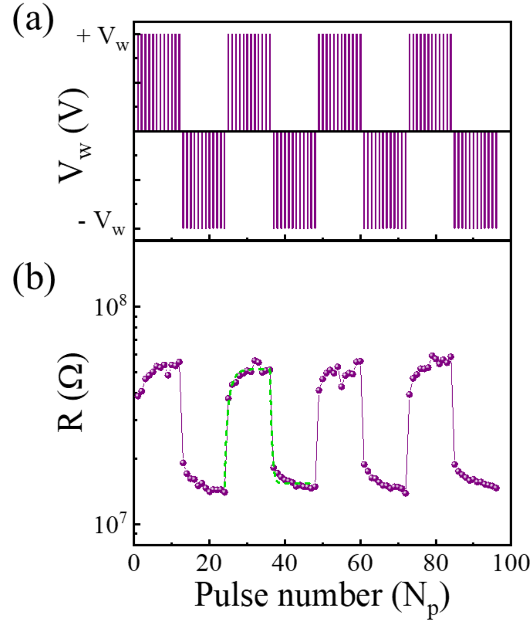

Figure 2. 17. (a) The sequence of pulses with amplitude ± V_w and duration = τ_w applied on tunnel junction. (b) Resistance dependence on the number of pulses (N_p). Green dashed lines represent the fitting results of resistance growth/decay, where τ_p = 1.28 ± 0.22 and τ_d = 0.41 ± 0.04. The different values obtained for τ_d and τ_p show the potentiation/depression asymmetry.

2.2.3.9. Spike-timing-dependent plasticity

Another essential feature required for neuromorphic applications is spike-timing-dependent plasticity (STDP). This mechanism was initially proposed to regulates the evolution of the synaptic strength according to the time between the firing of a pre and post-neuron ($\Delta t = t_{pre} - t_{post}$).[5,6] In biological systems, the STDP enables the synapse strength reconfiguration without any external control or any previous knowledge of the information to be processed.[13,70,188] The electrical signal (action potential, spike) transmitted through the synapse flows in only one direction, i.e., from the pre-neuron to the post-neuron, as sketched in Figure 2.18(a). According to STDP, if a pre-neuron spike just before the post-neuron ($\Delta t > 0$), the synapse should be strengthened, which indicates a causality between the first neuron and the second firing. Whereas if the post-neuron spikes first ($\Delta t < 0$), the electric potential will be transmitted forward in the chain of neurons, not crossing the pre-neuron from Figure 2.18(a). This would induce a weakening in the synapse since there is an anti-causal relationship between firing these two neurons.

It is worth mentioning that neuromorphic architecture engineering aims to conceive a system of artificial synapses and neurons. The artificial neurons are responsible for the spike generation,

integration of signal coming from a group of synapses, and requires a combination of several elements in a circuit.[189–192] On the other hand, the component that can substitute the biological synapse is a memristor, whose resistance can be progressively modulated by an external voltage signal (plasticity). Neuromorphic hardware systems, as complex as they can be, ultimately rely on synapse modulation to perform a specific task. This thesis focuses on studying HZO ferroelectric tunnel junctions and the modulation of their conductance by applying external voltage pulses that could be employed as memristive elements.

The FTJ conductivity is probed in a special arrangement that intends to simulate the synapse strength modulation. Note that in biological synapses (Figure 2.18(a)), the transmission of the spikes causes a potential difference in both "electrodes". In order to reproduce this in FTJ, it would be necessary to apply almost simultaneously two independent voltage pulses, one in the LSMO bottom electrode and another in the Pt top electrode. In this thesis, a simpler arrangement is proposed where both voltage pulses are applied to the top electrode (Figure 2.18(b)) whereas the LSMO bottom electrode remains grounded. The shape of the voltage pulses (spikes) mimics the action potential and has a duration of 50 µs. Figure 2.18(c) shows V_{pre} (red curve) and - V_{post} (blue curve). As both pulses are applied to the top electrode, they overlap, and the result is a V_{total} waveform ($V_{total} = V_{pre} - V_{post}$), represented in green, that changes its shape as the delay time Δt changes. The TFAnalizer 2000 counts with a single output for voltage waveform; thus, a Matlab script is used to calculate the V_{total} waveform previously for the 21 different Δt ranging from - 50 to + 50 µs. Then, a measurement sequence with the 21 waveforms ($V_{total}(\Delta t)$) is generated to apply once $V_{total}(\Delta t)$ at the time to the FTJ. Figure 2.18(d) shows the measurement sequence containing only four $V_{total}(\Delta t)$ for illustration where Δt equals + 50, + 5, - 15 and – 50 µs. After applying each spike, the junction's resistance is measured at $V_R = 0.9$ V extracted from a reading $I(V)$ curve as in Figure 2.6.

Note that the V_{pre} and V_{post} maximum voltage does not exceed a threshold, i.e., the ferroelectric coercive voltage. When $|\Delta t|$ is large, the V_{total} maximum voltage is lower than the ferroelectric coercive field, and the junction's resistance does not change. However, when $|\Delta t|$ is short, V_{total} momentarily exceeds the threshold voltage, leading to an increase or decrease of the junction's resistance depending on the sign of Δt. A discussion of the STDP results and the FTJ resistance effect will be given in Chapter 5.

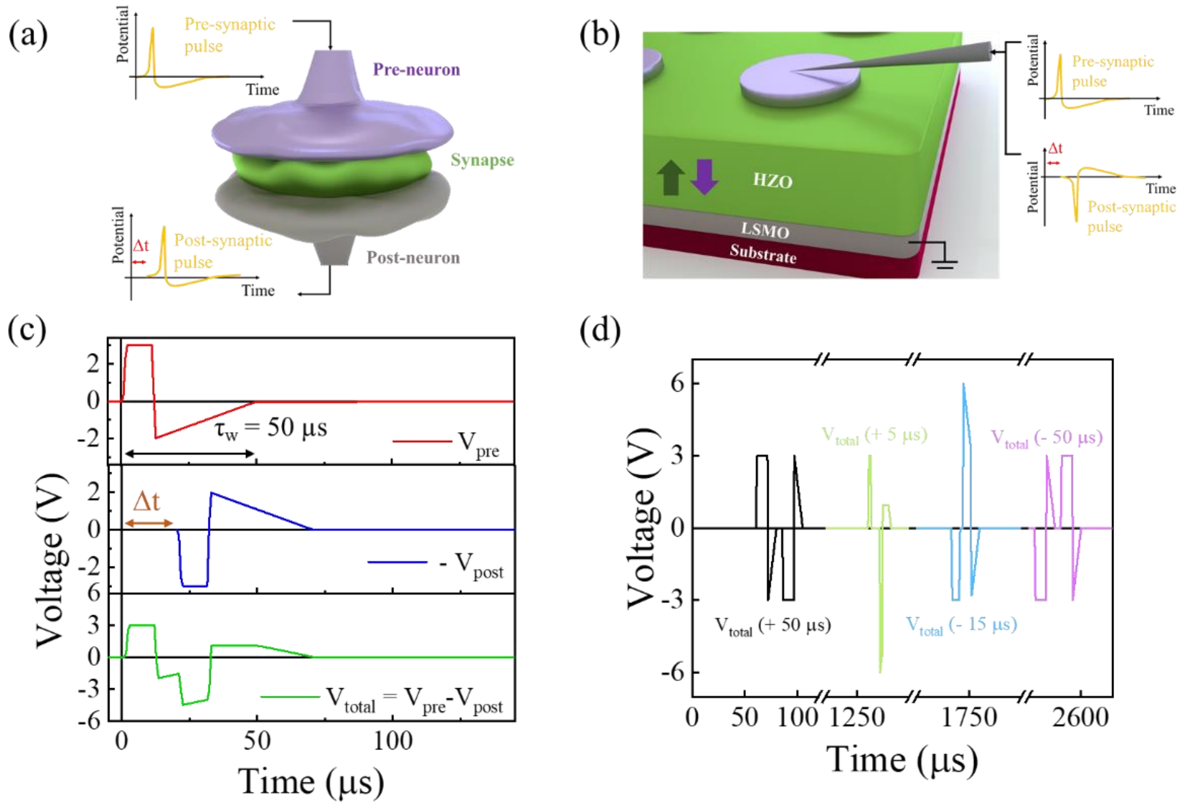

Figure 2. 18. (a) Sketch of pre- and post-neuron connected to a synapse, whose conductance is modulated by the delay time Δt between pre- and post-synaptic pulses. (b) Sketch of HZO ferroelectric tunnel junction, where the top electrode is biased, and the bottom electrode remains grounded. (c) The sequence of waveforms (spikes) applied on the top electrode for spike-timing-dependent plasticity measurement. Both spikes have a duration of 50 µs, as indicated in the top panel. The bottom panel shows the superimposed spikes for Δt = + 20 µs. (d) V_{total} waveforms calculated for different Δt that are applied to the top electrode sequentially.

2.3. Structural characterization

The microstructure of epitaxial HZO films plays a critical role in tunnel junction performance, as discussed in the introduction chapter. In addition to the ferroelectric characterization, four main techniques were used to identify the microstructure: atomic force microscope (AFM), piezo force microscopy (PFM), X-ray diffraction (XRD), and scanning transmission electron microscopy (STEM).

2.3.1. Atomic force microscopy (AFM)

AFM is a scanning probe technique that collects information from a film's topography taking advantage of van der Waals forces between the surface and a nanometric tip connected to a cantilever. The mechanism is based on detecting the cantilever's movement by reflecting a laser

beam, as Figure 2.15 indicates. The cantilever and tip scan a defined area of the sample and give information from the surface roughness.

In order to investigate HZO topography, two machines were used to obtain topography maps: i) Keysight 5100 AFM and ii) Asylum Research MFP-3D Origin+ AFM system equipped with silicon tips with 7 nm radius. In the first case, the measurements were performed at the technical service at ICMAB handled by the technicians Maite Simón Sorbed and Andrés Gómez Rodriguez. In the second, the measurements were performed by Huan Tan at the new AFM equipment located at MULFOX laboratory. The topography image was analyzed by me using Gwyddion open software.

In both cases, the topography images were acquired using the Tapping mode. The cantilever oscillates vertically near or at the cantilever's resonant frequency (≈ 70 kHz) using a piezoelectric crystal. As the oscillating cantilever interacts with the surface, the oscillation is necessarily reduced due to energy loss caused by the tip contacting the surface. The AFM then translates this reduction in oscillation amplitude into information about surface topography. Throughout the image recording, a feedback system ensures constant tip-sample force. This force is maintained at the lowest possible level to avoid damaging the surface.

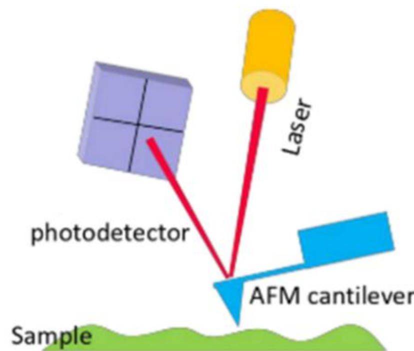

Figure 2. 19. Sketch of AFM mechanism.

2.3.2. Piezo Force Microscopy (PFM)

In the Asylum Research MFP-3D Origin+ AFM system, an extra mode can be used to perform ferroelectric domain mapping or perform *I*(*V*) curves using the nanometric tip as an electrical contact. This mode exploits the converse piezoelectric effect: when an a.c. an electric field is

applied to a ferroelectric material, the surface vibrates.[193] The sample's polarization state can be determined by measuring the magnitude and phase from this piezoelectric vibration signal.

The domain mapping is performed by scanning the sample's surface with the tip in contact while applying a local electric field. The system measures the electromechanical response from the sample by monitoring the cantilever mechanical motion. The amplitude response is a measurement of the effective piezoelectric coefficient (d_{33}), which can be related to the polarization magnitude. The polarization direction is determined from the PFM phase signal. With this technique, it is possible to contact the junction's electrode or the bare surface from the ferroelectric.

The tip used is ElectriMulti 75-G from BugdetSensors with chromium (5 nm) / platinum (25 nm) coating on both sides of the cantilever. The radius of this tip is < 25 nm. The measurements were acquired and analyzed by Huan Tan at the equipment located at MULFOX laboratory as part of her Ph.D. research project.

2.3.3. X-ray Diffraction (XRD)

XRD was used to investigate the phase composition, thickness, and crystallographic texture (orientation) of HZO films grown epitaxially. Diffraction occurs from periodic structures that are exposed to waves with wavelength comparable to the spacing between objects.[194] As X-rays have wavelengths of ≈ 1 Å, they will diffract from objects with a periodic spacing of this order, i.e., atoms in a crystal. Diffraction patterns are formed from the constructive interferences when the path difference between two x-rays is equal to an integer multiple from the wavelengths. Bragg's equation does the description of this effect

$$n\lambda = 2d\sin\theta \qquad \textit{Eq 2. 10}$$

Where θ = half of the scattering angle (2θ), λ = X-ray wavelength, d = distance between diffraction planes. A sketch of this effect is shown in Figure 2.16(a).

In a crystal, atoms' periodicity is in three dimensions, and they are symmetrically arranged. The smallest repeating unit that can be defined is a unit cell. The real space cell's lengths in three independent directions (*a, b, c*) are indicated in Figure 2.16(b), where a cubic cell is taken as an example. There are six other lattice types (tetragonal, hexagonal, orthorhombic, rhombohedral, monoclinic, and triclinic). The high degree of order and periodicity in a crystal defines sets of crystallographic planes occupied by the atoms in the crystal. The planes are indexed by an integer

triple *hkl* (Miller index), which corresponds to specific points of its intersection with the unit cell edges. A family of parallel planes is defined by *hkl* index, which is exemplified by the family of planes (110) displayed in Figure 2.16(c).

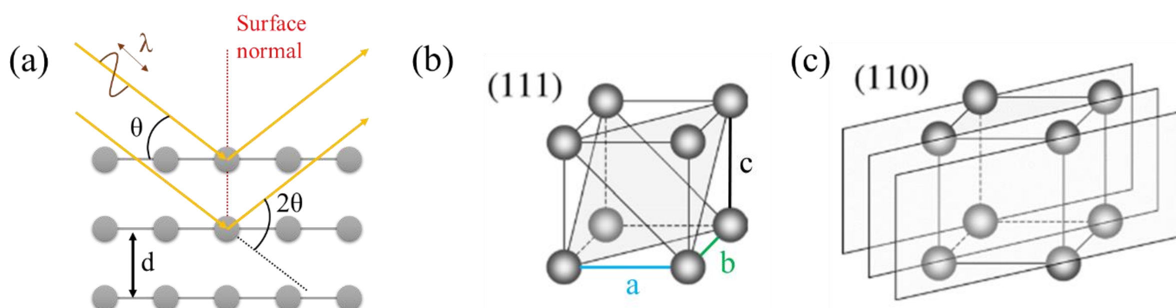

Figure 2. 20. (a) Sketch of Bragg's law. (b) Cubic unit cell with lattice parameters in three independent directions and identification of lattice plane (111). (c) A set of parallel planes (110) are represented in a cubic cell.

A setup that allows the sample's rotation in all directions is necessary to assess different diffraction planes. Therefore, four angles are used to explore the sample, as sketched in Figure 2.17. The incident x-ray angle is defined as θ, and the diffracted beam angle is 2θ taking as reference the sample surface. The rotation around the surface normal corresponds to angle ϕ, while the rotation in-plane (perpendicular to normal) is represented by χ and ω.

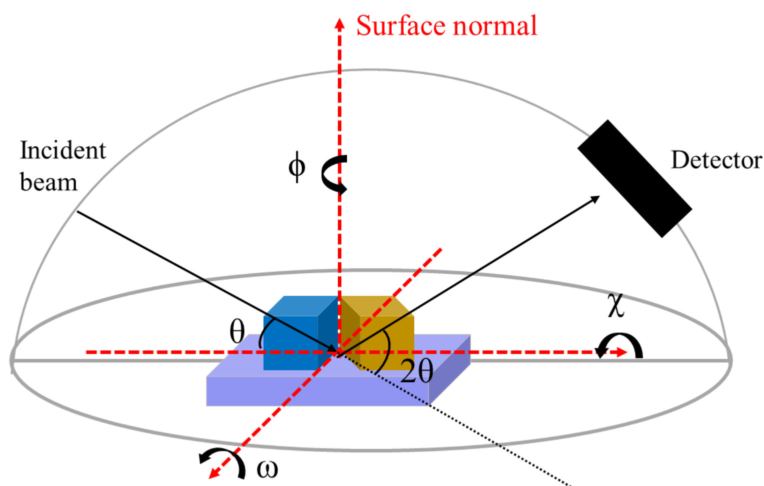

Figure 2. 21. Axes and degrees of freedom for rotation in an XRD measurement.

A simple scan is used to measure Bragg reflections (position, shape, intensity) to extract information from the microstructure of a film. X-ray reflectivity (XRR) is a specific type of scan used to determine the thickness of films and calibrate a material growth in PLD.

***θ-2θ* scans** Also called *ω-2θ*. The diffraction pattern is collected by varying the incoming x-ray beam's incidence angle while measuring the scattered intensity. Symmetric *θ-2θ* is a direct measurement of d_{hkl} spacing of places parallel to the surface for a (001) oriented crystal, corresponding to a scan along the (*00l*) family of planes.[195]

In the case of this thesis, films are grown epitaxially. Epitaxial films have a highly ordered atomic arrangement that requires a matching between layer and substrate crystal lattices instead of polycrystalline films, in which the crystallites can be randomly oriented or textured (Figure 2.18(a, b)).[196] Estandia et al. have shown that HZO films are epitaxial[53], i.e., HZO grains show specific out-of-plane and in-plane orientations. Nevertheless, the grains exhibit four variants that are rotated 90º in-plane. As an example, Figure 2.18(c, d) shows a sketch from the top and cross-sectional view, respectively, of the epitaxial relationship for m-HZO grains that are rotated in-plane. This effect arises from the twinning of the crystal on a 4-fold in-plane symmetry of the substrate.

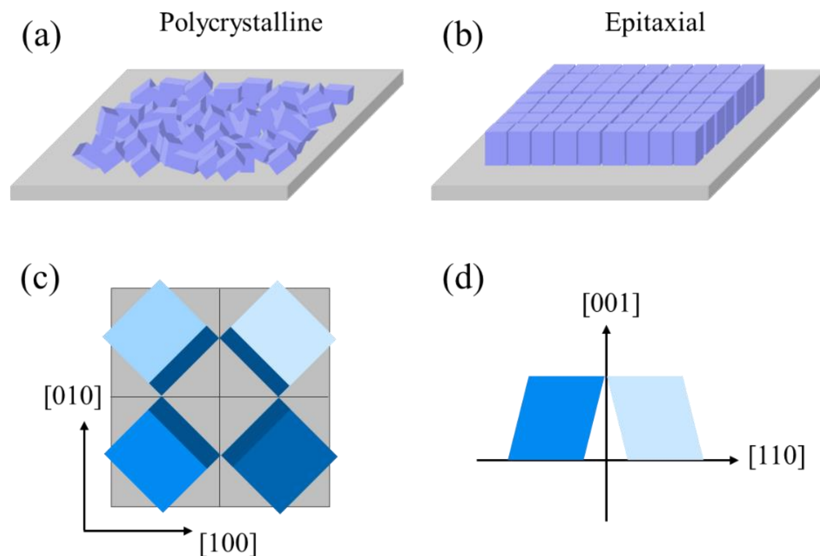

Figure 2. 22. Representation of structural differences between (a) polycrystalline and (b) epitaxial film. (c) Top and (d) cross-sectional view of four crystal variants from m-HZO with 90º rotation in-plane.

In order to observe the four HZO crystal variants with an X-ray diffraction measurement, the sample should be rotated in-plane. This technique is called a *2θ-χ* scan, which combines the data from X-ray diffracted at a fixed *2θ* angle when the sample is rotated by *χ* in-plane.

X-ray reflectivity (XRR) XRR are *θ-2θ* scans made at low angles (*2θ* ≈ 0.5° - 8°), i.e., the incident x-ray beam reaches the surface at very low incidence. One part of the beam is reflected at the surface, and the other part penetrates the layer with thickness *t* and is reflected at the interface between film and substrate. These parallel beams create interference fringes at specific angles. Bragg's law is then satisfied, but instead of d_{hkl}, the layer thickness *t* is calculated. With this information, the growth rate (nm/cycle) of the film is calculated by $\frac{thickness}{PLD\ cyles}$.

Two-dimensional X-ray diffraction (2θ-χ frame) This measurement uses a two-dimensional detector, which allows diffracted X-ray to be collected simultaneously for a range of *θ* and *χ*. The configuration of data recorded by the 2D detector is shown in Figure 2.19(a). The rectangle indicates the data collected by a one-dimensional detector.[197] Also, Figure 2.19(b) exhibits an example of a *2θ-χ* scan recorded for an HZO (4.6 nm) / LSMO / STO (001). The o-HZO (111) reflection is a bright circular spot at *2θ* ≈ 30º, whereas the m-HZO (002) has a peak at *2θ* ≈ 34º. In general, an elongated peak along *χ* signals higher mosaicity. The corresponding *θ-2θ* is obtained by integrating the *2θ-χ* within a *χ* = ± 10º angular range, indicated by the green line. The intense (00*l*) reflection from the substrate and LSMO can also be identified.

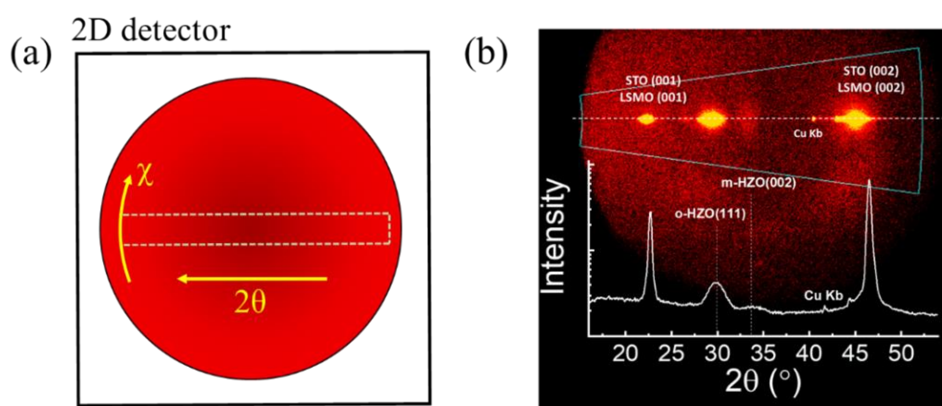

Figure 2. 23. (a) Illustration of image data acquired from the 2D detector. The horizontal axis corresponds to an increasing 2θ scan, and the arc represents increasing χ. The rectangle indicates data recorded by a 1D detector. (d) Example of 2θ-χ frame collected at HZO (4.6 nm) / LSMO / STO (001) sample. By integrating within a χ range (indicated region), a θ-2θ plot can is obtained.

XRD 2θ-χ scans were carried out by a Bruker-AXS D8 Advance diffractometer equipped with a Vantec 500 detector with Cu-$K_{\alpha 1}$ radiation, and its corresponding θ-2θ scans were obtained by integration within a χ range. XRR measurements were performed by Siemens D5000 diffractometer (one-point detector) using Cu-K_{α} radiation (λ K_{α} = 1.54056 Å and λ K_{β} = 1.54439 Å). The instruments are located at the X-Ray Diffraction Lab in ICMAB, and the measurements were performed by Anna Crespi, Joan B. Esquius, and Javier Campos.

2.3.4. Scanning Transmission Electron Microscopy (STEM)

The microstructure of HZO films is also investigated by STEM. In this technique, a highly energetic monochromatic electron beam is focused by electromagnetic lenses on a thin sample specimen, which typically has a thickness of less than a hundred nanometers. The beam is scanned on the specimen, providing a varying signal for each position of the beam. The short wavelength from the beam and its small size on the specimen (beam size can be smaller than 1 Å) allow high spatial resolution and acquisition of images where the film's crystal column structure can be appreciated.

Electrons scattering elastically at high angles depend strongly on the atomic number (Z) of the sample atoms through the approximate Z^2 dependence of the Rutherford scattering cross-session. Therefore, a high-angle annular dark-field (HAADF) imaging mode was used. The detection at high angles removes the coherent effect of diffraction, and the resulting incoherent image provides a compositional map of the sample with high atomic-number contrast.[198] The image is described as incoherent because the intensity measured is a convolution between the intensity of the microscope point-spread function (illuminating probe) and the object function with localized peaks at the column positions.[199] An example of an HAADF image is shown in Figure 2.25(a).

Also, a complementary electron energy-loss spectroscopy (EELS) technique is used to build chemical composition maps. For this, electrons scattered at low angles are collected, and their energy loss is measured. The spectrum consists of electron counting versus energy. The region of low-loss (E < 100 eV) contains primary electrons that did not undergo a noticeable energy loss (zero-loss peak), plasmon peaks (collective oscillations of valence electrons), and low lying core state excitation.[200] However, the region above 100 eV contains the so-called core-loss region.

The element-specific core excitations are caused by the ionization, in which electrons are ejected from an inner, or core, shell (K, L, M, ...) of atoms in the specimen to an unoccupied higher lying state of the crystal or even to a free electron state.[201] In order of electrons transition, they must absorb energy greater equal or than the critical ionization energy, E_c, which depends on the specific atom and electron shell and, therefore, it is uniquely defined. Characteristic signals appear in the spectrum at energy losses corresponding to E_c, so-called *ionization edges*, which identify the presence of a specific element in the specimen. The intensity can be related directly to the quantity of the element present. One spectrum can be collected for each pixel scanned on the specimen, thus providing chemical information with high spatial resolution. Figure 2.24 shows a sketch relating the EEL spectra and the transition of core electrons into the conduction band.

The ionization edges have small intensity fluctuations just above the edge onset, termed *energy-loss near-edge structure* (ELNES). It has been found that they are directly related to the distribution of empty states left by the ionized electrons and can be interpreted in terms of the bonding state (coordination, valence, and type of bonding) of the ionized atom.

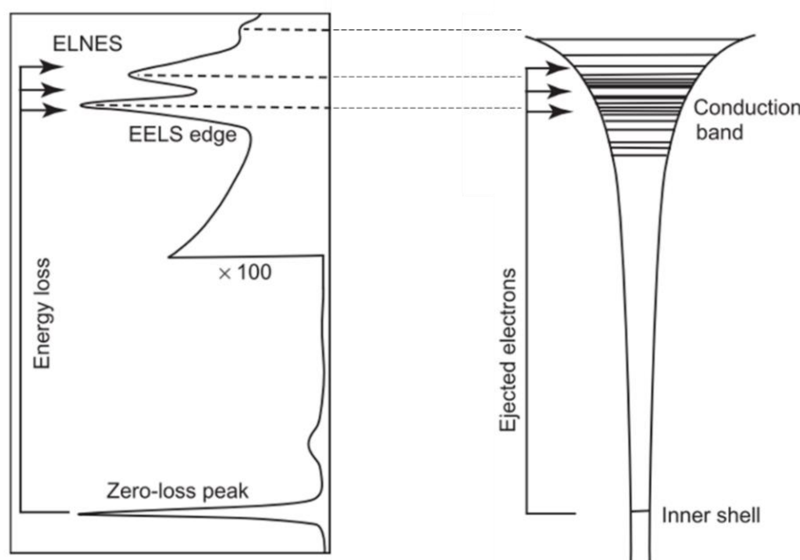

Figure 2. 24. Correspondence between EEL spectra, the transition of electrons from inner shell states to the conduction band, and appearance of ELNES fine structure used to identify element distribution in region scanned with the electron beam. Image adapted from [200].

It is possible to obtain two-dimensional EELS images by moving the electron beam along a sample region while acquiring EEL spectra.[202–204] By this analysis, one can map the image's pixels that

contain a signal from a particular element, i.e., ionization edge. As an example, Figure 2.21 shows an Annular Dark Field (ADF) image acquired simultaneously with the electron EEL spectrum image. The elemental maps were obtained from the Pt-M at 2122 eV (in red), Ti-L at 456 eV (in blue), and Zr-L at 2222 eV (in yellow) edges. In addition, Sr-L_3 at 1940 eV and Hf-M at 1662 eV edges will be used. The Hf-M edge is just before the onset of Sr-L_3 edge, and, thus, only M_5 and M_4 contribute.

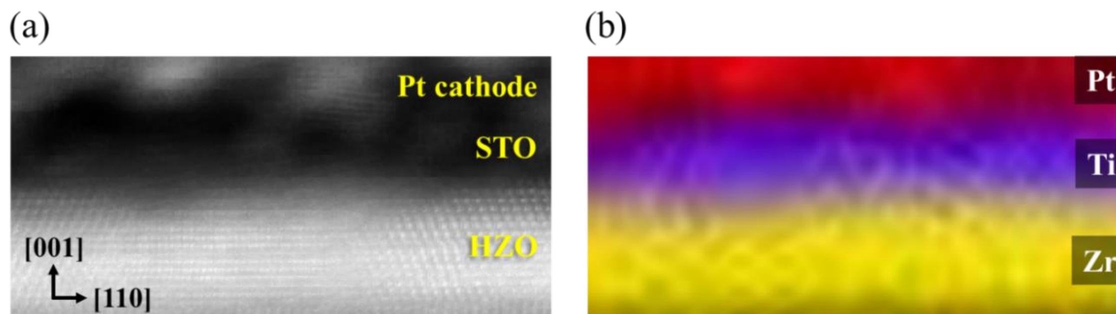

Figure 2. 25. (a) ADF image acquired simultaneously with (b) electron EEL spectrum image in sample Pt / STO (2 nm) HZO (4.6 nm) / LSMO / STO (001).

The images and the EEL spectra presented in this thesis were obtained with an aberration-corrected STEM for microstructural analysis with atomic resolution. They and were provided by Saul Estandía as part of his Ph.D. research project supervised by Dr. Jaume Gàzquez from MULFOX group in ICMAB and Dr. Matthew F. Chisholm from the Center for Nanophase Materials Sciences, Oak Ridge National Laboratory (US). Two microscopes were used:

i. NION UltraSTEM operated at 200 kV equipped with a NION corrector at the Center for Nanophase Materials Sciences, Oak Ridge National Laboratory (US).
ii. JEOL JEM ARM200cF operated at 200 kV equipped with a CEOS aberration corrector and GIF Quantum ER spectrometer at the Universidad Complutense de Madrid, Spain.

Chapter 3. Ferroelectric and Ionic-based Contributions to Electroresistance in HZO

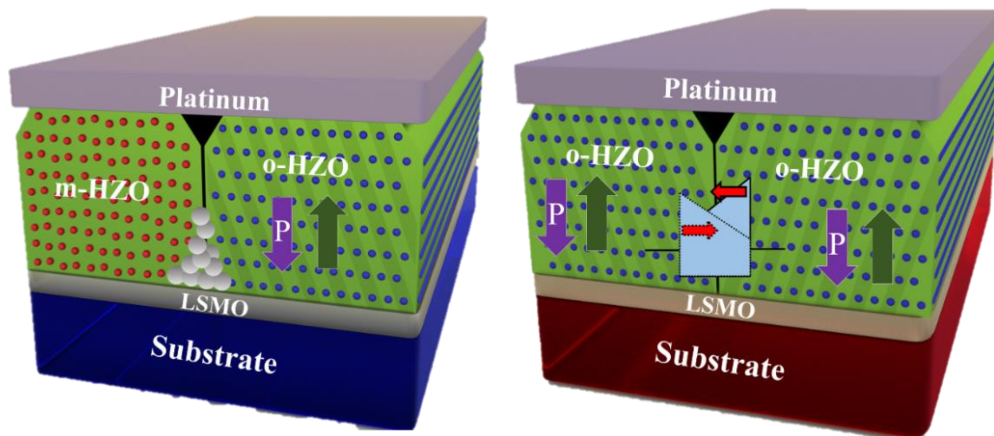

The results of this chapter have been published in "Sulzbach, M. C., Estandía, S., Long, X., Lyu, J., Dix, N., Gàzquez, J., Chisholm, M. F., Sánchez, F., Fina, I., Fontcuberta, J., Unraveling Ferroelectric Polarization and Ionic Contributions to Electroresistance in Epitaxial $Hf_{0.5}Zr_{0.5}O_2$ Tunnel Junctions. *Adv. Electron. Mater.* 2020, 6, 1900852" from where the figure above is adapted.

The microscopic mechanisms leading to resistance change in $Hf_{0.5}Zr_{0.5}O_2$ (HZO) tunnel junctions are an intricate interplay between ferroelectric polarization switching, barrier modulation, and defect-related transport mechanisms. The fundamental role of HZO film´s microstructure in determining the balance between these contributions is demonstrated. The HZO film presents coherent or incoherent grain boundaries associated with the coexistence of monoclinic and orthorhombic phases, which are dictated by the mismatch with the substrates in the epitaxial growth. These grain boundaries are the toggle that allows obtaining either large (up to ~ 450 %) and fully reversible genuine polarization controlled electroresistance when only the orthorhombic phase is present or an irreversible and extremely large (~10^3 – 10^5 %) electroresistance when both phases coexist.

3.1. Introduction

The epitaxial growth of ferroelectric HZO thin films has opened the door for studying and engineering ferroelectric tunnel junctions (FTJ) compatible with the current CMOS technology. Nevertheless, FTJ is not only sensitive to polarization effect but may also be affected by ionic and defect-related charge motion inside the dielectric lattice. For example, ferroelectric tunnel barriers composed of $BaTiO_3$ [35,54,145] and $BiFeO_3$ [205] display contributions to electroresistance (*ER*) due to ionic motion. In the case of ultrathin HZO films, its ferroelectric character has been assessed by a piezoelectric force microscope (PFM) and by recording *P*(*V*) loops in micrometric electrodes. Nevertheless, at this point, a question arises: can ferroelectric-related *ER* be observed in epitaxial HZO tunnel barriers and exploited to create Hf-based FTJ?

The electroresistance in non-ferroelectric oxides, including HfO_2, has been explored mainly for its resistive switching effect to create memory devices and logic elements. In these oxides, the resistance can be switched between high (HRS) and low (LRS) states by applying an appropriate voltage that induces conductance changes, mostly originated from the motion of oxygen vacancies that modify the conductivity in some areas of the film. The mechanism responsible for the resistive switching has been largely discussed. In monoclinic HfO_2, Bersuker et al.[97] have found out that the forming is related to a soft breakdown of the dielectric, which creates filamentary conductive paths inside the film. The filaments are preferentially formed in grain boundaries from the polycrystalline film, taking advantage of the already high oxygen vacancies concentration. When the electric field is applied, the vacancies drift and diffuse through the film creating the filament

with low oxygen concentration connecting both electrodes. This state corresponds to the LRS or ON state. In contrast, when the electric field reverses polarity, the vacancies closer to the electrically biased electrode diffuse through the oxide, breaking the low conduction channel and restoring the film's insulating character. This state corresponds to the HRS or OFF. A more detailed description of this effect can be found in the Introduction Chapter.

Indeed, the electroresistance effect in doped-HfO_2 ferroelectric tunnel junctions has been reported.[16,18,162,206] Nevertheless, data does not allow to conclude if it is due to polarization-related effects or it results from an association with electric-field charge motion. For instance, Wei et al. [206] reported current-voltage curves, $I(V)$, in 2 nm HZO barriers and argued that the electrical transport across the barrier could be described using the Brinkman model.[73] However, the barrier properties dependence on the polarization direction was not explored; thus, the connection between *ER* and *P* remained undisclosed. Ambriz-Vargas et al.[16,162] also reported $I(V)$ measurements on 2.8 nm HZO polycrystalline barriers. Nonetheless, the voltage excursion was analyzed in a narrow voltage region, in which the curve is almost linear. The fitting of these curves with the Brinkman model prevents robust extraction of barrier parameters and possible change due to polarization reversal since it is not sensitive to curvature variation in the sigmoidal $I(V)$. Yoong et al.[18] reported $I(V)$ data on HZO epitaxial barriers with 10 nm HZO films after different writing pulses accompanied by polarization curve extracted from PFM measurement. In their case, transport data were analyzed using a thermionic emission over a polarization-modulated barrier as the dielectric thickness does not allow direct tunneling. The $P(V)$ extracted from PFM is fully saturated at 4 V. In contrast, the $I(V)$ curves measured after ± 7, ± 8, and ± 9 V vary significantly, indicating that even though the ferroelectric is saturated, the barrier properties are still being modified, which suggests that another mechanism apart from polarization dictates barrier properties.

In this chapter, the polarization and ionic contributions on the electroresistance in HZO (4.6 nm) ferroelectric tunnel junctions will be disentangled. In order to do that, current and polarization curves, $I(V)$ and $P(V)$ respectively, are recorded at room temperature in junctions with 314 μm^2 area. Also, the resistance dependence on a writing voltage pulse, $R(V_w)$, is explored. The HZO films are grown on single crystalline cubic substrates with different in-plane lattice parameters, taking advantage of the structural mismatch between HZO and strained LSMO-coated substrates, which determines the microstructure of the HZO.[53] The microstructure is interpreted as the

abundance of ferroelectric orthorhombic (o-HZO), paraelectric monoclinic (m-HZO) grains, and the grain boundaries (GB) formed between them. It has been shown that incoherent grain boundaries are instrumental for electric-field controlled resistive switching.[97] Therefore, by varying the relative amount of coherent and incoherent GB, their role in electroresistance can be disentangled.

3.2. Samples

Epitaxial HZO films with 4.6 nm nominal thickness were grown on LSMO (22 nm) conducting buffer (001) single-crystalline $SrTiO_3$ (STO), $GdScO_3$ (GSO), $TbScO_3$ (TSO), and $(LaAlO_3)_{0.3}(Sr_2TaAlO_6)_{0.7}$ (LSAT) substrates by pulsed laser deposition (PLD). A pseudocubic setting is used for scandates. The bulk cell parameters of these single crystalline substrates are a_s^{STO} = 3.905 Å, a_s^{GSO} = 3.97 Å, a_s^{TSO} = 3.958 Å and a_s^{LSAT} = 3.868 Å. A full characterization of HZO films deposited on these substrates is presented elsewhere.[53]

Ex-situ sputtered circular platinum top electrodes with 20 μm diameter (area ≈ 314 μm^2) were grown through a shadow mask. Details on the PLD and sputtering deposition are described in the Experimental Methods chapter.

3.3. Junctions grown on STO (001) substrates

This section explored the ferroelectric and structural characterization of junctions grown in STO (001) substrates. The FTJ heterostructure and electrical arrangement are sketched in Figure 3.1(a). Each junction is identified with a code J_n. Figure 3.1(b) shows an X-ray diffraction (XRD) 2θ-χ frame and corresponding θ-2θ scan obtained by integration of χ within ± 10º angular range. Intense (00*l*) substrate and LSMO reflections are indicated as well as the ferroelectric o-HZO (111) reflection and the m-HZO (002) small broad peak. The large intensity from the o-HZO (111) peak indicates its prevalence in the film compared to m-HZO.

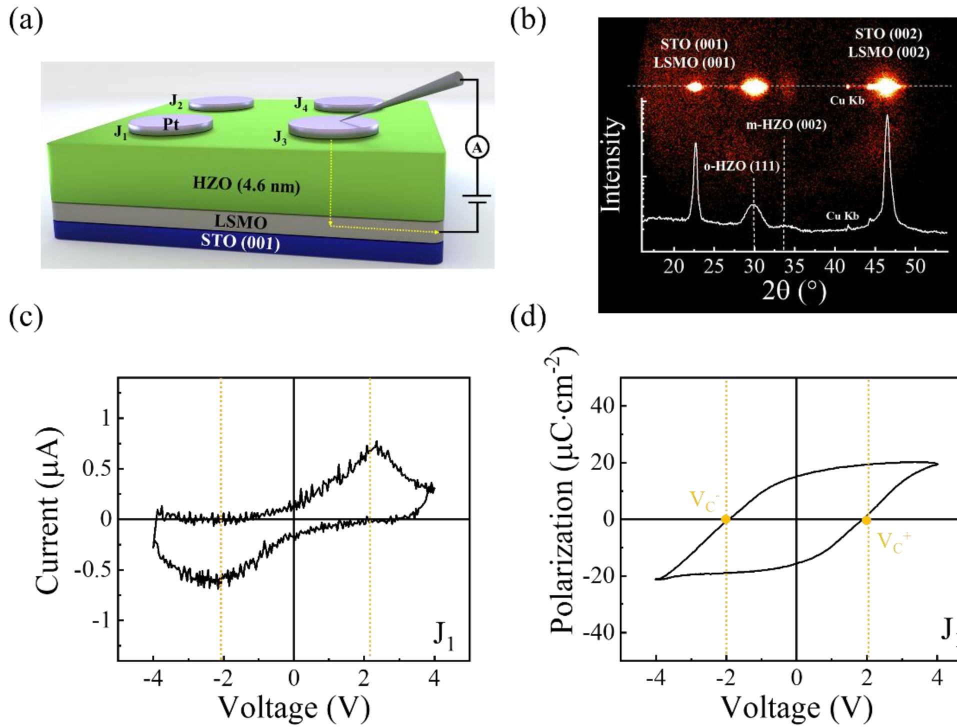

Figure 3. 1. (a) Sketch of the sample and contact arrangement for electrical measurement. (b) XRD 2θ-χ frame of the sample represented in (a) and corresponding θ-2θ scan obtained by integration of χ within ± 10º angular range. (c) Current-voltage, I(V), curve recorded in junction J_1 with DLCC at 1 kHz and V_{max} = 4 V. Yellow dashed vertical lines indicate the coercive voltage ($V_c \approx \pm 2$ V). (d) Corresponding polarization P(V) curve.

Figure 3.1(c) shows the $I(V)$ curve recorded in junction J_1 at 1 kHz with dynamic leakage current compensation (DLCC) on a pristine device. In addition to DLCC, a second compensation was performed to remove the linear contribution from the electric susceptibility (χ) to allow correct identification of coercive fields. Details on this compensation are described in Appendix 1 and the Experimental Methods Chapter. The corresponding $P(V)$ curve is shown in Figure 3.1(c). The coercive voltage and remnant polarization extracted correspond to $V_c^+ \approx V_c^- \approx 2$ V and $P_R \approx 16$ μC·cm^{-2}. These ferroelectric characteristics are consistent with previous reports.[123,126,127]

At this point one can investigate the electroresistance response in Pt / HZO (4.6 nm) / LSMO // STO (001) junctions. The $I(V)$ curve shown in Figure 3.2(a) is measured in junction J_2 at a higher frequency (5 kHz) with DLCC to allow meaningful comparison of the coercive field with the writing pulse amplitude (V_w) necessary to induce electroresistance. The polarization switching peak occurs at $V_c \approx \pm 2$ V (vertical dashed line), which is coherent with the value obtained in Figure 3.1(c, d). The small loop observed close to V_{max} is a spurious effect due to the high frequency of

the measurement (Appendix 2). As explained in detail in the Experimental Methods chapter, the pulse sequence to measure *ER* corresponds to a sequence of writing pulses with amplitude V_w and duration τ_w = 100 μs applied on the top electrode while the bottom electrode is grounded. A sketch of one writing pulse followed by a reading *I*(*V*) is depicted in Figure 3.2(b). In this chapter, the shape of the writing pulse is a triangle. After a delay time τ_D = 0.5 s, a reading *I*(*V*) curve is collected for a linear bipolar *V*(*t*) pulse ranging from – 1 V to + 1 V to avoid polarization reversal.

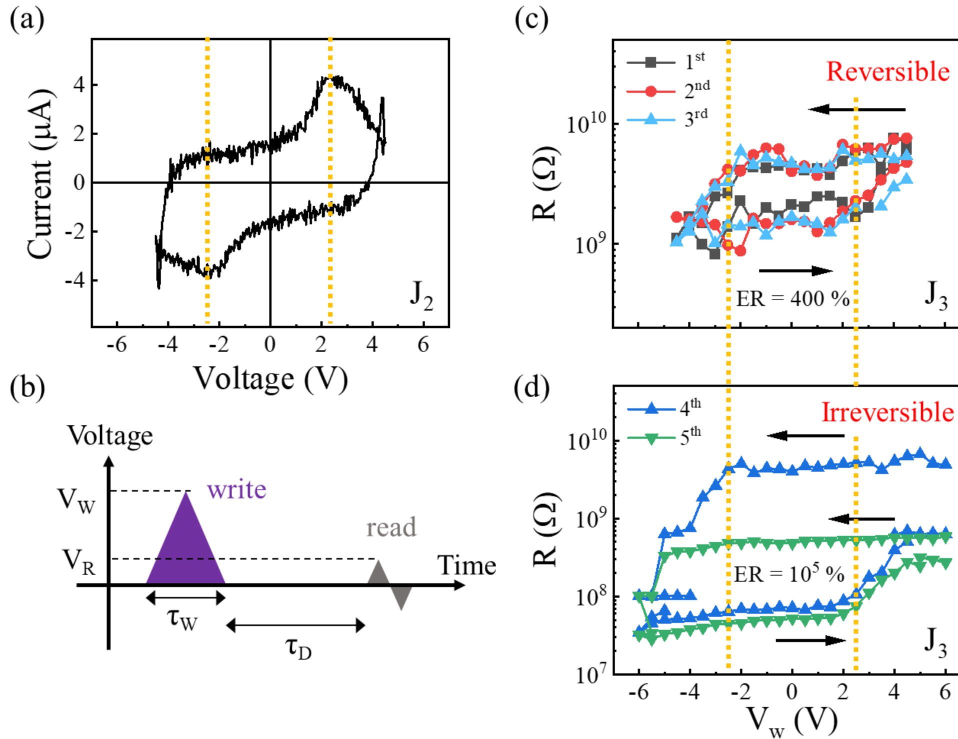

Figure 3. 2. (a) I(V) loop from Pt / HZO / LSMO // STO measured at 5 kHz with DLCC and V_{max} = 4.5 V before performing $R(V_w)$ measurement. (b) Sketch of the writing/reading measurement protocol. The writing amplitude (V_w), pulse duration (τ_w), dwell time (τ_D), and reading voltage V_R are indicated. (c) Dependence of the junction resistance R for $|V_w| \leq 4.5$ V. Three consecutive cycles are shown to illustrate reversibility. (d) $R(V_w)$ sequence of two cycles for $|V_w| \leq 6$ V showing irreversibility. Dashed vertical lines indicate V_c of the HZO film extracted from (a).

The resistance is calculated for V_R = 0.9 V. Figure 3.2(c) shows the resistance dependence with V_w in junction J_3 for $|V_{max}| \leq 4.5$ V. The increasing/decreasing resistance at $V_w \approx 2.5$ V coincides with the V_c of the ferroelectric as indicated by the vertical dashed lines. Three consecutive loops are measured, demonstrating the reversibility of the process. The calculated *ER* reaches 400 % with no forming step needed. In contrast, when V_w increases to ± 6 V, the *ER* dramatically increases (≈ 10^5 %). The two sequential measurements are shown in Figure 3.2(d) have very different $R(V_w)$

responses in which the large step at $V_w \approx$ - 5.5 V (blue curve) give rise to an irreversible change in *R*. These data strongly suggest that two distinct mechanisms can induce *ER,* and the writing voltage controls the appearance of either one or other effect. The first mechanism causes *ER* due to polarization reversal and appears for $|V_w| \leq 4.5$ V. Whenever V_w is larger, the second effect becomes relevant. The 4th curve (blue symbols) in Figure 3.2(d) indicates that both effects can coexist in HZO tunnel junctions: a first resistance drop at $V_w \approx \pm 2$ V due to polarization reversal is followed by a second larger drop at $V_w \approx$ - 5.5 V related to an irreversible resistive switching process. These two effects are not a consequence of each other, as reported in polycrystalline HfO_2 thin films.[82]

The resistance dependence on the writing voltage amplitude is measured in junction J_2 according to Method 2 described in the Experimental Methods chapter. This configuration is used to have further details on the two *ER* mechanism and their reversibility. Figure 3.3(a) displays two clear regions (I and II), and the transition from Region I to II happens at a V_w labeled as V_{GB}. In Region I, where $|V_w| < 5$ V, the resistance increases for $V_w > 0$ and decreases for $V_w < 0$. The resistance values are consistent with those observed in Figure 3.2(c). Note the resistance does not vary for $|V_w| < 2$ V, indicating that a writing amplitude larger than V_c must be applied to induce any change. This observation strongly suggests that the *ER* in Region I is related to polarization reversal. On the other hand, in Region II ($|V_w| > 5$ V), a significant decrease in resistance is observed irrespective of the writing pulse polarity. The *ER* values calculated for each V_w are displayed in Figure 3.3(b). The electroresistance increases with V_w in Region I, reaching 340 % at ± 4.5 V. At $V_{GB} = 5$ V, the *ER* has a well-pronounced maximum of 2000 %. Note that these *ER* values are slightly different from those in Figure 3.2(c, d) due to the different pulse trains used.

It is worth mentioning that the junctions remain ferroelectric after the application of $|V_w| \leq 7.5$ V. However, increasing V_w to 8 V leads to irreversible changes in the junction, which decreases resistance, and there is no evidence of ferroelectric switching (Appendix 3). Besides, most junctions in the sample exhibit two regions (I and II) and similar resistance behavior to the one seen in Figure 3.3(a). The $R(V_w)$ data for six different junctions are exhibit in Appendix 4. The writing amplitude necessary to induce the transition from Region I to II (V_{GB}) is insensitive to the writing time duration (τ_w) and delay time (τ_D) within the range $\tau_D = 0.2 - 1$ s and $\tau_w = 10 - 500$ µs.

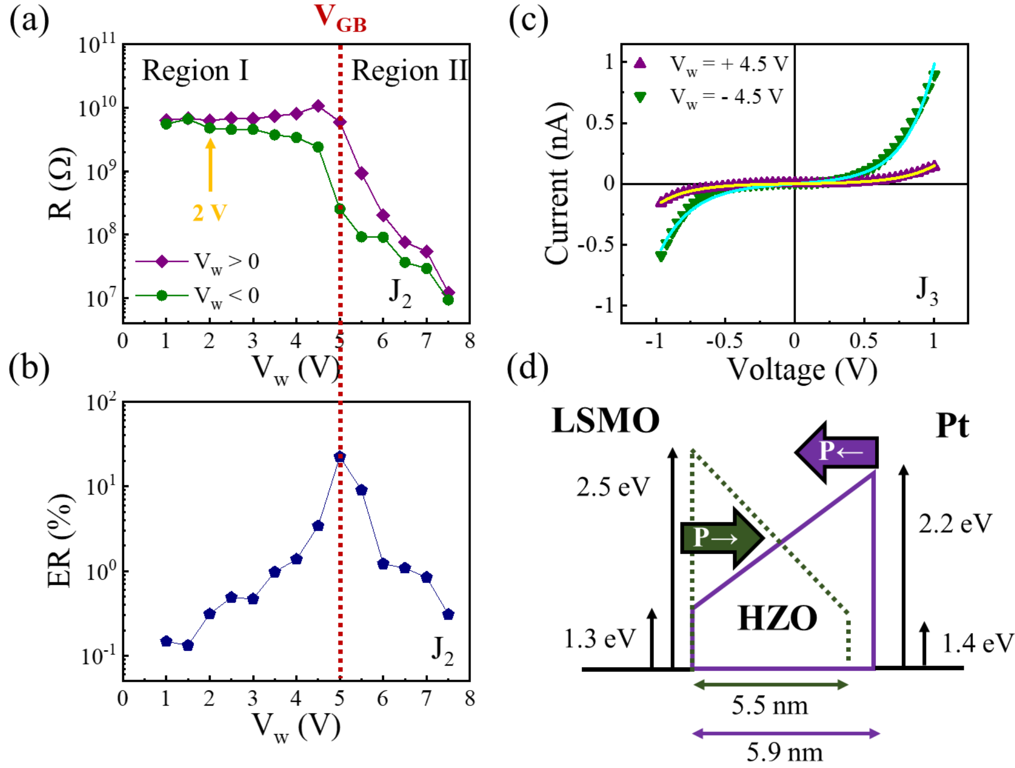

Figure 3. 3. (a) Resistance dependence on V_w in Pt / HZO / LSMO // STO junction for positive ($V_w > 0$) and negative ($V_w < 0$) writing pulses. (b) Extracted value of electroresistance from data in (a). (c) I(V) curve recorded after writing pulse V_w = + 4.5 V (purple symbols) and – 4.5 V (green symbols) during reading step. Solid lines are the results from the fitting using the Brinkman model described in the text. (d) Sketch of junction energy barrier profile upon P reversal, in which ϕ_{LSMO}, ϕ_{Pt}, and t_{eff} are extracted from the fitting in (c). The effective thickness reduction is sketched in the Pt/HZO interface, although it does not necessarily happen at this position.

The shape of the *I*(*V*) curves is used to investigate the *ER*'s origin in the reversible Region I. Figure 3.3(c) shows that the *I*(*V*) collected in junction J_3 after application of V_w = ± 4.5 V. The sigmoidal and asymmetric curve is commonly found in trapezoidal tunnel barriers.[161] The resistance is smaller for V_w = - 4.5 V (green symbols) than for V_w = + 4.5 V (purple symbols), in agreement with the $R(V_w)$ from junction J_2. Data is fitted (solid lines) using the Brinkman model[73] to extract the barrier heights at the Pt / HZO (ϕ_{Pt}) and HZO / LSMO (ϕ_{LSMO}) interfaces and the effective barrier width (t_{eff}). It is possible to calculate the mean barrier height, $\phi_{mean} = \frac{\phi_{Pt} + \phi_{LSMO}}{2}$, and the difference between them, $\Delta\phi = \phi_{LSMO} - \phi_{Pt}$ from the trapezoidal barrier. The fitted values corresponding to V_w = + 4.5 V in Figure 3.3(c) are ϕ_{LSMO} = 1.3 eV, ϕ_{Pt} = 2.2 eV, t_{eff} = 5.9 eV, ϕ_{mean} = 1.75 eV and $\Delta\phi$ = - 0.9 eV. In the other hand, for V_w = - 4.5 V are ϕ_{LSMO} = 2.5 eV, ϕ_{Pt} = 1.4 eV,

t_{eff} = 5.5 eV, ϕ_{mean} = 1.95 eV and $\Delta\phi$ = + 1.1 eV. The properties of the barrier extracted from the fittings are shown in Table 3.1. The error bars represent the fitted parameters' dispersion to $I(V)$ data collected after three sequential writing steps with V_w = ± 4.5 V, shown in Appendix 5. Importantly, repeating the cycles on the same junction leads to almost identical barrier properties (Appendix 5). The energy barrier heights are larger than those found in similar devices using BTO as ferroelectric junctions,[39] which is expected due to the lower electron affinity of HfO_2 (≈ 2.0 eV) compared to BTO (≈ 3.9 eV).[207,208] According to sketch in Figure 3.3(c), $V_w > 0$ induces negative surface charges to be accumulated at the Pt/HZO interface in opposition to positive surface charges at the HZO/LSMO interface, which imposes a polarization P pointing towards LSMO. The asymmetric barrier heights at the interfaces (ϕ_{LSMO} = 1.3 eV, ϕ_{Pt} = 2.2 eV) produce a trapezoidal barrier as predicted by Zhuravlev et al. [209] and agree with results obtained in similar BTO ferroelectric junctions.[55,210] For $V_w < 0$, positive surface charges are now accumulated at the Pt/HZO interface and negative at the HZO/LSMO, resulting in polarization reversal (P points towards platinum).

V_w (V)	t_{eff} (nm)	ϕ_{LSMO}(eV)	ϕ_{Pt}(eV)	ϕ_{mean} (eV)	$\Delta\phi$ (eV)
+ 4.5	5.9 ± 0.05	1.3 ± 0.2	2.2 ± 0.2	1.75 ± 0.03	- 0.9 ± 0.03
- 4.5	5.5 ± 0.01	2.5 ± 0.1	1.4 ± 0.3	1.95 ± 0.07	+ 1.1 ± 0.07

Table 3. 1. Parameters extracted from fitting shown in Figure 3.3(c) are effective thickness (t_{eff}), barrier height at interfaces HZO/LSMO (ϕ_{LSMO}), and Pt/HZO (ϕ_{Pt}). Based on these values, the average barrier height (ϕ_{mean}) and the difference between heights ($\Delta\phi$) are calculated. Error bars represent the fitted parameters' dispersion from I(V) data collected after three sequential writing steps with V_w = ± 4.5 V (Appendix 5).

Even though the difference between barrier heights ($\Delta\phi$) reverses almost symmetrically from – 0.9 eV to + 1.1 eV when inverting V_w polarity, the average barrier height (ϕ_{mean}) does not change significantly. At first sight, these fitting results are conflicting with Figure 3.3(a) that shows lower junction resistance $V_w < 0$, which resulted in $ER \approx 400$ %. In order to solve this contradiction, the effective thickness must be inspected more carefully. As indicated in Table 3.1 and Figure 3.3(d), the effective barrier height decreases from 5.9 (± 0.05) nm when V_w = + 4.5 V to 5.5 (± 0.01) nm when V_w = - 4.5 V. This thickness difference ($\Delta t_{eff} \approx 0.4$ nm) becomes the responsible for the lower resistance observed when $V_w < 0$, as the electron`s conductance is exponentially dependent on the barrier thickness. Therefore, even though the barrier height reverses almost symmetrically upon P

reversal, the width increases for $V_w > 0$, which increases the junction's resistivity. Finally, it is possible to conclude that the *ER* in Region I is associated with modulation of the tunnel barrier properties by polarization reversal. Data fitting performed in *I(V)* curves recorded after $V_w = \pm 6$ V (Appendix 5) shows poorer quality suggesting that tunneling conduction might coexist with other conduction mechanisms, as it is discussed next.

3.4. $Hf_{0.5}Zr_{0.5}O_2$ film microstructure dependence on the substrate

The abrupt drop of resistance that marks the transition to Region II happens for both writing voltage pulse polarities (V_w^+ and V_w^-) and is observed in most junctions of the sample (Appendix 4). This behavior is analogous to the forming step observed in HfO_2 and other materials in which an electric field induces the formation of a conductive channel, taking advantage of grain boundaries.[97] The relative amount of monoclinic and orthorhombic phases, and their respective grain boundaries, is different between samples grown on STO and GSO substrates. The structural mismatch between HZO and the LSMO buffer layer favors the growth of the orthorhombic phase with respect to the monoclinic when the HZO/LSMO is grown on substrates with a larger lattice parameter than STO (a_s^{STO} = 3.905 Å), as in the case of GSO (a_s^{STO} = 3.97 Å). Thus, HZO films grown on LSMO/GSO are composed mainly of orthorhombic grain (o-HZO), while films grown on LSMO/STO contain a mixture of orthorhombic and monoclinic (m-HZO) grains.

Figure 3.4 shows HAADF-STEM cross-sectional views from (a) HZO/LSMO//STO, (b) HZO/LSMO//GSO, and (c) HZO/LSMO//LSAT films. The images were obtained along the [110] zone axes of the substrate and show a clear contrast between HZO film and LSMO electrode. Even though the images were acquired on 9 nm thick HZO heterostructures, it is not expected that thinner films grown on STO (001) substrate to increase the relative amount of monoclinic phase with respect to the orthorhombic.[127] Appendix 6 contains a larger field of view in the three films. Figure 3.4(a) shows the microstructure of the HZO film grown on LSMO//STO in which monoclinic and orthorhombic grains can be identified with lateral size in the range of 10 – 15 nm. Orthorhombic and monoclinic grains are (111) and (001)-textured on the (001) substrate, respectively, producing non-coherent grain boundaries between phases. Figure 3.4(b) contains a higher magnification image from the grain boundary region. The atomic arrangement in these highly mismatched grain boundaries significantly deviates from the grain structure, which points to a complex atomic reordering at the grain boundary that extends up to several atomic planes. In

contrast, the HZO/LSMO//GSO film's microstructure is expressively different (Figure 3.4(c)). The HZO film is also composed of grains, but only (111)-oriented orthorhombic grains are present. As expected from the epitaxial growth of a (111) textured film onto an (001) cubic substrate, twinning is observed, i.e., two adjacent o-HZO grains with identical out-of-plane texture can be rotated in-plane. Figure 3.4(d) displays a higher magnification of the coherent grain boundary formed between twins o-HZO grains, in which the in-plane rotation is indicated. Notice that this grain boundary is thinner and less distorted than the one formed in HZO/LSMO//STO.

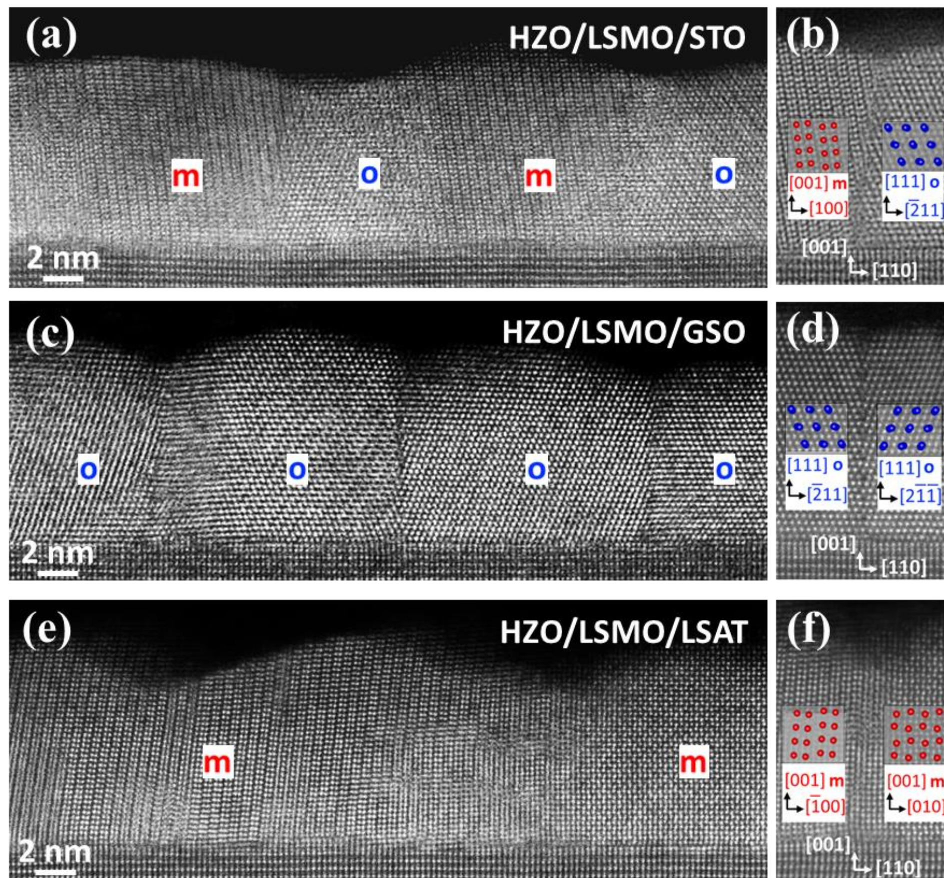

Figure 3. 4. Cross-section atomic-resolution images from 9 nm thick HZO films with heterostructure (a) HZO/LSMO//STO, (b) HZO/LSMO//GSO, and (c) HZO/LSMO//LSAT. Images were acquired along the [110] zone axes of the substrates. Monoclinic grains are signaled in red and orthorhombic grain in blue. (b, d, f) Higher magnification images of the grain boundaries. Red and blue circles represent the projected monoclinic (space group $P2_1/c$) and orthorhombic (space group $Pca2_1$) structures. The epitaxial relationship for the monoclinic phase is [010]m-HZO(001)//[110]LSMO(001), [001]m-HZO(001)//[001]LSMO(001) and [100]m-HZO(001)//[1-10]LSMO(001). In the case of the orthorhombic phase, it is [-211]o-HZO(111)//[110]LSMO(001) and [111]o-HZO(001)//[001]LSMO(001), where all indices refer to the cubic or pseudocubic unit cell. LSMO and the substrates have a cube-on-cube epitaxial relationship.

In summary, o-HZO and m-HZO crystallites can be identified in films grown in STO substrate (Figure 3.4(a, b)), thus incoherent and highly distorted grain boundaries necessarily exist. In contrast, films grown on GSO exhibit a homogeneous texture corresponding to the o-HZO (111) phase, and incoherent o-HZO/m-HZO interfaces are absent. On the other hand, only large monoclinic crystallites are visible in films grown on LSAT (Figure 3.4(e). The grain boundary in Figure 3.4(f) is highly distorted, being, therefore, also incoherent.

3.5. Ferroelectric tunnel junctions grown on GSO (001) and LSAT (001) substrates

Having established the HZO microstructure dependence on the substrate, $R(V_w)$ data with increasing V_w is collected in Pt/HZO/LSMO//GSO and Pt/HZO/LSMO/LSAT barriers, and the appearance of Region I and II is investigated. $I(V)$ curves from these junctions are depicted in Appendix 7. Note that the HZO thickness is kept at 4.6 nm to compare data from FTJ grown on STO (001) substrates. Figure 3.5 includes data from Figure 3.3(a) for comparison purposes. The resistance of Pt/HZO/LSMO//GSO tunnel junctions displays two well-defined states, $R(V_w^+)$ and $R(V_w^-)$, developing at $V_w \approx 4.5$ V and remaining roughly constant up to V_{GB}. The resistance state's stability indicates that the energy barrier does depend on the polarity of the writing voltage (V_w^+ or V_w^-) and not on its magnitude, which is expected from a ferroelectric barrier with saturated polarization. The fingerprint of ionic-related *ER* that, in Pt/HZO/LSMO//STO devices happens at $V_{GB} \approx 5$ V, is shifted for much larger voltages in Pt/HZO/LSMO//GSO tunnel junctions, reaching $V_{GB} \approx 13$ V (Figure 3.5(b)). This observation supports the view that, in this sample, conducting channels formed along m-HZO/o-HZO grain boundaries are mostly suppressed. The transition to region II in this sample indicates that conductive channels can be formed within coherent grain boundaries (o-HZO/o-HZO), but an extremely large electric field (≈ 28 kV·cm^{-2}) is necessary. Consistently, $R(V_w)$ data obtained in tunnel junctions grown on $TbScO_3$ substrates (Pt/HZO/LSMO//TSO) shows only evidence of polarization-related resistive switching, and the ionic-related decay of resistance is absent up to 23 V (Appendix 8).

Moreover, Figure 3.5(c) shows the resistance dependence on the V_w for Pt/HZO/LSMO//LSAT junctions. The residual existence of orthorhombic grains in the HZO film induces a small electroresistance in Region I and 150 % electroresistance displayed in the $R(V_w)$ loop (Figure 3.5(f)) measured with $V_{max} < V_{GB}$. Indeed, Estandía et al.[53] have reported that, even though no orthorhombic grain could be identified in STEM cross-section images from HZO/LSMO//LSAT

heterostructure, there is a ferroelectric response in PUND measurements suggesting an extremely reduced presence of o-HZO. In the $R(V_w)$ data from Figure 3.5(c), the large presence of monoclinic grains reduces the *ER* amplitude in Region I and confirms that the incoherent grain boundaries are responsible for the formation of conductive channels when the electric field approaches $V_{GB} \approx 5$ V. The $I(V)$ curve from junction L_1 shows a small ferroelectric response (Appendix 7), consistent with the report from Estandía et al.

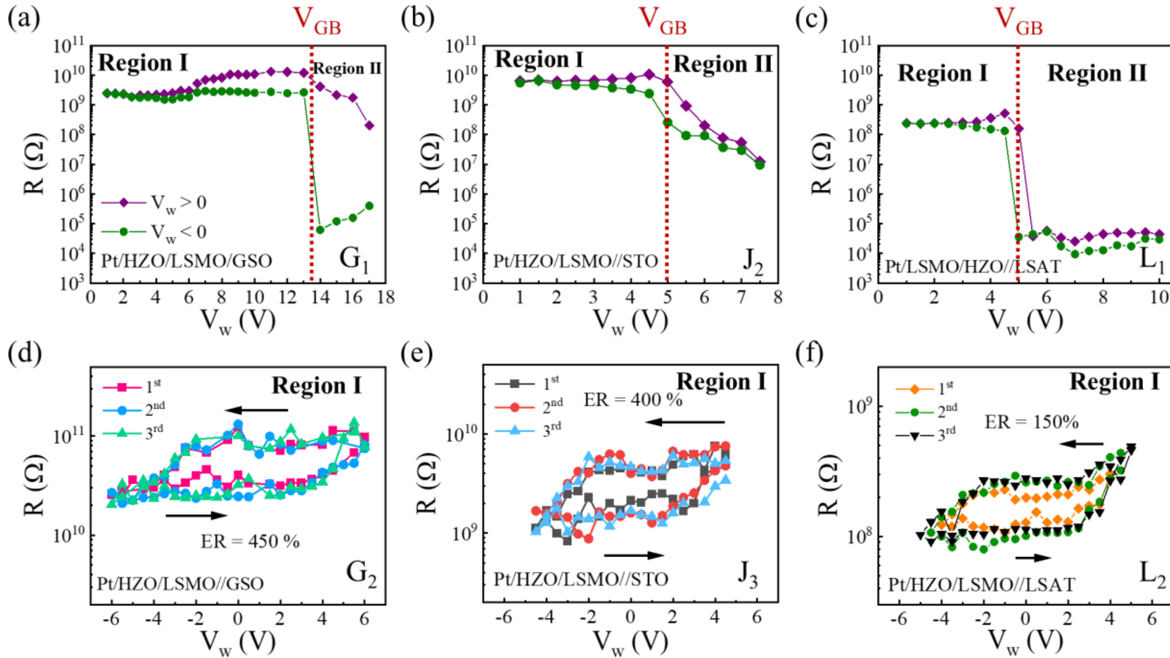

Figure 3. 5. Resistance dependence on the writing voltage V_w in Pt/HZO/LSMO junctions grown on (a) GSO, (b) STO, and (c) LSAT substrates. Data from (b) is taken from Figure 3.3(a) for comparison. (d, e, f) Electroresistance loops measured in junctions with structure indicated. The loops are fully reversible when $V_{max} < V_{GB}$. ER value in each case is indicated.

Figures 3.5(d, e, f) show three resistance loops acquired in the FTJ grown on GSO, STO, and LSAT, respectively. In the three cases, the maximum voltage is smaller than V_{GB} in order to observe *ER* only due to polarization reversal. The indicated values of *ER* demonstrate a correlation of this value and the abundance of ferroelectric orthorhombic grains.

3.6. Conclusion

The experiments and discussion above disclose the critical role of the grain boundaries formed between orthorhombic and monoclinic grains in the electroresistance of epitaxial HZO tunnel barriers. The coexistence of polarization-related and ionic-like conductive mechanisms in tunnel

barriers has been observed and disentangled. The first one gives rise to a fully reversible behavior, whereas the latter is induced for large voltages and causes an irreversible change in resistance. Moreover, it has been observed that the change in barrier height upon polarization reversal is necessary, and the modulation of the effective tunneling thickness determines the tunneling current. This conclusion indicates the pivotal role of the ferroelectric/electrode interface.

Finally, the HZO microstructure engineering through appropriate substrate selection reduces the density of incoherent grain boundaries in the system. These grain boundaries are the highway for ionic movement. Therefore, by reducing their presence, the polarization-related *ER* can be enhanced and optimized, reaching up to 450 %.

3.7. Appendix

Appendix 1.

The yellow vertical dashed lines indicate the FE switching peak position and, thus, the coercive field. Direct integration of the current response in time results into the black *P*(*V*) curve shown in Figure A3.1(b). In this curve, the coercive fields, represented by the green dashed lines, do not correspond to the position of the switching peaks in Figure A3.1(a). This effect is due to the linear contribution from electric susceptibility (χ) that is superimposed to the FE switching contribution (Eq. 2.4). Therefore, a second compensation is performed to remove this contribution by linear subtraction of a constant slope ($\chi \approx \epsilon_r = 31$). A detailed explanation of this procedure can be found in the Experimental Chapter.

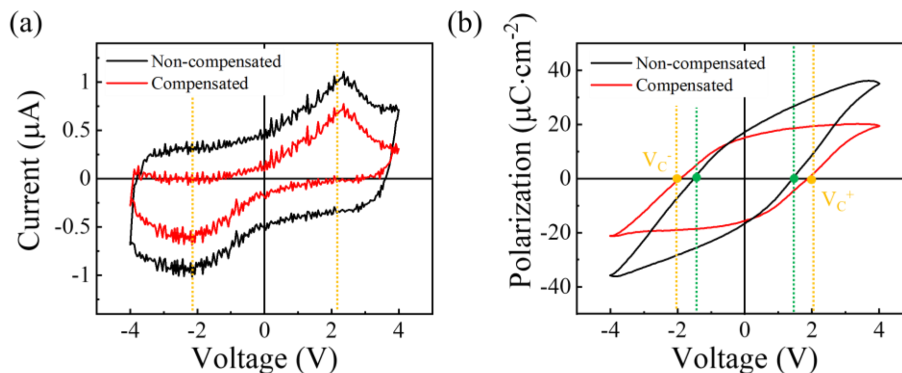

Figure A3. 1. (a) I(V) curve recorded at 1 kHz in the Pt/HZO/LSMO//STO tunnel junction from Figure 3.1(c) in the main text. The black curve corresponds to the raw measurement obtained with DLCC compensation mode. The red curve is obtained after a second compensation to subtract the electric susceptibility (χ) contribution. (b) P(V) curves are obtained by integration of the current

in time. The black curve corresponds to the DLCC raw measurement and the red curve after the subtraction of χ.

Appendix 2.

$I(V)$ curve in Pt/HZO/LSMO//STO junction is measured with DLCC at different frequencies. Spurious peaks at $V \approx V_{max}$ emerges at high frequencies.

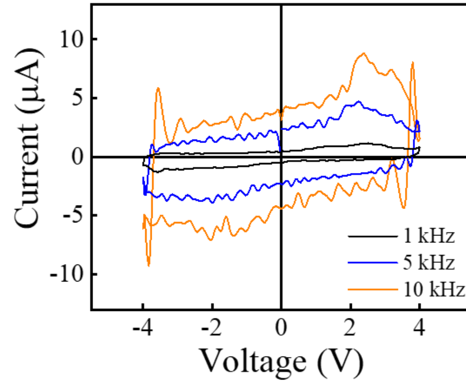

Figure A3. 2. I(V) curve recorded at 1, 5, and 10 kHz in ferroelectric tunnel junction with structure Pt/HZO/LSMO//STO. Spurious peaks emerge close to the maximum voltage at high frequency.

Appendix 3.

Figure A3.3(a) shows an $I(V)$ curve measured at 5 kHz and DLCC from the pristine J_2 junction, and after the application of $V_w = \pm 7.5$ V. Both curves show the peak related to ferroelectric switching, indicating that the junction remains ferroelectric with unchanged coercive field ($|V_c|$ ≈ 2 V). Nevertheless, a higher writing amplitude ($V_w = \pm 8$ V) leads to irreversible changes in the junction, i.e., decreased resistance and no evidence of ferroelectric switching (Figure A3.3(b)).

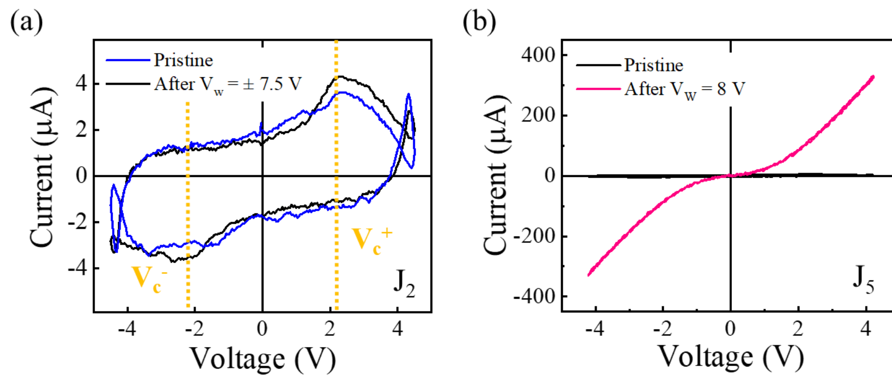

Figure A3. 3. (a) I(V) curve collected at 5 kHz and DLCC in junction J_2 at its pristine state and after the application of writing pulse, $V_w = \pm 7.5$ V. Vertical dashed lines indicate that the coercive

field does not change. (b) I(V) curves measured in junction J_5 show the irreversible change in junction after $V_w = \pm 8$ V.

Appendix 4.

The resistance dependence on the writing voltage amplitude (V_w) is found in most junctions of the Pt / HZO / LSMO // STO (001) sample. Different junctions have been measured to determine the resistance dependence on the delay time (τ_D) between the writing pulse and reading *I(V)*. For this, the writing pulse duration τ_w = 100 µs was fixed, and only the delay time was varied. Figure A3.4(a-c) shows the $R(V_w)$ data acquired in junctions J_6, J_7, J_8 for (a) τ_D = 0.2 s, (b) τ_D = 0.5 s and (c) τ_D = 1 s. The initial resistance is similar, but for τ_D = 0.2 s, the electroresistance in region II does not develop so clearly as for τ_D = 0.5 or 1 s. Nevertheless, the transition to region II at V_{GB} is ≈ 5 V.

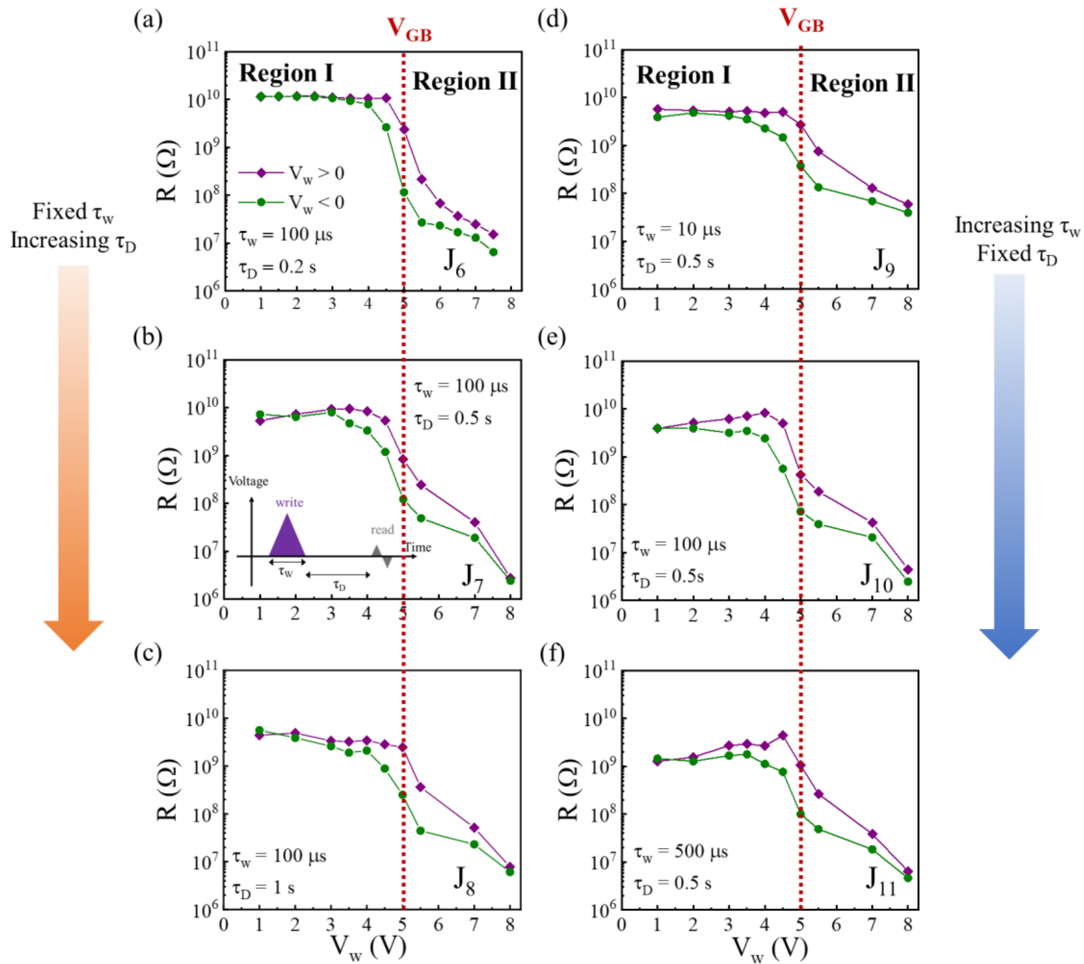

Figure A3. 4. $R(V_w)$ curves collected in junctions J_6, J_7 and J_8 in sample Pt / HZO (4.6 nm) / LSMO / STO (001) using (a) τ_D = 0.2 s, (b) τ_D = 0.5 s (c) τ_D = 1 s as delay time between writing pulse are

reading resistance but fixed writing time duration τ_w = 100 µs. Inset in (b) shows a sketch of writing and reading pulses with the corresponding duration and delay time. The transition from Region I to II is indicated by vertical dashed line V_{GB}. In junctions J_9, J_{10} and J_{11}, the τ_w was varied from (c) 10 µs, (d) 100 µs to (e) 500 µs when the delay time was fixed at τ_D = 0.5 s.

In a different experiment, the resistance of junctions J_9, J_{10}, and J_{11} is measured for different writing times (τ_w) when keeping the delay time (τ_D) fixed. Resistance recorded for (d) τ_w = 10 µs, (e) τ_w = 100 µs and (f) τ_w = 500 µs writing pulse duration for fixed τ_D = 0.5 s are shown below. Data demonstrates that, within this duration times, the transition from Region I to II is not affected and remains at $V_{GB} \approx 5$ V.

Appendix 5.

I(V) reading data collected after Figure 3.3(c) are shown below. Figure A3.5(a, b) are obtained after writing with $V_w = \pm 4.5$ V, while Figure A3.5(c) are recorded after $V_w = \pm 6$ V. The effective thickness (t_{eff}), barrier heights from both interfaces (ϕ_{LSMO} and ϕ_{Pt}) extracted from the fitting and the calculated mean barrier height ($\phi_{mean} = \frac{\phi_{Pt} + \phi_{LSMO}}{2}$) and the difference between heights ($\Delta\phi = \phi_{LSMO} - \phi_{Pt}$) is shown in Table 3.2.

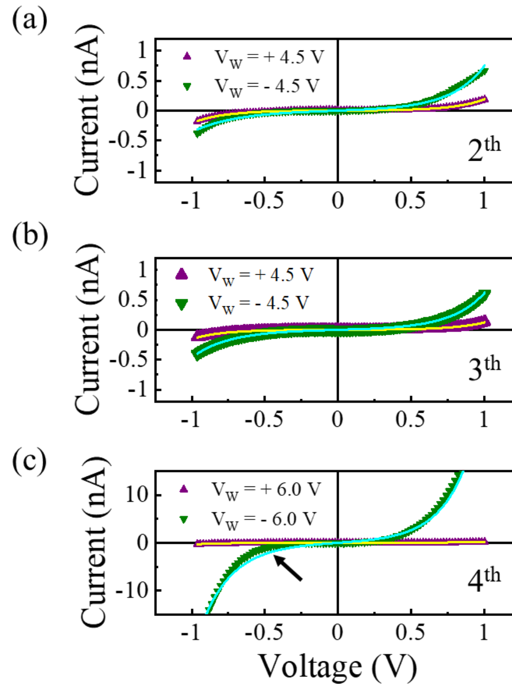

Figure A3. 5. I(V) curves recorded in the order labeled in the panels for (a, b) $V_w = \pm 4.5$ V and (c) $V_w = \pm 6$ V. Solid lines represent results from the fitting using the Brinkman model.[73]

The fittings in Figure A3.5(a, b) are in good agreement with the data. However, the fitting for data collected after $|V_w|$ = 6 V has poorer quality, particularly in the region indicated by the arrow in Figure A3.5(c), suggesting that another conduction mechanism coexists with the tunneling conduction. Note that the fittings are obtained by minimizing the χ^2 through the equation $\chi^2 = \sum(experimental\ data - fitting)^2$. The fitting model is described in the Introduction.

V_w (V)	t_{eff} (nm)	ϕ_{LSMO}(eV)	ϕ_{Pt}(eV)	ϕ_{mean} (eV)	$\Delta\phi$ (eV)
4.5	5.7	1.8	2.3	2.05	- 0.9
-4.5	5.6	2.4	1.5	1.95	+ 1.1
4.5	6.0	1.6	2.1	1.85	- 0.5
-4.5	5.4	2.4	1.7	2.05	+ 0.7
6.0	5.9	1.3	2.5	1.9	- 1.2
-6.0	5.5	1.8	1.4	1.6	+ 0.4

Table 3. 2. Parameters extracted fitting data in Figure A2 using the Brinkman model.

Appendix 6.

HAADF-STEM cross-sectional views from samples grown on STO, GSO, and LSAT substrates. The three layers composing the film, i.e., HZO, LSAT, and substrates, produce different contrasts due to the different atomic number *Z* of the elements present in each layer.

In agreement with previous reports, the orthorhombic phase's growth is favored on substrates with large lattice parameters (a_s^{GSO} = 3.97 Å), whereas the monoclinic phase is more abundant when the lattice parameter of the substrate is smaller (a_s^{LSAT} = 3.868 Å). In STO substrate (a_s^{STO} = 3.905 Å), m-HZO and o-HZO crystallites coexist. No monoclinic grain was observed in the image range from Figure A3.6(b), neither orthorhombic grains were identified in Figure A3.6(c).

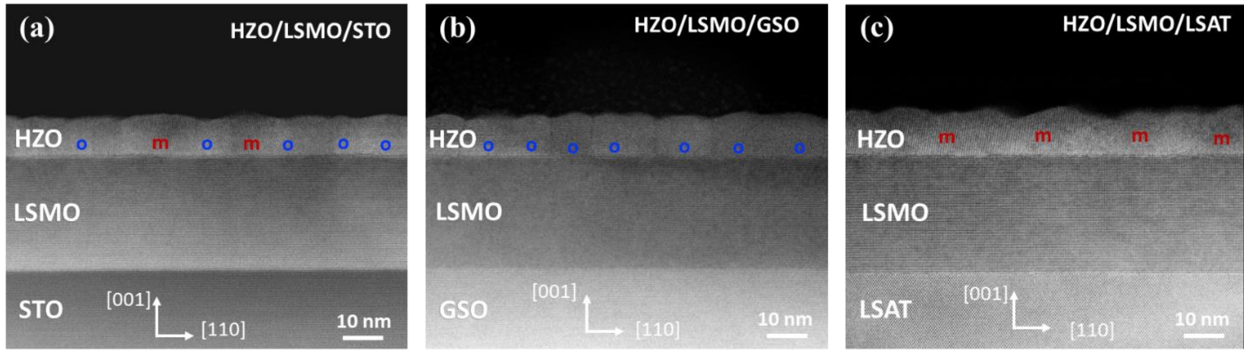

Figure A3. 6. Large field of view cross-section images of (a) HZO/LSMO//STO, (b) HZO/LSMO//GSO, and (c) HZO/LSMO/LSAT. Images were obtained along the [110] zone axes of the substrate. Scale bar of 10 nm is indicated in each image.

Appendix 7.

The *I(V)* curves are collected in Pt/HZO (4.6 nm)/LSMO//Substrate junctions, where the substrate can be STO, LSAT, or GSO. The measurement was performed at 5 kHz with DLCC compensation. Pt/HZO/LSMO//LSAT junctions are highly leaky, and the maximum voltage used was 4 V, in opposition to the V_{max} = 4.5 V used for Pt/HZO/LSMO//STO and Pt/HZO/LSMO//GSO. Figure A3.7 shows that the leakage contribution was successfully subtracted from junctions on STO and GSO. Nevertheless, in Pt/HZO/LSMO//LSAT, a spurious peak appears at $V \approx V_{max}$, indicating that the leakage was not fully compensated.

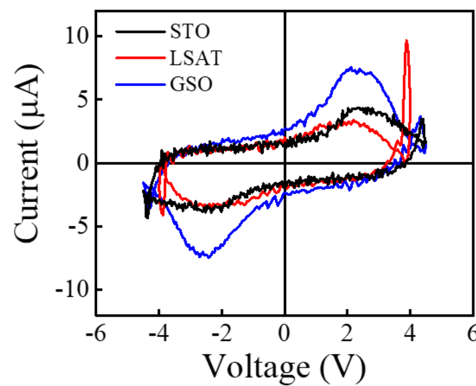

Figure A3. 7. I(V) curves measured in Pt/HZO/LSMO junctions grown in STO, LSAT, or GSO substrates. Measurement was done at 5 kHz using DLCC. The junction in LSAT has a small switching peak around 2 V.

The HZO film on LSAT substrate shows a small switching peak around $V_c^+ \approx +2$ V and $V_c^- \approx -1.8$ V. A small ferroelectric response is expected compared with junction grown on STO and GSO substrates, as the film is composed of a large majority of monoclinic grains (m-HZO). Even though

Figure 3.4(c) and A3.6(c) only show monoclinic grains, the presence of o-HZO cannot be disregarded. Estandía et al.[53] also observed a small ferroelectric response in similar junctions.

Appendix 8.

Junctions with structure Pt/HZO/LSMO//TSO also have been analyzed. The *I(V)* curve in Figure A3.8(a), measured with DLCC at 5 kHz, indicates a clear switching peak around $V_c^+ \approx V_c^- \approx 2.8$ V. $R(V_w)$ data demonstrates a resistance saturation suggesting that the barrier does not change after the ferroelectric is fully saturated. Besides, there is no transition to Region II up to 23 V and, thus, no formation of conductive channels. Considering that the TSO (a_s^{TSO} = 3.958 Å) structure is similar to GSO (a_s^{GSO} = 3.97 Å), the $R(V_w)$ and *I(V)* responses are expected to be similar.

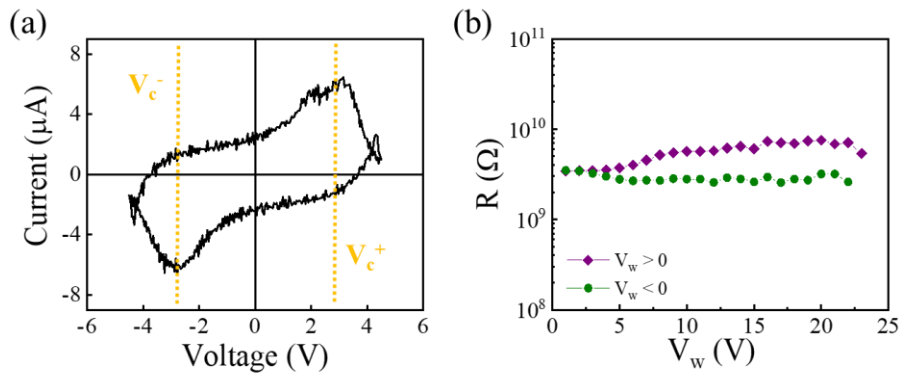

Figure A3. 8. (a) I(V) curve recorded at Pt/HZO/LSMO//TSO sample at 5 kHz with DLCC. (b) Resistance dependence for positive (purple symbols) and negative (green symbols) writing amplitude (V_w).

Chapter 4. Suppression of Conduction Channels and Enlargement of FE Switching Window

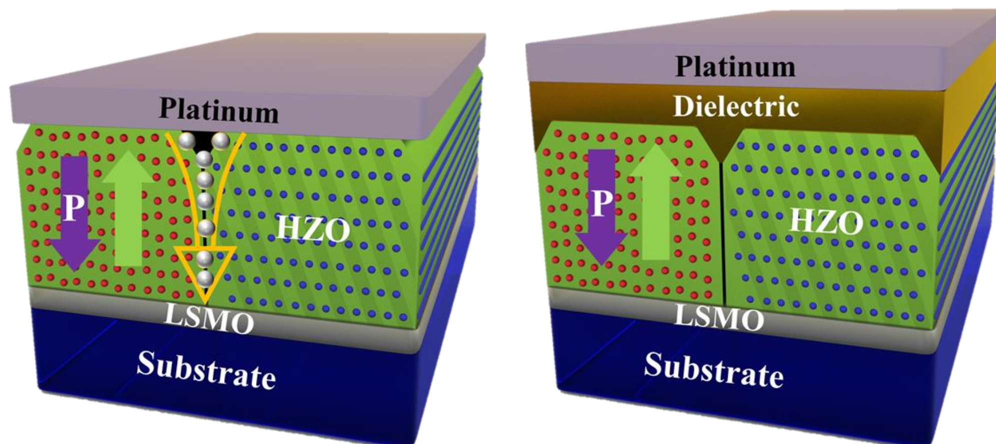

The results of this chapter have been published in "Sulzbach, M. C., Estandía, S., Gàzquez, J., Sánchez, F., Fina, I., Fontcuberta, J., Blocking of Conducting Channels Widens Window for Ferroelectric Resistive Switching in Interface-Engineered $Hf_{0.5}Zr_{0.5}O_2$ Tunnel Devices. *Adv. Funct. Mater.* 2020, 30, 2002638" from where the figure above is taken.

$Hf_{0.5}Zr_{0.5}O_2$ (HZO) films contain a network of grain boundaries. In HZO epitaxial films grown on $SrTiO_3$ (001) substrates, for instance, twinned orthorhombic (o-HZO) ferroelectric crystallites coexist with a residual paraelectric monoclinic (m-HZO) phase, and grain boundaries are formed between them. These boundaries contribute to the resistive switching in addition to the genuine ferroelectric polarization switching electroresistance (*ER*) and have detrimental effects on device performance. This chapter shows that using a suitable nanometric capping layer deposited on HZO film, a radical improvement of the tunnel device's operation window can be achieved. Crystalline $SrTiO_3$ (STO) and amorphous AlO_x are explored as capping layers. It is observed that these layers conformally coat the HZO surface, increase the yield and homogeneity of electroresistance, and strengthens the endurance. Data show that the capping layer acts as a blocking layer for ionic-like transport channels across grain boundaries. It is suggested that they can supply oxygen to the oxygen-getters grain boundaries in HZO. This scenario could be envisaged that these and other oxides could also be explored in fully compatible CMOS technology.

4.1. Introduction

The growth of ferroelectric $Hf_{0.5}Zr_{0.5}O_2$ (HZO) thin films has been stabilized by different techniques, such as atomic layer deposition, sputtering and pulsed-laser deposition. In general, the films display a coexistence of orthorhombic ferroelectric (o-HZO), monoclinic paraelectric (m-HZO) crystallites, and other phases. Recently, epitaxial HfO_2-based ferroelectric growth on single crystalline substrate has been reported on YSZ,[117,120,211,212] perovskites substrates[18,123,125,127] and Si.[126,213,214] In Chapter 3, it has been shown that ferroelectric tunnel junctions composed of HZO epitaxial thin films have two unrelated mechanisms that cause variation in resistance or electroresistance (*ER*): polarization switching and ionic-based motion. The first one occurs at low voltage, which coincides with the coercive field of the ferroelectric (V_c) and is associated with the polarization reversal, thus, involving only the motion of polarization charges (displacive currents). A second contribution arises at voltages above a certain threshold (V_{GB}), assigned to field-induced ionic motion.

Indeed, Max et al.[82] have early recognized that *I(V)* curves from ferroelectric HfO_2-based tunnel barriers can include mixed contributions from resistive switching (RS) associated with the formation/destruction of conductive filaments (CF) and to polarization reversal, challenging their understanding and control. Wei et al. [206] reported current-voltage curves, *I*(*V*), in 2 nm epitaxial

HZO barriers and argued that the electrical transport across the barrier could be described using the Brinkman model.[73] However, the barrier properties dependence on the polarization direction was not explored; thus, the connection between *ER* and *P* remained undisclosed. Ambriz-Vargas et al.[16,162] also reported *I*(*V*) measurements on 2.8 nm HZO polycrystalline barriers. Nonetheless, the voltage excursion was analyzed in a narrow voltage region, in which the curve is almost linear. The fitting of these curves with the Brinkman model prevents robust extraction of barrier parameters and possible change due to polarization reversal since it is not sensitive to curvature variation in the sigmoidal *I*(*V*). Yoong et al.[18] reported *I*(*V*) data on HZO epitaxial barriers with 10 nm HZO films after different writing pulses accompanied by polarization curves extracted from PFM measurement. In their case, transport data were analyzed using a thermionic emission over a polarization-modulated barrier as the dielectric thickness does not allow direct tunneling. The *P*(*V*) extracted from PFM is fully saturated at 4 V. In contrast, the *I*(*V*) curves measured after ± 7, ± 8, and ± 9 V vary significantly, indicating that even though the ferroelectric is saturated, the barrier properties are still being modified, which suggests that another mechanism apart from polarization dictates barrier properties.

The fact that even in epitaxially grown HZO films on single crystalline perovskite substrates contain crystallites of the paraelectric m-HZO phase in addition to the o-HZO phase increases the difficulty to assess the contribution of each effect. It is worth emphasizing the work by Estandia et al.[53] in which he has reported that HZO films grown on $LaAlO_3$ (LAO), $SrTiO_3$ (STO), and $RScO_3$ (R being rare earth) single crystalline (001)-oriented substrates, buffered by a suitable oxide metallic electrode ($La_{2/3}Sr_{1/3}MnO_3$, LSMO), display a systematic increase of the o-HZO/m-HZO ratio from LAO to $RScO_3$. Besides, the ferroelectric o-HZO phase is found to be (111) oriented on the cubic (001) surface of the substrates and, thus, o-HZO is intrinsically twinned.[53] Therefore, grain boundaries between twinned o-HZO crystallites (denoted GB-I, coherent), as well as grain boundaries between o-/m-HZO and m-/m-HZO grains (denoted GB-II, incoherent), should exist in the film (Figure 4.1(a)) and must be considered to determine the origin of *ER*. As detailed in the previous chapter, these GBs' presence dramatically affects the RS since GB are highways for ionic motion (Figure 4.1(b)). It was observed that the ionic contribution was prevalent in films containing mixed GB-I and GB-II grain boundaries, whereas the genuine polarization-related *ER* prevails in films containing majority GB-I. The relative amount of the grain boundary type can be controlled and engineered by the appropriate choice of substrate.[53]

In order to confirm the role of grain boundaries in ionic-related RS, a simple approach to block the charge leakage along with GB in HZO tunnel barriers is proposed. In this regard, a suitable nanometric oxide layer is deposited on an HZO surface conformally capping the GB within the film, and the consequences on their *ER* are investigated. As the presence of the oxide layer causes an extra voltage drop across the device, it is expected V_{GB} to be shifted to higher voltages or be eventually suppressed, as in Figure 4.1(c, d), contributing to enhancing the robustness of the ferroelectric related *ER*.

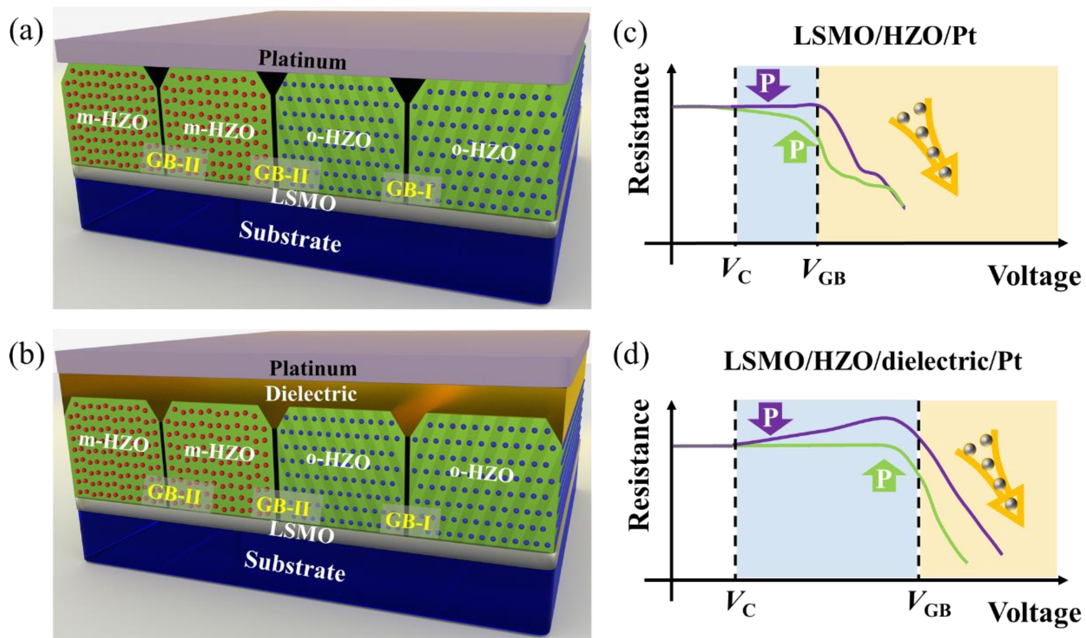

Figure 4. 1. Sketch of epitaxial ferroelectric HZO films grown on $SrTiO_3$//LSMO substrate containing o- and m-HZO crystallites, few nanometers in size and grain boundaries (GB-I and GB-II) within. (a) HZO film is covered by a metallic Pt electrode. (b) A dielectric layer is inserted between the HZO film and the metallic Pt electrode. (c) Sketch of the dependence of the resistance of ferroelectric HZO barrier on the writing voltage using the Pt electrode on the HZO surface as in (a). The purple curve represents R values when a positive bias is applied at the Pt electrode (P pointing towards LSMO), and the green curve corresponds to a negative bias being applied to Pt (P pointing towards platinum). (d) Corresponding $R(V_w)$ sketch for heterostructure in (b). The voltages V_c and V_{GB} are the coercive field of the ferroelectric and the opening of the conducting channel within the grain boundaries of the HZO film, respectively. Up-down arrows indicate the polarization direction, and dot-filled arrows the ionic motion.

In this chapter, the voltage-dependent *ER* in capped thin HZO (4.6 nm) films with amorphous AlO_x and crystalline $SrTiO_3$ dielectric layers of different thicknesses (1 – 2 nm range) is investigated. The films were grown on $SrTiO_3$ and $GdScO_3$ (GSO) substrates, controlling GB-I and GB-II's relative abundance in the film.

4.2. Samples

Epitaxial HZO films with 4.6 nm nominal thickness were grown on STO (001) and GSO (001)-oriented ($GdScO_3$ is indexed using pseudo-cubic setting) single crystalline substrates (5 x 5 mm^2) buffered with $La_{2/3}Sr_{1/3}MnO_3$ (22 nm thick) conducting electrodes by pulsed laser deposition (PLD). Further details on the deposition can be found in the Experimental Methods chapter and elsewhere.[53,127] Note that single-crystalline STO and GSO used as substrates have bulk cell parameters (pseudo-cubic) of 3.905 and 3.97 Å, respectively.

Subsequently, either STO or AlO_x capping layers were deposited in situ above the HZO film. The deposition of polycrystalline $SrTiO_3$ was performed at P_{O2} = 0.02 mbar, T = 700 ºC and cooling to room temperature under P_{O2} = 0.2 mbar. The amorphous AlO_x layer was obtained by ablation of an Al_2O_3 target at room temperature and P(Ar) = 0.1 mbar. The thickness of the STO and AlO_x capping layers was chosen to be t = 0, 1, and 2 nm by controlling the number of laser pulses based on calibrated growth rates previously determined. Thicker capping layers create a thick capacitor, dramatically reducing the tunneling current.[74] Also, other conduction mechanisms, like thermionic injection, become more relevant than direct tunneling.[18,74] Note that the dielectric films used here, STO and AlO_x, have the main purpose of sealing the grain boundaries present in the HZO film.

Circular Pt top electrodes of 20 µm of diameter were grown through a shadow mask by sputtering. The reference sample in which no dielectric was deposited between the ferroelectric and platinum is labeled as HZO. For the sake of simplicity, the samples with 1 or 2 nm STO capping are named HZO/STO1 and HZO/STO2, respectively. In the case of 1 and 2 nm AlO_x capping, the samples are denominated HZO/AlO1 and HZO/AlO2, respectively. In section 4.4, the samples grown on GSO substrate are labeled with GSO// in front.

4.3. Capping junctions grown on STO (001) substrates

The redistribution of oxygen vacancies in HZO films has been associated with phase transition and wake-up effect.[130,136] Besides, it was shown that the migration of oxygen from a polycrystalline HZO film to the interface with the top electrode leads to a less effective screening and unstable polarization.[215] In the case of this work, STO and AlO_x capping layers could provide oxygen to the HZO film or even introduce oxygen vacancies into the system that could destabilize the orthorhombic ferroelectric phase formation. Therefore, after the deposition of the capping

layers, the junction heterostructures are investigated to ensure the phase composition, i.e., m-/o-HZO relative abundance is not affected by the dielectric. In this section, the X-ray diffraction (XRD) technique is used to investigate the phase composition of uncapped and capped HZO junctions grown on STO (001) substrates. Also, these devices' electrical characterization is explored, and the capping layer's role is established.

4.3.1. X-ray Diffraction

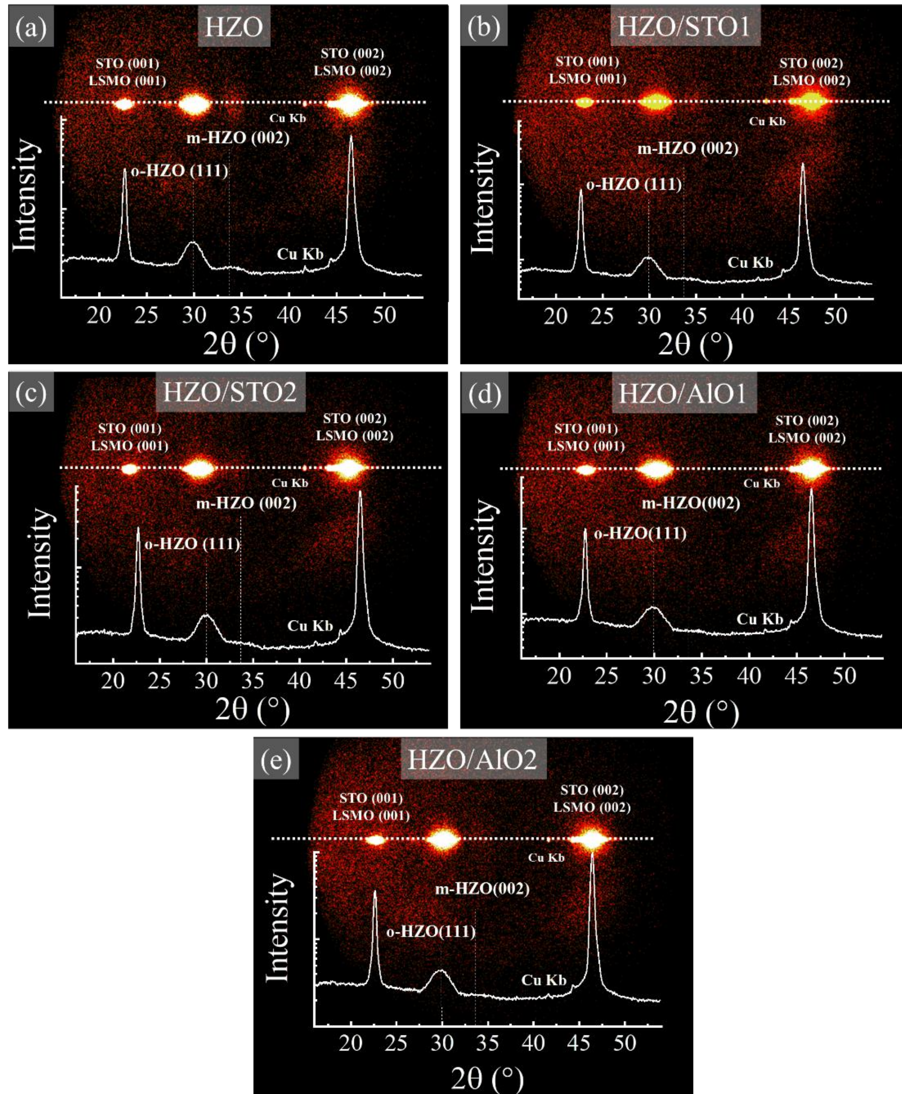

Figure 4. 2. X-ray diffraction 2θ-χ frames and corresponding θ-2θ integrated within χ = ± 10º angular range for (a) HZO, (b) HZO/STO1, (c) HZO/STO2 films, (d) HZO/AlO1 and (e) HZO/AlO2.

Figure 4.2 shows the X-ray diffraction 2θ-χ frame and the corresponding integrated θ-2θ scan (around χ = ± 10º) of the HZO samples grown on STO substrates. Figure 4.2(a) displays data for

the junction HZO without any capping, whereas Figure 4.2(b, c, d, e) exhibits data for HZO/STO1, HZO/STO2, HZO/AlO1, and HZO/AlO2, respectively. The intense (00*l*) reflections of the substrate and LSMO bottom electrodes can be observed in all θ-2θ scans, together with a strong (111) reflection from the ferroelectric o-HZO (2θ ≈ 29º). A small and broad peak at m-HZO (002) position (2θ ≈ 34º), indicating that o-HZO is prevalent in the film. The spurious peak around 42º marked with * corresponds to the Cu-K_β signal that was not filtered to achieve best signal-to-noise ratio. Pole figures indicate the existence of four variants of the [111] textured HZO crystallites.[53] The 2θ-χ frames collected in the samples in Figure 4.2 are virtually identical, which allows concluding the deposition of crystalline STO and amorphous AlO_x does not compromise the crystallinity of the HZO.

4.3.2 Electrical characterization

At this point, having established the crystallinity of HZO films is not affected by the deposition of STO or AlO_x capping layers, the ferroelectric properties of these films can be explored. Illustrative *I*(*V*) curves recorded at 5 kHz using Positive-Up-Negative-Down (PUND) technique on HZO, HZO/STO1, and HZO/AlO1 devices are shown in Figure 4.3(a). The inset shows the electrical arrangement on the heterostructure. Figure 4.3(b) displays the *P*(*V*) loops obtained by integrating the current response in time and assessing the films' ferroelectric nature. The coercive voltage extracted from the switching peaks position in the HZO sample is $V_c^+ \approx V_c^- \approx 3$ V. Data indicates a remnant polarization of $P_R \approx 14$ μC·cm^{-2} and is consistent with previous reports[127,216] and the results from chapter 3. A minor modification in the shape of the *I*(*V*) curve for sample HZO/STO1 is observed in comparison with the uncapped sample, however, not affecting the coercive fields. In opposition, HZO/AlO1 sample has a significant reduction of the switching peak amplitude, resulting in smaller P_R (≈ 8 μC·cm^{-2}) and a shift of the coercive fields to slightly larger V_C.

Figure 4.3(c) shows the *I*(*V*) curves collected in HZO/STO2 and HZO/AlO2 junctions using the same conditions that Figure 4.3(a). The *I*(*V*) from the bare HZO sample is included for comparison. By increasing the dielectric layer's thickness, being STO or AlO_x, the switching peak reduces amplitude in agreement with the reduction observed for HZO/AlO1. The *P*(*V*) curves in Figure 4.3(d) depict the increase in the coercive fields, clearer for the 2 nm AlO_x capping layer. These results are expected[210] due to the better insulating properties and lower permittivity of AlO_x ($\epsilon_r \approx 10$)[217] compared with STO ($\epsilon_r \approx 250$).[218,219] Also, it is expected that the *ER* response in these

films will be reduced considering the reduction in the remnant polarization observed for the 2 nm capped junctions.

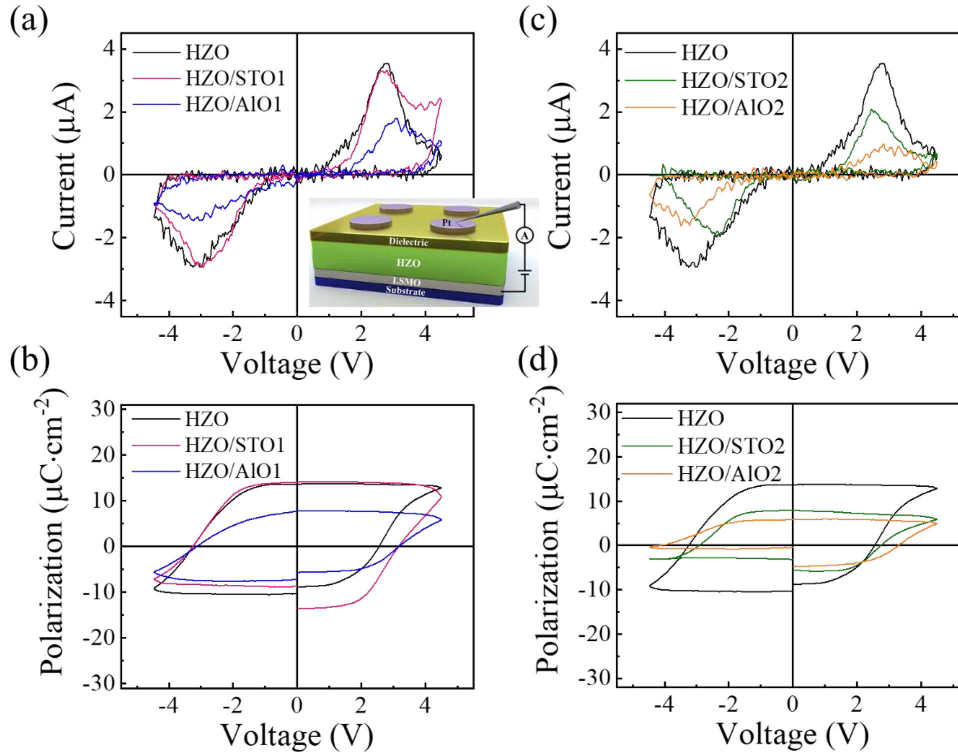

Figure 4. 3. (a) Current-voltage curves with V_{max} = 4.5 V and (b) corresponding P(V) loops of junctions in sample HZO, HZO/STO1, HZO/AlO1 recorded at 5 kHz with PUND. Inset shows measurement configuration on the heterostructure. (c) I(V) curves and (b) corresponding P(V) were measured under the same conditions in samples HZO/STO2 and HZO/AlO2. HZO curves are included for comparison purposes.

4.3.3. Electroresistance

At this point, one can determine the *ER* response of HZO capped and uncapped tunnel junctions. The *ER* measurement consists of applying a writing trapezoid pulse with amplitude V_w and duration τ_w = 300 μs on the top electrode from the structure shown in the inset of Figure 4.2(a). In order to avoid ferroelectric switching during the reading step, the reading *I*(*V*) curve is collected after a delay time τ_D = 0.5 s and by applying a linear $V_R(t)$ in a small voltage range, which is from – 1 V to + 1 V. The resistance is calculated at V_R = 0.9 V. Further details on the measurement procedure can be found in the Experimental Methods chapter.

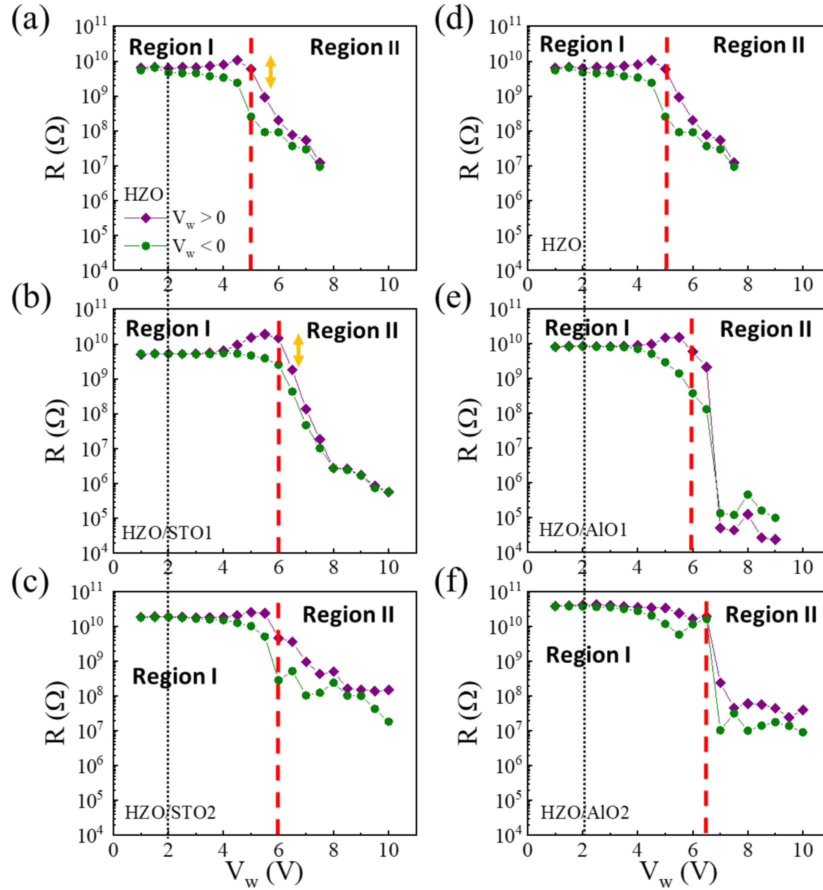

Figure 4. 4. R(V_w) data of junctions in (a, d) HZO, (b) HZO/STO1, (c) HZO/STO2 samples after positive ($V_w > 0$, purple symbols) and negative ($V_w < 0$, green symbols) writing pulse. Equivalent data for (e) HZO/AlO1 and (f) HZO/AlO2 devices.

Figure 4.4(a) exhibits the resistance (*R*) dependence on the writing voltage amplitude (V_w) of a junction in the HZO sample. These data were presented in chapter 3, in which it was discussed the appearance of two well-defined regions, labeled I and II, that are associated with the electroresistance rising from different mechanisms. Region I has *ER* mainly dictated by polarization reversal that changes the barrier height and effective thickness of the HZO tunnel barrier and, thus, the tunneling transport. Indeed, above a certain voltage threshold (around 2 V), the writing voltage dictates an increase or reduction (for $V_w > 0$ and $V_w < 0$, respectively) of the junction's resistance, as typically observed in ferroelectric tunnel junctions.[39,157] However, the transition to region II at $V_{GB} \approx 5$ V marks a conducting channel opening that results in resistance decay for both writing voltage polarities and *ER* decrease. In Chapter 3, it was discussed that V_{GB} is a fingerprint of the onset of non-polarization-related conducting paths along grain boundaries.[168,216]

A major finding is presented in Figure 4.5(b, c), where the $R(V_w)$ data collected in junctions containing STO capping layer are depicted. The red vertical lines indicate the clear shifted transition to Region II due to the capping layer's presence. The V_{GB} for samples HZO/STO1 and HZO/STO2 is about 6 V, which is 20 % larger than V_{GB} (HZO) ≈ 5 V. The wider region I in STO-capped HZO layers implies the resistance contrast ($\Delta R = R(V_w^+) - R(R_w^-)$) in Region I increases for larger V_w until the ferroelectric reaches total saturated polarization without the opening of conducting channels by ionic-motion. The electroresistance at the maximum V_w (< V_{GB}) for HZO/STO1 in Figure 4.4(b) is marginally larger (390 %) than from the 340 % observed in the HZO sample (Figure 4.4(a)), indicated by the yellow arrows. This effect is expected, and it was explored in different composite barrier structures taking advantage of the increase in the barrier's asymmetry.[210,220,221] On the other hand, in the case of HZO/STO2 (Figure 4.4(c)), the resistance increases with the capping layer (series resistance) irrespective of the polarity. This effect limits the observable *ER* since the effects of polarization reversal on the barrier properties are overlapped with the dramatic decrease of the tunneling current across the composite barrier. Similar dependence on the *ER* amplitude with V_w was obtained in most HZO/STO1, and HZO/STO2 measured junctions are exhibited in Appendix 1. An identical set of measurements has been performed in the samples capped with AlO_x layers. Illustrative data from junctions in HZO/AlO1 and HZO/AlO2 samples are shown in Figure 4.4(e, f), and the V_{GB} increase and, consequently, the expansion of Region I is observed. The best improvement in capped devices is for HZO/AlO1, in which the electroresistance reaches ≈ 700 %. The results from Figure 4.4 strongly suggest that, upon capping the HZO film with either STO or AlO_x dielectric layers, larger voltages must be applied to induce the opening of conductive channels along the grain boundaries within the HZO film.

The microstructure of HZO epitaxial films shows that GBs can be coherent or incoherent, as discussed in the previous chapter, depending on the film's crystallites. The ferroelectric o-HZO phase (111) textures on cubic (001) substrates display threefold twin planes, which give rise to a network of coherent GBs (GB-I). Nevertheless, the residual presence of the m-HZO phase in films on STO (001) substrate implies the existence of incoherent GBs between m-HZO and o-HZO (GB-II). Ultimately, Figure 4.4 indicates that the capping layers had a major effect on the GB-II by retarding the formation of conducting channels across the film. Nevertheless, when high external voltages are applied to the capacitor, the suppression of ionic motion is no longer effective, and

the transition from Region I to II happens. This evidence suggests that the conductive filaments can be formed in the residual incoherent grain boundaries when a high electric field is applied even though the dielectric is capping the HZO film. The granular character of STO and AlO_x capping layers can be the reason and are exhibited in Appendix 2.

4.4. Capping junctions grown on GSO (001) substrates

It should be expected that capping layers have a smaller effect in HZO films where most grains are o-HZO and, thus, GB-I are more abundant. As mentioned, it has been demonstrated[53] that epitaxial HZO films on scandate substrates ($GdScO_3$ or $TbScO_3$, for example) yield most o-HZO ferroelectric grains and their associated grain boundaries are GB-I, pushing towards larger V_{GB} to transition to Region II.[216] Therefore, to validate the hypothesis that the capping layer blocks mainly change transport along incoherent grain boundaries, one could investigate the effect of capping in junctions grown on scandate substrates. For this purpose, HZO (4.6 nm) films were grown on GSO (001) (using pseudo cubic setting) substrate buffered with LSMO conducting electrode, as described in section 4.2. Accordingly, a 2 nm thick STO capping layer was deposited to form a GSO//HZO/STO2 junction.

Figure 4.5(a) shows the $I(V)$ curve measured at 5 kHz using PUND on a sample without capping (GSO//HZO) and on GSO//HZO/STO2. As observed in Figure 4.3(c), the STO capping reduces the switchable polarization. The inset shows the $P(V)$ curves obtained by integrating the $I(V)$ in time and displays a decrease in the remnant polarization from 16 $\mu C \cdot cm^{-2}$ in GSO//HZO to ≈ 8 $\mu C \cdot cm^{-2}$ in GSO//HSO/STO2. As a matter of comparison, the $I(V)$ and corresponding $P(V)$ curves from the HZO and HZO/STO2 grown on STO substrates are included in Figure 4.5(b). Note that, as HZO films grown on scandate substrates have a larger amount of o-HZO than when grown on STO, it is expected that the remnant polarization at GSO//HZO is larger than at the HZO sample. Besides, the coercive fields from GSO//HZO and GSO//HZO/STO2 junctions coincide for positive voltages ($V_c^+ \approx + 3$ V), whereas for negative voltages, there is a marginal shift for lower voltages in the GSO//HSO/STO2 sample ($V_c^- \approx - 2.7$ V). These values agree with the coercive fields from films grown on STO (Figure 4.5(b)).

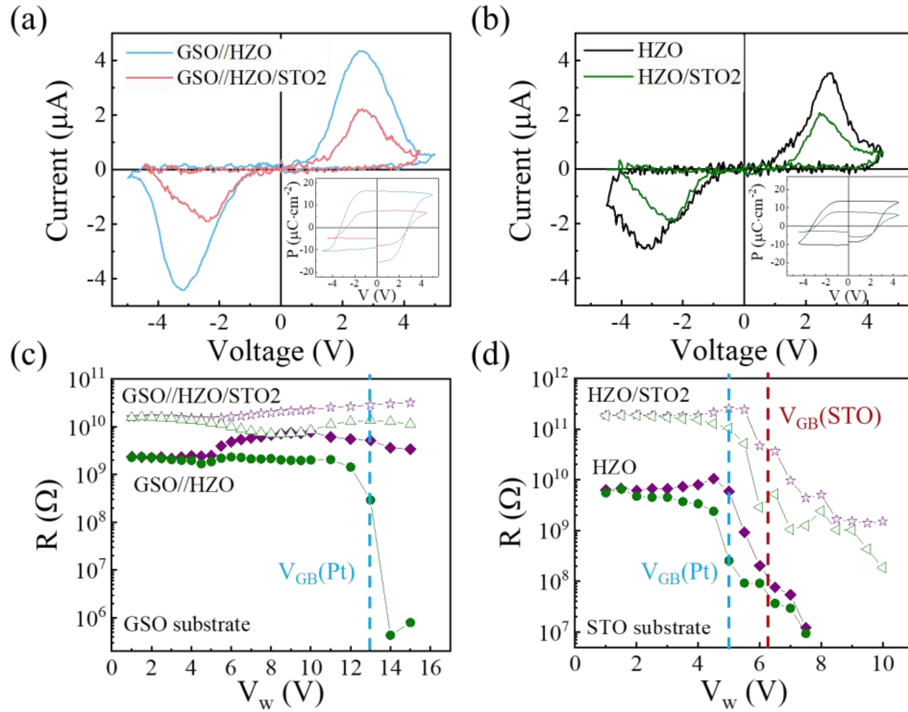

Figure 4. 5. I(V) curves collected at 5 kHz with PUND on (a) GSO//HZO and GSO//HZO/STO2 and (b) HZO and HZO/STO2 samples grown on STO substrate. Insets show corresponding P(V) loops. The resistance $R(V_w)$ recorded on indicated junctions grown on (c) GSO and (d) STO substrate. Data from (c) and (d) are adapted from Figures 4.3 and 4.4. For clarity, HZO/STO2 resistance data have been multiplied by 10. Vertical dashed lines in (c, d) indicate V_{GB}.

Figure 4.5(c) shows the $R(V_w)$ of representative junctions on both samples measured using the same protocol as in Figure 4.4. It is observed that in sample GSO//HZO, V_{GB} occurs at a large voltage ($V_{GB} \approx 12 - 13$ V), sharply contrasting with $V_{GB} \approx 5$ V observed in HZO grown on STO substrate (Figure 4.5(d), filled symbols). This remarkable shift is the fingerprint of the near absence of voltage-induced conducting channels across GB-I in the GSO//HZO sample. The $V_{GB} \approx 12$ V demonstrates that extremely high voltages are necessary to induce channels to form within coherent grain boundaries. Therefore, one can compare this data with the $R(V_w)$ obtained from the GSO//HZO/STO2 sample shown in Figure 4.5(b). Note that the junction's resistance increases one order of magnitude with the dielectric layer. In this case, the electroresistance remains stable in an expanded voltage range up to $V_w = 15$ V, which was the largest explored writing voltage amplitude. This result indicates that up to 15 V, no conductive filaments were formed in GSO//HZO/STO2 samples, and the ER has no contribution from ionic driven RS. The combination of this result and the $R(V_w)$ data collected in the HZO/STO2 sample (Figure 4.5(d), open symbols) implies that the capping successfully cancels any residual contributions of ionic conduction that may exist across

GB-I. Also, this observation provides a hint that ionic conductance across GB-I is more limited than across GB-II.

4.5. Endurance

Considering that capping layers can suppress the opening of conductive channels within grain boundaries, it is expected that its presence also impacts stability and endurance. Therefore, the *ER* response in junctions with and without the dielectric is investigated in this section. Figure 4.6(a, b, c) shows the resistance collected in HZO, HZO/STO1, and HZO/AlO1 samples after a writing step of V_w = + 5 V (purple columns) and V_w = - 5 V (green columns). OFF and ON resistance states on HZO junctions have mean values of 3.4×10^9 and 3.3×10^8 Ω with a standard deviation of 2.6×10^9 and 3.8×10^8 Ω, respectively. Clearly, data in Figure 4.6(b, c) show less spread of values when comparing with Figure 4.6(a). In HZO/STO1, the OFF and ON resistance mean values are 1.5×10^{10} and 5.2×10^9 Ω with a standard deviation of 1.4×10^{10} and 1.5×10^9 Ω, respectively. In HZO/AlO1, the mean value is 8×10^9 and 1.3×10^9 Ω with standard deviation 3.3×10^9 and 8.3×10^8 Ω for OFF and ON, respectively. The spread of *ER* amplitude ($\sigma(ER)$) is reduced by about a factor of 7 when comparing data from bare HZO, where $\sigma(ER) \approx 1400$ %, and HZO/STO1, where $\sigma(ER) \approx 113$ %. The relative change of $\sigma(ER)$ (%) = $\sigma(ER)$/mean(ER) is also improved, although being roughly only by a factor of 3: 56 % for HZO/STO1 and 114 % for HZO. This fact originates from the increase of overall resistance for capped junctions, i.e., the denominator in $ER = \frac{R_{OFF}-R_{ON}}{R_{ON}}$ Increases as well as the numerator, decreasing the *ER*.

Besides, the capping has proven to increase the endurance of the *ER* response. To address this issue, repeated $R(V_w)$ loops had been performed on a given junction, either on bare or on capped HZO films, as displayed in Figure 4.6(d, e, f). It can be appreciated that the three consecutive loops collected in the HZO sample are reversible but exhibit fluctuation in the values of resistance. In contrast, the loops for HZO/STO1 do not have similar variations and are reproducible. In the case of HZO/AlO1, the consecutive loops have a slight vertical shift. However, the electroresistance value remains constant, and the reversibility is evident.

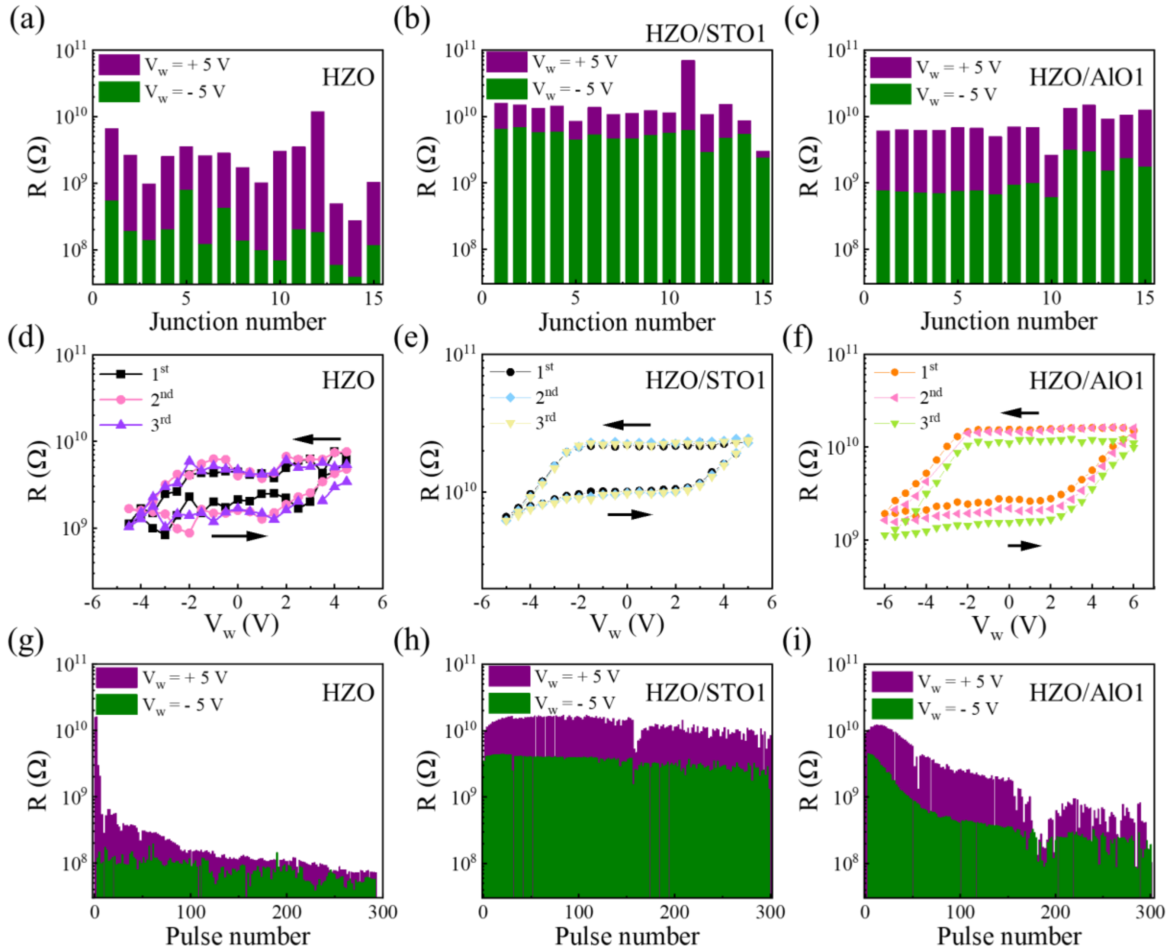

Figure 4. 6. Resistance values recorded after writing with V_w = ± 5 V on a set of 15 junctions on (a) HZO, (b) HZO/STO1, and (c) HZO/AlO1 sample. Reproducibility of R(V_w) loops collected consecutively on (d) uncapped and (e, f) capped samples as indicated. (g, h, i) Endurance of resistive states on indicated junctions for 300 pulses of V_w = ± 5 V and τ_w = 300 μs. After each writing pulse, the resistance was measured at V_R = 0.9 V.

The most remarkable feature of junctions with capping is depicted in Figure 4.6(g, h, i). Alternating trapezoidal positive and negative pulses (V_w = ± 5 V and τ_w = 300 μs) are applied to a junction, and its resistance is measured after each pulse. The endurance of ON and OFF states is probed by following the resistance evolution with the pulse number. In Figure 4.6(g), the OFF state dramatically decreases after only ten writing pulses, reducing the electroresistance and demonstrating poor stability. On the other hand, the same measurement performed in HZO/STO1 sample shows a very different outcome. In the first 30 pulses, the OFF state gradually increases resistance, suggesting a wake-up-like process might take place until R is stabilized. Then, both states remain stable up to 160 pulses. After a decrease at ≈ 160 pulses, R recovers, maintaining

slightly lower average values but the fluctuation increases. Despite that, both states preserve the *ER* amplitude even after 300 pulses. In the case of HZO/AlO1, a peculiar endurance is observed. In the very first 15 pulses, the OFF state gradually increases, similarly to HZO/STO1. Nevertheless, its value, as well as the ON state, continuously decreases (around one order magnitude) up to 150 pulses. Then, a significant dispersion appears, and the states become unstable. These data suggest that the HZO/STO1 junction's robust ER response largely contrasts with the poorer performance on the bare HZO junction.

4.6. Scanning Tunneling Electron Microscopy

In order to get further details on the role of the capping layer on the performance of composite tunnel junctions, their microstructure is studied employing scanning tunneling electron microscopy (STEM) in combination with electron energy loss spectroscopy (EELS). The STEM specimens were prepared using an FEI Helios nanolab 650 by the technical service at Universidad de Málaga. These samples were characterized by Dr. Jaume Gàzquez and Saul Estandía using a JEOL JEM ARM200cF operated at 200 kV equipped with a CEOS aberration corrector (for atomic resolution) and GIF Quantum *ER* spectrometer at the Universidad Complutense de Madrid (Spain). The images were acquired in High Angle Annular Dark Field (HAADF) image mode, also referred to as *Z*-contrast, since each atomic column's brightness roughly scales with the square of the atomic number *Z*.[199] Further details on the experimental protocol for STEM and EELS measurements are described in the Experimental Methods chapter.

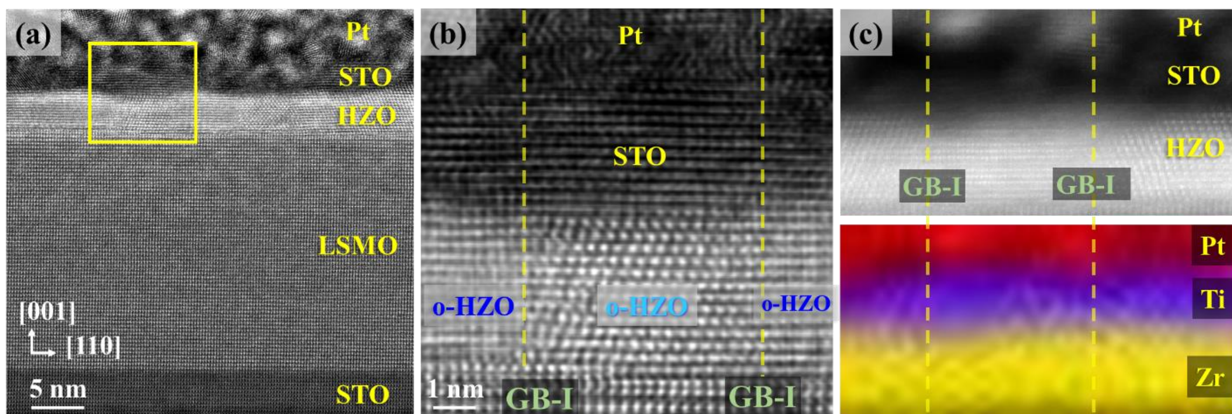

Figure 4. 7. Z-contrast cross-section image from HZO/STO2 heterostructure viewed along the [110] STO substrate zone axis. The layers corresponding to STO substrate, LSMO, HZO, STO capping, and Pt layer can be distinguished. (b) Zoom of region market in yellow in (a) where two GB-I are visible as well as the STO covering of the HZO film. (c) The top panel shows the HAADF

image acquired simultaneously with the electron EEL spectra. The bottom panel shows an elemental map that was obtained by signal acquisition from Pt-M (red), Ti-L (blue), and Zr-L_3 (yellow) edges. Vertical dashed lines indicate the position of GB-I.

Figure 4.7(a) exhibits a HAADF image of the structure from the sample HZO/STO2. The layered structure can be identified along with the excellent nature of the bottom electrode, the HZO crystalline nature, and the conformal coating of the polycrystalline STO layer and Pt top electrode. In the field-of-view of Figure 4.7(b), o-HZO crystallites (111) textures can be identified. As mentioned, the growth of (111)-HZO textured on (001) cubic substrates implies the existence of twined HZO crystals.[53] The grains appearing on the left and the right of the image (dark blue) are orthorhombic and have [111] (pointing upwards) and [0-11] (pointing rightwards) directions containing in the observation plane. The grain in the middle (light blue) is also orthorhombic, but it is rotated with respect to the others that contain [111] (upwards) and [-211] (rightwards) directions in the observation plane. The different orientation of these o-HZO grains produces grain boundaries type GB-I. The EELS elemental maps were obtained from Pt-M (red), Ti-L (blue), and Zr-L_3 (yellow) edges and show conformal coating of Ti and, thus, STO on HZO. For disclosure, an extended cross-section image is depicted in Figure 4.8. The top panel's HAADF image was acquired simultaneously with the EEL image (bottom panel) to demonstrate the sealing of HZO grain boundaries in a wide-ranging field-of-view.

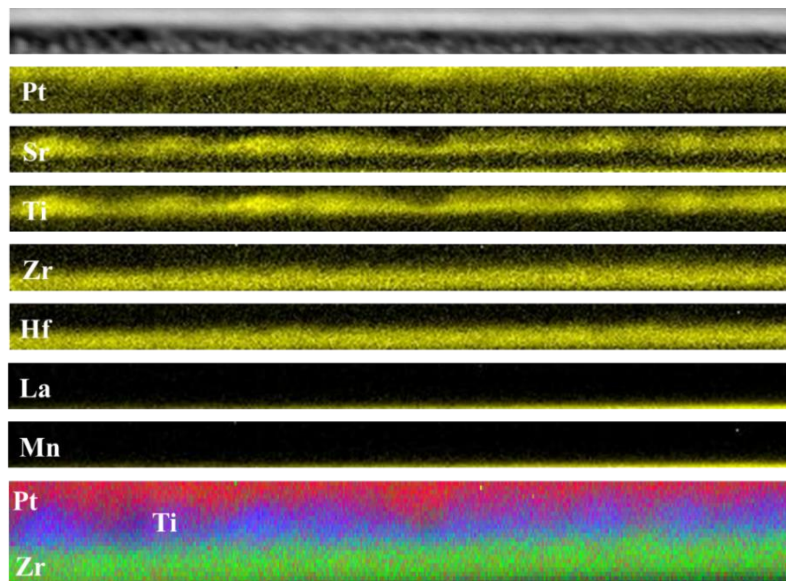

Figure 4. 8. The top panel shows a HAADF image collected simultaneously with EEL spectra images from a large area in the sample HZO/STO2. In the lower panels, the corresponding EELS elemental maps are generated from the Pt-M, Sr-L_3, Ti-L, Zr-L_3, Hf-M, La-L, and Mn-L edges.

Even though no grain boundaries can be seen in this large image, Ti's continuous covering, thus, STO, on HZO, can be confirmed. The lowest panel, Pt, Ti, and Zr signals are represented by red, blue, and green, respectively.

Note that the continuous coverage of the HZO film is also observed in the HZO/STO1 sample. Figure 4.9(a, b) shows HAADF cross-section images acquired in this sample, where the two types of grain boundaries, GB-I and GB-II, are identified.

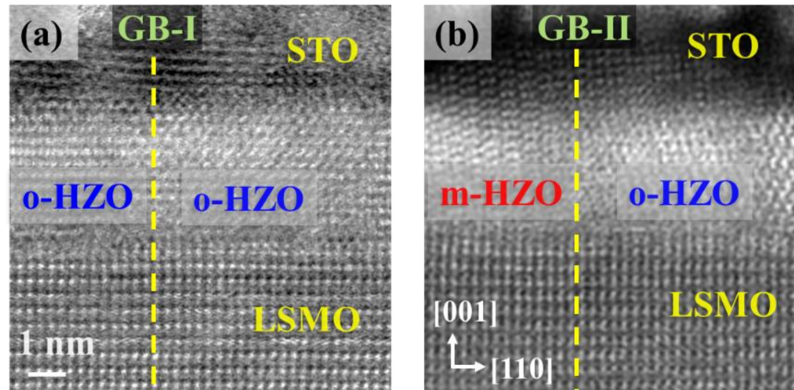

Figure 4. 9. Cross-section Z-contrast image of HZO/STO1 heterostructure viewed along the [110] STO substrate zone axis. The grain boundaries (a) GB-I and (b) GB-II are indicated.

To get an insight into the possible chemical role of the capping barrier on HZO capping junctions, the fine structure of both O-K and Ti-L edges is analyzed. The profiles in the HZO and STO in different regions of the films are compared. Figure 4.10(a) shows a HAADF image in the HZO/STO2 sample indicating the arrows at the right side where EELS spectra were collected. In Figure 4.10(b), the O-K peak obtained on the HZO close to the STO capping and right above the LSMO layer does not allow to discern any change in the electronic structure, suggesting the HZO film remains unchanged either close or far from the STO capping. In contrast, the Ti-L edge spectra in Figure 4.10(c) were collected from the STO on the substrate or in the capping layer. The capping layer's signal shows a remarkable shift of the Ti-L edge, indicating a reduction of the valence state of Ti^{m+}. More precisely, the observed energy shift corresponds to a nominal Ti^{3+} state, differing from the expected Ti^{4+} as observed in the signal from the substrate. This observation suggests that the oxygen from the capping layer may have migrated to the grain boundaries in the HZO, acting as an oxygen reservoir.

Oxygen motion that induces reduction/oxidation of HZO/metal interfaces has been explored in previous studies.[222,223] For example, Hamouda et al.[215] reported that TiN top electrodes in

polycrystalline TiN/HZO/TiN heterostructures could extract oxygen from the HZO, creating an oxidized interfacial layer. Interface sensitive techniques have been used to characterize the thin TiO_xN_y interlayer formed between the TiN top electrode and HZO ferroelectric layer. Nevertheless, the Ti-L edge spectrum presented in Figure 4.10(c) suggests that STO capping layer might supply oxygen to the HZO grain boundaries instead of scavenging it. However, there is no evidence of a large variation of oxygen concentration in the HZO layer, as Figure 4.10(b) shows, indicating that, if present, oxygen exchange between STO and HZO is very small. In order to fully address the role of STO and possible oxygen supply, dedicated studies of the STO/HZO interfaces must be performed with high-resolution interface techniques. Also, if the oxygen from STO drift and diffuse to fill oxygen vacancies in grain boundaries, experiments that can analyze these limited and small regions should be employed.

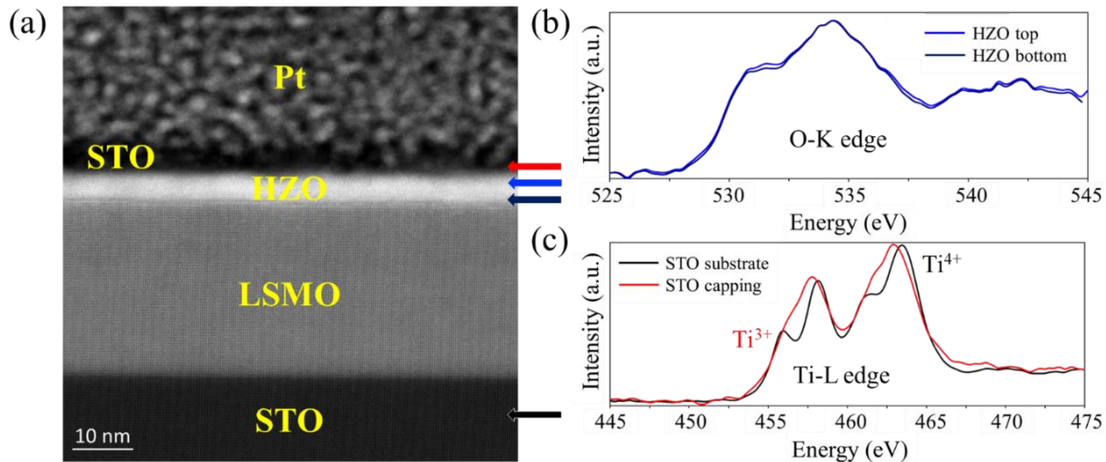

Figure 4. 10. (a) HAADF cross-section image of the HZO/STO2 heterostructure, where each layer can be differentiated. The arrows mark the region where the different spectra were obtained. (b) O-K edge peak obtained from the HZO close to the STO capping (uppermost region) and the HZO just above the LSMO layer (lowermost region). (c) Ti-L edge spectra collected from STO at the substrate and at the capping layer. Whereas the edge of the STO in the substrate has the fine structure of Ti^{4+}, the Ti-L edge of the STO in the capping layer has a fine structure of Ti^{3+}, indicating that the STO capping layer is reduced.

It should be mentioned that recently Max et al.[82,164] reported an attempt to introduce a nanometric AlO_x layer in ferroelectric HZO devices. The dielectric layer was grown on a symmetric metal/HZO/metal polycrystalline structure to break the junction's symmetry and exploit the tunnel transport through the AlO_x barrier. The approach was radically different from the one taken here: they took advantage of the charge transport modulation by the polarization reversal of the

ferroelectric barrier. Ryu et al. also explored a similar approach in metal/Al_2O_3/HZO/Si structure.[221] Although it cannot be excluded that the STO and AlO_x layers in the present case may affect changing the barrier's energy profile, data show that the most prominent effect is blocking the ionic channels that are responsible for the ionic-related *ER* in HZO.

4.7. Conclusion

This chapter has shown that capping the HZO film with ultrathin crystalline $SrTiO_3$ or amorphous AlO_x layers allows a radical improvement of the operation window for genuine ferroelectric electroresistance in tunnel devices. The capping layer's presence decreases the device-to-device electroresistance variability by a factor of 7 and increases the robustness and endurance of ferroelectric tunnel junctions. STEM images have demonstrated that the polycrystalline STO coating is conformal and seal grains and grain boundaries in HZO. Nevertheless, the capping layer's crystallinity is not essential to upgrade the electroresistive response, giving a similar effect observed with amorphous AlO_x capping. The ultimate reason for the effects of the capping in the FTJ functionalities remains to be disclosed. The Ti reduction observed by STEM/EELS analyzes that occur in the STO capping may suggest that this layer acts as an oxygen source for the grain boundaries of HZO.

4.8. Appendix

Appendix 1.

The *ER* dependence on the writing voltage amplitude (V_w) for different junctions in samples with bare HZO and STO capping layers is depicted in Figure A4.1. In all cases, the writing pulse duration is τ_w = 300 μs. As the writing voltage increases, the dispersion of results shrinks, and close to V_{GB}, the absolute *ER* value decreases. The transition to Region II happens for larger voltages, and the resistance drops for both ON and OFF resistive states. This effect is associated with ionic motion and the formation of conducting channels along grain boundaries within the HZO film.

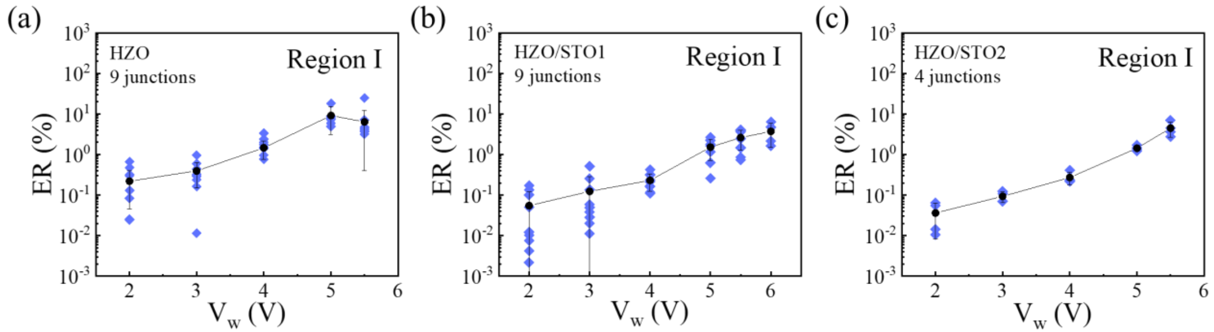

Figure A4. 1. ER(V_w) data for (a) HZO, (b) HZO/STO1, and (c) HZO/STO2 samples. The number of junctions measured in each sample is indicated in the corresponding graph.

Appendix 2.

Topography images from atomic force microscopy (AFM) were obtained at the surface of samples grown on STO substrates. The roughness mean square values acquired from the images are 0.3, 0.3, and 0.2 nm for HZO, HZO/STO2, and HZO/AlO2 samples, respectively. Even though the roughness is similar, Figure A4.2 reflects the capping layers' granular character in contrast with the smooth surface of the bare HZO sample.

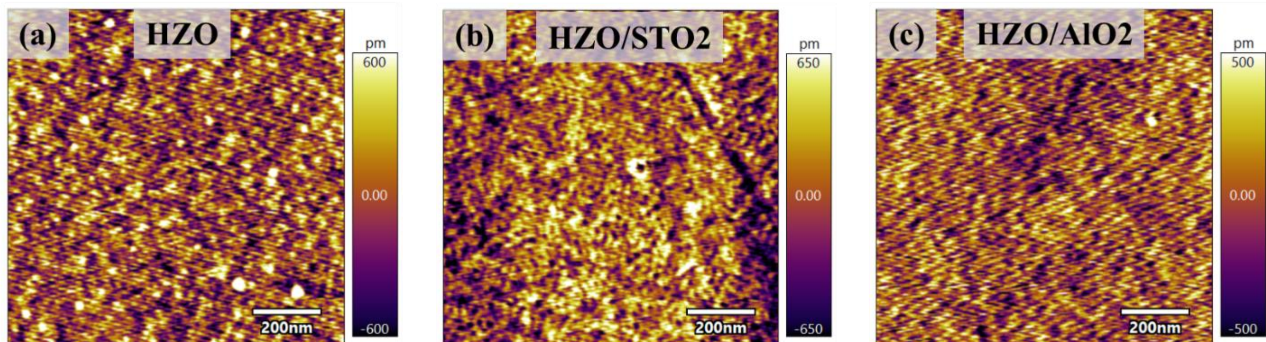

Figure A4. 2. Topography images from AFM collected on the surface of (a) HZO, (b) HZO/STO2, and (c) HZO/AlO2 samples. The diagonal line in (b) is mechanical damage caused in the surface of the film due to manual manipulation of the sample.

Chapter 5. Ferroelectric and Resistive Switching in Ultrathin Tunnel Junctions

---

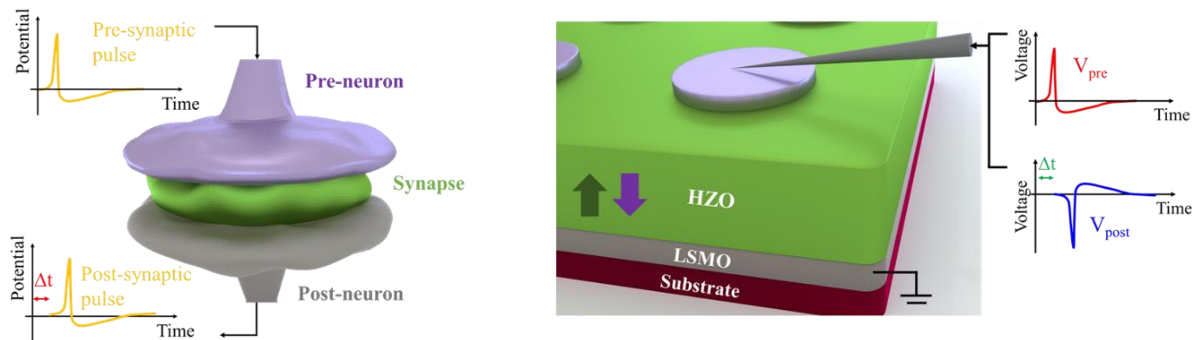

The results of this chapter will be submitted to publication.

In the quest for reliable and power-efficient memristive devices, ferroelectric tunnel junctions (FTJ) are investigated as potential candidates. CMOS-compatible ferroelectric hafnium oxides are at the forefront. However, in epitaxial tunnel devices with thicknesses around ≈ 4 - 6 nm, the relatively high tunnel energy barrier produces a large resistance that challenges their implementation. Here, we show that ferroelectric and electroresistive switching can be obtained in ultrathin 2 nm epitaxial $Hf_{0.5}Zr_{0.5}O_2$ (HZO) tunnel junctions in large area capacitors (≈ 300 μm^2). We observe that the resistance area product is reduced to about 160 $\Omega\cdot cm^2$ and 65 $\Omega\cdot cm^2$ for OFF and ON resistance states, respectively. These values are two orders of magnitude smaller than those obtained in equivalent 5 nm HZO tunnel devices while preserving a similar OFF/ON resistance ratio (210 %). The ultrathin FTJ shows memristive and spike-timing-dependent plasticity (STDP) behavior and good retention. Electroresistance and polarization loops closely coincide, signaling ferroelectric switching as a driving mechanism for resistance change. However, it is shown that ferroelectricity and ionic-like mechanism still coexist and impact the electroresistance.

5.1. Introduction

Epitaxial growth of hafnium oxide films has been demonstrated to be instrumental in identifying and control displacive and ionic contributions to *ER*.[206,216,224,225] The improved crystalline quality of epitaxial films helped to mitigate the ionic conductivity phenomena widely studied in polycrystalline HfO_2[97,226–228] and ZrO_2[229] films and are known to be mostly associated with existing grain boundaries. Indeed, epitaxial engineering allows to control the presence of grain boundaries in HZO films and understand their contribution to ferroelectric properties and *ER*, leading to its near-complete suppression by appropriate substrate selection.[53] As explored in Chapters 3 and 4, HZO films grown on $GdScO_3$ display only the ferroelectric orthorhombic phase. However, epitaxial hafnium oxide FTJ, typically 4 – 8 nm thick, shows extremely high resistance values. The reason is intrinsic: hafnium oxide, where Hf^{4+}:$5d^0 6s^0$, and zirconium oxide, with Zr^{4+}:$4d^0 5s^0$, have lower affinity[230] than oxide perovskite ($3d^n 4s^0$) ferroelectrics.[231–233] It follows that the tunnel barrier height in a metal/ferroelectric/metal junction will be larger in HfO_2 than in oxide perovskite ferroelectrics,[72], resulting in low tunneling current and high resistance values. The high resistance is desirable for some applications, for instance, in ferroelectric complementary resistive switching devices.[234,235] However, a sizable current is required to achieve fast and reliable reading operation of memory devices. An equilibrium between these two features is yet to

be found.[236] Three strategies can be arranged to reduce device resistance. The first is to use metals with lower work function[237] to reduce tunneling barrier height at the expense of the metal's usually higher reactivity. The second is to induce Fowler-Nordheim tunneling at the expense of using higher reading voltages.[74] The third and last is to reduce the barrier thickness. The recent discovery of robust ferroelectric properties in sub-5 nm HZO capacitors,[19,238] even reaching a thickness of 1 nm HZO,[116] open the door to investigate the correlation between ferroelectricity and *ER*.

In this chapter, ferroelectric ultrathin HZO films are grown by PLD using scandate single-crystalline substrates to boost the ferroelectric o-HZO phase's selective growth and minimize incoherent grain boundaries in the film.[53] It is shown that ferroelectricity coexists with tunnel *ER* in HZO films as thin as 2 nm in large capacitor structures (≈ 20 μm diameter), and their univocal relationship is disclosed. As expected, the resistance is reduced by about two orders of magnitude compared with 5 nm tunneling barriers, and the *ER* reaches ≈ 210 % at room temperature. Their memristive behavior is explored as long as their spike-timing-dependent plasticity (STDP).

5.2. Samples

Epitaxial HZO films with thicknesses 2, 3, and 5 nm are grown on $GdScO_3$ (001)-oriented single crystalline substrates ($GdScO_3$ is indexed in the pseudocubic setting) buffered by a 22 nm thick $La_{2/3}Sr_{1/3}MnO_3$ (LSMO) layer by PLD. Details about the growth technique and deposition parameters are described in the Experimental Methods chapter. Circular Pt top electrodes of 20 μm of diameter were grown through a shadow mask by sputtering.

5.3. Structural characterization

According to Estandia et al.[53], and as was explored in Chapters 3 and 4, HZO films grown on scandate substrates are composed predominantly of orthorhombic grains, in opposition to HZO grown on STO substrates. In ultrathin films, other factors become critical, like the roughness of the ferroelectric layer. Therefore, this section will focus on the structural characterization of the HZO films grown using Atomic Force Microscope (AFM) measurements to determine the topography and average roughness and X-ray diffraction (XRD) to verify the phase composition and the m-/o-HZO ratio.

5.3.1. Topography

Figure 5.1(a, b, c) shows (5x5) μm^2 AFM topography images collected in 2, 3, and 5 nm HZO films, respectively. It is possible to observe a similar topography in all the films, in which terraces and steps are present, as reported elsewhere.[127] The insets display an enlarged image of a (1x1) μm^2 scan and indicate the terraces. The roughness mean square values (RMS) are 0.13, 0.13, and 0.17 nm for 2, 3, and 5 nm samples, respectively, which ensure a good quality of the films.

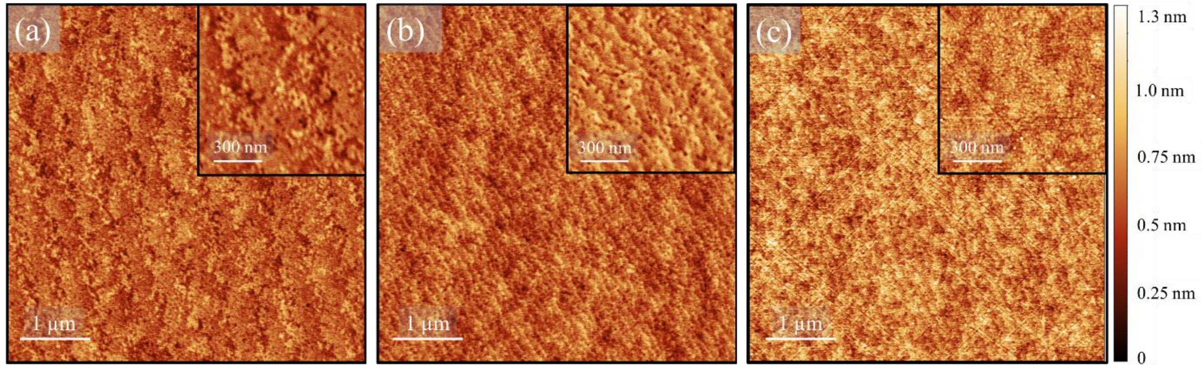

Figure 5. 1. AFM topography images for (a) 2 nm, (b) 3 nm, and (c) 5 nm HZO films grown on GSO substrates. Main images are acquired in a region with an area (5x5) $\mu m^{2,}$ and the inset shows a zoomed image from (1x1) μm^2 scan.

5.3.2. X-ray Diffraction

In classical perovskite, surface-energy-driven size effects at low dimensions favor the high-symmetry paraelectric phase (cubic) over the low-symmetry ferroelectric phase (tetragonal).[116,239] In fluorite structures as the doped-HfO_2, the non-centrosymmetric orthorhombic phase has higher symmetry than the bulk-stable centrosymmetric monoclinic phase. Therefore, surface energies help to counteract depolarization fields in fluorite-structure ferroelectrics in the ultrathin regime. The confinement strain provided by the epitaxial grown on the template of the substrate favors the symmetry-lowering polar distortion stabilization.[53]

Therefore, it would be expected that ultrathin films grown in GSO substrates maintain the microstructure observed in previous studies[53,216] and the one explored in Chapters 3 and 4, i.e., mainly composed of orthorhombic grains. The phase composition of 2, 3, and 5 nm HZO films studied here is then investigated by X-ray diffraction. Figure 5.2(a) (background image) shows the XRD 2θ-χ frame of the HZO (2 nm) sample. The diffraction spots corresponding to (001) and (002) reflections of the substrate and LSMO electrode and those from o-HZO are visible. It is also

included the integrated θ-2θ scans along χ (± 10°), in the 20° < 2θ < 50° angular range, which is dominated by the strong diffraction spots of the substrate (GSO) and bottom electrode (LSMO). Zoom in the 20° < 2θ < 42° range allows identifying the (111) o-HZO diffraction. Data exhibit o-HZO (111) reflection at 2θ ≈ 30º and the absence of the m-HZO (002). The diffraction peak of o-HZO narrows and its intensity increases for thicker HZO films, as in Figure 5.2(b, c). The data for 3 and 5 nm films show no remarkable difference, except for the presence of Pt (111) at 2θ ≈ 40º reflection in Figure 5.2(b) due to the Pt electrodes. Finer details of the evolution of HZO reflection can be appreciated in Appendix 1 and 2. Ultimately, data suggests that HZO films' microstructure with thickness in the range 2 – 5 nm is composed basically by orthorhombic grains. If any monoclinic grain is present, its quantity is significantly reduced to identify with the XRD performed here.

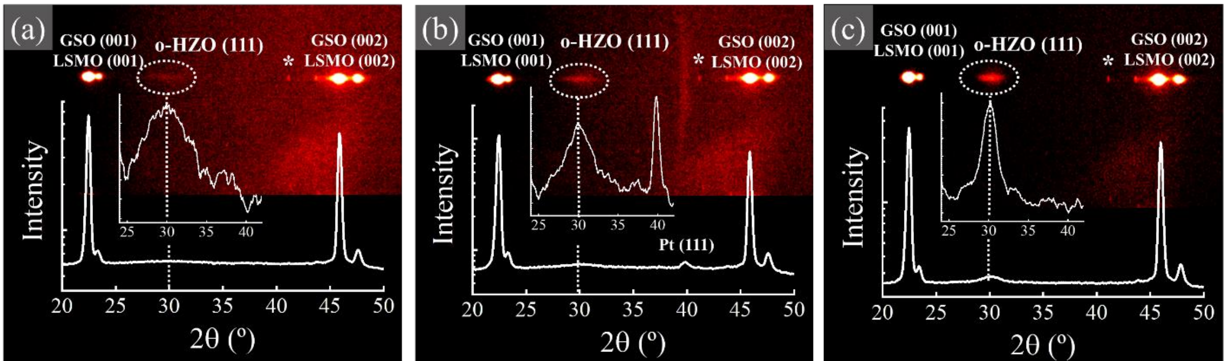

*Figure 5. 2. XRD 2θ-χ frames of HZO/LSMO bilayers on $GdScO_3$ for samples with a) 2, b) 3, and c) 5 nm HZO, respectively. Integrated scan along χ and corresponding zoom around o-HZO (111) reflection are also included. The bright spots marked with an * are an artifact from the detector.*

5.4. HZO (2 nm) tunnel junction

In this section, the thinnest FTJ composed by HZO (2 nm) is explored, and further characterization of its microstructure and functionalities are shown. As observed in Figure 5.2(a), it is expected that this sample is entirely composed of o-HZO grains, in agreement with data collected in 9 nm HZO shown in chapter 3. However, to further detail its microstructure, Scanning Transmission Electron Microscopy (STEM) images are acquired. Moreover, the film's ferroelectric character is assessed using a piezo force microscope (PFM) and macroscopic electrical measurements. The memristic behavior of the sample is also explored, and spike-timing-dependent plasticity is found.

5.4.1. Scanning Transmission Electron Microscopy

The STEM specimen with HZO (2 nm) films covered with a platinum electrode was prepared by an FEI Helios nanolab 650 focus ion beam by the technical service at Universidad de Málaga. These samples were characterized by Dr. Jaume Gàzquez and Saul Estandía using a JEOL JEM ARM200cF operated at 200 kV equipped with a CEOS aberration corrector (for atomic resolution) and GIF Quantum *ER* spectrometer at the Universidad Complutense de Madrid (Spain). Further details are described in the Experimental Methods chapter or elsewhere.[53] The contrast of the high angle annular dark-field (HAADF) imaging mode, which scales approximately as the square of the atomic number *Z*, permits the observation of the cations sublattices in the HZO as in the LSMO films.

Figure 5.3(a) shows a high-magnification STEM-HAADF image of a pristine electrode. It is possible to identify the GSO substrate as long as the LSMO, HZO, and Pt films. The platinum top electrode is polycrystalline, as expected from a sputtering deposited film. Accordingly to the scale bar, the LSMO film's thickness is ≈ 26 – 27 nm and the platinum ≈ 24 nm, contrasting with the nominal thickness. Nevertheless, the number of PLD pulses for the LSMO growth and the sputtering time for Pt is the same for all the samples investigated here, so the thickness of these layers in the 3 and 5 nm HZO samples is expected to be the same. Note that the scale bar indicates the ≈ 2 nm thick HZO film with accuracy in Figures 5.3(a, b). An isolated m-HZO grain is observed next to several o-HZO grains. Figure 5.3(b) enlarges the region from Figure 5.3(a) marked in yellow and displays the minor fraction of m-HZO, even though it does not provide an accurate quantitative estimation of its relative fraction of the entire film. Indeed, m-HZO grains are observed in some frames. These monoclinic grains are (002) textured that are next to (111) oriented o-HZO. The monoclinic grain image is enlarged in the inset in Figure 5.3(b), where the simulated cation sublattice of the monoclinic phase (space group $P2_1/c$) is superimposed.

Therefore, the HAADF images reveal that a large majority of o-HZO grains coexist with seldom m-HZO grains. These results, along with the XRD 2θ-χ frames and 2θ scans (Figure 5.2(a)) that do not show a distinct monoclinic reflection, suggest that the amount of m-HZO phase is relatively small. This conclusion is consistent with the STEM images observed in thicker HZO films[216] and favoring non-centrosymmetric grains in ultrathin films. Nevertheless, as m-HZO grains are present and grain boundaries type GB-II, spurious ionic-motion contribution could appear.

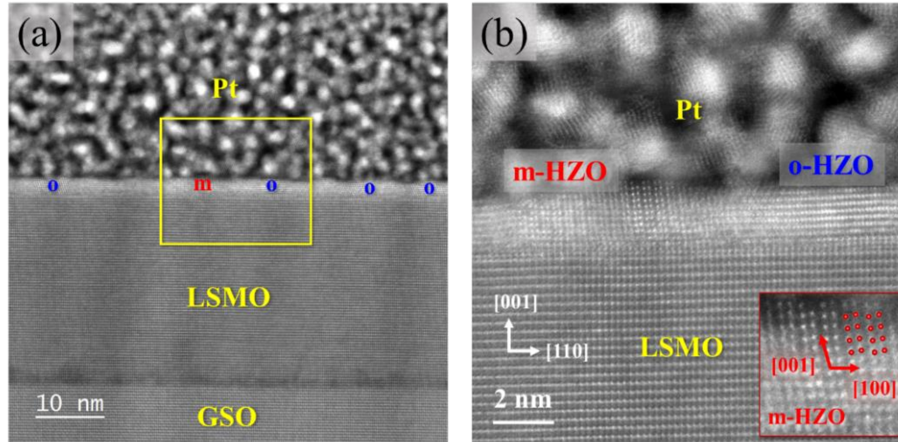

Figure 5. 3. A cross-section HAADF-STEM image of the HZO/LSMO heterostructure was recorded along the substrate's pseudocubic [110] zone axes. (a) The film's region where the Pt top electrode, HZO, LSMO, and GSO films can be differentiated. One m-HZO (red "m" grain is indicated next to another o-HZO (blue "o"). (b) Enlarged view of the marked region in which the m- and o-HZO grains are indicated. The inset shows the monoclinic grain with the monoclinic phase's simulated cation sublattice (space group $P2_1/c$) superimposed.

5.4.2 Electrical characterization

The electrical characterization of HZO (2 nm) films is performed in two distinct ways: directly on the surface of the ferroelectric by PFM or macroscopically on large electrodes. In the case of the PFM, the conductive tip coated with Pt on both sides (Multi75E-G, BudgetSensors) is used as the top electrode. The results obtained with the two measurements can determine the oxide film's ferroelectricity character unequivocally.

5.4.2.1. Piezoresponse force microscopy (PFM)

The PFM measurements were performed using an MFP-3D Asylum Research Microscope (Oxford Instrument Co.) by Huan Tan as part of her Ph.D. research project, and a dual AC resonance tracking (DART) method was employed to achieve better sensitivity. Figure 5.4(a) shows the voltage-dependent PFM amplitude and phase loop for a pristine region, collected by placing the tip on the bare HZO surface as the inset sketches. The PFM voltage hysteresis loop is always collected at remanence using a dwell time of 5 milliseconds. The same figure included the loops after field-training the region with N_c = 100 cycles, in which the voltage was ranged from – 8 V to + 8 V, to discard any possible "wake-up" effect of the HZO film. The phase loop indicates a phase change of 180º upon poling. The amplitude is almost zero at the coercive fields, which is expected for an intrinsic ferroelectric response. Data from pristine and cycled samples have similar PFM

response; the only perceptible differences are a minor increase in the piezoelectric amplitude and coercive field, in addition to a decrease of the imprint field ($E_{imp} = \frac{E_c^{+} + Ec^{-}}{2}$).

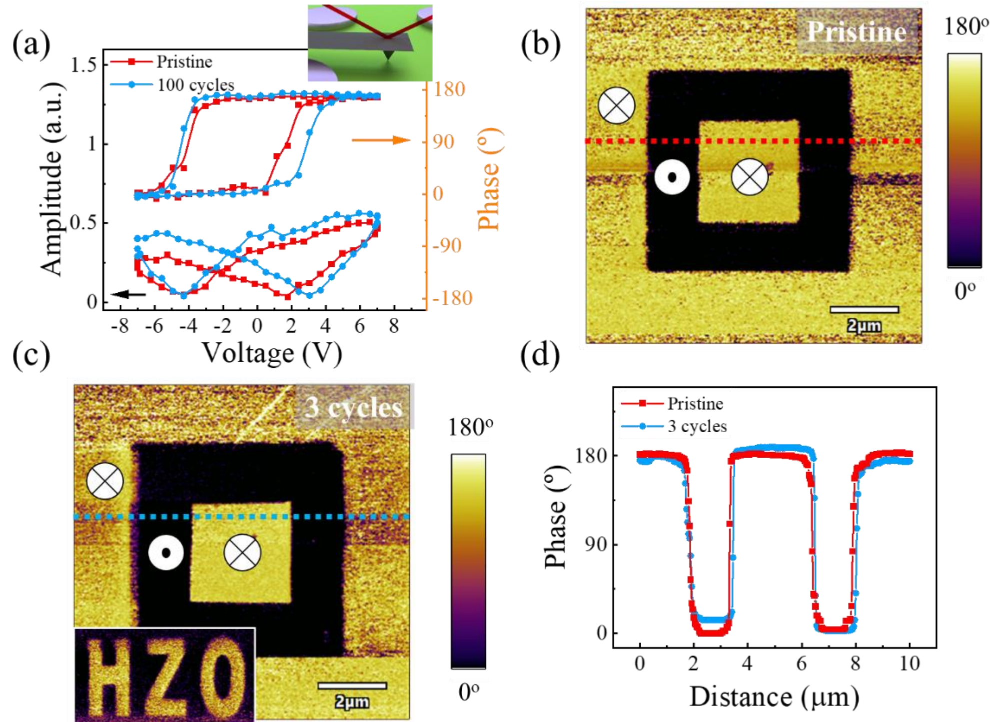

Figure 5. 4. (a) PFM phase and amplitude loops of HZO (2 nm) pristine and voltage-cycled (N_C = 100) sample. Inset: illustration of signal (laser) collection and monitoring cantilever deformation. PFM phase map collected in (10 x 10) μm² region for (b) pristine and (c) cycled sample (N_C = 3). Bright and dark regions were obtained by poling with + 6 V and - 6 V, respectively. Inset in (c) shows (5 x 10) μm² PFM phase map collected in a region poled with a different ("HZO") pattern. (d) Phase dependence on the distance acquired in horizontal dashed lines shows in (b) and (c).

Figure 5.4(b) shows a PFM phase map collected in a (10x10) μm² area of the pristine sample after poling using V_w = - 6 V or + 6 V. The dark region represents the area poled with a negative voltage and the bright region with positive. Figure 5.4(c) shows a PFM phase map recorded after field-cycling the same region three times (N_c = 3) previously to final V_w = ± 6 V poling. The close similarity of the images and the PFM loops in Figure 5.4(a) strongly indicate that cycling does not modify the film's ferroelectric character. Note that the bright outer regions in the PFM phase maps have not been poled, indicating the as-grown polarization state is downwards in both samples. The inset shows a different pattern in a (5x10) μm² area also obtained by poling the HZO surface with ± 6 V. The amplitude map collected simultaneously with the phase for pristine and cycled sample

is shown in Appendix 3. A horizontal scan of the phase in Figures 5.4(b, c) indicated by the dashed lines confirms the 180º phase inversion between regions poled positively and negatively.

5.4.2.2. Macroscopic measurements

The electrical characterization of HZO (2 nm) films was also performed in circular Pt electrodes of 20 µm of diameter. The *I*(*V*) curves collected at 1 kHz with DHM mode in a pristine junction are shown in Figure 5.5(a). The inset shows the electrical arrangement, where the LSMO bottom electrode is grounded while the top Pt electrode is biased. The pristine *I*(*V*) has a sigmoidal shape, as expected for trapezoidal barriers[209]. The calculated current density (*J*) at 0.5 V is ≈ 0.09 $A\cdot cm^{-2}$, which is in the same order as the one obtained by Wei et al.[206] in Co/HZO (2 nm)/LSMO//STO tunnel devices (J(0.5 V) ≈ 0.06 $A\cdot cm^{-2}$). However, no sign of ferroelectric switching is observed. Despite this, the electroresistance is measured on this junction by recording five sequential $R(V_w)$ loops for writing maximum pulse amplitude of V_{max} = 8 V and duration τ_w = 300 µs. The resistance is measured after each writing pulses (V_w) by applying a linear $V_R(t)$ bipolar triangular pulse in a small voltage range (from – 1 V to + 1 V) and calculated at V_R = 0.9 V. The resistance in Figure 5.5(b) is ≈ $3\cdot 10^5$ Ω and negligible electroresistance (*ER* ≈ 1 %) is found.

As the junction shows no *ER*, a field-training is performed by applying continuously bipolar rectangular pulses with 3 V amplitude in a frequency of 100 Hz on the top electrode, as described in the Experimental Methods chapter. This step follows the same cycling approach implemented in the PFM characterization (Figure 5.4(a, c)). After a certain number of cycles (N_c), a reading *I*(*V*) was measured with DHM mode at 1 kHz. As Figure 5.5(a) shows, the *I*(*V*) after $N_c = 5\cdot 10^3$ (pink symbols) and 10^4 (blue symbols) cycles show a dramatic decrease of current. Considering that the sample's microstructure is composed of o-HZO grains and sporadic m-HZO and, thus, GB-I and GB-II, the high current in the pristine sample may be associated with current leakage taking place at incoherent grain boundaries. With cycling, these channels are deactivated, and the leakage is significantly reduced.

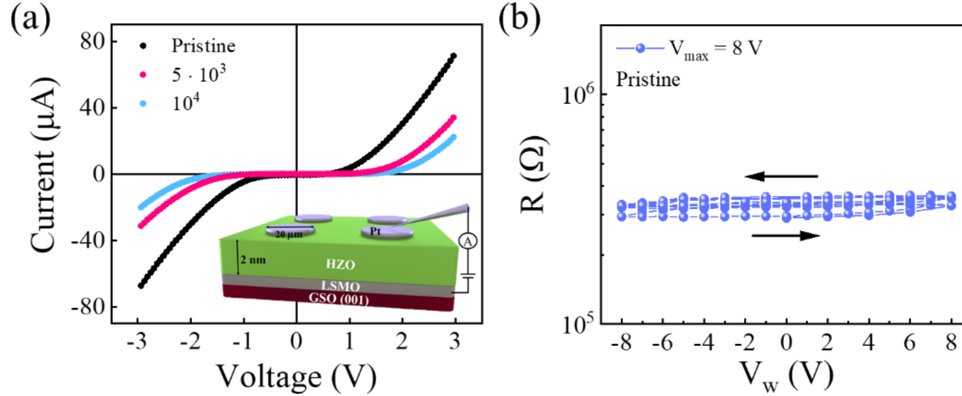

Figure 5. 5. (a) I(V) curves collected at 1 kHz and V_{max} = 3 V with DHM mode in pristine junction, after N_c = 5·10^3 and 10^4 cycles. Inset shows the electric arrangement of electrodes for electric measurements. (b) Resistance dependence on the writing voltage amplitude (duration 300 μs) was performed in a pristine junction, where no significant electroresistance is observed. Five sequential loops are depicted.

In order to evaluate the contributions to current, the *I*(*V*) curves from Figure 5.5(a) are fitted using the Brinkman model[73] associated with a parallel resistance (*R*), representing a leakage channel. A sketch of the circuit is exhibited in Figure 5.6(a). As the leakage current decreases with cycling, the resistance *R* should increase its value. The fitting results obtained only by the Brinkman model or (Brinkman model + *R*) are compared by calculating the χ^2, i.e., the goodness of the fitting. Figure 5.6(b) shows the χ^2 dependence with the number of cycles (N_c). The calculated values for the *R* are also indicated. Both models have a similar χ^2 dependence and, as expected, the resistance *R* increases.

Figure 5.6(c) displays the *I*(*V*) curve measured in the pristine junction and the fittings for both models. Neither fit appropriately the low voltage region ($|V| < 1$ V), indicating that the parallel resistance that contributes linearly to the current is not enough to describe the leaky behavior in the junction correctly. In Figure 5.6(d), the *I*(*V*) fitting after 10^4 cycles with both models results in a similar χ^2 value, suggesting the leakage does not contribute significantly to the conduction, so the parallel resistance is no longer critical. The fittings intend to shed light on the fact that the tunneling becomes the significant contribution for current and leakage dramatically decreases after the field training. The extracted values of barrier heights and parallel resistance are shown in Table 5.1. The value of *R* increase from ≈ 10^5 in the pristine state to ≈ 5·10^7 Ω after 10^4 cycles.

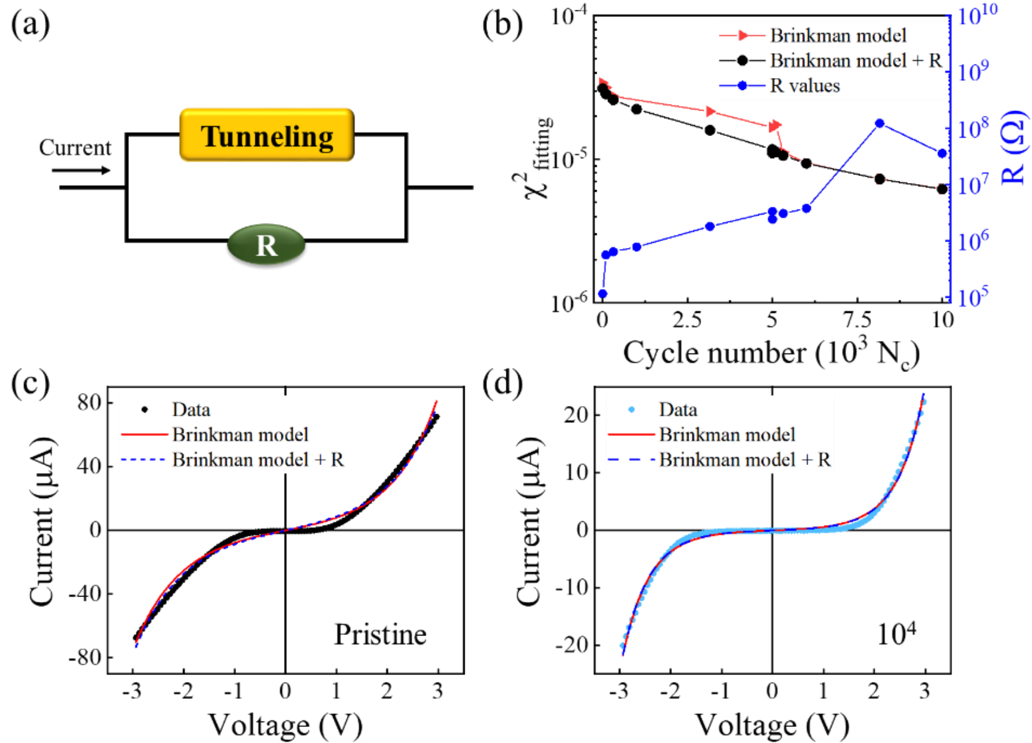

Figure 5. 6. (a) Sketch of the equivalent circuit used for fitting I(V) curves. The current has two contributions: tunneling and leakage, represented here as a parallel resistance. R's value increases as the sample are cycled, and the leakage contribution to the I(V) is reduced. (b) Calculated χ^2 from fittings using only the Brinkman model (black symbols) and using the Brinkman model associated with a parallel resistance (red symbols). I(V) curves from (c) pristine device and (d) after $N_c = 10^4$ cycles and associated fittings using both models.

As investigated in Chapter 3, the m-HZO and o-HZO phase's coexistence leads to HZO barriers with a smaller resistance. Note that the thickness remains fixed at 3.15 nm; otherwise, the calculation will only vary the effective thickness to fit the data correctly. Even though the *I*(*V*) curves could not be perfectly fitted, these results clearly show that field-cycling favors non-tunnel transport blocking across the HZO barrier. Based on the available information, it cannot be excluded that this effect might be related to the typical "wake-up" in ferroelectric HfO_2, either involving a field-induced phase transformation of the residual m-HZO into o-HZO or redistribution of oxygen vacancies inside the insulator. In order to identify if there is phase transformation associated with the training effect, techniques like high-resolution transmission electron microscopy associated with diffraction techniques like selected area diffraction pattern (SADP)[240] could be used to compare the microstructure of pristine and cycled HZO.

Cycle number	t_{eff} (nm)	ϕ_{LSMO} (eV)	ϕ_{Pt} (eV)	R (Ω)
1	3.15	3.17	3.19	$3.6 \cdot 10^5$
$5 \cdot 10^3$	3.15	3.46	3.40	$3.3 \cdot 10^6$
10^4	3.15	3.57	3.46	$3.58 \cdot 10^7$

Table 5. 1. Barrier parameters extracted from fittings are shown in Figure 5.6. The effective thickness (t_{eff}) was fixed at 3.15 nm, while the barrier height for both interfaces (ϕ_{LSMO} and ϕ_{Pt}) and parallel resistance (R) were fitted.

After training the junction with $N_c = 10^4$ cycles, the ferroelectric character of the film can be assessed by recording the $I(V)$ curve at 5 kHz using the PUND technique (Figure 5.7(a)). The corresponding $P(V)$ loop obtained by integrating the current is displayed in Figure 5.7(b). The current peaks associated with polarization switching are evident. The coercive voltage extracted from the switching peak position is $V_c^+ \approx + 2.8$ V and $V_c^- \approx - 2.5$ V, giving rise to a small imprint field $V_{imp} = + 0.1$ V. Note that the imprint field here is different from the PFM data in Figure 5.4(a), where $V_{imp} = - 0.6$ V, which is probably due to the large number of cycles performed in the capacitor in contrast to the only 100 cycles performed at the bare HZO surface. The remnant polarization obtained from the $P(V)$ loop is $P_R \approx 2$ μC·cm^{-2}.

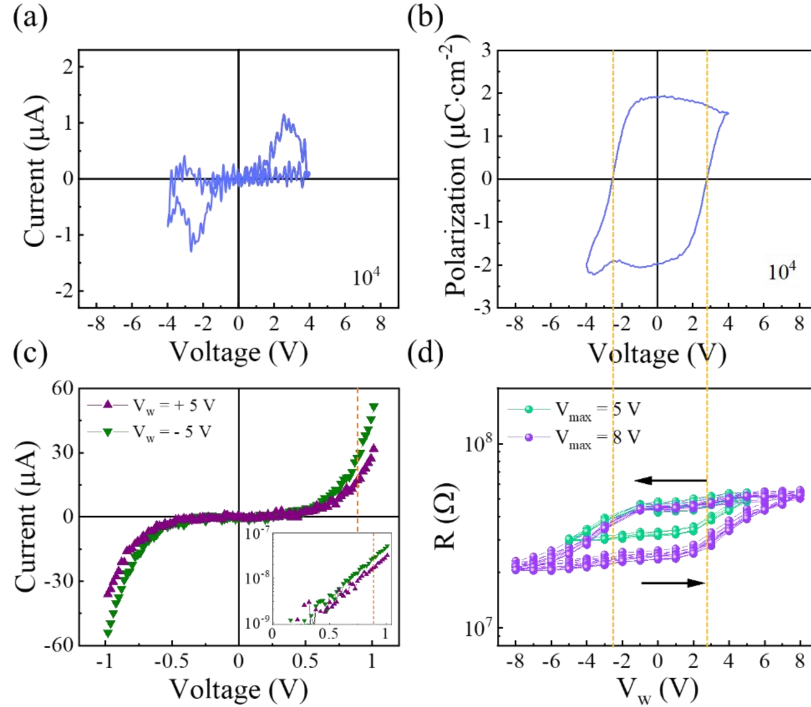

Figure 5. 7. (a) Current-voltage I(V) recorded in 2 nm HZO junction at 5 kHz and V_{max} = 4 V with PUND after $N_c = 10^4$ training cycles. (b) P(V) loop obtained by integrating the current in (a). (c) Reading I(V) curves collected after pre-polarizing with V_w = + 5 V (purple symbols) and V_w = - 5

V (green symbols). Inset: logarithm scale of current (units in the main panel). (d) Resistance dependence on writing voltage amplitude in junction after 10^4 cycles. The junction is the same as in (a, b). Five sequential loops are shown for each V_{max}. Dashed vertical lines in (b) and (d) indicate the coercive voltages (V_c^+, V_c^-).

Figure 5.7(c) shows the reading *I*(*V*) curves corresponding to two resistance states after pre-polarizing the junction with $V_w = \pm 5$ V pulses with duration $\tau_w = 300$ µs. It can be appreciated that the curves are sigmoidal and slightly asymmetric, as found in trapezoidal tunnel barriers. Importantly, the conductance for $V_w = -5$ V (green symbols) is larger than for $V_w = +5$ V (purple symbols), indicating that the writing voltage sets the junction resistance. The inset shows the logarithmic scale of the *I*(*V*) reading curves for positive voltages, and the conductance difference can be more clearly identified. The vertical dashed lines at $V_R = 0.9$ V indicate the voltage reading for calculating the resistance. Figure 5.7(d) shows the electroresistance $R(V_w)$ loops collected after 10^4 cycles, where five sequential loops for each V_{max} are displayed and illustrate the ER's robustness. The loops recorded at $V_{max} = 5$ V (green symbols) are performed initially. The resistance rapidly changes around $V_w = \pm 3$ V, leading to well-defined high/low (OFF/ON) resistance states. If V_{max} is increased to 8 V (purple symbols), similar behavior is observed. The OFF/ON ratio for $V_{max} = 5$ V is 150 % and for $V_{max} = 8$ V is 210 %. Note that the OFF resistance state is maintained for both V_{max}, whereas the ON state decreases. The close coincidence $V_c \approx V_w$, i.e., where the resistance starts to change, suggests the *ER* is due to polarization-controlled tunnel transport across the 2 nm barrier. Consistently, Appendix 4 shows the derivatives d(*P(V)*)/d*V* and d(*ER*(V_w))/d*V* display closely coincident maxima at similar values ($V = V_c$), as expected from a common origin.[82,161] Following Cheema et al.,[116] a voltage-polarity-dependent current-voltage hysteresis was used to disregard resistive switching mediated by the dielectric breakdown and filamentary-type switching as a source of the observed *ER* (Appendix 5). The electroresistance data in Figure 5.7(d) is characteristic of ferroelectric memristors and indicates that an appropriate pulse amplitude and duration can modulate the device resistance.

In order to show the endurance of the resistive states in 2 nm HZO tunnel junctions, voltage pulses with alternated polarity (amplitude $|V_w| = 8$ V) and duration $\tau_w = 300$ µs are applied to a previously cycled electrode. Figure 5.8(a) shows the resistance recorded after each writing pulse up to $N_p = 300$. The OFF/ON resistance values are consistent with the ones obtained in Figure 5.7(d). It can be appreciated that in the first 100 pulses, the OFF state has a gradual increase of resistance, indicating a possible "wake-up" as observed in HfO_2 films[130,136] or an ionic-related

contribution. Nevertheless, the average OFF and ON resistances are maintained after 300 pulses as well as the *ER*, as observed for thicker HZO films grown on STO substrates (Figure 4.6(g, h, i)). Besides, the ultrathin HZO junctions have a remarkable retention time, which is a crucial feature for non-volatile data storage. Figure 5.8(b) display the time evolution of OFF/ON states that were set by writing pulses of V_w = ± 5 V and ± 8 V and τ_w = 300 μs. The OFF resistance obtained for V_w = + 5 V and + 8 V are similar, contrasting with the smaller ON state for V_w = – 8 V than for – 5 V. A related asymmetric switching has been observed in other ferroelectric-based tunneling junctions.[37,62,67,221] Wen et al.[67] attributed the asymmetric ON-to-OFF and OFF-to-ON behavior to the formation of space charge regions at the oxide-metallic electrode interface. Chanthbouala et al.,[62], in contrast, associated the asymmetry to the distinct nucleation of up/down domains and subsequent propagation, ruled by the Kolmogorov-Avrami-Ishibashi (KAI) model, which is the usual case for epitaxial systems.[241] A similar scenario may also hold here. It is worth mentioning that polycrystalline HfO_2-based ferroelectrics, where a distribution of local switching times (t_o) exists, the polarization reversal is better described by the Nucleation Limited Switching (NLS) or other models.[242,243] The epitaxial nature of our films seems to narrow the switching time distribution and, thus, lead to a limiting (KAI) model, which corresponds to a polarization reversal via homogeneous polar regions nucleation and domain-wall motion. More importantly, these results show the OFF/ON states do not suffer degradation within the explored time window (10^3 seconds), indicating the states last for longer times.

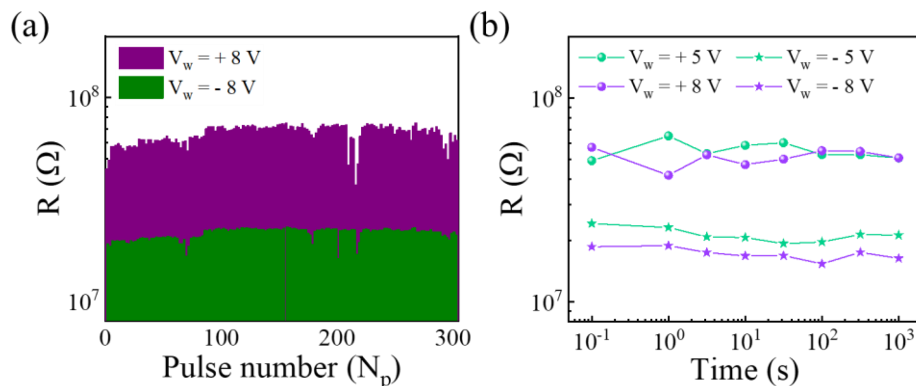

Figure 5. 8. (a) Endurance of OFF/ON resistive states obtained by applying 300 alternated writing pulses with amplitude V_w = ± 8 V and duration τ_w = 300 μs. The junction has been previously trained by $N_c = 10^4$ cycles. (b) Retention of R states after writing pulse with an amplitude as indicated and τ_w = 300 μs was applied to 2 nm HZO device. Junction in (b) is different from the one measured in (a). However, both have been cycled $N_c = 10^4$ previously.

5.4.3 Memristive

The modulation of resistance through an external writing pulse is critical for applying ferroelectric junctions in CMOS-compatible devices. To further explore the memristive abilities, the resistance state of a 2 nm HZO has been recorded after each writing pulse in the sequence of N_p, as shown in Figure 5.9(a). Here, 12 trapezoidal pulses with the same amplitude (V_w), duration (τ_w), and polarity are applied, followed by other 12 identical pulses with opposite polarity. The gradual variation of resistance depends not only on the (V_w, τ_w) parameters of the writing voltage pulse and the number N_p, mimicking potentiation/depression processes of synapses in biological neuronal systems. Depression is associated with increasing resistance (decrease of synaptic conductivity) and potentiation to a decrease (an increase of synaptic conductivity).

Further details on this experiment are provided in the Experimental Methods chapter. Figure 5.9(b) shows the resistance dependence on the number of writing pulses ($R(N_p)$) for different combinations of amplitude and duration (V_w, τ_w) as indicated. The percentage of R increase or decrease depends on the parameters (V_w, τ_w). Pulses with $V_w = \pm$ 5 V and $\pm$ 8 V and τ_w = 3 μs and 300 μs are used. Nevertheless, in all cases, longer durations and larger amplitudes enhance the change in resistance.

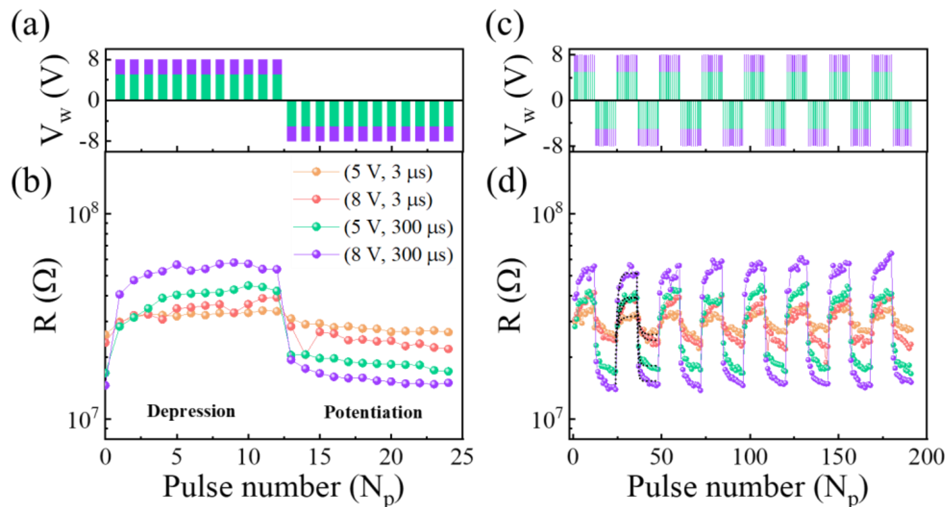

Figure 5. 9. (a) Pulse train with N_p = 12 positive writing pulses followed by N_p = 12 negative and (b) resistance dependence on the number of pulses for a 2 nm HZO tunnel junction. Each symbol represents the amplitude and duration of the writing pulses and is indicated in the label. (c) Voltage pulse sequence applied to the junction for repetition of measurement in (a) for eight potentiation/depression cycles and (d) corresponding resistance dependence on the pulse number. Symbol colors are the same as the label in (a).

Time-dependence polarization switching experiments are limited by the time constant of the system, i.e., the ferroelectric capacitor, bottom electrode series resistance, and measuring circuit. As detailed in Figure 2.9 from the Experimental Methods chapter, the time constant of the system is around 500 ns, and, thus, pulses with shorter duration cannot be used to study the memristive behavior using this circuit. By repeating the pulse train in Figure 5.9(a) eight times, as shown in figure 5.9(c), the potentiation/depression cycles' reproducibility in the ultrathin HZO junction can be demonstrated. The resistance evolution is depicted in Figure 5.9(d), and it also establishes the robustness of the memristive response.

Consistent with earlier findings,[184,187] the potentiation/depression data fit into an exponential model represented in Figure 5.9(d) by the dashed black lines. The $R(N_p)$ change is fitted by $R_{p,d} = R_0^{p,d} + A_{p,d} e^{-\left(N_p - N_0^{p,d}\right)/\tau_{p,d}}$, where p = potentiation, d = depression, R_0 = initial resistance, N_p = number of pulses, N_0 = number of first positive (depression) or negative (potentiation) pulse and τ = non-linearity of the effect.[184,186] This dependence shows that the appropriate combination of voltage, number of pulses, and duration can induce memristive behavior. As closer τ_p and τ_d are, the smaller the non-linearity of potentiation and depression effects, indicating a polar opposite behavior with the same number of pulses required to induce one or the other. As a matter of fact, for application, this would be the ideal behavior. The results obtained for the fittings in Figure 5.9(b) are shown in Table 5.2. The asymmetry observed on τ_p and τ_d shows that more pulses are necessary for increase the resistance (depression) than for decrease (potentiation).

(V_w, τ_w)	**τ_d**	**τ_p**
(5 V, 3 μs)	2.12 ± 0.48	1.47 ± 0.42
(8 V, 3 μs)	3.22 ± 0.51	1.45 ± 0.19
(5 V, 300 μs)	1.38 ± 0.15	0.81 ± 0.08
(8 V, 300 μs)	1.28 ± 0.22	0.66 ± 0.09

Table 5. 2.Non-linearity for potentiation (τ_p) and depression (τ_d) extracted from fittings in Figure 5.9(d).

Ferroelectric junctions show features that have been explored recently[69,187,244,245] for application in neuromorphic networks. In addition to the potentiation/depression abilities, a modulation of resistance that depends on the timing between electrical inputs is required for implementation in circuits that aim unsupervised learning.[70] To study this effect on artificial memories, it is worth

recalling how the synapse, the memory building block in the brain, works. As described in the Introduction chapter, electrical information is transmitted between neurons through action potential or spikes. The relative timing between the arrival of a spike in a pre-neuron and the firing of the post-neuron ($\Delta t = t_{pre} - t_{post}$) is a crucial point that defines the main rule of synaptic learning.[5] This rule is called spike-timing-dependent plasticity (STDP). In short, it determines that if the pre-neuron fires before than the post-neuron, the synapse that connects them is strengthened, as sketched in Figure 5.10(a). However, if the post-neuron spikes before, the synapse is weakened. As a consequence, the synapse strength or plasticity can be modulated by the timing (Δt) between a pre- and post-synaptic pulse.

When artificial junctions are explored, usually the two electrodes of the two-terminal device are biased. In each electrode, one voltage pulse, $V_{pre}(t)$ or $V_{post}(t+\Delta t)$, is applied separated by a time shift Δt, mimicking the pre- and post-synaptic signals. The junction resistance or conductance is measured, and its dependence on the Δt (plasticity) is established. Here, a simpler arrangement is proposed where both voltage pulses are applied to the top electrode (Figure 5.10(b)), whereas the LSMO bottom electrode remains grounded. The shape of the voltage pulses (spikes) mimics the action potential and has a duration of 50 µs. Figure 5.10(c) shows V_{pre} (red curve) and - V_{post} (blue curve). The time-shift (Δt) varies between – 50 µs and + 50 µs. Note that t_{pre} and t_{post} are the time corresponding to the signal trigger. V_{pre} and V_{post} are independent voltage pulses but, as they are applied in the top electrode with a reduced separation Δt, their waveforms overlap, creating a $V_{total} = V_{pre} - V_{post}$ pulse. Further description of the experimental set-up and waveform generation can be found in the Experimental Methods chapter.

Previously to applying any V_{total}, the junction's initial resistance (R_0) is collected in the depolarized junction. These values are converted into conductance (G) according to the relation $G = 1/R$. Then, after each $V_{total}(\Delta t)$, the junction's conductance is measured, and the variation of conductance (ΔG) is calculated by $\Delta G(\%) = \frac{(G_{spike} - G_0)}{G_{min}} x\ 100\%$, where G_0 = initial conductance ($G_0 = 1/R_0$), G_{spike} = conductance after the spikes, and G_{min} = the minimum value between G_0 and G_{spike}. The conductance change ($G(\Delta t)$) for the 2 nm HZO junction is displayed in Figure 5.10(d). Long delay times mean the pre and post-pulses barely overlap, and the ferroelectric threshold, i.e., coercive field, is not achieved, leaving the conductance unchanged. If the post-synaptic pulse is applied after the pre-synaptic pulse ($\Delta t > 0$), the junction increases conductance (decrease resistance).

When the post-synaptic pulse is sent before ($\Delta t < 0$), the conductance decreases (increase resistance). For small $|\Delta t| < 20$ µs, the conductance variation is larger since the overlapping of pre-and post-synaptic spikes reaches high voltages. The shape of the curve has the conventional STDP asymmetric Hebbian learning [246–248] in which the conductance is depressed if $\Delta t < 0$ and increased for $\Delta t > 0$, and it has been observed in some memristive devices.[70,249] The observed $G(\Delta t)$ modulation ratio is similar[62] or larger[221] than earlier reported on HZO ferroelectric tunnel barriers[69,221] that show a much larger resistance area product ($\approx 10^5$ Ω·cm^2) than the barriers reported here.

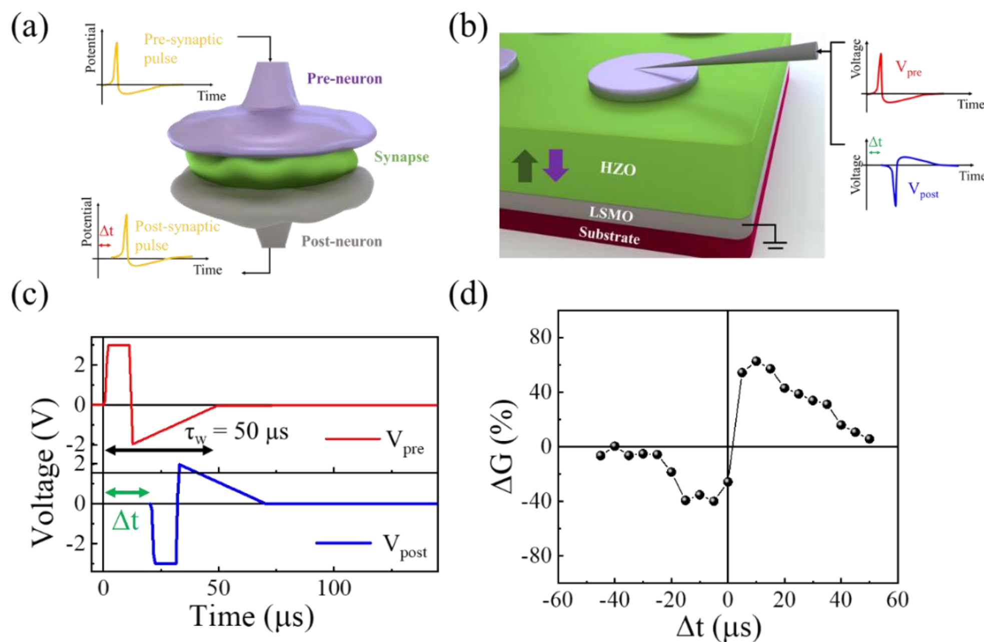

Figure 5. 10. (a) Sketch of the pre- and post-neuron and synapse connecting them. Electrical impulse (b) Sketch of the electrical arrangement to characterize spike-timing-dependent plasticity of 2 nm HZO junction. (c) Pre- and post-synaptic voltage waveforms (spikes) applied on the platinum top electrode while the bottom electrode remains grounded. The duration of each pulse is 50 µs. (d) Modulation of conductance ΔG in the function of the Δt.

5.5. Thicker HZO junctions

Having analyzed the structure, polarization, and memristive capabilities of 2 nm HZO films, a similar analysis can be executed on thicker HZO tunnel junctions grown on GSO substrates. As described in section 2.2, capacitors with 3 and 5 nm thick HZO were also grown. The film's roughness and the phase composition are shown in Figure 5.1(b, c) and Figure 5.2(b, c), respectively. The $I(V)$ and $P(V)$ data collected by PUND at 5 kHz in 3 and 5 nm HZO junctions

are shown in Figure 5.11(a, b), respectively. The coercive voltage extracted from these loops ($V_c^{+,-} \approx \pm$ 3 V) indicates a similar value to the 2 nm film. The remnant polarization is $P_R \approx$ 5 μC·cm^{-2} and ≈ 25 μC·cm^{-2} for the 3 and 5 nm HZO, respectively, illustrating the expected increase of P_R with thickness.[127] PFM amplitude and phase loops were collected on the sample surface and Pt electrode for the 3 nm films and indicate similar coercive fields than obtained in the macroscopic measurements (Appendix 6). PFM phase maps were also collected on the bare surface of 3 nm films (Appendix 7). It is worth mentioning that Figure 5.11(a, b) was measured after training the junctions for a certain number of N_c cycles. Nevertheless, the number of cycles required to obtain sizable and stable *ER* and $P(V)$ loops reduces when increasing the thickness. In the case of 3 nm junctions, $N_c = 2{\cdot}10^3$ cyles are necessary and, for the 5 nm capacitor, only eight cycles can perfectly stabilize the *ER* in $R(V_w)$ loops. The effect of training on the leakage current in the three HZO thicknesses is demonstrated in Appendix 8.

The $R(V_w)$ loops collected on the pristine 3 and 5 nm HZO junctions are displayed in Figure 5.11(c, d) for pulses with τ_w = 300 μs. The 3 nm device exhibits an OFF/ON ratio of ≈ 143 % *ER* for V_{max} = 8 V. However, the resistance states are not stable, and there is a vertical resistance drift to higher values in sequential loops. For V_{max} = 5 V, the *ER* is only 100 %. Nevertheless, the resistance starts to change for $V_w \approx V_c$, indicated by the vertical dashed lines, suggesting the *ER* due to polarization reversal is being overshadowed. As the pristine junction has high leakage, any variation of *R* related to polarization reversal is minimized. In the pristine 5 nm HZO films, the resistance loop (Figure 5.11(d)) display an OFF/ON ratio of 150 % for V_{max} = 6 V and 190 % for V_{max} = 8 V. For such thick films, the $R(V_w)$ loops is already well developed in a fresh device.

After field-cycling the junction by the number of pulses indicated, the $R(V_w)$ loops are recorded. The 3 nm (Figure 5.11(e)) FTJ shows not only an increase in the absolute resistance of around one order magnitude but also displays a clear *ER* with an OFF/ON ratio of 145 % (V_{max} = 5 V) and 280 % (V_{max} = 8 V). In the 5 nm film, Figure 5.11(f) shows OFF/ON ratio of 130 % for V_{max} = 5 V and 200 % for V_{max} = 8 V after N_c = 8 cycles, which are similar to those recorded in the pristine state. The resistance starts to change for writing voltage amplitudes similar to the coercive voltage demonstrated in the $P(V)$ loops, strongly suggesting the *ER* is due to polarization switching of the ferroelectric.

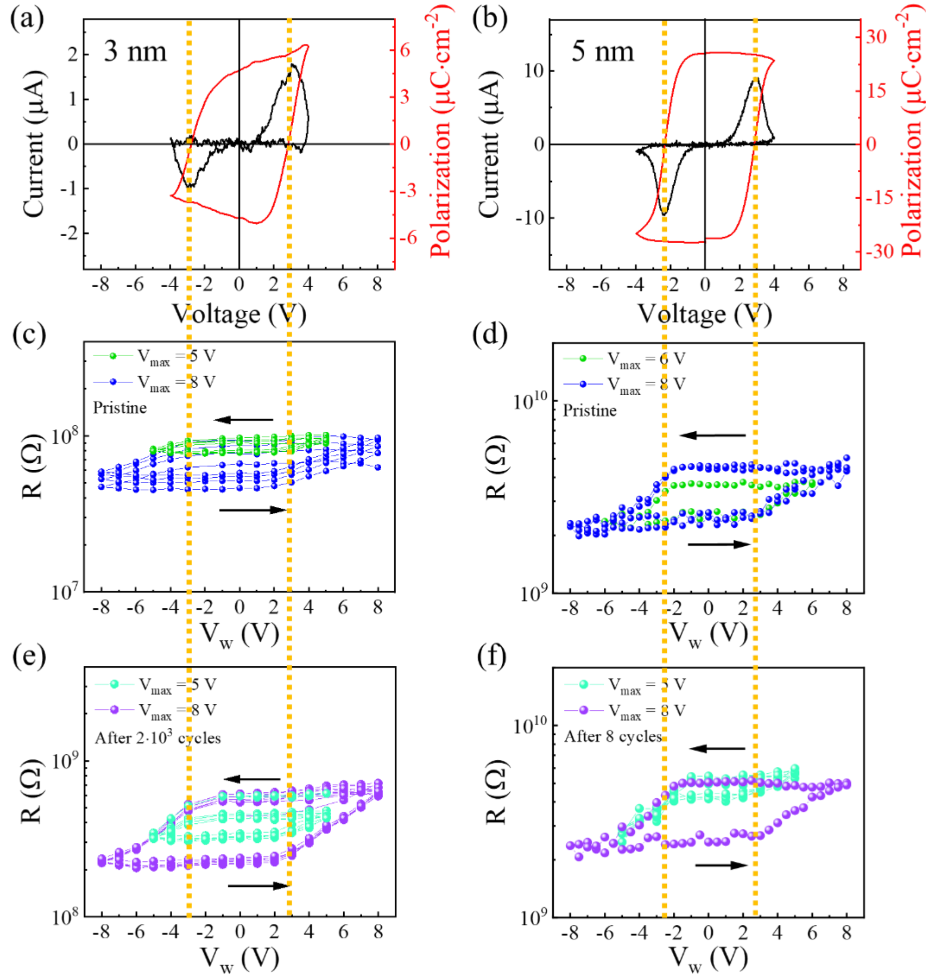

Figure 5. 11. I(V) and P(V) loops recorded at 5 kHz with PUND in HZO ferroelectric tunnel junction with (a) 3 and (b) 5 nm. These loops were obtained after training each junction with N_c = 2.10^3 and 8 cycles for 3 and 5 nm, respectively. Resistance dependence on V_w was obtained before cycling in HZO with (c) 3 and (d) 5 nm thickness. Resistance loops collected for (e) 3 and (f) 5 nm HZO capacitors after training. All $R(V_w)$ data was obtained by applying writing pulses with 300 µs duration.

Ultimately, these observations indicate that field-cycling is only relevant to reduce the leakage current and stabilize *ER* in HZO films thinner than 3 nm, probably reflecting that interfacial carrier accumulation and defects are seemingly more relevant in ultrathin films. Figure 5.12 summarizes the resistance of FTJ in their pristine states and after cycling as a function of their thickness. For pristine 2 and 3 nm devices, the resistance is ≈ $3 \cdot 10^5$ and ≈ $4 \cdot 10^7$ Ω, respectively, and, as mentioned, there is no significant *ER*. After cycling, the absolute resistance increases, and the electroresistance emerges. Importantly, Figure 5.12 emphasizes that cycled ultrathin 2 nm HZO junctions have a resistance value of about two orders of magnitude smaller than 5 nm HZO with a

similar *ER* response. This *ER* is obtained in ultrathin tunnel devices that also present OFF and ON resistance area product ≈ 160 Ω·cm^2 and 65 Ω·cm^2, respectively. These values are several orders of magnitude smaller than previously found in polycrystalline HZO ferroelectric tunnel junction measured at similar voltages (≈ 10^4 - 10^6 Ω·cm^2).[69,163,221,250,251] In epitaxial films, similar resistance area product values have been reported, although the conductance and *ER* have been partially assigned to ionic motion.[206,224] Remarkably, in 1 nm HZO films with 4:1 Hf:Zr ratio[116] directly grown on Si or in TiN/HZO (2.5 nm)/Pt[16] structures, where *ER* has been attributed to ferroelectric switching, similar small resistance values have been reported.

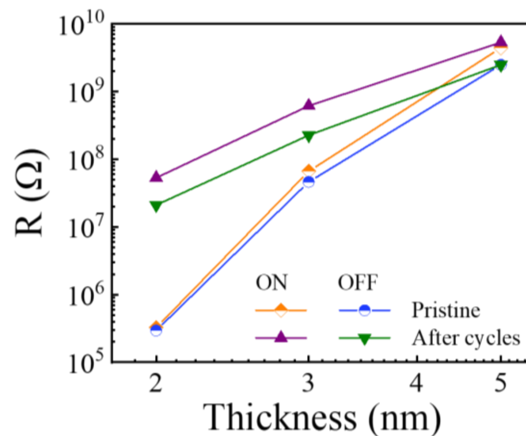

Figure 5. 12. ON and OFF states dependence on HZO thickness collected in pristine and cycled junctions as indicated.

5.6. Conclusion

The observation of ferroelectric and piezoelectric polarization loops and *ER* in ultrathin (2 nm) HZO large ferroelectric capacitor (≈ 300 μm^2) has been explored. The epitaxial layers of HZO grown on $GdScO_3$ are mainly constituted by the ferroelectric orthorhombic phase and display a well-behaved ferroelectric and piezoresponse. The close coincidence between the coercive fields extracted from *P(V)* and $R(V_w)$ loops as well as the PFM phase loops indicate the electroresistance originates from ferroelectric polarization reversal. Interestingly, the *ER* is obtained in ultrathin tunnel devices with a reduced resistance area product of ≈ 160 Ω·cm^2 and 65 Ω·cm^2 for OFF and ON resistance states, respectively. Memristive behavior was obtained by controlling the amplitude, duration, and number of voltage pulses applied to the ferroelectric. Also, HZO resistance's plasticity demonstrated the conductance could be modulated up to 60 % in spike-timing-dependent plasticity.

It has been found out that in the pristine state, these ferroelectric tunnel junctions display a substantial leakage current that precludes observation of polarization switching and electroresistance. Upon cycling, leakage is suppressed, the junction's resistance increases, *ER* is stabilized, and the switching peak corresponding to polarization reversal emerges in *I*(*V*) curves. Observation of long data retention with reduced resistance area products shall contribute to further exploiting HZO ultrathin junctions in neuromorphic devices. Moreover, when increasing the HZO thickness, the field-cycling is gradually less relevant and, for 5 nm, no longer required.

5.7. Appendix

Appendix 1.

Integrated θ-2θ scans obtained around χ (± 10º) in Figure 5.2(a, b, c) are combined in Figure A5.1. Data from all films display a clear presence of o-HZO (111) reflection at 2θ ≈ 30º and the absence of the m-HZO (002). It is possible to observe that as thinner the HZO film gets, the broader and lower in intensity the peak for o-HZO (111) reflection becomes.

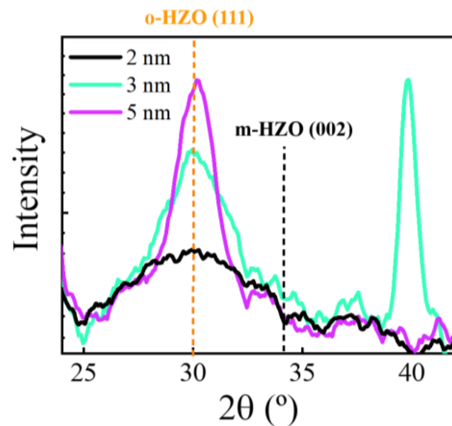

Figure A5. 1. Zoom around o-HZO (111) peak of the integrated scans in Figure 5.2 for 2, 3, and 5 nm sample. Data shows an absence of m-HZO peak, indicated by the black vertical dashed line. The narrow peak at ≈ 40º is associated with the Pt (111) reflection due to Pt electrodes.

Appendix 2.

Figure A5.2(a, b) shows 2θ scans and zoom, respectively, collected for HZO films with 2, 3, and 5 nm thick. The most prominent peaks are ascribed to the LSMO bottom electrode and GSO substrate, as indicated. Several peaks marked with * correspond to non-filtered W K_β, Cu K_β, and W K_β lines for increasing angles between 35 and 45º. The source light is not filtered to achieve the

best signal-to-noise ratio. The spectra are similar to Figure 5.2 and give rise to a similar conclusion. Data for all films display the presence of o-HZO (111) reflection and the absence of m-HZO (002).

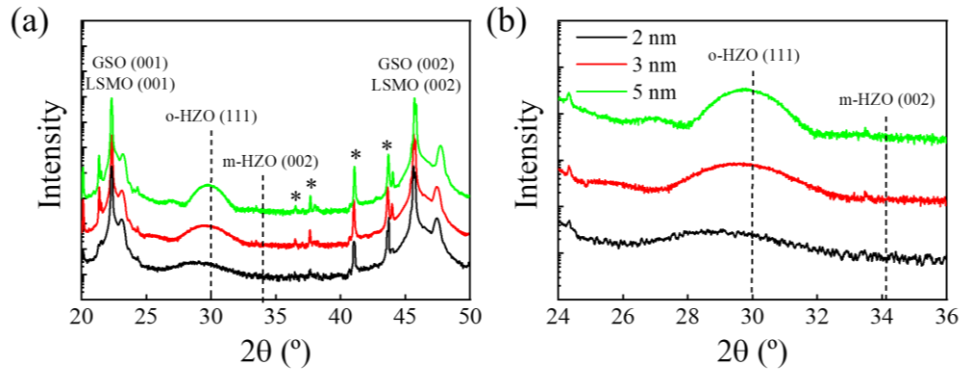

Figure A5. 2. XRD 2θ scan in HZO films with 2, 3 and 5 nm in (a) 20º < 2θ < 50º and (b) 24º < 2θ < 36º ranges.

Appendix 3.

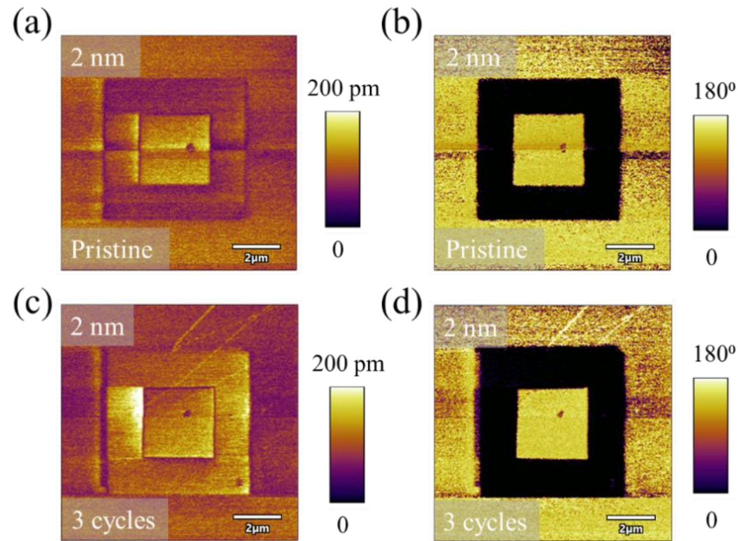

Figure A5. 3. PFM (a) amplitude and (b) phase images collected on HZO (2 nm) sample in the pristine state. After the region was field-cycled three times, the measurement was repeated by poling with ± 6 V and acquiring PFM (c) amplitude and (d) phase.

Figure A5.3(a, b) shows the amplitude and phase PFM maps, respectively, collected in the HZO (2 nm) sample for the pristine state. Huan Tan acquired images as part of her Ph.D. research project. In Figure A5.3(c, d), PFM amplitude and phase maps, respectively, performed after cycling the region three times (N_c = 3) previously to poling with V_w = ± 6 V. The absence of

significant difference among images indicates the absence of a critical wake-up effect related to the emergence of ferroelectricity.

Appendix 4.

By comparing the derivatives of $P(V)$ and $R(V_w)$ with the voltage shown respectively in Figures 5.7(b) and 5.7(d), it can be observed the maxima take place at the same position. This observation indicates a connection between the origin of *ER* and ferroelectric switching.

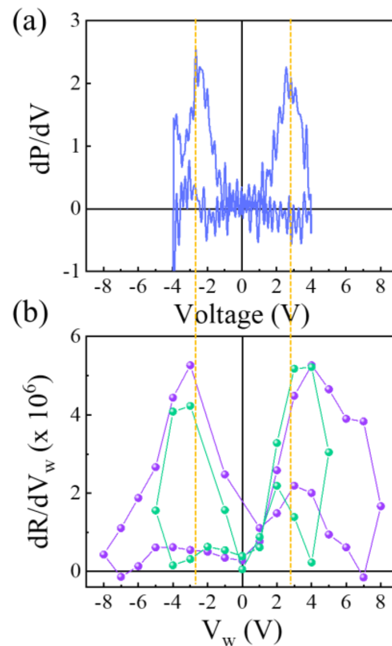

Figure A5. 4. (a) Derivative of polarization curve from Figure 5.7(b) with the voltage (dP/dV) and (b) Derivative of resistance loops with writing voltage amplitude (dR/dV_w) from Figure 5.7(d). Vertical dashed lines show coincidence of maxima peaks, suggesting a common origin.

Appendix 5.

A voltage triangular shaped pulse was applied to the 2 nm HZO sample following two sequences: - 1 → + 1V (Figure A5.5(a)) or + 1 → - 1 V (Figure A5.5(b). The current response was measured to disclose possible non-polarization-drive resistive switching mechanism, for example, ionic-related. Both Figure A5.5(c, d) demonstrate identical responses without hysteresis that rules out a dielectric breakdown and filamentary mechanism in the voltage range explored. For filamentary-mediated resistive switching, the sense of hysteresis is dependent on the direction of the voltage sweep, i.e., the initial polarity of the voltage waveform, which dictated the filament formation.[252]

Therefore, these data indicate that the conductance will only be changed if a writing voltage larger than the coercive field ($V_w > V_c$) is applied to the junction, causing polarization-driven switching.

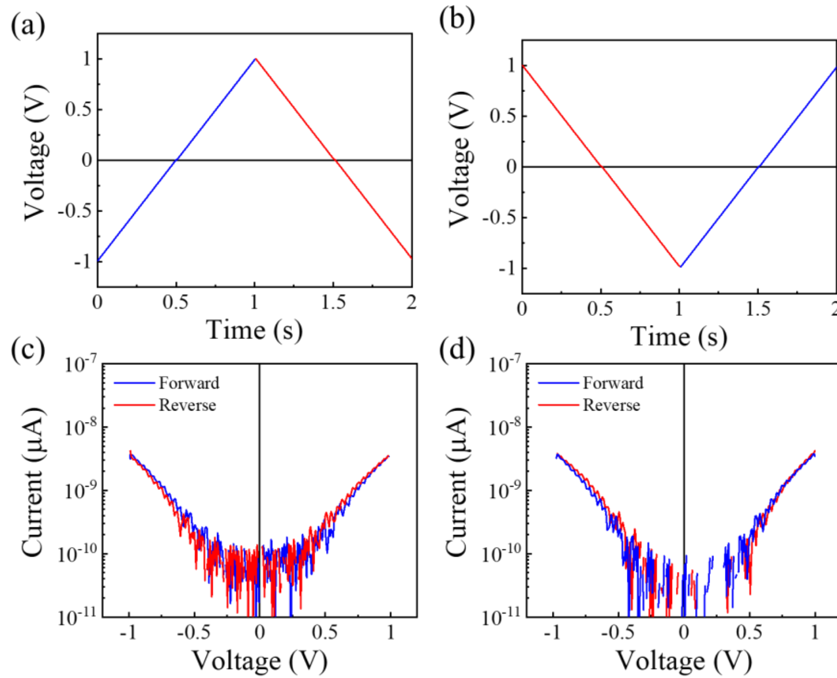

Figure A5. 5. Current-voltage curve for (a, c) negative-positive-negative voltage excursion and (b, d) for positive-negative-positive. Identical curves discard resistive switching mediated by filament formation mechanism, which would rise a hysteresis with different direction (counter-clockwise or clockwise)

Appendix 6.

Figure A5.6(a, b) shows the PFM amplitude and phase loops collected on the 3 nm sample surface and the Pt electrode, respectively. In both cases, the region measured was previously cycled N_c = 100 times. It can be observed that figure A5.6(b) obtained on the electrode displays higher Vc and less imprint. For comparison, the $I(V)$ and $P(V)$ loops recorded at 5 kHz using PUND on the electrode are also shown in Figure A5.6(c). The coercive field coincides with both data obtained on the electrode but not for the one collected on the surface as indicated by the vertical dashed lines. The different electrical contact between HZO/AFM platinum tip and the HZO/platinum top electrode accounts for this difference.

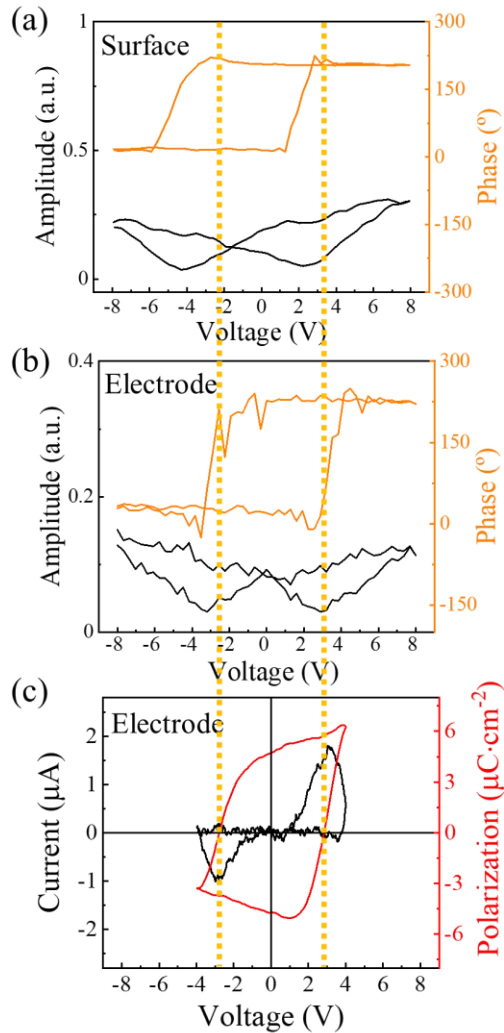

Figure A5. 6. PFM amplitude and phase loops collected on N_c = 100 cycled HZO (3 nm) sample on (a) film surface and on (b) platinum top electrode. (c) I(V) and P(V) loops recorded at 5 kHz with PUND in a previously $N_c = 10^4$ cycled electrode of the same sample.

Appendix 7.

Figure A5.7(a, b) shows the PFM amplitude and phase maps, respectively, obtained in the pristine 3 nm HZO sample. Huan Tan acquired images as part of her Ph.D. research project. Figure A5.7(c, d) displays the same maps but recorded after training the entire visible region with N_c = 3 cycles. The absence of significant difference between pristine and cycled images indicates the absence of a significant wake-up effect, as seen in the PFM data collected on the 2 nm HZO film.

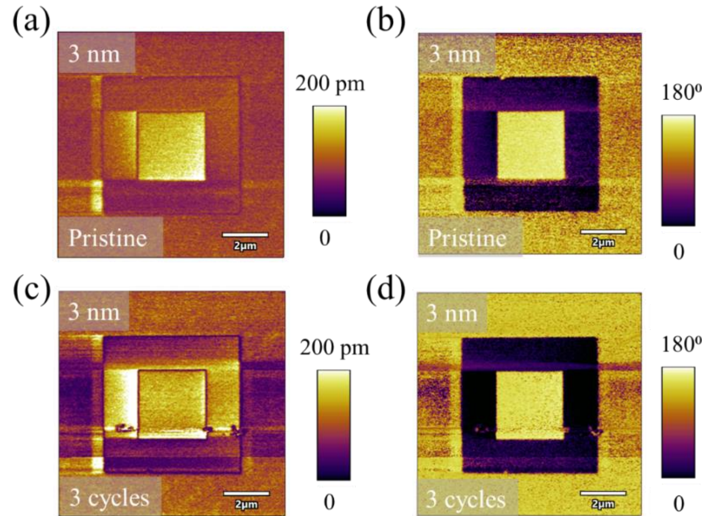

Figure A5. 7. PFM (a) amplitude and (b) phase images collected on HZO (3 nm) sample in the pristine state. After cycling three times, the (c) amplitude and (d) phase were measured again. No visible difference can be seen in the images.

Appendix 8.

The leakage current in a junction was measured by applying a bipolar triangular voltage pulse ($V(t)$) in a small voltage range ($-1 < V < +1$), and the current response was measure simultaneously. The current density (J) is obtained by dividing the $I(t)$ curve by the area of the capacitor ($\approx$ 300 μm^2) for pristine and cycled devices. Figure A5.8(a) shows, as expected, that the current density for the pristine state increases for thinner HZO films. The junctions with each thickness were field-trained by $N_c = 10^4$, $2 \cdot 10^{3,}$ and 8 cycles for the 2, 3, and 5 nm thick HZO films, respectively, and the resulting current density is then measured (Figure A5.8(b)). The film with 5 nm barely changes its J after cycling, but the thinner films decrease its conductance. The 2 nm film displays the most significant decrease in J, going from $\approx 10^6$ to $\approx 5 \cdot 10^3$ $\mu A \cdot cm^{-2}$ at 1 V. These results clearly illustrate the effect of field-training HZO tunnel junctions, especially in ultrathin film.

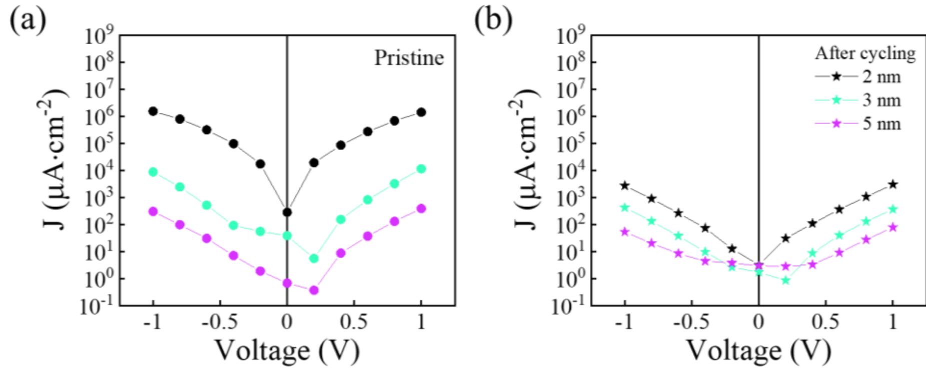

Figure A5. 8. Current density measured in (a) pristine and (b) cycled junction for 2, 3, and 5 nm thick HZO tunnel barriers.

Chapter 6. Conclusion

In this thesis, $Hf_{0.5}Zr_{0.5}O_2$ (HZO) ferroelectric tunnel junctions (FTJ) are investigated as resistive switching and memristive elements for application in the field of nonvolatile memory devices. Electrical characterization has demonstrated the coexistence of two mechanisms responsible for resistance change: electrostatic modulation of the barrier due to polarization reversal and ionic motion. The first one is reversible, robust, and allowed the stabilization of multistate as expected for a memristive element. The second one resembles a soft breakdown of dielectrics and generates large but irreversible changes in resistance.

The recent discovery made by Estandía et al.[53] that the relative abundance of the orthorhombic ferroelectric and monoclinic paraelectric phases can be engineered using an appropriate substrate allowed to grow samples with controlled microstructure. Resistance switching caused by modulation of the ferroelectric/electrode barrier properties resulted in significant electroresistance values. The detailed structural analysis allowed to correlate the second mechanism to forming conductive filaments within grain boundaries inside the HZO film. Oxygen vacancies electric-field-driven motion takes advantage of high mobility in grain boundaries between different HZO phases (o-/m-HZO) to create a conductive path, similarly to classical redox mechanisms in non-FE HfO_2-based ReRAMs. This observation suggests that electroresistance measured in HfO_2-based oxides must be carefully analyzed in order to identify correctly the mechanism that is originating it. In the attempt to suppress the ionic motion, an extra dielectric layer was introduced in the FTJ. Not only the non-FE resistive switching was indeed suppressed, increasing the voltage operation window for genuine ferroelectric switching, but also a dramatic increase in performance was observed. A lower device-to-device variability was obtained, and the endurance had a substantial increase. Two different dielectrics have been tested, and both presented similar results, suggesting they might act as oxygen vacancy getters that suppress the motion inside the ferroelectric. The drawback of these findings is that the device's resistance increased one order of magnitude with the extra dielectric, which might require a large reading voltage for memory applications.

Even though the detailed study of resistive switching mechanisms proposed in this thesis brings more enlightenment of the HZO-based device's properties, it becomes clear that the ferroelectric film's microstructure has a critical role. This result suggests that polycrystalline HZO capacitors, usually grown for CMOS compatible technology, should be carefully studied to ensure the polarization reversal indeed causes the electroresistance observed.

Besides, the observation of robust and reproducible potentiation/depression cycles and spike-timing-dependent plasticity (STDP) in ultrathin (2 nm) HZO tunnel junctions suggests this material has pivotal abilities to be implemented in systems that are inspired in biological synapses. It was shown that even though highly functional, the high electrical conductivity of the pristine cell requires electric field training to achieve stable remnant polarization and ferroelectric switching properties. The effect of training is consistent with redistribution of oxygen vacancies within the insulator matrix as early discussed by Max et al.,[82] Starschich et al.[136], and Pesic et al.[130]

This thesis's results establish ground information for applying HZO ferroelectric tunnel junction in future neuromorphic devices. This thesis focused on the study of individual FTJ and the understanding of its resistive switching properties. In order to implement them as elements in neuromorphic networks, the performance of an array of FTJ interconnected must be deeply understood.

Annex. Patterning of Ferroelectric Tunnel Junctions using Optical Lithography

As a part of the research project developed during this thesis, a collaboration with prof. Riccardo Bertacco from Polifab Institute at Politecnico di Milano (Italy) was proposed to pattern ferroelectric tunnel junctions with reduced area. His group has developed and optimized the processing in semiconductor wafers. My international stay had a duration of 1 and half months, and it was organized to allow adaptation of the standard semiconductor techniques to my ferroelectric films. The junctions to be pattern were $BaTiO_3$ (BTO) and $Hf_{0.5}Zr_{0.5}O_2$ (HZO) films with different thicknesses. The goal was to define ferroelectric tunnel junctions from 100 μm^2 to 4 μm^2 using optical lithography techniques associated with other microfabrication processes in a clean room environment.

Optical lithography is a widely used technique for the microfabrication of electronics. It is based on transferring a bidimensional image (pattern) to a radiation-sensitive polymeric material (photoresist). By following a sequence with several lithography steps, it is possible to define a three-dimension columnar device that combines the small junction area with the possibility of creating high-density microchips. The process detailed below has been developed and optimized by Dr. Gretta Radaelli and Dr. Marco Asa in Polifab.[55,253] The processes employed in Polifab have also counted with the training and supervision of Dr. Christian Rinaldi, Dr. Alessia Romeo, Dr. Claudio Somaschini, Lorenzo Livietti, and Dr. Daniella Petti. The lithography process was done in samples previously deposited in ICMAB with structures shown in Table A.1. The bottom electrode in all samples is a 20 nm thick layer of LSMO, and the ferroelectric BTO and HZO films have different thicknesses. In samples 8 and 9, a continuous 20 nm layer of platinum was deposited by sputtering in-situ after the ferroelectric deposition in the pulsed laser deposition (PLD). The substrates have a size of (10 x 10) mm^2 to allow homogeneous deposition of the photoresist, and, in total, 36 junctions can be patterned in each substrate.

The photolithography process contains several steps and combines deposition and etching techniques to define the final pattern. As an introduction to the technique, a one-step lithography

process is described in section I. The photoresist employed in Polifab is the image reversal positive photoresist AZ 5214E from Micro Chemicals© Gmbh. Image reversal photoresists can be either positive or negative, depending on the steps taken during the UV light exposition and a soft bake. In each step, either the positive or negative character of the resist AZ 5214E is used, and it will be indicated. The process to design FTJ requires three-step lithography, and they will be described in section II.

Sample	**Structure**
1	BTO (2 nm) / LSMO // LSAT (001)
2	BTO (3 nm) / LSMO // LSAT (001)
3	BTO (4 nm) / LSMO // LSAT (001)
4	BTO (5 nm) / LSMO // LSAT (001)
5	HZO (2.5 nm) / LSMO // STO (001)
6	HZO (3.6 nm) / LSMO // STO (001)
7	HZO (5.5 nm) / LSMO // STO (001)
8	Pt (20 nm) / BTO (4nm) / LSMO // STO (001)
9	Pt (20 nm) / HZO (4nm) / LSMO // STO (001)

Table A. 1. The initial structure of samples deposited in ICMAB and to be patterned using optical lithography in Polifab.

I. One-step lithography

The basic procedures of one-step optical lithography will be described in this section. In addition to the resist deposition, exposition, and development, deposition and etching techniques are also employed during the processing. For illustration, the resist represented is positive, which means that the regions exposed to UV light are removed in the development step. The first step is cleaning the sample surface, which contains organic and inorganic contamination that can affect the polymer's adherence after being exposed to air. Therefore, the sample is immersed in an ultrasonic bath (frequency = 40 Hz) of acetone and isopropanol for 3 minutes. Then, it is soft baked in a hot plate (T = 110ºC) for 90 seconds to desorb water. Then, samples are transferred to an oxygen plasma cleaning chamber (Plasma Asher – PVA TEPLA 200) and exposed for 3 minutes (P_{O2} = 1 mbar and 250 W) to remove any residual organic contamination at the surface. After, the wafer is ready for the beginning of the optical lithography (Figure A.1(a)).

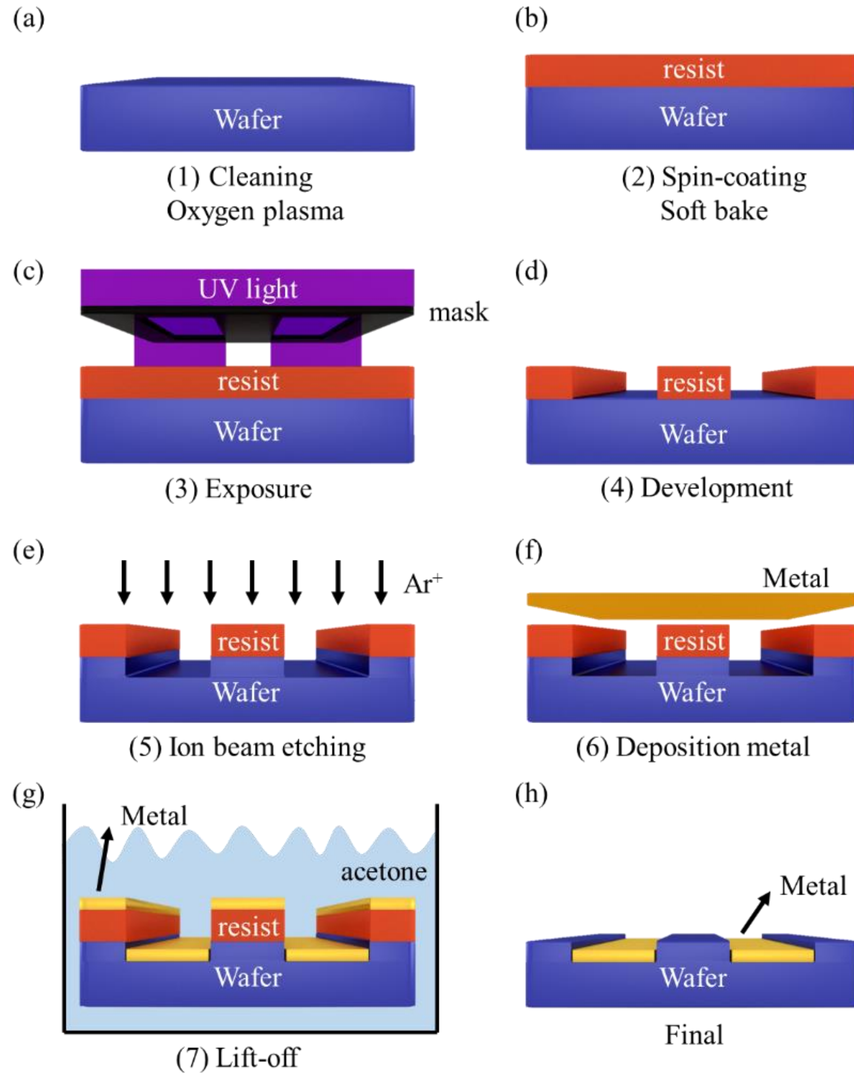

Figure A. 1. Sketch of basic procedures in optical lithography. (a) After surface cleaning, the wafer is ready for lithography. (b) The photoresist is deposited on the surface, and the sample is soft bake on a hot plate. (c) Exposition to UV light through a mask, which defines the pattern to be transferred. (d) The sample is immersed in solvent for removal of regions that were exposed to UV light. (e) Argon ion beam etching removes material from regions unprotected by the photoresist. (f) A layer of metal is deposited on the sample, covering the regions unprotected. (g) The sample is immersed in acetone for lift-off, i.e., complete removal of photoresist. (h) Final patterned sample.

Figure A.1(b) sketches the photoresist layer created on the sample surface after spin coating. This technique consists of the dispense of some photoresist drops on a wafer which starts to rotate at high speed (Spin Coater - Karl Süss RC8). The spin coater in Polifab imposes a rotation of 6000 rpm for 60 seconds to spreads the resist, creating a thick layer. Note that the sample substrates are chosen to be (10x10) mm^2 to ensure a homogeneous resist thickness (≈ 1.6 µm). Nevertheless, at

the corners, the resist still has a slighter thicker layer (≈ 1.8 μm) measured by a profilometer. For this reason, these regions will not contain junctions but only alignment marks for adjustment of lithography patterns. The pattern shown in Figure A.2 is included in the mask pattern from Figure A.1(c). Next, the sample is soft baked in a hot plate at a fixed temperature and time to evaporates the solvent left in the polymer.

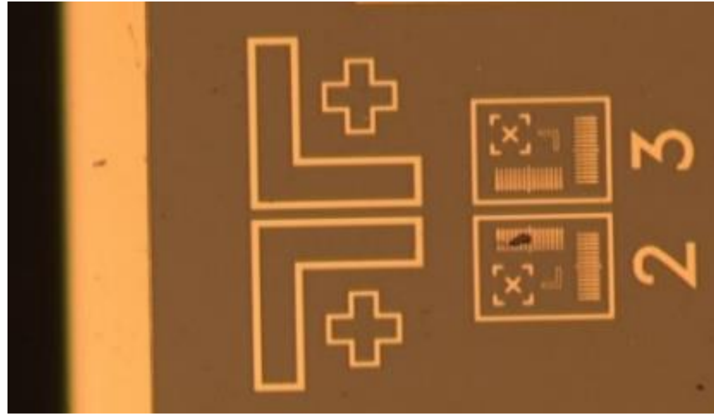

Figure A. 2. Alignment marks are used to align the first lithography pattern with possible sequential steps. They are located at the edges of the substrate. Image obtained after photoresist was developed. Bright color corresponds to the color of the substrate, and dark color is the color of the resist that was not removed.

When the sample is cooled down after the soft bake, it is exposed to UV radiation (Figure A.1(c)) that modifies the resist chemical properties, increasing its solubility in the case of the positive resist. In Polifab, the exposition can be done using a chromium mask or a laser writer.

a) *Chromium mask*: the mask is a glass crystal that contains an image defined by a layer of Cr that absorbs the radiation coming from a UV source and protects the underlying resist. A sketch is shown in Figure A.1(c). The pattern of the Cr mask is directly transferred to the resist. The mask is positioned near the sample in the Karl Suss MA56 mask aligner. The set (mask + sample) is exposed to UV radiation originated from the Hg-I line (365 nm) of a mercury lamp that provides 10 mW/cm^2 power density. Calibration of exposing time indicates that 36 seconds to UV light in this equipment is enough to define (2 x 2) μm^2 junctions.
b) Laser writer: this machine (Maskless Aligner - Heidelberg MLA100) is a direct writing tool that draws the photoresist's desired pattern using a light beam. The light source is a high-power LED with a wavelength of 365 nm.

After the exposition, the sample is immersed in the solvent AZ100 DEV from MicroChemicals© GmbH for 60 seconds (Figure A.1(d)) to remove the soluble/exposed area. The maximum resolution that can be transferred to the photoresist, also called a critical dimension (CD), is limited by the diffraction limit of the light, the mask's quality, and the photoresist's properties. In Polifab, the resolution obtained with the photoresist AZ 1215E with both machines is in the order of 1 µm.

In some cases, it is desirable to remove material from the sample that is unprotected by the photoresist. In section II, this process will be used twice. For this purpose, an ion beam etching is performed (Sputtering and Ion Beam Etching System - Kenosistec VS80) using Ar^+ ions, represented in Figure A.1(e). The sample is transferred to the machine chamber, where a rich argon atmosphere is ensured (Ar flux = 7 sccm). A filament (cathode) located at the top of the chamber emits electrons through the thermionic effect and accelerated towards the electrically biased sample holder (anode). The electrons ionize the Ar atoms, giving rise to Ar+ ions and free electrons, contributing to ionizing more Ar atoms and sustaining the plasma. The Ar^+ are then accelerated towards the sample, breaking the bonds between atoms and ejecting material. The voltage between the cathode and anode is set as 40 V, and the emission current from the filament is ≈ 50 mA. The etching time is calibrated using a flag, a platinum layer deposited on a glass substrate. The flag is exposed to etching for some time and is then removed from the chamber. The surface's conductivity is tested with a multimeter and, if it is very low, indicates that the metallic layer was entirely removed. However, if the conductivity is high, the sample is put back into the chamber and exposed to more etching time. By repeating this process several times for short periods of etching time, the etching rate can be calculated considering the total time necessary to remove the platinum. Note that, in a sample partially covered by photoresist, the etching step only reduces the resist's thickness, and therefore the film beneath is protected.

In general, after the ion beam etching, a metal is deposited to fill the gaps from Figure A.1(f). The deposition can be done with any technique, such as sputtering, evaporation, or even PLD. Finally, the remaining resist can be removed entirely from the sample through a lift-off process, which is obtained by immersing the sample in acetone until fully detached (Figure A.1(g)). The AZ 5414E photoresists do not require long lift-off times (≈ 2 minutes). Nevertheless, if a thick layer of metal is above the resist layer, longer times can be necessary (≈ hours). The final structure is then obtained, and it is sketched in Figure A.1(h).

II. Three-step lithography and patterning FTJ

The one-step lithography is often used for simple top electrode pattering in tunnel junctions. Nevertheless, devices with an area smaller than 100 μm^2 require a sequence of steps since it must ensure the junction and a larger area to allow the electrical contact from needles or wire bonding. This section will describe the 3-step optical lithography used to pattern ferroelectric tunnel junctions in detail.

a. Step 1 – MESA patterning

The base structure of the top electrode is defined in this step, which is called MESA. Here, the platinum top electrode layer is deposited continuously in all samples' surfaces, and each tunnel junction is insulated from the other.

As described in Figure A.1(a), the samples are cleaned with an ultrasonic bath in acetone and isopropanol and an oxygen plasma cleaner to remove the surface's organic contamination. In Table A.1, samples 1 – 7 were deposited in ICMAB without a metallic layer right above the ferroelectric film. For this reason, the samples were immediately transferred to a sputtering chamber (Sputtering System - AJA ATC Orion 8) to deposit a continuous 20 nm thick platinum layer, as sketched in Figure A.3(a). A flag, i.e., a platinum film deposited directly on a glass substrate, is deposited simultaneously with the films, which will be used later to calibrate the etching time in section b. The platinum deposition parameters are: power = 12 W and work pressure = 5 mtorr (Argon atmosphere). The deposition rate was calibrated previously with XRR measurements as detailed in the Experimental Methods chapter. At this point, samples from 1 to 9 have the same structure platinum/ferroelectric/LSMO/substrate, and the lithography processing is the same for all. However, for simplicity, the description below will be given for one sample.

Next, the photoresist is deposited on the platinum's surface by spin coating using the same parameters indicated in Figure A.1(b) and soft bake for 90 seconds at 110 ℃ in a hot plate without cover. The sample is then exposed to 35 seconds of radiation (Karl Süss MA6/BA8, dose = 125 mJ/cm^2) through Mask 1 (Figure A.3(b)). The square-like drawings of Mask 2 are regions protected from radiation so, after the ≈ 2 minutes of development in solvent AZ 726MIF, these parts of the resist remaining on the surface, as indicated in Figure A.3(c).

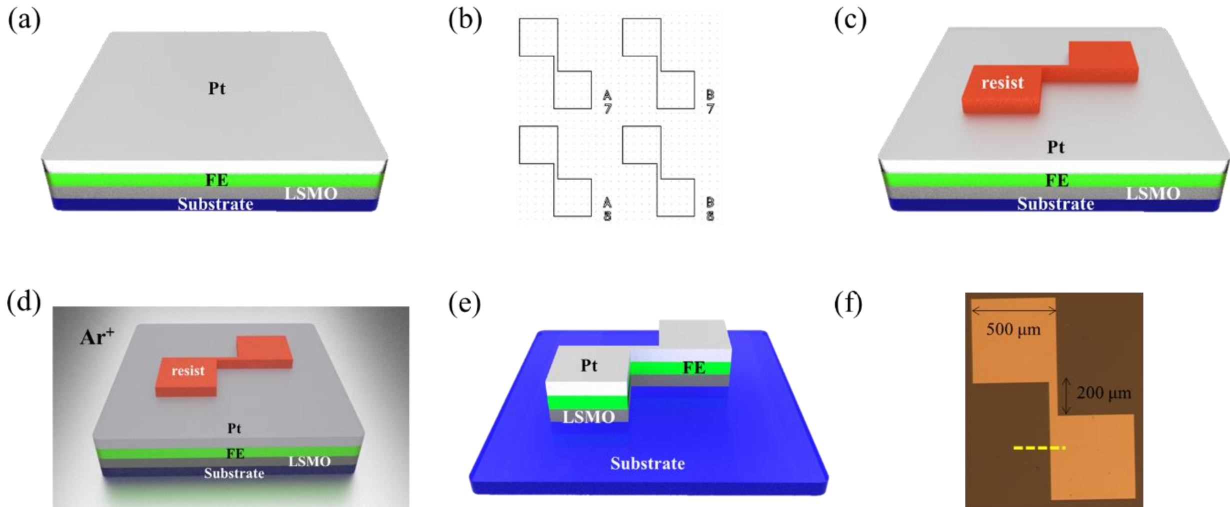

Figure A. 3. MESA structure patterning. (a) Platinum 20 nm thick continuous layer deposition in samples 1 – 7 by sputtering. (b) Top view of Mask 1 image. (c) After photoresist deposition, the sample was exposed to radiation using Mask 1, and resist was developed. (d) Argon ion beam etching of sample for removal of material not protected by resist. (e) The final structure was obtained after resist lift-off. (f) Top view optical microscopy from MESA structure after step (e).

Then, the sample was exposed to argon ion beam etching (Figure A.3(d)) defines the MESA structure. The regions not protected for the resist are removed. The etching time was calculated using the etching rates listed in the equipment manual (Sputtering and Ion Beam Etching System - Kenosistec VS80). Here a larger etching time than necessary is not crucial since it only leads to erosion of the insulating substrate. However, a short etching leaves the bottom electrode part, which can cause a short circuit of the junctions. The latter can be easily recognized with a substrate electrical measurement. If there is a short circuit, platinum or LSMO films remain on the surface, and the sample must be etched for more time. After the extra etching time, the sample is removed from the chamber, and the electrical measurement is performed again. This procedure is made until there is no short circuit on the surface, indicating the full removal of the LSMO electrode. Then, the resist can be removed by acetone lift-off, and the final structure is shown in Figure A.3(e). A top view optical microscopy image of the samples is exhibited in Figure A.3(f), where the squares' dimensions are also indicated. The bright area indicates where Pt/ferroelectric/LSMO layers are located, and the dark area only contains the substrate. A profilometer measurement at the yellow horizontal line in Figure A.3(f) indicates the step's height as ≈ 60 nm.

b. Pillar / junction area definition

Having the MESA structure defined in section a, the junction area can be defined as a pillar that contains the ferroelectric layer and the top platinum electrode. Previously to the deposition of a new layer of the photoresist in Figure A.4(a), some primer drops are spin-coated in the surface (speed = 6000 rpm, time = 60 seconds) to ensure adherence to the resist. Then, the primer is soft-baked at 120 ºC for 90 seconds on the hot plate without cover. Only when the sample is cooled down, the resist is spin-coated and soft bake. In this step, the image reversal of the resist will be used.

The sample is brought to the laser writer machine (Maskless Aligner – Heidelberg MLA100), where the laser will irradiate (dose = 30 mJ/cm^2) the regions of the sample inside the drawing of Mask 2 (Figure A.4(a)). The two big squares will ensure electrical access to the bottom LSMO electrode, whereas the small square in between them is the ferroelectric junction pillar. The mask contains pillars with areas varying from 100 to 4 μm^2. The region irradiated by UV is now more soluble than the surroundings, and a development step can easily remove it. Nevertheless, we want this resist area to remain on the surface. Therefore, the resist is inverted (image reversal) by the following process:

a. Soft bake sample at 115 ºC for 90 seconds on a hot plate without cover
b. Expose sample to flood radiation without any mask for 80 seconds and dose = 120 mJ/cm^2 (Karl Süss MA6/BA8).
c. Sample immersion in AZ 726MIF solvent for 42 seconds.

Now, the area exposed by the laser writer remains after the development, and the rest is removed. The result of this process is sketched in Figure A.4(b). As one can see, the small red pillar of resist between the two squares must be well adhered to the platinum surface; otherwise, the FTJ will be damaged. A second argon ion beam etching is performed (Figure A.4(c)) to remove the platinum surrounding the small red pillar and insulate the LSMO bottom electrode's access and the platinum top electrode. Note that the flag deposited with the samples described in 2.1 is used as a reference for this step's etching time. The flag is exposed to etching with the samples, and when the flag indicates full removal of platinum, the etching stops since the platinum layer in the flag, and the sample has the same thickness. Electrical measurements confirmed the complete removal of platinum on the surface of the flag. An excessive etching leads to erosion of the bottom layer and

consequent disconnection of the bottom electrode from the junction. Meanwhile, a short etching leaves a part of the top layer, which short-circuits the junctions. The sample structure after the etching is represented in Figure A.4(d).

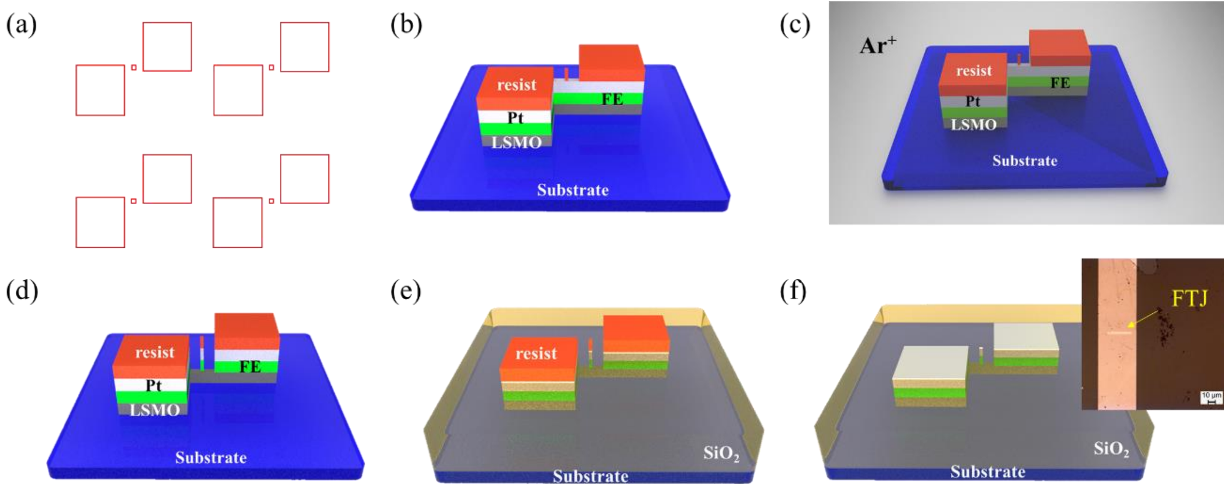

Figure A. 4. FTJ patterning. (a) Top view image of Mask 2. (b) Resist deposition and image reversal steps to ensure region exposed to UV radiation remains on the sample. (c) Argon ion beam etching to remove platinum layer not covered by the resist. (d) Sample structure after etching. (e) Deposition of SiO_2 layer to sustain FTJ pillar and insulate the top and bottom electrodes electrically. (f) Sample after resist lift-off in acetone. Inset: Top view optical microscopy from the sample at this stage indicating where the FTJ pillar is located.

The FTJ pillar is unstable mechanically, and a supporting layer of SiO_2 is deposited. The thick SiO_2 layer (≈ 30 nm) is deposited by e-beam evaporation (Evatec BAK 640) and also electrically insulates top and bottom electrodes (Figure A.4(e)). Next, the samples are left in acetone overnight for a slow lift-off step. Figure A.4(f) shows the final result of this step, and the inset shows an example of the junction. The brighter area indicated in yellow shows where the pillar Pt/ferroelectric/LSMO is located, and the SiO_2 layer covers the surrounding areas. Optical microscopy images of all 36 junctions in each sample were taken to guarantee the lithography was performed correctly and measurement of the junction's final area (brighter area of the inset in Figure A.4(f)).

c. Contact deposition

The last step of lithography is the definition of the top layer of metal that will allow needles to contact both electrodes. For this, another primer layer primer is spin-coated over the SiO_2 film and soft bake for 90 seconds at 120 ºC. Then, the resist is deposited and soft baked at 110 ºC for 90

seconds on a hot plate without cover. The inset of Figure A.5(a) shows Mask 3. The squares region is where the resist is exposed to UV light (dose = 230 mJ/cm^2, Maskless Aligner Heidelberg MLA100). After the exposition, the sample is developed for 60 seconds in AZ 726MIF solvent. Figure A.5(a) shows the resist covering all the samples except the area where metal will be deposited. Previously to metal deposition, the sample is exposed to oxygen plasma for 3 minutes (Plasma Asher – PVA TEPLA 200) to remove any residual resist inside the gaps.

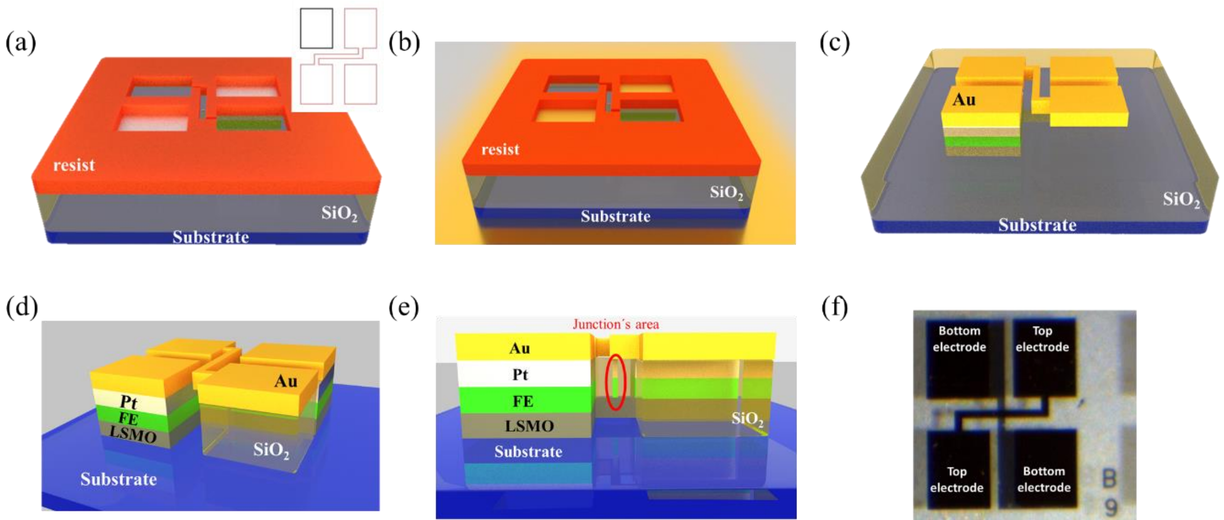

Figure A. 5. Contact deposition. (a) The photoresist was deposited, and Mask 3 (inset) was drawn with the laser writer. The sample was developed, and the region exposed to UV is removed. (b) Deposition of chromium and gold, respectively, fills the gaps in the resist and pattern macroscopic electrical contacts. (d) Side view of the sample indicating support of Au/Cr layer by SiO_2 film. (e) Side view showing the location of FTJ and cross-section of the sample. (f) Top view optical microscopy of junction B9 illustrating where access to top and bottom electrodes are located.

A 48 nm layer of chromium followed by a 27 nm layer of gold is deposited by sputtering (magnetron sputtering system – Leybold LH Z400), indicated in Figure A.5(b). Finally, the last layer of resist is removed by lift-off in acetone resulting in the structure sketched in Figure A.5(c). The side view of the final structure is shown in Figure A.5(d, e), in which it is possible to see that the SiO_2 layer sustains the Au/Cr layer. The junction pillar is embedded in the SiO_2 matrix, avoiding short circuits and creating a current path through the ferroelectric film. A top view optical microscopy image from one junction is exhibited in Figure A.5(f), where the accesses to the bottom and top electrode are indicated. Each junction receives an identification label located right beside the contacts (B9 in Figure A.5(f)).

III. FTJ characterization

The characterization of ferroelectric tunnel junctions patterned with the process detailed in section II is divided into structural and electrical. The first one was performed at the stage shown in Figure A. 4(f) during the lithography process when the junction area could be seen at the sample surface through optical microscopy. The second is achieved after the lithography is completed and explores the conductivity of the films.

a. Structural / Optical microscopy

Samples 1 to 9 have been patterned using the steps detailed in section II. Each junction has been photographed with optical microscopy to measure the FTJ area, as shown in the inset in Figure A.4(f). In some junctions, the SiO_2 did not electrically insulate correctly top and bottom electrodes due to problems of adhesion of the film. The optical microscopy images and an estimation of the number of junctions that have the FTJ pillar well defined and insulated are shown in Table A.2. Note that each sample contains 36 tunnel junctions. Samples 8 and 9 have a reduced number of correctly patterned junctions because the SiO_2 layer (Figure A.4(c)) did not adhere to the surface appropriately and detached during the last step (section c), resulting in short-circuited junctions.

Sample	Structure	Correctly patterned
1	BTO (2 nm) / LSMO // LSAT (001)	30 / 36
2	BTO (3 nm) / LSMO // LSAT (001)	30 / 36
3	BTO (4 nm) / LSMO // LSAT (001)	30 / 36
4	BTO (5 nm) / LSMO // LSAT (001)	29 / 36
5	HZO (2 nm) / LSMO // STO (001)	19 / 36
6	HZO (3 nm) / LSMO // STO (001)	30 / 36
7	HZO (6 nm) / LSMO // STO (001)	27 / 36
8	Pt (20 nm) / BTO (4 nm) / LSMO // STO (001)	5 / 36
9	Pt (20 nm) / HZO (5 nm) / LSMO // STO (001)	23 / 36

Table A. 2. The number of junctions in each sample that were successfully patterned using the methodology described in section II.

Figure A.6 shows a comparison between a device correctly patterned (L2) and one that failed (G1) in the BTO (3 nm) sample. Junction L2 in Figure A.6(a) shows a well-defined area which is indicated by the arrow. The surrounding is covered by the SiO_2 layer, which insulates the LSMO

bottom electrode from the macroscopic gold contact deposited in the last step of lithography. In opposition, Figure A.6(b) exhibits one junction that the SiO_2 layer around the pillar detached from the surface giving direct access from the top electrode to the bottom.

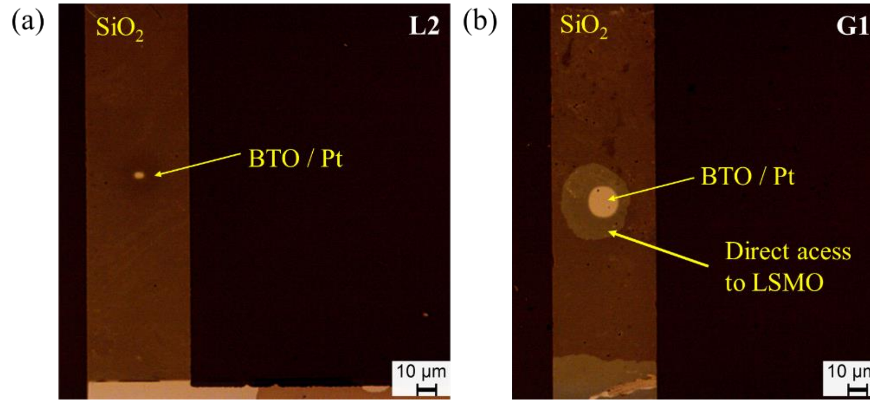

Figure A. 6. Optical microscopy image of two junctions from sample BTO (3nm). (a) Junction L2 has the SiO_2 well adhered, and the only path where the current will flow is through the pillar. (b) On the other hand, in junction G1, the SiO_2 around the pillar was not well adhered to the surface, and it was removed during the lift-off process. When a top electrode is deposited, a short circuit between the top Au electrode and the LSMO area is exposed.

b. Electrical characterization

Next, the junctions that were correctly patterned are electrically characterized in ICMAB. In order to do that, the bottom electrode is grounded, and the top is biased, as Figure A.7(a) sketches. The conductivity of each junction is explored by measuring the current response while applying a bipolar triangular voltage pulse, $V(t)$, with range [- 1; + 1] V and frequency 1 Hz (Figure A.7(b)). Since each FTJ in the same sample has a different area, the current density is calculated and used to compare their conductivity with values obtained in the literature for similar devices. Therefore, the current density is calculated by dividing the current measured at V_{read} = 0.5 V by the area of the junction measured with the optical microscopy images mentioned in 3.1.

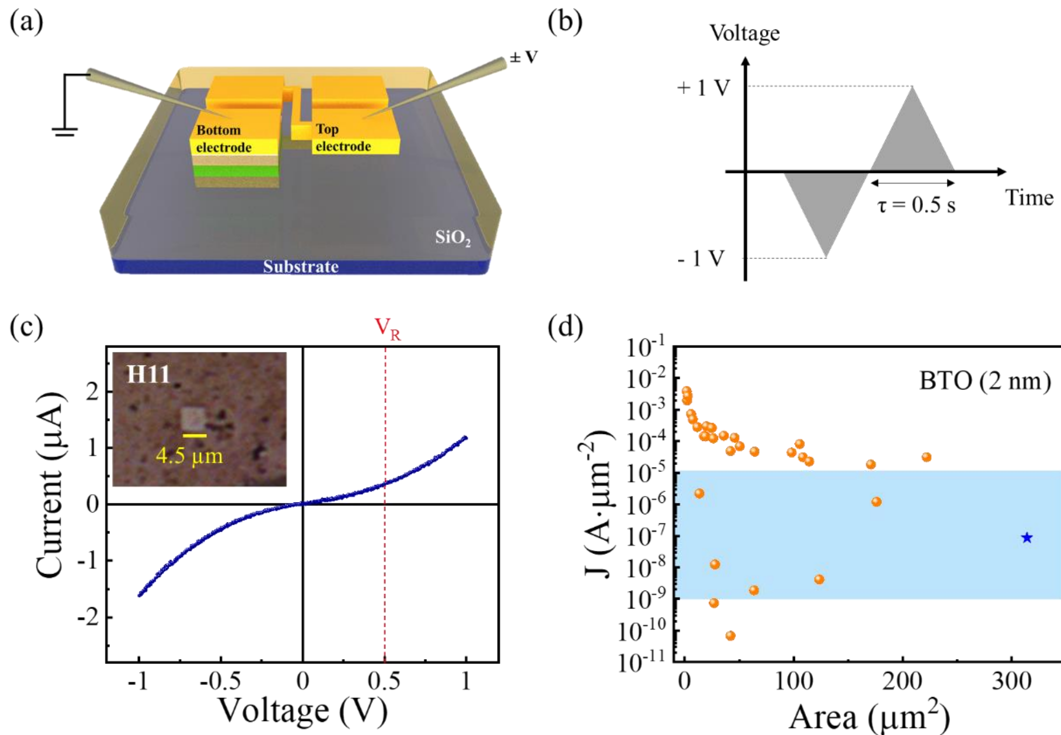

Figure A. 7. (a) Sketch of the electrical arrangement used to characterize the ferroelectric tunnel junctions patterned electrically. (b) Voltage pulse applied at the top electrode in order to measure the conductivity of devices. (c) Example of I(V) curve collected while pulse in (b) is applied to junction H11 from sample 1. Vertical dashed line indicates reading voltage for calculation of current density. Inset: the brightest spot in the center is the junction square pillar with side = 4.5 µm. (d) Dependence on current density on the area from all junctions in sample 1. The blue star represents current density measured in the sample with top electrode patterned with a shadow mask, as described in the Experimental Methods chapter. Blue area indicates a range of current densities observed in FTJ with a similar structure published in the literature.

Figure A.7(c) displays an example of the $I(V)$ curve from junction H11 in sample 1 (2 nm BTO). In the inset, an optical microscopy image from the junction is shown. The area is well defined (≈ 20.2 µm^2), and the SiO_2 layer adheres to the surface. The current is measured at V_{read} = 0.5 V, and the current density (J) is calculated. This measurement was performed for all FTJ in the sample and the J values extracted are plotted in Figure A.7(d). As a matter of comparison, the current density from a Pt/BTO (2 nm)/LSMO junction patterned with the standard method of shadow mask described in the Experimental Chapter is included (blue star, $J \approx 10^{-7}$ A·µm^2). It is possible to see that for the reduced areas, J reaches ≈ 10^{-2} A·µm^2 and, as the area increase, this value reduces to ≈ 10^{-5} - 10^{-6}A·µm^2 for area =150 µm^2. However, close to zero, there is an exponential-like decay of the current density, indicating a strong area dependence, which is not expected from tunnel

junctions. This observation suggests that some structural leakage effect might contribute to the large conductivity observed. A reduced number of junctions deviate from the trend and display a lower current density. Radaelli et al.[55] observed current densities in the order of 10^{-9} A·μm^2 in Pt/BTO (2 nm)/LSMO tunnel devices patterned with a similar optical lithography process. In the study of Co/BTO (2 nm)/LSMO, Chanthbouala et al.[173] have shown current density devices ranging from 10^{-5} to 10^{-7} A·μm^{2,} and Kim et al.[54] found J ranging from 10^{-10} to 10^{-9} A·μm^2. Therefore, the blue region indicated in Figure A.7(d) indicates the range of current densities observed previously in FTJ with 2 nm BTO films.

- BTO tunnel junctions

The electrical characterization of the other samples composed of BTO films is further explored in this section. The current density measured in all BTO samples is shown in Figure A.8.

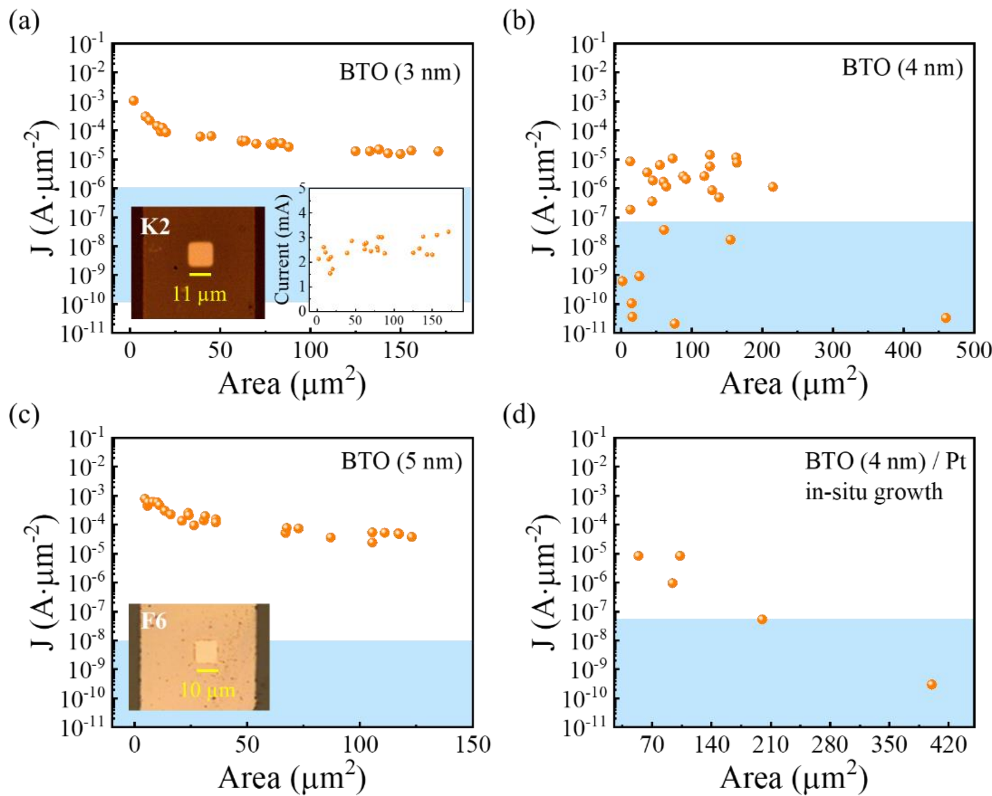

Figure A. 8. Current density dependence on the area for ferroelectric tunnel junction with (a) 3 nm (sample 2), (b) 4 nm (sample 3), (c) 5 nm (sample 4) thick BTO films, and (d) 4 nm BTO covered by Pt grown in situ (sample 8) patterned with optical lithography. Inset in (a) shows optical microscopy image for junction K2 and current dependence on the area for the BTO (3 nm) sample. Inset in (c) shows an optical microscopy image of junction F6.

In samples 2 and 4 (3 nm and 5 nm BTO, respectively), the exponential-like trend for small areas, as observed in Figure A.7(d), is visible (Figure A.8(a, c)). Also, *J*'s absolute value in these samples varies from ≈ 10^{-3} to 10^{-5} A·µm^{-2}, which suggests the FTJ conductivity does not scale with the ferroelectric thickness as expected for tunneling behavior.[72,74] The blue area, indicating the values obtained in studies with similar capacitors, does not contain any junction. The insets in Figure A.8(a, b) show optical microscopy images from junctions K2 and F6, respectively, in which the access to the junction is well patterned, and there is no detachment of the SiO_2 around the pillar. Nevertheless, the electrical results suggest a large leakage that can be associated with short-circuit cause during the lithography patterning, even though optical microscopy images do not indicate failures. The inset in Figure A.8(a) shows the current instead of the current density for junctions in the BTO (3 nm sample). If short-circuited, the current flowing should be only dictated by the electrodes' resistance ($R = V/I$) and, considering their low resistivity, the expected current is high. The inset shows current in the order of 1 – 3 mA independently on the electrode area, which is consistent with the short-circuit hypothesis.

Structure	J (A·µm^{-2})	Contact area (µm^2)	Reference
Pt / BTO (2 nm) / LSMO	10^{-9}	25	[55]
Pt / BTO (4 nm) / LSMO	10^{-11}	60	[55]
Pt / BTO (4 nm) / LSMO	10^{-8}	250	[56]
Ti / BTO (3.2 nm) / SRO	10^{-10}	0.2	[210]
Co / BTO (2 nm) / LSMO	10^{-5} - 10^{-7}	0.03 – 0.4	[173]
Co / BTO (2 nm) / LSMO	10^{-9} - 10^{-10}	20	[54]
Pt / BTO (2.8 nm) / Nb:STO	10^{-6} -10^{-8}	700	[67]
Cr / BTO (3 nm) / LSMO	10^{-10} -10^{-11}	0.5	[254]
LCMO / BTO (3 nm) / LSMO	10^{-8}	225	[255]

Table A. 3. Current density values extracted from BTO tunnel junctions in the indicated references.

There is no clear trend in the case of 4 nm BTO, yet the collected *J* from these junctions has a large scattering of values going from ≈ 10^{-11} to 10^{-5} A·µm^{-2}. Several junctions have current density nearer to values observed in the literature. In the case of Figure A.8(d), only two junctions have *J* close to the ones from previous studies. Qian et al. [56] measured current densities of ≈ 10^{-8} A·µm^{-2} in Pt/BTO (4 nm)/LSMO capacitors patterned with standard shadow mask top electrodes (area 250

μm^2). In tunnel junctions patterned with the optical lithography process described in section II, Radaelli et al.[55] found $J \approx 10^{-11}$ A·μm^{-2} in Pt/BTO (4 nm)/LSMO for devices with 60 μm^2. Table A.3 shows the current densities measured in the ferroelectric tunnel junction composed by BTO layers used to compare and determine the blue regions indicated in Figures A.7(d) and A.8.

Tunnel junctions typically display a sigmoidal and asymmetric *I(V)* curve, which indicates a barrier height between ferroelectric/electrode that modulates tunneling electrons' conductance.[73,74] Figure A.9 shows *I(V)* curves collected in junctions from sample 1 (2 nm BTO), and two distinct behaviors can be observed. Figure A.9(a) display the current response in 4 junctions with area varying from 3 to 105 μm^2. The curves show a clear ohmic character even though the current measured in junction I10 is double the one from J10. Note that the scale is miliampere and the calculated resistance at V_R = 0.5 V indicates R(J10) = 56 Ω and R(G10) = 200 Ω. Radaelli et al.[55,253] found the resistance in similar BTO (2 nm) junctions as ≈ 10^6 Ω. Therefore, the junctions that display ohmic behavior with extremely low resistance will not be considered further into the electrical characterization analysis. The electrical characterization indicates that these junctions are short-circuited, and the observed resistance is related to the LSMO or Pt layers. All junctions in Sample 8 are ohmic.

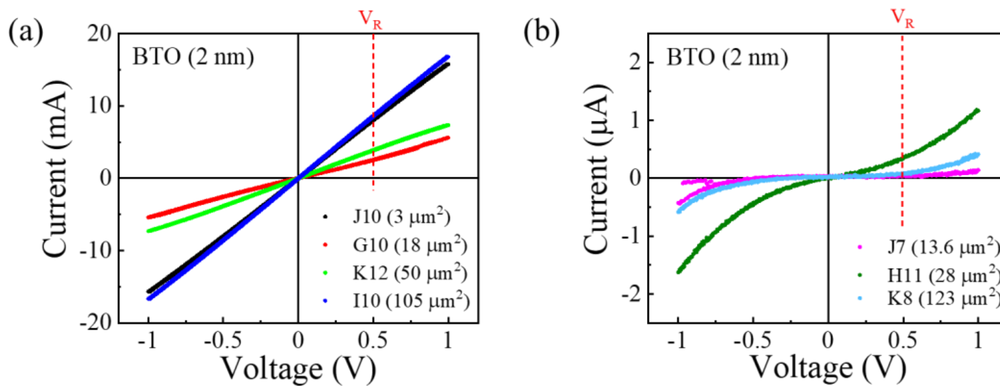

Figure A. 9. Current-voltage curves collected in the indicated junctions from sample 1 (2 nm BTO). Junctions show (a) ohmic conduction or (b) sigmoidal I(V) typical from tunnel junctions.

On the other hand, Figure A.9(b) shows the *I(V)* curves collected in junctions (area from 13.6 to 123 μm^2) in the same sample but exhibiting significantly different behavior. These curves are sigmoidal and asymmetric, suggesting tunnel conduction. Their resistance varies from R(H11) ≈ 1.4 x 10^6 Ω and R(J7) ≈ 1.3 x 10^7 Ω, consistent with the literature's values.[55,56,255] The resistance was investigated by R(V_w) loops in junctions that show similar *I(V)*. Figure A.10(a) shows two

sequential asymmetric *I(V)* curves collected at 1 Hz and V_{max} = 8 V and 9 V, respectively, for junction G12 in sample 1. At $V \approx + 6$ V, the current drop suggests a resistive switching that caused a transition from ON to OFF state. The current increases dramatically around – 7.5 V (green vertical dashed line), resembling a resistive switching from OFF to ON states for opposite voltage polarity. The next *I*(*V*) curve (blue curve) is measured with V_{max} = 9 V in order to observe the positive peak with more clarity.

Nevertheless, as the inset shows, the previous peak at positive voltage completely vanishes. It can be seen a current drop around – 6.5 V, but with a much lower amplitude than in the previous curve. Moreover, this drop for both curves happens at different voltages, which should not be expected if the resistive switching mechanism is related to ferroelectric switching (switching happening at V_c). Next, the electroresistance is measured for writing pulses with a duration of 1 ms (description in Experimental Methods chapter) and $|V_{max}|$ = 8 V, the resistance variation is minimal, as shown in Figure A.10(b). The inset shows an optical microscopy image from the capacitor with an area ≈ of 100 μm^2. Besides, the V_w necessary to induce a change (red vertical dashed line) is ≈ 5 V, not corresponding to the current drop of neither of the *I(V)* curves in Figure A.10(a). For positive V_w, there is no clear switching. This result indicates that the resistive switching observable in Figure A.10(a) is most likely not correlated to the resistance change in Figure A.10(b).

In sample 3, the junction D11 with area = 77 μm^2 is taken as an example. The *I(V)* curve collected at 1 Hz and V_{max} = 8 V is displayed in Figure A.10(c). Around $V \approx + 4$ V, the current response changes the slope, suggesting resistive switching from ON to OFF state. When a negative voltage is applied, the change in slope around $V \approx - 5$ V is evidence of OFF to ON state switching. Moreover, the asymmetric *I(V)* shape is consistent with previous reports in BTO tunnel junctions. Figure A.10(d) shows the $R(V_w)$ loop recorded for writing voltage pulses with 1 ms duration. Even though a change in *R* can be observed, positive V_w induces a decrease in resistance (OFF to ON), contradicting the *I(V)* from Figure A.10(c). Low voltage pulses amplitude (≈ - 1 V) is already enough to cause a resistance increase, which does not correlate with Figure A.10(c). Large negative voltages seem to stabilize the resistance, but no similar behavior is observed for positive voltage. The clockwise direction of the loop is opposite to the ones observed in the literature.[55,56] Note that the absolute resistance for the 2 nm BTO junction in Figure A.10(b) is ≈ 10^9 Ω and for the 4 nm junction in Figure A.10(d) is ≈ 10^8. This observation is contradictory to the expected resistance

arising from tunneling conduction in trapezoidal barriers. The current density exponential dependence on the barrier's thickness dictates thicker junctions must have larger resistances for similar barrier heights between ferroelectric/electrodes.[39,74] Samples 2, 4, and 8 did not show any *I(V)* curve that resembles ionic-like resistive switching.

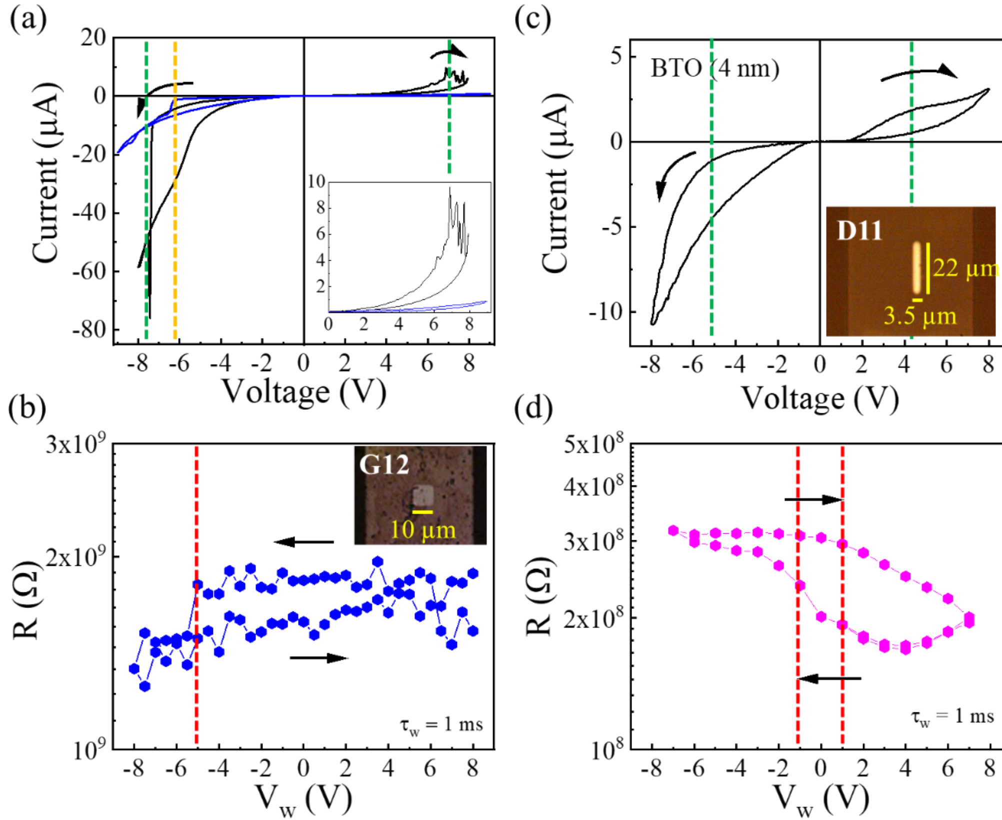

Figure A. 10. (a) I(V) curves collected at 1 Hz in junction G12 (area = 100 μm²) from sample 1 (2 nm BTO). Vertical dashed lines indicate voltage where the current has a change in the slope. Inset shows zoom for positive voltages for clearer visualization of a second I(V) curve (blue curve). Units are indicated in the main graph. (b) R(V_w) loop obtained by applying 1 ms pulses. Inset shows an optical microscopy image of junction G12. (c) I(V) curve collected at 1 Hz in junction D11 (area = 77 μm²) from sample 3 (4 nm BTO). Inset shows an optical microscopy image of junction D11. (d) R(V_w) loop obtained by applying 1 ms pulses.

Ultimately, it was shown here that some BTO junctions patterned with optical lithography have large ohmic conduction, and others show a sigmoidal *I(V)* curve indicating a trapezoidal barrier is formed. In the first case, it is argued that a short-circuit between the bottom and top electrodes was created during the optical lithography, most likely due to detachment of the SiO_2 insulation layer even though not observable in the optical microscopy images. On the other hand, the devices with sigmoidal *I(V)* indicate resistive switching when a larger excursion of voltage is performed.

Nevertheless, the $R(V_w)$ loops collected exhibit poor *ER* and a change in resistance at V_w (red vertical lines) smaller than the voltage where the alleged resistive switching happens (green vertical lines). This last observation indicates that both effects are not correlated. It is worth mentioning that no evidence of ferroelectric switching was found in the BTO tunnel junctions.

- HZO tunnel junctions

The HZO tunnel junction patterned with the lithography process described in section II shows similar electrical behavior to the BTO capacitors. Most junctions show a large current density independently on the HZO layer's thickness, as Figure A.11 exhibits. Similar to Figure A.8(a, c), *J* has an exponential decay for devices with area < 150 μm^2 for samples 5, 6, and 9 (Figures A.11(a, b, c)). The inset in Figure A.11(a) shows an optical microscopy image for junction L12 (area ≈ 100 μm^2).

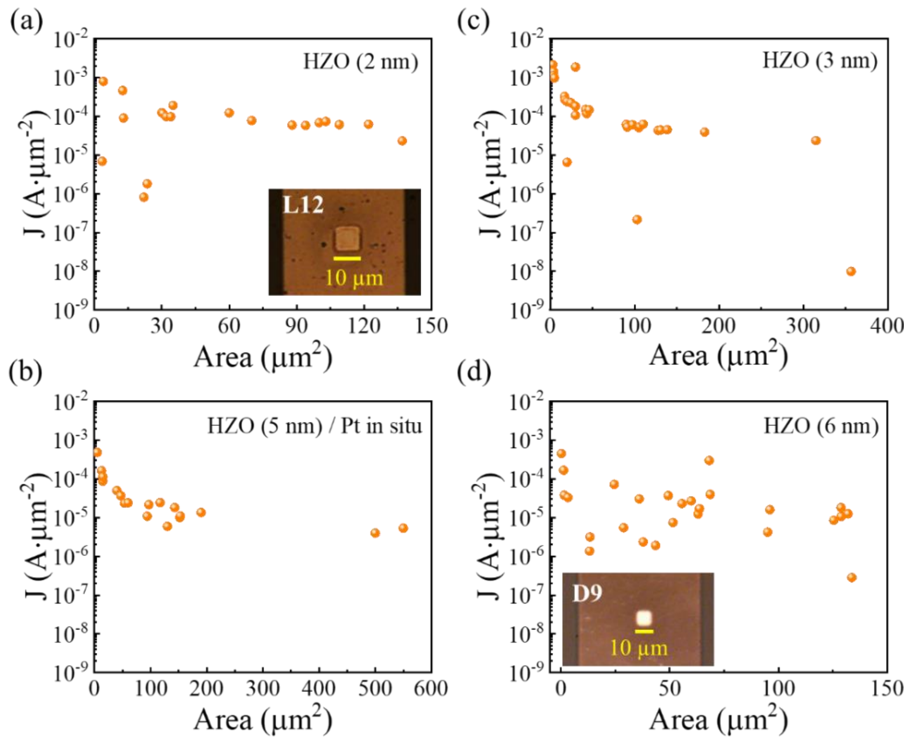

Figure A. 11. Current density dependence on the area for samples (a) 5 (b) 6, (c) 9 and (d) 7. Inset in (a) and (d) show optical microscopy images from junctions L12 and D9, respectively, with an area of ≈ 100 µm^2.

Differently from films with 2, 3, or 5 nm HZO, Figure A.11(d) obtained from sample 7 (6 nm HZO) does not display a clear trend on the current density. The inset demonstrates the top view

optical microscopy image from junction D9 with an area of 100 μm^2. Nevertheless, the values remain around 10^{-5} $A{\cdot}\mu m^{-2}$ even though the thickness of the HZO is three times larger than in Figure A.11(a), suggesting that these samples might have also suffered short-circuit during the lithography patterning.

The shape of the reading *I(V)* curves also resembles the behavior from the BTO samples. Figure A.12(a) displays two representative junctions that exhibit ohmic conduction with the current in the order of miliampere. On the other hand, few capacitors display sigmoidal *I(V)* curves as expected for trapezoidal tunnel junctions. The few junctions with non-ohmic conduction as the ones shown in Figure A.12(a) still have large current levels, in the range of 0.1 to 1 mA at 1 V. The current densities calculated for these devices are significantly larger than the *J* obtained in FTJ with similar thicknesses but patterned with standard shadow mask technique. Table A.4 demonstrates the current density in these HZO capacitors (extracted from the main text). In 2 nm HZO, *J* is not larger than 10^{-9} $A{\cdot}\mu m^{-2}$. As the barrier thickness increases, the current density reaches 10^{-12} $A{\cdot}\mu m^{-2}$. The comparison with the data from Figure A.11 and Table A.4 corroborates the hypothesis that junctions patterned with optical lithography have been damaged during the lithography process, even though the optical microscopy images do not indicate a detachment from the SiO_2 or imperfect patterning. There is no evidence of *ER* in the $R(V_w)$ loop collected in any junction from samples with HZO, and for this reason, they are not included here.

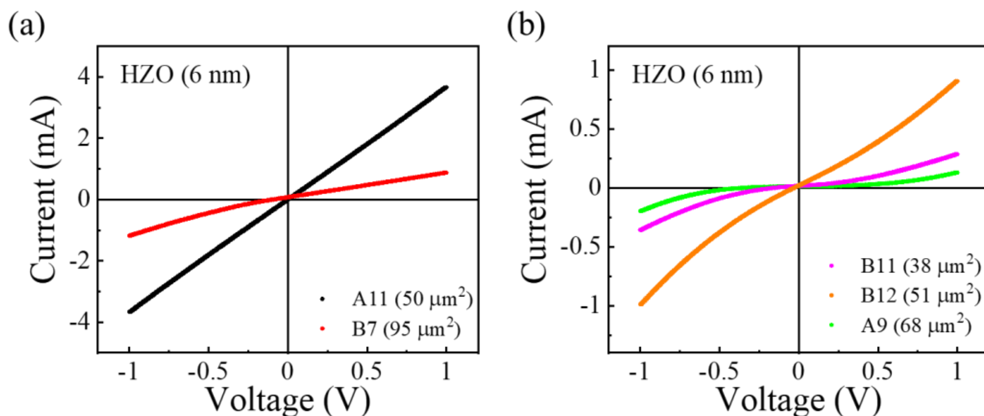

Figure A. 12. Current-voltage curves collected in sample 7 /6 nm HZO) tunnel junctions with different areas. The curves' shape indicates a clear difference between an (a) ohmic conduction and (b) exponential-like typical from tunnel barriers.

In conclusion, the junctions patterned with optical lithography in Polifab do not show the expected electric behavior for ferroelectric tunnel junctions. Even though images obtained by optical

microscopy at the end of the second step (Figure A.4(f)) suggest the etching of the pillar and the SiO_2 insulating layer were correctly prepared, the devices have been most likely short-circuited. The current density, for this reason, shows a much larger value than samples with the top electrode patterned with standard shadow mask technique. Junctions that do not show a clear short-circuit curve display *I(V)* curves with hysteresis that could suggest resistive switching. However, the variation of resistance that should arise from this effect cannot be disclosed in the $R(V_w)$ loops.

Structure	**J (A·µm^{-2})**	**Contact area (µm^2)**
Pt / HZO (2 nm) / LSMO	10^{-9}	314
Pt / HZO (3 nm) / LSMO	10^{-10}	314
Pt / HZO (4 nm) / LSMO	10^{-11}	314
Pt / HZO (7 nm) / LSMO	10^{-12}	314

Table A. 4. Current density collected in tunnel junctions with different HZO thickness patterned with standard shadow mask technique.

Bibliography

[1] Mark Lapedus, *DRAM Scaling Challenges Grow*, **2019**.

[2] R. Harris, *Is ReRAM the end of NAND flash?*, **2012**.

[3] S. Slesazeck, T. Mikolajick, *Nanotechnology* **2019**, *30*, 352003.

[4] D. Ielmini, H.-S. S. P. P. Wong, *Nat. Electron.* **2018**, *1*, 333.

[5] G. Bi, M. Poo, *J. Neurosci.* **1998**, *18*, 10464.

[6] Y. Dan, M. Poo, *Science.* **1992**, *256*, 1570.

[7] L. S. Smith, In *Brain Inspired Cognitive Systems 2008* (Eds.: Hussain, A.; Aleksander, I.; Smith, L. S.; Barros, A. K.; Chrisley, R.; Cutsuridis, V.), Springer New York, New York, NY, **2010**, pp. 167–182.

[8] L. A. Camuñas-Mesa, B. Linares-Barranco, T. Serrano-Gotarredona, *Materials (Basel).* **2019**, *12*, 1.

[9] S. D. Ha, S. Ramanathan, *J. Appl. Phys.* **2011**, *110*, 071101.

[10] L. Chua, *Appl. Phys. A* **2011**, *102*, 765.

[11] B. Linares-Barranco, T. Serrano-Gottaredona, T. Serrano-Gotarredona, *Nat. Preced.* **2009**, *3010*, 2.

[12] C. Zamarreño-Ramos, L. A. Camuñas-Mesa, J. A. Pérez-Carrasco, T. Masquelier, T. Serrano-Gottaredona, B. Linares-Barranco, *Front. Neurosci.* **2011**, *5*, 1.

[13] T. Serrano-Gottaredona, T. Masquelier, T. Prodromakis, G. Indiveri, B. Linares-Barranco, *Front. Neurosci.* **2013**, *7*, 1.

[14] G. S. Snider, In *2008 IEEE/ACMInternational Symposium on Nanoscale Architectures*, **2008**, pp. 85–92.

[15] D. Kuzum, S. Yu, H. S. Philip Wong, *Nanotechnology* **2013**, *24*, 1.

[16] F. Ambriz-Vargas, G. Kolhatkar, M. Broyer, A. Hadj-Youssef, R. Nouar, A. Sarkissian, R. Thomas, C. Gomez-Yáñez, M. A. Gauthier, A. Ruediger, *ACS Appl. Mater. Interfaces*

2017, *9*, 13262.

[17] Z. Fan, J. Chen, J. Wang, *J. Adv. Dielectr.* **2016**, *6*, 1630003.

[18] H. Y. Yoong, H. Wu, J. Zhao, H. Wang, R. Guo, J. Xiao, B. Zhang, P. Yang, S. J. Pennycook, N. Deng, X. Yan, J. Chen, *Adv. Funct. Mater.* **2018**, *28*, 1806037.

[19] J. Lyu, T. Song, I. Fina, F. Sánchez, *Nanoscale* **2020**, *12*, 11280.

[20] S. Oh, T. Kim, M. Kwak, J. Song, J. Woo, S. Jeon, I. K. Yoo, H. Hwang, In *IEEE Electron Device Letters*, **2017**, pp. 732–735.

[21] S. Yu, Y. Wu, R. Jeyasingh, D. Kuzum, H. S. P. Wong, *IEEE Trans. Electron Devices* **2011**, *58*, 2729.

[22] C. Ferreyra, M. J. Sánchez, M. Aguirre, C. Acha, S. Bengió, J. Lecourt, U. Lüders, D. Rubi, *Nanotechnology* **2020**, *31*, 155204.

[23] M. Lanza, *Materials (Basel).* **2014**, *7*, 2155.

[24] R. Waser, R. Dittmann, C. Staikov, K. Szot, *Adv. Mater.* **2009**, *21*, 2632.

[25] J. Y. Chen, C. L. Hsin, C. W. Huang, C. H. Chiu, Y. T. Huang, S. J. Lin, W. W. Wu, L. J. Chen, *Nano Lett.* **2013**, *13*, 3671.

[26] D. H. Kwon, K. M. Kim, J. H. Jang, J. M. Jeon, M. H. Lee, G. H. Kim, X. S. Li, G. S. Park, B. Lee, S. Han, M. Kim, C. S. Hwang, *Nat. Nanotechnol.* **2010**, *5*, 148.

[27] I. Valov, R. Waser, J. R. Jameson, M. N. Kozicki, *Nanotechnology* **2011**, *22*, 289502.

[28] R. G. Neale, D. L. Nelson, G. E. Moore, *Electronics* **1970**, 56.

[29] A. L. Lacaita, *Solid. State. Electron.* **2006**, *50*, 24.

[30] A. Rana, C. Li, G. Koster, H. Hilgenkamp, *Sci. Rep.* **2020**, *10*, 3293.

[31] B. H. Park, B. S. Kang, S. D. Bu, T. W. Noh, J. Lee, W. Jo, *Nature* **1999**, *401*, 682.

[32] R. Oligschlaeger, R. Waser, R. Meyer, S. Karthäuser, R. Dittmann, *Appl. Phys. Lett.* **2006**, *88*, 042901.

[33] P. W. M. Blom, R. M. Wolf, J. F. M. Cillessen, M. P. C. M. Krijn, *Phys. Rev. Lett.* **1994**,

73, 2107.

[34] A. Q. Jiang, C. Wang, K. J. Jin, X. B. Liu, J. F. Scott, C. S. Hwang, T. A. Tang, H. Bin Lu, G. Z. Yang, *Adv. Mater.* **2011**, *23*, 1277.

[35] M. Qian, I. Fina, M. C. Sulzbach, F. Sánchez, J. Fontcuberta, *Adv. Electron. Mater.* **2019**, *5*, 1800646.

[36] P. Maksymovych, S. Jesse, P. Yu, R. Ramesh, A. P. Baddorf, S. V. Kalininl, S. V Kalinin, S. V. Kalininl, *Science.* **2009**, *324*, 1421.

[37] V. Garcia, M. Bibes, *Nat. Commun.* **2014**, *5*, 1.

[38] E. Y. Y. Tsymbal, A. Gruverman, V. Garcia, M. Bibes, A. Barthélémy, *MRS Bull.* **2012**, *37*, 138.

[39] A. Gruverman, D. Wu, H. Lu, Y. Wang, H. W. W. Jang, C. M. M. Folkman, M. Y. Zhuravlev, D. Felker, M. Rzchowski, C.-B. Eom, E. Y. Tsymbal, *Nano Lett.* **2009**, *9*, 3539.

[40] E. Y. Tsymbal, H. Kohlstedt, *Science.* **2006**, *313*, 181.

[41] D. B. Strukov, G. S. Snider, D. R. Stewart, R. S. Williams, *Nature* **2008**, *453*, 80.

[42] J. Valasek, *Phys. Rev.* **1921**, *17*, 475.

[43] I. S. Zheludev, In *Physics of Crystalline Dielectrics*, Springer US, Boston, MA, **1971**, pp. 149–204.

[44] Ashcroft, Merm, *Solid State Physics*, **1976**.

[45] R. R. Mehta, B. D. Silverman, J. T. Jacobs, *J. Appl. Phys.* **1973**, *44*, 3379.

[46] A. V. Bune, V. M. Fridkin, S. Ducharme, L. M. Blinov, S. P. Palto, A. V. Sorokin, S. G. Yudin, A. Ziatkin, *Nature* **1998**, *391*, 874.

[47] T. Tybell, C. H. Ahn, J. M. Triscone, *Appl. Phys. Lett.* **1999**, *75*, 856.

[48] T. Yamamoto, *Integr. Ferroelectr.* **1996**, *12*, 161.

[49] Y. S. Kim, D. H. Kim, J. D. Kim, Y. J. Chang, T. W. Noh, J. H. Kong, K. Char, Y. D.

Park, S. D. Bu, J. G. Yoon, J. S. Chung, *Appl. Phys. Lett.* **2005**, *86*, 1.

[50] A. G. Zembilgotov, N. A. Pertsev, H. Kohlstedt, R. Waser, *J. Appl. Phys.* **2002**, *91*, 2247.

[51] D. G. Schlom, L.-Q. Chen, C.-B. Eom, K. M. Rabe, S. K. Streiffer, J.-M. Triscone, *Annu. Rev. Mater. Res.* **2007**, *37*, 589.

[52] K. J. Choi, *Science.* **2004**, *306*, 1005.

[53] S. Estandía, N. Dix, J. Gazquez, I. Fina, J. Lyu, M. F. Chisholm, J. Fontcuberta, F. Sánchez, *ACS Appl. Electron. Mater.* **2019**, *1*, 1449.

[54] D. J. Kim, H. Lu, S. Ryu, C.-W. Bark, C.-B. Eom, E. Y. Tsymbal, A. Gruverman, *Nano Lett.* **2012**, *12*, 5697.

[55] G. Radaelli, D. Gutiérrez, F. Sánchez, R. Bertacco, M. Stengel, J. Fontcuberta, *Adv. Mater.* **2015**, *27*, 2602.

[56] M. Qian, I. Fina, F. Sánchez, J. Fontcuberta, *Adv. Electron. Mater.* **2019**, *5*, 1800407.

[57] H. Yamada, V. Garcia, S. Fusil, S. Boyn, M. Marinova, A. Gloter, J. Grollier, E. Jacquet, C. Carrétéro, C. Deranlot, M. Bibes, A. Barthélémy, *ACS Nano* **2013**, *7*, 5385.

[58] S. Boyn, A. M. Douglas, C. Blouzon, P. Turner, A. Barthélémy, M. Bibes, S. Fusil, J. M. Gregg, V. Garcia, *Appl. Phys. Lett.* **2016**, *109*, 1.

[59] D. Pantel, H. Lu, S. Goetze, P. Werner, D. Jik Kim, A. Gruverman, D. Hesse, M. Alexe, *Appl. Phys. Lett.* **2012**, *100*, 232902.

[60] D. Lee, S. M. Yang, T. H. Kim, B. C. Jeon, Y. S. Kim, J. G. Yoon, H. N. Lee, S. H. Baek, C. B. Eom, T. W. Noh, *Adv. Mater.* **2012**, *24*, 402.

[61] S. V. Kalinin, B. J. Rodriguez, A. Y. Borisevich, A. P. Baddorf, N. Balke, H. J. Chang, L. Q. Chen, S. Choudhury, S. Jesse, P. Maksymovych, M. P. Nikiforov, S. J. Pennycook, *Adv. Mater.* **2010**, *22*, 314.

[62] A. Chanthbouala, V. Garcia, R. O. Cherifi, K. Bouzehouane, S. Fusil, X. Moya, S. Xavier, H. Yamada, C. Deranlot, N. D. Mathur, M. Bibes, A. Barthélémy, J. Grollier, *Nat. Mater.* **2012**, *11*, 860.

[63] V. Nagarajan, S. Prasertchoung, T. Zhao, H. Zheng, J. Ouyang, R. Ramesh, W. Tian, X. Q. Pan, D. M. Kim, C. B. Eom, H. Kohlstedt, R. Waser, *Appl. Phys. Lett.* **2004**, *84*, 5225.

[64] D. D. Fong, G. B. Stephenson, S. K. Streiffer, J. A. Eastman, O. Aucielo, P. H. Fuoss, C. Thompson, *Science.* **2004**, *304*, 1650.

[65] H. Béa, S. Fusil, K. Bouzehouane, M. Bibes, M. Sirena, G. Herranz, E. Jacquet, J. P. Contour, A. Barthélémy, *Japanese J. Appl. Physics, Part 2 Lett.* **2006**, *45*, 187.

[66] S. Boyn, A. Chanthbouala, S. Girod, C. Carrétéro, A. Barthélémy, M. Bibes, J. Grollier, S. Fusil, V. Garcia, *Appl. Phys. Lett.* **2018**, *113*, 232902.

[67] Z. Wen, C. Li, D. Wu, A. Li, N. Ming, *Nat. Mater.* **2013**, *12*, 617.

[68] S. Boyn, S. Girod, V. Garcia, S. Fusil, S. Xavier, C. Deranlot, H. Yamada, C. Carrétéro, E. Jacquet, M. Bibes, A. Barthélémy, J. Grollier, *Appl. Phys. Lett.* **2014**, *104*, 052909.

[69] B. Max, M. Hoffmann, H. Mulaosmanovic, S. Slesazeck, T. Mikolajick, *ACS Appl. Electron. Mater.* **2020**, *2*, 4023.

[70] S. Boyn, J. Grollier, G. Lecerf, B. Xu, N. Locatelli, S. Fusil, S. Girod, C. Carrétéro, K. Garcia, S. Xavier, J. Tomas, L. Bellaiche, M. Bibes, A. Barthélémy, S. Saïghi, V. Garcia, *Nat. Commun.* **2017**, *8*, 1.

[71] J. G. Simmons, *J. Appl. Phys.* **1963**, *34*, 1793.

[72] H. Kohlstedt, N. A. Pertsev, J. Rodríguez Contreras, R. Waser, *Phys. Rev. B* **2005**, *72*, 125341.

[73] W. F. Brinkman, R. C. C. Dynes, J. M. M. Rowell, *J. Appl. Phys.* **1970**, *41*, 1915.

[74] D. Pantel, M. Alexe, *Phys. Rev. B* **2010**, *82*, 134105.

[75] S. Boyn, Ferroelectric tunnel junctions: memristors for neuromorphic computing, Université Paris-Saclay, **2016**.

[76] M. Qian, Resistive switching in nanometric BaTiO3 ferroelectric junctions, Universitat Autònoma de Barcelona, **2018**.

[77] G. Gerra, A. K. Tagantsev, N. Setter, K. Parlinski, *Phys. Rev. Lett.* **2006**, *96*, 107603.

[78] C. . Jia, J. Rodríguez Contreras, J. Schubert, M. Lentzen, U. Poppe, H. Kohlstedt, K. Urban, R. Waser, *J. Cryst. Growth* **2003**, *247*, 381.

[79] X. Luo, B. Wang, Y. Zheng, *ACS Nano* **2011**, *5*, 1649.

[80] D. I. Bilc, F. D. Novaes, J. Íñiguez, P. Ordejón, P. Ghosez, *ACS Nano* **2012**, *6*, 1473.

[81] Z. Tang, J. Zeng, Y. Xiong, M. Tang, D. Xu, C. Cheng, Y. Xiao, Y. Zhou, *AIP Adv.* **2013**, *3*, 122117.

[82] B. Max, M. Pešić, S. Slesazeck, T. Mikolajick, *J. Appl. Phys.* **2018**, *123*, 134102.

[83] X. Ou, Y. Shuai, W. Luo, P. F. Siles, R. Kögler, J. Fiedler, H. Reuther, S. Zhou, R. Hübner, S. Facsko, M. Helm, T. Mikolajick, O. G. Schmidt, H. Schmidt, *ACS Appl. Mater. Interfaces* **2013**, *5*, 12764.

[84] H. Y. Lee, Y. S. Chen, P. S. Chen, T. Y. Wu, F. Chen, C. C. Wang, P. J. Tzeng, M.-J. Tsai, C. Lien, *IEEE Electron Device Lett.* **2010**, *31*, 44.

[85] B. Butcher, S. Koveshnikov, D. C. Gilmer, G. Bersuker, M. G. Sung, A. Kalantarian, C. Park, R. Geer, Y. Nishi, P. D. Kirsch, R. Jammy, In *IIRW IEEE Transactions in Device and Material Reliability (TDMR)*, **2011**, p. 146.

[86] B. Govoreanu, G. S. Kar, Y. Y. Chen, V. Paraschiv, S. Kubicek, A. Fantini, I. P. Radu, L. Goux, S. Clima, R. Degraeve, N. Jossart, O. Richard, T. Vandeweyer, K. Seo, P. Hendrickx, G. Pourtois, H. Bender, L. Altimime, D. J. Wouters, J. A. Kittl, M. Jurczak, In *IEEE International Electron Devices Meeting, Washington, DC, USA,* **2011**, pp. 729–732.

[87] T. Mikolajick, S. Slesazeck, M. H. Park, U. Schroeder, *MRS Bull.* **2018**, *43*, 340.

[88] V. Cosnier, P. Besson, V. Loup, L. Vandroux, S. Minoret, M. Cassé, X. Garros, J.-M. Pedini, S. Lhostis, K. Dabertrand, C. Morin, C. Wiemer, M. Perego, M. Fanciulli, *Microelectron. Eng.* **2007**, *84*, 1886.

[89] S. Stemmer, *J. Vac. Sci. Technol. B Microelectron. Nanom. Struct.* **2004**, *22*, 791.

[90] J. K. Schaeffer, S. B. Samavedam, D. C. Gilmer, V. Dhandapani, P. J. Tobin, J. Mogab, B.-Y. Nguyen, B. E. White, S. Dakshina-Murthy, R. S. Rai, Z.-X. Jiang, R. Martin, M. V. Raymond, M. Zavala, L. B. La, J. A. Smith, R. Garcia, D. Roan, M. Kottke, R. B.

Gregory, *J. Vac. Sci. Technol. B Microelectron. Nanom. Struct.* **2003**, *21*, 11.

[91] J. K. Freericks, *Nat. Phys.* **2010**, *6*, 559.

[92] B. Feng, R. Ishikawa, A. Kumamoto, N. Shibata, Y. Ikuhara, *Nano Lett.* **2019**, *19*, 2162.

[93] E. Navickas, Y. Chen, Q. Lu, W. Wallisch, T. M. Huber, J. Bernardi, M. Stöger-Pollach, G. Friedbacher, H. Hutter, B. Yildiz, J. Fleig, *ACS Nano* **2017**, *11*, 11475.

[94] A. M. Saranya, D. Pla, A. Morata, A. Cavallaro, J. Canales-Vázquez, J. A. Kilner, M. Burriel, A. Tarancón, *Adv. Energy Mater.* **2015**, *5*, 1500377.

[95] F. Chiabrera, A. Morata, M. Pacios, A. Tarancón, *Solid State Ionics* **2017**, *299*, 70.

[96] M. Lanza, K. Zhang, M. Porti, M. Nafría, Z. Y. Shen, L. F. Liu, J. F. Kang, D. Gilmer, G. Bersuker, *Appl. Phys. Lett.* **2012**, *100*, 123508.

[97] G. Bersuker, D. C. Gilmer, D. Veksler, P. Kirsch, L. Vandelli, A. Padovani, L. Larcher, K. McKenna, A. Shluger, V. Iglesias, M. Porti, M. Nafría, *J. Appl. Phys.* **2011**, *110*, 124518.

[98] K. P. McKenna, A. L. Shluger, *Microelectron. Eng.* **2009**, *86*, 1751.

[99] T. S. Böscke, J. Müller, D. Bräuhaus, U. Schröder, U. Böttger, *Appl. Phys. Lett.* **2011**, *99*, 102903.

[100] E. H. Kisi, *J. Am. Ceram. Soc.* **1998**, *81*, 741.

[101] E. H. Kisi, C. J. Howard, *Key Eng. Mater.* **1998**, *153–154*, 1.

[102] X. Sang, E. D. Grimley, T. Schenk, U. Schroeder, J. M. Lebeau, *Appl. Phys. Lett.* **2015**, *106*.

[103] S. Mueller, J. Mueller, A. Singh, S. Riedel, J. Sundqvist, U. Schroeder, T. Mikolajick, *Adv. Funct. Mater.* **2012**, *22*, 2412.

[104] J. Müller, T. S. Böscke, D. Bräuhaus, U. Schröder, U. Böttger, J. Sundqvist, P. Kcher, T. Mikolajick, L. Frey, P. Kücher, T. Mikolajick, L. Frey, *Appl. Phys. Lett.* **2011**, *99*, 2011.

[105] M. H. Park, Y. H. Lee, T. Mikolajick, U. Schroeder, C. S. Hwang, *MRS Commun.* **2018**, *8*, 795.

[106] P. Polakowski, J. Müller, *Appl. Phys. Lett.* **2015**, *106*, 232905.

[107] M. Trentzsch, S. Flachowsky, R. Richter, J. Paul, B. Reimer, D. Utess, S. Jansen, H. Mulaosmanovic, S. Müller, S. Slesazeck, J. Ocker, M. Noack, J. Müller, P. Polakowski, J. Schreiter, S. Beyer, T. Mikolajick, B. Rice, In *2016 IEEE International Electron Devices Meeting (IEDM), San Francisco, CA*, **2016**, pp. 11.5.1-11.5.4.

[108] U. Schroeder, S. Mueller, J. Mueller, E. Yurchuk, D. Martin, C. Adelmann, T. Schloesser, R. van Bentum, T. Mikolajick, *ECS J. Solid State Sci. Technol.* **2013**, *2*, N69.

[109] J. Muller, T. S. Boscke, S. Muller, E. Yurchuk, P. Polakowski, J. Paul, D. Martin, T. Schenk, K. Khullar, A. Kersch, W. Weinreich, S. Riedel, K. Seidel, A. Kumar, T. M. Arruda, S. V. Kalinin, T. Schlosser, R. Boschke, R. Van Bentum, U. Schroder, T. Mikolajick, J. Müller, T. S. Böscke, S. Müller, E. Yurchuk, P. Polakowski, J. Paul, D. Martin, T. Schenk, K. Khullar, A. Kersch, W. Weinreich, S. Riedel, K. Seidel, A. Kumar, T. M. Arruda, S. V. Kalinin, T. Schlösser, R. Boschke, R. Van Bentum, U. Schröder, T. Mikolajick, In *2013 IEEE International Electron Devices Meeting*, IEEE, **2013**, pp. 280–283.

[110] H. Takasu, *J. Electroceramics* **2000**, *4*, 327.

[111] M. H. Park, Y. H. Lee, H. J. Kim, Y. J. Kim, T. Moon, K. Do Kim, S. D. Hyun, T. Mikolajick, U. Schroeder, C. S. Hwang, *Nanoscale* **2018**, *10*, 716.

[112] Y. Li, J. Li, R. Liang, R. Zhao, B. Xiong, H. Liu, H. Tian, Y. Yang, T.-L. Ren, *Appl. Phys. Lett.* **2019**, *114*, 142902.

[113] J. Müller, T. S. Böscke, U. Schröder, S. Mueller, D. Bräuhaus, U. Böttger, L. Frey, T. Mikolajick, *Nano Lett.* **2012**, *12*, 4318.

[114] M. H. Park, Y. H. Lee, H. J. Kim, T. Schenk, W. Lee, K. Do Kim, F. P. G. Fengler, T. Mikolajick, U. Schroeder, C. S. Hwang, *Nanoscale* **2017**, *9*, 9973.

[115] R. Materlik, C. Kunneth, A. Kersch, *J. Appl. Phys.* **2015**, *117*.

[116] S. S. Cheema, D. Kwon, N. Shanker, R. dos Reis, S. L. Hsu, J. Xiao, H. Zhang, R. Wagner, A. Datar, M. R. McCarter, C. R. Serrao, A. K. Yadav, G. Karbasian, C. H. Hsu,

A. J. Tan, L. C. Wang, V. Thakare, X. Zhang, A. Mehta, E. Karapetrova, R. V. Chopdekar, P. Shafer, E. Arenholz, C. Hu, R. Proksch, R. Ramesh, J. Ciston, S. Salahuddin, *Nature* **2020**, *580*, 478.

[117] T. Li, N. Zhang, Z. Sun, C. Xie, M. Ye, S. Mazumdar, L. Shu, Y. Wang, D. Wang, L. Chen, S. Ke, H. Huang, *J. Mater. Chem. C* **2018**, *6*, 9224.

[118] M. H. Park, H. J. Kim, Y. J. Kim, Y. H. Lee, T. Moon, K. Do Kim, S. D. Hyun, F. Fengler, U. Schroeder, C. S. Hwang, *ACS Appl. Mater. Interfaces* **2016**, *8*, 15466.

[119] S. Starschich, S. Menzel, U. Böttger, *J. Appl. Phys.* **2017**, *121*, 154102.

[120] T. Shimizu, K. Katayama, T. Kiguchi, A. Akama, T. J. Konno, O. Sakata, H. Funakubo, *Sci. Rep.* **2016**, *6*, 1.

[121] T. Mimura, T. Shimizu, H. Uchida, O. Sakata, H. Funakubo, *Appl. Phys. Lett.* **2018**, *113*, 102901.

[122] K. Katayama, T. Shimizu, O. Sakata, T. Shiraishi, S. Nakamura, T. Kiguchi, A. Akama, T. J. Konno, H. Uchida, H. Funakubo, *J. Appl. Phys.* **2016**, *119*, 1.

[123] J. Lyu, I. Fina, R. Solanas, J. Fontcuberta, F. Sánchez, *Appl. Phys. Lett.* **2018**, *113*, 082902.

[124] T. Li, M. Ye, Z. Sun, N. Zhang, W. Zhang, S. Inguva, C. Xie, L. Chen, Y. Wang, S. Ke, H. Huang, *ACS Appl. Mater. Interfaces* **2019**, *11*, 4139.

[125] Y. Wei, P. Nukala, M. Salverda, S. Matzen, H. J. Zhao, J. Momand, A. S. Everhardt, G. Agnus, G. R. Blake, P. Lecoeur, B. J. Kooi, J. Íñiguez, B. Dkhil, B. Noheda, *Nat. Mater.* **2018**, *17*, 1095.

[126] J. Lyu, I. Fina, J. Fontcuberta, F. Sánchez, *ACS Appl. Mater. Interfaces* **2019**, *11*, 6224.

[127] J. Lyu, I. Fina, R. Solanas, J. Fontcuberta, F. Sánchez, *ACS Appl. Electron. Mater.* **2019**, *1*, 220.

[128] M. Hyuk Park, H. Joon Kim, Y. Jin Kim, T. Moon, C. Seong Hwang, M. H. Park, H. J. Kim, Y. J. Kim, T. Moon, C. S. Hwang, *Appl. Phys. Lett.* **2014**, *104*, 072901.

[129] Y. Goh, S. Jeon, *Nanotechnology* **2018**, *29*, 335201.

[130] M. Pešić, F. P. G. Fengler, L. Larcher, A. Padovani, T. Schenk, E. D. Grimley, X. Sang, J. M. LeBeau, S. Slesazeck, U. Schroeder, T. Mikolajick, *Adv. Funct. Mater.* **2016**, *26*, 4601.

[131] J. Lyu, Epitaxial Ferroelectric Thin Films on Si(001): strain tuning of BaTiO 3 and stabilization of polar phase in Hf0.5Zr0.5O2, **2019**.

[132] P. D. Lomenzo, Q. Takmeel, C. Zhou, C. M. Fancher, E. Lambers, N. G. Rudawski, J. L. Jones, S. Moghaddam, T. Nishida, *J. Appl. Phys.* **2015**, *117*, 134105.

[133] M. Hoffmann, U. Schroeder, T. Schenk, T. Shimizu, H. Funakubo, O. Sakata, D. Pohl, M. Drescher, C. Adelmann, R. Materlik, A. Kersch, T. Mikolajick, *J. Appl. Phys.* **2015**, *118*, 072006.

[134] M. Hyuk Park, H. Joon Kim, Y. Jin Kim, W. Lee, T. Moon, C. Seong Hwang, *Appl. Phys. Lett.* **2013**, *102*, 0.

[135] M. H. Park, H. J. Kim, Y. J. Kim, Y. H. Lee, T. Moon, K. Do Kim, S. D. Hyun, C. S. Hwang, *Appl. Phys. Lett.* **2015**, *107*, 0.

[136] S. Starschich, S. Menzel, U. Böttger, *Appl. Phys. Lett.* **2016**, *108*, 032903.

[137] P. Jiang, Q. Luo, X. Xu, T. Gong, P. Yuan, Y. Wang, Z. Gao, W. Wei, L. Tai, H. Lv, *Adv. Electron. Mater.* **2021**, *7*, 2000728.

[138] H. J. Kim, M. H. Park, Y. J. Kim, Y. H. Lee, T. Moon, K. Do Kim, S. D. Hyun, C. S. Hwang, *Nanoscale* **2016**, *8*, 1383.

[139] A. Sawa, *Mater. Today* **2008**, *11*, 28.

[140] K. Yin, M. Li, Y. Liu, C. He, F. Zhuge, B. Chen, W. Lu, X. Pan, R. W. Li, *Appl. Phys. Lett.* **2010**, *97*, 042101.

[141] S. Ootsuki, H. Ikeno, Y. Umeda, H. Moriwake, A. Kuwabara, O. Kido, S. Ueda, I. Tanaka, Y. Fujikawa, T. Mizoguchi, *Appl. Phys. Lett.* **2011**, *99*, 233109.

[142] C. Mitra, C. Lin, J. Robertson, A. A. Demkov, *Phys. Rev. B* **2012**, *86*, 155105.

[143] Y. Yao, H. Fu, *Phys. Rev. B* **2011**, *84*, 064112.

[144] D. B. Strukov, R. S. Williams, *Appl. Phys. A* **2009**, *94*, 515.

[145] Q. H. Qin, L. Äkäslompolo, N. Tuomisto, L. Yao, S. Majumdar, J. Vijayakumar, A. Casiraghi, S. Inkinen, B. Chen, A. Zugarramurdi, M. Puska, S. van Dijken, *Adv. Mater.* **2016**, *28*, 6852.

[146] M. F. Chisholm, W. Luo, M. P. Oxley, S. T. Pantelides, H. N. Lee, *Phys. Rev. Lett.* **2010**, *105*, 1.

[147] Y. M. Kim, A. Morozovska, E. Eliseev, M. P. Oxley, R. Mishra, S. M. Selbach, T. Grande, S. T. Pantelides, S. V. Kalinin, A. Y. Borisevich, *Nat. Mater.* **2014**, *13*, 1019.

[148] H. J. Chang, S. V. Kalinin, A. N. Morozovska, M. Huijben, Y. H. Chu, P. Yu, R. Ramesh, E. A. Eliseev, G. S. Svechnikov, S. J. Pennycook, A. Y. Borisevich, *Adv. Mater.* **2011**, *23*, 2474.

[149] E. Dagotto, T. Hotta, A. Moreo, *Phys. Rep.* **2001**, *344*, 1.

[150] M. B. Salamon, M. Jaime, *Rev. Mod. Phys.* **2001**, *73*, 583.

[151] J. C. Gonzalez-Rosillo, S. Catalano, I. Maggio-Aprile, M. Gibert, X. Obradors, A. Palau, T. Puig, *Small* **2020**, *16*, 2001307.

[152] J. D. Ferguson, Y. Kim, L. F. Kourkoutis, A. Vodnick, A. R. Woll, D. A. Muller, J. D. Brock, *Adv. Mater.* **2011**, *23*, 1226.

[153] H. Jeen, W. S. Choi, J. W. Freeland, H. Ohta, C. U. Jung, H. N. Lee, *Adv. Mater.* **2013**, *25*, 3651.

[154] L. Yao, S. Majumdar, L. Äkäslompolo, S. Inkinen, Q. H. Qin, S. van Dijken, *Adv. Mater.* **2014**, *26*, 2789.

[155] J. C. Gonzalez-Rosillo, R. Ortega-Hernandez, B. Arndt, M. Coll, R. Dittmann, X. Obradors, A. Palau, J. Suñe, T. Puig, *Adv. Electron. Mater.* **2019**, *5*, 1.

[156] K. Szot, R. Dittmann, W. Speier, R. Waser, *Phys. status solidi – Rapid Res. Lett.* **2007**, *1*, R86.

[157] V. Garcia, S. Fusil, K. Bouzehouane, S. Enouz-Vedrenne, N. D. Mathur, A. Barthélémy, M. Bibes, *Nature* **2009**, *460*, 81.

[158] Z. Yan, Y. Guo, G. Zhang, J.-M. Liu, *Adv. Mater.* **2011**, *23*, 1351.

[159] A. Cardona Rodríguez, I. C. Arango, M. F. Gomez, C. Dominguez, J. Trastoy, C. Urban, S. Sulekar, J. C. Nino, I. K. Schuller, M. E. Gomez, J. G. Ramírez, *Solid State Commun.* **2019**, *288*, 38.

[160] S. S. Nonnenmann, E. M. Gallo, J. E. Spanier, *Appl. Phys. Lett.* **2010**, *97*, 102904.

[161] H. Kohlstedt, A. Petraru, K. Szot, A. Rüdiger, P. Meuffels, H. Haselier, R. Waser, V. Nagarajan, *Appl. Phys. Lett.* **2008**, *92*, 2006.

[162] F. Ambriz-Vargas, G. Kolhatkar, R. Thomas, R. Nouar, A. Sarkissian, C. Gomez-Yáñez, M. A. Gauthier, A. Ruediger, *Appl. Phys. Lett.* **2017**, *110*, 093106.

[163] Y. Goh, J. Hwang, S. Jeon, *ACS Appl. Mater. Interfaces* **2020**, *12*, 57539.

[164] B. Max, T. Mikolajick, M. Hoffmann, S. Slesazeck, In *2019 IEEE 11th International Memory Workshop (IMW), Monterey, CA, USA*, IEEE, **2019**, pp. 1–4.

[165] J. Yoon, S. Hong, Y. W. Song, J. H. Ahn, S. E. Ahn, *Appl. Phys. Lett.* **2019**, *115*, 153502.

[166] V. Iglesias, M. Porti, M. Nafría, X. Aymerich, P. Dudek, T. Schroeder, G. Bersuker, *Appl. Phys. Lett.* **2010**, *97*, 262906.

[167] V. Mikheev, A. Chouprik, Y. Lebedinskii, S. Zarubin, A. M. Markeev, A. V. Zenkevich, D. Negrov, *Nanotechnology* **2020**, *31*, 215205.

[168] S. Petzold, A. Zintler, R. Eilhardt, E. Piros, N. Kaiser, S. U. Sharath, T. Vogel, M. Major, K. P. McKenna, L. Molina-Luna, L. Alff, *Adv. Electron. Mater.* **2019**, *5*, 1900484.

[169] K. McKenna, A. Shluger, *Appl. Phys. Lett.* **2009**, *95*, 222111.

[170] J. Schou, *Appl. Surf. Sci.* **2009**, *255*, 5191.

[171] L. Pintilie, I. Vrejoiu, D. Hesse, M. Alexe, *J. Appl. Phys.* **2008**, *104*, 114101.

[172] Z. Wen, L. You, J. Wang, A. Li, D. Wu, *Appl. Phys. Lett.* **2013**, *103*, 132913.

[173] A. Chanthbouala, A. Crassous, V. Garcia, K. Bouzehouane, S. Fusil, X. Moya, J. Allibe, B. Dlubak, J. Grollier, S. Xavier, C. Deranlot, A. Moshar, R. Proksch, N. D. Mathur, M. Bibes, A. Barthélémy, *Nat. Nanotechnol.* **2012**, *7*, 101.

[174] L. Pintilie, C. Dragoi, Y. H. Chu, L. W. Martin, R. Ramesh, M. Alexe, *Appl. Phys. Lett.* **2009**, *94*, 232902.

[175] P. Maleeswaran, D. Nagulapally, R. P. Joshi, A. K. Pradhan, *J. Appl. Phys.* **2013**, *113*.

[176] R. Meyer, R. Waser, K. Prume, T. Schmitz, S. Tiedke, *Appl. Phys. Lett.* **2005**, *86*, 142907.

[177] I. Fina Martínez, Ferroelectricity and magnetoelectric coupling in magnetic ferroelectrics and artificial multiferroic heterostructures, Universitat de Barcelona, **2012**.

[178] J. F. Scott, L. Kammerdiner, M. Parris, S. Traynor, V. Ottenbacher, A. Shawabkeh, W. F. Oliver, *J. Appl. Phys.* **1988**, *64*, 787.

[179] I. Fina, L. Fábrega, E. Langenberg, X. Martí, F. Sánchez, M. Varela, J. Fontcuberta, *J. Appl. Phys.* **2011**, *109*, 074105.

[180] S. González-Casal, I. Fina, F. Sánchez, J. Fontcuberta, *ACS Appl. Electron. Mater.* **2019**, *1*, 1937.

[181] Y. A. Genenko, J. Glaum, M. J. Hoffmann, K. Albe, *Mater. Sci. Eng. B Solid-State Mater. Adv. Technol.* **2015**, *192*, 52.

[182] D. C. Lupascu, J. Rödel, *Adv. Eng. Mater.* **2005**, *7*, 882.

[183] M. Si, X. Lyu, P. R. Shrestha, X. Sun, H. Wang, K. P. Cheung, P. D. Ye, *Appl. Phys. Lett.* **2019**, *115*, 1.

[184] M. Jerry, P.-Y. Chen, J. Zhang, P. Sharma, K. Ni, S. Yu, S. Datta, In *IEEE International Electron Devices Meeting (IEDM)*, **2017**, p. 6.2.

[185] B.-B. Tian, N. Zhong, C.-G. Duan, *Chinese Phys. B* **2020**, *29*, 097701.

[186] A. J. Tan, K. Chatterjee, J. Zhou, D. Kwon, Y. H. Liao, S. Cheema, C. Hu, S. Salahuddin, *IEEE Electron Device Lett.* **2020**, *41*, 240.

[187] L. Chen, T. Y. Wang, Y. W. Dai, M. Y. Cha, H. Zhu, Q. Q. Sun, S. J. Ding, P. Zhou, L.

Chua, D. W. Zhang, *Nanoscale* **2018**, *10*, 15826.

[188] T. Masquelier, R. Guyonneau, S. J. Thorpe, *Neural Comput.* **2009**, *21*, 1259.

[189] G. Lecerf, J. Tomas, S. Boyn, S. Girod, A. Mangalore, J. Grollier, S. Saighi, In *Proceedings - IEEE International Symposium on Circuits and Systems*, **2014**, pp. 1568–1571.

[190] J.-Q. Yang, R. Wang, Z. Wang, Q. Ma, J. Mao, Y. Ren, X. Yang, Y. Zhou, S. Han, *Nano Energy* **2020**, *74*, 104828.

[191] S. Dutta, V. Kumar, A. Shukla, N. R. Mohapatra, U. Ganguly, *Sci. Rep.* **2017**, *7*, 1.

[192] H. Mulaosmanovic, E. Chicca, M. Bertele, T. Mikolajick, S. Slesazeck, *Nanoscale* **2018**, *10*, 21755.

[193] A. Gruverman, M. Alexe, D. Meier, *Nat. Commun.* **2019**, *10*, 1.

[194] M. Birkholz, *Principles of X-ray Diffraction*, **2014**.

[195] N. Dix, Preparation and characterization of biferroic nanostructures with magneto electric coupling, **2017**.

[196] B. Ingham, M. F. Toney, *X-ray diffraction for characterizing metallic films*, **2013**.

[197] N. Widjonarko, *Coatings* **2016**, *6*, 54.

[198] N. D. Browning, M. F. Chisholm, S. J. Pennycook, *Nature* **1993**, *366*, 143.

[199] P. D. Nellist, S. J. Pennycook, *Ultramicroscopy* **1999**, *78*, 111.

[200] J. Verbeek, S. Hens, P. Potapov, D. Schryvers, In *Encyclopedia of Analytical Science (Second Edition)* (Eds.: Worsfold, P.; Townshend, A.; Poole, C.), **2005**, p. 324.

[201] V. J. Keast, A. J. Scott, R. Brydson, D. B. Williams, J. Bruley, *J. Microsc.* **2001**, *203*, 135.

[202] D. A. Muller, L. F. Kourkoutis, M. Murfitt, J. H. Song, H. Y. Hwang, J. Silcox, N. Dellby, O. L. Krivanek, *Science..* **2008**, *319*, 1073.

[203] M. Bosman, V. J. Keast, J. L. García-Muñoz, A. J. D'Alfonso, S. D. Findlay, L. J. Allen, *Phys. Rev. Lett.* **2007**, *99*, 086102.

[204] M. Varela, M. P. Oxley, W. Luo, J. Tao, M. Watanabe, A. R. Lupini, S. T. Pantelides, S. J. Pennycook, *Phys. Rev. B* **2009**, *79*, 085117.

[205] A. Tsurumaki, H. Yamada, A. Sawa, *Adv. Funct. Mater.* **2012**, *22*, 1040.

[206] Y. Wei, S. Matzen, G. Agnus, M. Salverda, P. Nukala, T. Maroutian, Q. Chen, J. Ye, P. Lecoeur, B. Noheda, *Phys. Rev. Appl.* **2019**, *12*, 031001.

[207] S. Monaghan, P. K. Hurley, K. Cherkaoui, M. A. Negara, A. Schenk, *Solid. State. Electron.* **2009**, *53*, 438.

[208] P. W. Peacock, J. Robertson, *J. Appl. Phys.* **2002**, *92*, 4712.

[209] M. Y. Zhuravlev, R. F. Sabirianov, S. S. Jaswal, E. Y. Tsymbal, *Phys. Rev. Lett.* **2005**, *94*, 246802.

[210] L. Wang, M. R. Cho, Y. J. Shin, J. R. Kim, S. Das, J.-G. G. Yoon, J.-S. S. Chung, T. W. Noh, *Nano Lett.* **2016**, *16*, 3911.

[211] K. Katayama, T. Shimizu, O. Sakata, T. Shiraishi, S. Nakamura, T. Kiguchi, A. Akama, T. J. Konno, H. Uchida, H. Funakubo, *Appl. Phys. Lett.* **2016**, *109*, 112901.

[212] T. Mimura, K. Katayama, T. Shimizu, H. Uchida, T. Kiguchi, A. Akama, T. J. Konno, O. Sakata, H. Funakubo, *Appl. Phys. Lett.* **2016**, *109*, 052903.

[213] K. Lee, T. Y. Lee, S. M. Yang, D. H. Lee, J. Park, S. C. Chae, *Appl. Phys. Lett.* **2018**, *112*, 202901.

[214] J. Lyu, I. Fina, R. Bachelet, G. Saint-Girons, S. Estandía, J. Gázquez, J. Fontcuberta, F. Sánchez, *Appl. Phys. Lett.* **2019**, *114*, 222901.

[215] W. Hamouda, A. Pancotti, C. Lubin, L. Tortech, C. Richter, T. Mikolajick, U. Schroeder, N. Barrett, *J. Appl. Phys.* **2020**, *127*, 0.

[216] M. C. Sulzbach, S. Estandía, X. Long, J. Lyu, N. Dix, J. Gàzquez, M. F. Chisholm, F. Sánchez, I. Fina, J. Fontcuberta, *Adv. Electron. Mater.* **2020**, *6*, 1900852.

[217] P. Katiyar, C. Jin, R. J. Narayan, *Acta Mater.* **2005**, *53*, 2617.

[218] N. F. Muhamad, R. A. Maulat Osman, M. S. Idris, M. N. Mohd Yasin, *EPJ Web Conf.*

2017, *162*, 01052.

[219] J. Delahaye, T. Grenet, *J. Phys. D. Appl. Phys.* **2016**, *49*, 395303.

[220] M. Y. Zhuravlev, Y. Wang, S. Maekawa, E. Y. Tsymbal, *Appl. Phys. Lett.* **2009**, *95*, 052902.

[221] H. Ryu, H. Wu, F. Rao, W. Zhu, *Sci. Rep.* **2019**, *9*, 20383.

[222] P. Calka, M. Sowinska, T. Bertaud, D. Walczyk, J. Dabrowski, P. Zaumseil, C. Walczyk, A. Gloskovskii, X. Cartoixà, J. Suñé, T. Schroeder, *ACS Appl. Mater. Interfaces* **2014**, *6*, 5056.

[223] P. Calka, E. Martinez, V. Delaye, D. Lafond, G. Audoit, D. Mariolle, N. Chevalier, H. Grampeix, C. Cagli, V. Jousseaume, C. Guedj, *Nanotechnology* **2013**, *24*, 085706.

[224] Y. Wei, S. Matzen, C. P. Quinteros, T. Maroutian, G. Agnus, P. Lecoeur, B. Noheda, *Quantum Mater.* **2019**, *4*, 1.

[225] M. C. Sulzbach, S. Estandía, J. Gàzquez, F. Sánchez, I. Fina, J. Fontcuberta, *Adv. Funct. Mater.* **2020**, *2002638*, 1.

[226] Y. Y. Chen, B. Govoreanu, L. Goux, R. Degraeve, A. Fantini, G. S. Kar, D. J. Wouters, G. Groeseneken, J. A. Kittl, M. Jurczak, L. Altimime, *IEEE Trans. Electron Devices* **2012**, *59*, 3243.

[227] M. Lanza, G. Bersuker, M. Porti, E. Miranda, M. Nafría, X. Aymerich, *Appl. Phys. Lett.* **2012**, *101*, 193502.

[228] S. U. Sharath, T. Bertaud, J. Kurian, E. Hildebrandt, C. Walczyk, P. Calka, P. Zaumseil, M. Sowinska, D. Walczyk, A. Gloskovskii, T. Schroeder, L. Alff, *Appl. Phys. Lett.* **2014**, *104*.

[229] X. Wu, P. Zhou, J. Li, L. Y. Chen, H. B. Lv, Y. Y. Lin, T. A. Tang, *Appl. Phys. Lett.* **2007**, *90*, 11.

[230] B. D. Pelatt, R. Ravichandran, J. F. Wager, D. A. Keszler, *J. Am. Chem. Soc.* **2011**, *133*, 16852.

[231] S. J. Clark, J. Robertson, *Appl. Phys. Lett.* **2007**, *90*, 1.

[232] M. Cardona, *Phys. Rev.* **1965**, *140*.

[233] R. Schafranek, S. Li, F. Chen, W. Wu, A. Klein, *Phys. Rev. B - Condens. Matter Mater. Phys.* **2011**, *84*, 1.

[234] M. Qian, I. Fina, F. Sánchez, J. Fontcuberta, *Small* **2019**, *15*, 1805042.

[235] Z. Xi, C. Zheng, Z. Wen, *ACS Appl. Mater. Interfaces* **2018**, *10*, 6024.

[236] T. Schenk, M. Pešić, S. Slesazeck, U. Schroeder, T. Mikolajick, *Reports Prog. Phys.* **2020**, *83*.

[237] S. Boyn, V. Garcia, S. Fusil, C. Carrétéro, K. Garcia, S. Xavier, S. Collin, C. Deranlot, M. Bibes, A. Barthélémy, *APL Mater.* **2015**, *3*, 061101.

[238] S. Oh, H. Kim, A. Kashir, H. Hwang, *Appl. Phys. Lett.* **2020**, *117*, 0.

[239] W. J. Merz, *Phys. Rev.* **1950**, *78*, 52.

[240] K. Aryana, J. T. Gaskins, J. Nag, D. A. Stewart, Z. Bai, S. Mukhopadhyay, J. C. Read, D. H. Olson, E. R. Hoglund, J. M. Howe, A. Giri, M. K. Grobis, P. E. Hopkins, *Nat. Commun.* **2021**, *12*, 774.

[241] J. Y. Jo, S. M. Yang, T. H. Kim, H. N. Lee, J. G. Yoon, S. Park, Y. Jo, M. H. Jung, T. W. Noh, *Phys. Rev. Lett.* **2009**, *102*, 045701.

[242] M. Materano, P. D. Lomenzo, H. Mulaosmanovic, T. Mikolajick, M. Hoffmann, A. Toriumi, T. Mikolajick, U. Schroeder, *Appl. Phys. Lett.* **2020**, *117*, 262904.

[243] T. Y. Lee, K. Lee, H. H. Lim, M. S. Song, S. M. Yang, H. K. Yoo, D. I. Suh, Z. Zhu, A. Yoon, M. R. Macdonald, X. Lei, H. Y. Jeong, D. Lee, K. Park, J. Park, S. C. Chae, *ACS Appl. Mater. Interfaces* **2019**, *11*, 3142.

[244] S. Oh, H. Hwang, I. K. Yoo, *APL Mater.* **2019**, *7*.

[245] M. Jerry, S. Dutta, A. Kazemi, K. Ni, J. Zhang, P. Y. Chen, P. Sharma, S. Yu, X. S. Hu, M. Niemier, S. Datta, *J. Phys. D. Appl. Phys.* **2018**, *51*, 434001.

[246] H. Tan, S. Majumdar, Q. Qin, J. Lahtinen, S. Van Dijken, S. van Dijken, *Adv. Intell. Syst.* **2019**, *1*, 1900036.

[247] Y. Li, Y. Zhong, J. Zhang, L. Xu, Q. Wang, H. Sun, H. Tong, X. Cheng, X. Miao, *Sci. Rep.* **2014**, *4*, 4906.

[248] R. Kempter, W. Gerstner, L. J. van Hemmen, *Pysical Rev. E* **1999**, *59*, 4498.

[249] R. Guo, Y. Zhou, L. Wu, Z. Wang, Z. Lim, X. Yan, W. Lin, H. Wang, H. Y. Yoong, S. Chen, Ariando, T. Venkatesan, J. Wang, G. M. Chow, A. Gruverman, X. Miao, Y. Zhu, J. Chen, *ACS Appl. Mater. Interfaces* **2018**, *10*, 12862.

[250] S. Fujii, Y. Kamimuta, T. Ino, Y. Nakasaki, R. Takaishi, M. Saitoh, In *2016 Symposium on VLSI Technology Digest of Technical Papers*, **2016**, pp. 2–3.

[251] B. Max, M. Hoffmann, S. Slesazeck, T. Mikolajick, *IEEE J. Electron Devices Soc.* **2019**, *7*, 1175.

[252] G. Bersuker, D. C. Gilmer, In *Advances in Non-volatile Memory and Storage Technology*, Woodhead Publishing Limited, **2014**, pp. 288–340.

[253] G. Radaelli, Electric field control of remanent states in magnetic and ferroelectric tunnel junctions, Politecnico di Milano, **2014**.

[254] A. Zenkevich, M. Minnekaev, Y. Matveyev, Y. Lebedinskii, K. Bulakh, A. Chouprik, A. Baturin, K. Maksimova, S. Thiess, W. Drube, *Appl. Phys. Lett.* **2013**, *102*, 062907.

[255] Y. W. Yin, J. D. Burton, Y.-M. Kim, A. Y. Borisevich, S. J. Pennycook, S. M. Yang, T. W. Noh, A. Gruverman, X. G. Li, E. Y. Tsymbal, Q. Liu, *Nat. Mater.* **2013**, *12*, 397.

List of Figures

Figure 1. 1. Hierarchy of dielectric materials. 7
Figure 1. 2. Evolution of polarization in the function of the external electric field. The remnant polarization (P_R), coercive field (E_C), and saturated polarization (P_S) for both electric field polarities can be extracted. 8
Figure 1. 3. Sketch of charge distribution σ(x) at the interfaces of the ferroelectric layer with (a) ideal metal or (b) non-ideal metal electrodes. In (b), the metal screening charges are spread over a finite screening length λ_{eff}. In non-ideal metals, not all surface charges are compensated by the metal. Electrostatic potential profile φ(x) in the case of (c) ideal metal and (d) non-ideal metal electrodes. The incomplete compensation of charges at the interface gives rise to an internal depolarizing field E_d in the ferroelectric layer. 9
Figure 1. 4. Non-uniform ferroelectric domain distribution and memristive behavior. Measurements performed in Co/$BiFeO_3$ (4.5 nm)/$Ca_{0.96}Ce_{0.04}MnO_3$ tunnel junctions. (a) Resistance dependence on the writing voltage for 100 ns pulses. Intermediate resistance states are stabilized by decreasing the maximum amplitude. (b) Correlation of resistance state and fraction of domains with polarization pointing down (s) obtained by PFM images from 10 different junctions. PFM image for six resistance states in the same junction is shown in the side. The black line is a calculation from the parallel resistance model sketched in (c). Image adapted from [37]. 11
Figure 1. 5. Sketch of the capacitor-like structure of a ferroelectric tunnel junction. The ferroelectric grains' polarization points either towards the (a) top or the (b) bottom electrode. 12
Figure 1. 6. Sketch for electrical transport mechanisms in ferroelectric tunnel junctions. (a) Direct tunneling (DT), (b) Fowler-Nordheim tunneling (FNT), and (c) thermionic injection (TI). 12
Figure 1. 7. Electrostatic changes in asymmetric FTJ. The metallic electrodes M_1 and M_2 have screening lengths λ_1 and λ_2, respectively. Charge distribution at the interfaces of electrode/ferroelectrics for polarization (a) P→ and (b) P←. Due to an incomplete screening of the polarization charges, a finite depolarization field E_d emerges with direction-dependent on P. Electrical potential profile for (c) P→ and (d) P←. (e, f) Energy profile, where ϕ_{ON} and ϕ_{OFF} average barrier heights are related to the polarization direction and lead to different tunneling resistances. Adapted from [75]. 15
Figure 1. 8. Theoretical current densities considering direct tunneling (DT), thermionic emission (TI), and Fowler-Nordheim tunneling (FNT). (a) Current density (J) versus voltage (V) for 1.2, 3.2, and 4.8 nm BTO tunnel junction. (b) J versus V for 3.2 nm junction, showing the contribution of each conduction mechanism. The solid and dashed lines represent polarization P pointing right and left, respectively. Adapted from [37,74]. 17
Figure 1. 9. Crystal phases are illustrated for ZrO_2, where Zr atoms are represented in green and O atoms in red. (a) Tetragonal structure with space group $P4_2$/nmc. (b) Monoclinic phase with space group $P2_1$/c, where β = 80º. (c, d) Non-centrosymmetric orthorhombic phase with space group $Pca2_1$ in which polarization is observed for [001] and [001] directions, respectively. The O

atoms believed to be responsible for the polarization are highlighted in gold. Adapted from [115]. *21*
Figure 1. 10. (a) Sketch showing the lattice mismatch between the LSMO electrode and the substrates. (b) X-ray diffraction 2θ-χ frames of the HZO/LSMO bilayers. Intense diffraction peaks from the substrate and LSMO can be identified. The o-HZO (111) peak is a bright circular spot in the films grown in most substrates, whereas the m-HZO (002) reflection is generally elongated along χ, signaling higher mosaicity. Adapted from [53].. *23*
Figure 1. 11. (a) Polarization curves dependent on the external electric field recorded at 1 kHz in Pt/HZO/LSMO//STO epitaxially grown films. Taken from [127]. (b) Polarization-voltage curves collected in Pt/HZO (9.5 nm)/LSMO heterostructures epitaxially grown on different substrates as indicated. Taken from [53]. *24*
Figure 1. 12. (a) Current-voltage curve collected in Sr:HfO_2 for pristine, woken-up, and fatigued states. (b) Extracted dependence of positive and negative remnant polarization with the number of cycles. Adapted from [130]. *25*
Figure 1. 13. Cross-section STEM images on Gd:HfO_2 in the (a) pristine, (b) wake-up, and (c) fatigued states showing the transition of the bulk monoclinic and the tetragonal at the interface with the electrode to orthorhombic. Taken from [130].. *26*

Figure 2.1. Sketch of a plano-parallel capacitor with area A. *35*
Figure 2. 2. Sketch and photo of PLD setup at ICMAB. Adapted from [76]. *36*
Figure 2. 3. (a) Sketch of deposition arrangement of platinum top electrodes using sputtering. (b) Optical microscopy of Pt circular electrodes with a diameter of 20 μm..................................... *37*
Figure 2. 4. Top-bottom configuration for electric connections used to measure ferroelectric and transport measurements. *38*
Figure 2. 5. (a) Sketch of Lakeshore EMPX-HF system, including controls of vacuum and temperature. (b) Picture from the sample stage and probes connected to a sample. (c) Details from ZN50R-03-W tip. Taken from [76]. *39*
Figure 2. 6. (a) Sketch of pulses applied on the junction for transport characterization. (b) Reading I(V) recorded after polarization (writing) with positive or negative V_w. The junction's resistance is calculated for $V_R = 0.9$ V, indicated with a black vertical line. (c) Logarithmic scale of I(V) current. A horizontal dashed line around 10 pA indicates experimental setup sensitivity......................... *40*
Figure 2. 7. (a) Sketch of Method 1 for ER measurement. (b) Representative resistance loop obtained from the sequence in (a). (c) Sketch of Method 2. (d) Resistance dependence on writing pulse amplitude obtained from the sequence (c)... *41*
Figure 2. 8. Equivalent circuit from experimental setup and sample. *43*
Figure 2. 9. (a) Applied voltage signal to Pt/HZO (2 nm)/LSMO junction and (b) measured current. The fitting indicated by the dashed line calculates a $\tau_{RC} = 0.5$ μs.... *44*
Figure 2. 10. (a) Sketch of the voltage pulse sequence used for measurement with frequency v_0 using DHM mode. (b) I(V) curve obtained from (a). It is possible to identify coercive voltages (V_c^-

,V_c^+) and displacement current (I_{DE}). (c) The integration of current in time results in the polarization curve P(V). 45
Figure 2. 11. (a) Sequence of pulses applied to the sample using the PUND technique. (b) Representation of current response corresponding to each voltage pulse. (c) Final I(V) obtained by ($I_P - I_U$) and ($I_N - I_D$). The only current contribution visible is related to ferroelectric switching. 47
Figure 2. 12. Comparison between I(V) and P(V) curves recorded at 5 kHz with (a, b) DHM, (c, d) DLCC, and (e, f) PUND techniques for a junction with structure Pt / HZO (4.6 nm) / LSMO / GSO (001). 48
Figure 2. 13. (a) Sketch of pulse train applied for the training measurement. (b) I(V) for $\nu_{triangle}$ = 1 kHz obtained in pristine junction (black line) after $N_1 = 10^3$ cycles (pink line) and after $N_2 = 10^4$ cycles (blue line). (c) I(V) recorded with PUND at 5 kHz before and after junction training shown in (b). 51
Figure 2. 14. (a) Sketch of measurement. Reading I(V) is recorded after (t_1 and t_2) writing pulse. (b) Example of the evolution of resistance in time in which total retention time = 1000 seconds. 52
Figure 2. 15. (a) Sequence of writing pulses consists of alternating positive and negative V_w with a fixed duration (τ_D). (b) Example of endurance measurement for 100 pulses obtained with writing pulse sequence in (a). 53
Figure 2. 16. (a) Complete train of voltage pulses applied to the capacitor and measured current response. Junction is pre-polarized with V_w = + 4 V pulse with τ_w = 1μs duration. (b) Overlapped current peaks and applied voltage for the two consecutive negative pulses with indications of displacive peak and leakage plateau associated with tunneling through the HZO barrier. 54
Figure 2. 17. (a) The sequence of pulses with amplitude ± V_w and duration = τ_w applied on tunnel junction. (b) Resistance dependence on the number of pulses (N_p). Green dashed lines represent the fitting results of resistance growth/decay, where τ_p = 1.28 ± 0.22 and τ_d = 0.41 ± 0.04. The different values obtained for τ_d and τ_p show the potentiation/depression asymmetry. 56
Figure 2. 18. (a) Sketch of pre- and post-neuron connected to a synapse, whose conductance is modulated by the delay time Δt between pre- and post-synaptic pulses. (b) Sketch of HZO ferroelectric tunnel junction, where the top electrode is biased, and the bottom electrode remains grounded. (c) The sequence of waveforms (spikes) applied on the top electrode for spike-timing-dependent plasticity measurement. Both spikes have a duration of 50 μs, as indicated in the top panel. The bottom panel shows the superimposed spikes for Δt = + 20 μs. (d) V_{total} waveforms calculated for different Δt that are applied to the top electrode sequentially. 58
Figure 2. 19. Sketch of AFM mechanism. 59
Figure 2. 20. (a) Sketch of Bragg's law. (b) Cubic unit cell with lattice parameters in three independent directions and identification of lattice plane (111). (c) A set of parallel planes (110) are represented in a cubic cell. 61
Figure 2. 21. Axes and degrees of freedom for rotation in an XRD measurement. 61

Figure 2. 22. Representation of structural differences between (a) polycrystalline and (b) epitaxial film. (c) Top and (d) cross-sectional view of four crystal variants from m-HZO with 90º rotation in-plane 62
Figure 2. 23. (a) Illustration of image data acquired from the 2D detector. The horizontal axis corresponds to an increasing 2θ scan, and the arc represents increasing χ. The rectangle indicates data recorded by a 1D detector. (d) Example of 2θ-χ frame collected at HZO (4.6 nm) / LSMO / STO (001) sample. By integrating within a χ range (indicated region), a θ-2θ plot can is obtained. 63
Figure 2. 24. Correspondence between EEL spectra, the transition of electrons from inner shell states to the conduction band, and appearance of ELNES fine structure used to identify element distribution in region scanned with the electron beam. Image adapted from [200]. 65
Figure 2. 25. (a) ADF image acquired simultaneously with (b) electron EEL spectrum image in sample Pt / STO (2 nm) HZO (4.6 nm) / LSMO / STO (001). 66

Figure 3. 1. (a) Sketch of the sample and contact arrangement for electrical measurement. (b) XRD 2θ-χ frame of the sample represented in (a) and corresponding θ-2θ scan obtained by integration of χ within ± 10º angular range. (c) Current-voltage, I(V), curve recorded in junction J_1 with DLCC at 1 kHz and V_{max} = 4 V. Yellow dashed vertical lines indicate the coercive voltage ($V_c \approx \pm 2$ V). (d) Corresponding polarization P(V) curve. 71
Figure 3. 2. (a) I(V) loop from Pt / HZO / LSMO // STO measured at 5 kHz with DLCC and V_{max} = 4.5 V before performing R(V_w) measurement. (b) Sketch of the writing/reading measurement protocol. The writing amplitude (V_w), pulse duration (τ_w), dwell time (τ_D), and reading voltage V_R are indicated. (c) Dependence of the junction resistance R for $|V_w| \leq 4.5$ V. Three consecutive cycles are shown to illustrate reversibility. (d) R(V_w) sequence of two cycles for $|V_w| \leq 6$ V showing irreversibility. Dashed vertical lines indicate V_c of the HZO film extracted from (a). 72
Figure 3. 3. (a) Resistance dependence on V_w in Pt / HZO / LSMO // STO junction for positive (V_w > 0) and negative (V_w < 0) writing pulses. (b) Extracted value of electroresistance from data in (a). (c) I(V) curve recorded after writing pulse V_w = + 4.5 V (purple symbols) and – 4.5 V (green symbols) during reading step. Solid lines are the results from the fitting using the Brinkman model described in the text. (d) Sketch of junction energy barrier profile upon P reversal, in which ϕ_{LSMO}, ϕ_{Pt}, and t_{eff} are extracted from the fitting in (c). The effective thickness reduction is sketched in the Pt/HZO interface, although it does not necessarily happen at this position. 74
Figure 3. 4. Cross-section atomic-resolution images from 9 nm thick HZO films with heterostructure (a) HZO/LSMO//STO, (b) HZO/LSMO//GSO, and (c) HZO/LSMO//LSAT. Images were acquired along the [110] zone axes of the substrates. Monoclinic grains are signaled in red and orthorhombic grain in blue. (b, d, f) Higher magnification images of the grain boundaries. Red and blue circles represent the projected monoclinic (space group $P2_1/c$) and orthorhombic (space group $Pca2_1$) structures. The epitaxial relationship for the monoclinic phase is [010]m-HZO(001)//[110]LSMO(001), [001]m-HZO(001)//[001]LSMO(001) and [100]m-HZO(001)//[1-10]LSMO(001). In the case of the orthorhombic phase, it is [-211]o-HZO(111)//[110]LSMO(001)

and [111]o-HZO(001)//[001]LSMO(001), where all indices refer to the cubic or pseudocubic unit cell. LSMO and the substrates have a cube-on-cube epitaxial relationship. 77
Figure 3. 5. Resistance dependence on the writing voltage V_w in Pt/HZO/LSMO junctions grown on (a) GSO, (b) STO, and (c) LSAT substrates. Data from (b) is taken from Figure 3.3(a) for comparison. (d, e, f) Electroresistance loops measured in junctions with structure indicated. The loops are fully reversible when $V_{max} < V_{GB}$. ER value in each case is indicated. 79

Figure A3. 1. (a) I(V) curve recorded at 1 kHz in the Pt/HZO/LSMO//STO tunnel junction from Figure 3.1(c) in the main text. The black curve corresponds to the raw measurement obtained with DLCC compensation mode. The red curve is obtained after a second compensation to subtract the electric susceptibility (χ) contribution. (b) P(V) curves are obtained by integration of the current in time. The black curve corresponds to the DLCC raw measurement and the red curve after the subtraction of χ. 80
Figure A3. 2. I(V) curve recorded at 1, 5, and 10 kHz in ferroelectric tunnel junction with structure Pt/HZO/LSMO//STO. Spurious peaks emerge close to the maximum voltage at high frequency. 81
Figure A3. 3. (a) I(V) curve collected at 5 kHz and DLCC in junction J_2 at its pristine state and after the application of writing pulse, V_w = ± 7.5 V. Vertical dashed lines indicate that the coercive field does not change. (b) I(V) curves measured in junction J_5 show the irreversible change in junction after V_w = ± 8 V. 81
Figure A3. 4. R(V_w) curves collected in junctions J_6, J_7 and J_8 in sample Pt / HZO (4.6 nm) / LSMO / STO (001) using (a) τ_D = 0.2 s, (b) τ_D = 0.5 s (c) τ_D = 1 s as delay time between writing pulse are reading resistance but fixed writing time duration τ_w = 100 µs. Inset in (b) shows a sketch of writing and reading pulses with the corresponding duration and delay time. The transition from Region I to II is indicated by vertical dashed line V_{GB}. In junctions J_9, J_{10} and J_{11}, the τ_w was varied from (c) 10 µs, (d) 100 µs to (e) 500 µs when the delay time was fixed at τ_D = 0.5 s. 82
Figure A3. 5. I(V) curves recorded in the order labeled in the panels for (a, b) V_w = ± 4.5 V and (c) V_w = ± 6 V. Solid lines represent results from the fitting using the Brinkman model.[73] 83
Figure A3. 6. Large field of view cross-section images of (a) HZO/LSMO//STO, (b) HZO/LSMO//GSO, and (c) HZO/LSMO/LSAT. Images were obtained along the [110] zone axes of the substrate. Scale bar of 10 nm is indicated in each image. 85
Figure A3. 7. I(V) curves measured in Pt/HZO/LSMO junctions grown in STO, LSAT, or GSO substrates. Measurement was done at 5 kHz using DLCC. The junction in LSAT has a small switching peak around 2 V. 85
Figure A3. 8. (a) I(V) curve recorded at Pt/HZO/LSMO//TSO sample at 5 kHz with DLCC. (b) Resistance dependence for positive (purple symbols) and negative (green symbols) writing amplitude (V_w). 86

Figure 4. 1. Sketch of epitaxial ferroelectric HZO films grown on $SrTiO_3$//LSMO substrate containing o- and m-HZO crystallites, few nanometers in size and grain boundaries (GB-I and GB-II) within. (a) HZO film is covered by a metallic Pt electrode. (b) A dielectric layer is inserted

between the HZO film and the metallic Pt electrode. (c) Sketch of the dependence of the resistance of ferroelectric HZO barrier on the writing voltage using the Pt electrode on the HZO surface as in (a). The purple curve represents R values when a positive bias is applied at the Pt electrode (P pointing towards LSMO), and the green curve corresponds to a negative bias being applied to Pt (P pointing towards platinum). (d) Corresponding $R(V_w)$ sketch for heterostructure in (b). The voltages V_c and V_{GB} are the coercive field of the ferroelectric and the opening of the conducting channel within the grain boundaries of the HZO film, respectively. Up-down arrows indicate the polarization direction, and dot-filled arrows the ionic motion. 90
Figure 4. 2. X-ray diffraction 2θ-χ frames and corresponding θ-2θ integrated within $\chi = \pm 10^o$ angular range for (a) HZO, (b) HZO/STO1, (c) HZO/STO2 films, (d) HZO/AlO1 and (e) HZO/AlO2. 92
Figure 4. 3. (a) Current-voltage curves with $V_{max} = 4.5$ V and (b) corresponding P(V) loops of junctions in sample HZO, HZO/STO1, HZO/AlO1 recorded at 5 kHz with PUND. Inset shows measurement configuration on the heterostructure. (c) I(V) curves and (b) corresponding P(V) were measured under the same conditions in samples HZO/STO2 and HZO/AlO2. HZO curves are included for comparison purposes. 94
Figure 4. 4. $R(V_w)$ data of junctions in (a, d) HZO, (b) HZO/STO1, (c) HZO/STO2 samples after positive ($V_w > 0$, purple symbols) and negative ($V_w < 0$, green symbols) writing pulse. Equivalent data for (e) HZO/AlO1 and (f) HZO/AlO2 devices. 95
Figure 4. 5. I(V) curves collected at 5 kHz with PUND on (a) GSO//HZO and GSO//HZO/STO2 and (b) HZO and HZO/STO2 samples grown on STO substrate. Insets show corresponding P(V) loops. The resistance $R(V_w)$ recorded on indicated junctions grown on (c) GSO and (d) STO substrate. Data from (c) and (d) are adapted from Figures 4.3 and 4.4. For clarity, HZO/STO2 resistance data have been multiplied by 10. Vertical dashed lines in (c, d) indicate V_{GB}. 98
Figure 4. 6. Resistance values recorded after writing with $V_w = \pm 5$ V on a set of 15 junctions on (a) HZO, (b) HZO/STO1, and (c) HZO/AlO1 sample. Reproducibility of $R(V_w)$ loops collected consecutively on (d) uncapped and (e, f) capped samples as indicated. (g, h, i) Endurance of resistive states on indicated junctions for 300 pulses of $V_w = \pm 5$ V and $\tau_w = 300$ µs. After each writing pulse, the resistance was measured at $V_R = 0.9$ V. 100
Figure 4. 7. Z-contrast cross-section image from HZO/STO2 heterostructure viewed along the [110] STO substrate zone axis. The layers corresponding to STO substrate, LSMO, HZO, STO capping, and Pt layer can be distinguished. (b) Zoom of region market in yellow in (a) where two GB-I are visible as well as the STO covering of the HZO film. (c) The top panel shows the HAADF image acquired simultaneously with the electron EEL spectra. The bottom panel shows an elemental map that was obtained by signal acquisition from Pt-M (red), Ti-L (blue), and Zr-L_3 (yellow) edges. Vertical dashed lines indicate the position of GB-I. 101
Figure 4. 8. The top panel shows a HAADF image collected simultaneously with EEL spectra images from a large area in the sample HZO/STO2. In the lower panels, the corresponding EELS elemental maps are generated from the Pt-M, Sr-L_3, Ti-L, Zr-L_3, Hf-M, La-L, and Mn-L edges. Even though no grain boundaries can be seen in this large image, Ti's continuous covering, thus,

STO, on HZO, can be confirmed. The lowest panel, Pt, Ti, and Zr signals are represented by red, blue, and green, respectively. *102*
Figure 4. 9. Cross-section Z-contrast image of HZO/STO1 heterostructure viewed along the [110] STO substrate zone axis. The grain boundaries (a) GB-I and (b) GB-II are indicated. *103*
Figure 4. 10. (a) HAADF cross-section image of the HZO/STO2 heterostructure, where each layer can be differentiated. The arrows mark the region where the different spectra were obtained. (b) O-K edge peak obtained from the HZO close to the STO capping (uppermost region) and the HZO just above the LSMO layer (lowermost region). (c) Ti-L edge spectra collected from STO at the substrate and at the capping layer. Whereas the edge of the STO in the substrate has the fine structure of Ti^{4+}, the Ti-L edge of the STO in the capping layer has a fine structure of Ti^{3+}, indicating that the STO capping layer is reduced. *104*

Figure A4. 1. ER(V_w) data for (a) HZO, (b) HZO/STO1, and (c) HZO/STO2 samples. The number of junctions measured in each sample is indicated in the corresponding graph. *106*
Figure A4. 2. Topography images from AFM collected on the surface of (a) HZO, (b) HZO/STO2, and (c) HZO/AlO2 samples. The diagonal line in (b) is mechanical damage caused in the surface of the film due to manual manipulation of the sample. *106*

Figure 5. 1. AFM topography images for (a) 2 nm, (b) 3 nm, and (c) 5 nm HZO films grown on GSO substrates. Main images are acquired in a region with an area (5x5) $\mu m^{2,}$ and the inset shows a zoomed image from (1x1) μm^2 scan. *110*
*Figure 5. 2. XRD 2θ-χ frames of HZO/LSMO bilayers on $GdScO_3$ for samples with a) 2, b) 3, and c) 5 nm HZO, respectively. Integrated scan along χ and corresponding zoom around o-HZO (111) reflection are also included. The bright spots marked with an * are an artifact from the detector.* *111*
Figure 5. 3. A cross-section HAADF-STEM image of the HZO/LSMO heterostructure was recorded along the substrate's pseudocubic [110] zone axes. (a) The film's region where the Pt top electrode, HZO, LSMO, and GSO films can be differentiated. One m-HZO (red "m" grain is indicated next to another o-HZO (blue "o"). (b) Enlarged view of the marked region in which the m- and o-HZO grains are indicated. The inset shows the monoclinic grain with the monoclinic phase's simulated cation sublattice (space group $P2_1/c$) superimposed. *113*
Figure 5. 4. (a) PFM phase and amplitude loops of HZO (2 nm) pristine and voltage-cycled (N_C = 100) sample. Inset: illustration of signal (laser) collection and monitoring cantilever deformation. PFM phase map collected in (10 x 10) μm^2 region for (b) pristine and (c) cycled sample (N_C = 3). Bright and dark regions were obtained by poling with + 6 V and - 6 V, respectively. Inset in (c) shows (5 x 10) μm^2 PFM phase map collected in a region poled with a different ("HZO") pattern. (d) Phase dependence on the distance acquired in horizontal dashed lines shows in (b) and (c). *114*
Figure 5. 5. (a) I(V) curves collected at 1 kHz and V_{max} = 3 V with DHM mode in pristine junction, after N_c = $5{\cdot}10^3$ and 10^4 cycles. Inset shows the electric arrangement of electrodes for electric

measurements. (b) Resistance dependence on the writing voltage amplitude (duration 300 μs) was performed in a pristine junction, where no significant electroresistance is observed. Five sequential loops are depicted. *116*
Figure 5. 6. (a) Sketch of the equivalent circuit used for fitting I(V) curves. The current has two contributions: tunneling and leakage, represented here as a parallel resistance. R's value increases as the sample are cycled, and the leakage contribution to the I(V) is reduced. (b) Calculated χ^2 *from fittings using only the Brinkman model (black symbols) and using the Brinkman model associated with a parallel resistance (red symbols). I(V) curves from (c) pristine device and (d) after* $N_c = 10^4$ *cycles and associated fittings using both models.* *117*
Figure 5. 7. (a) Current-voltage I(V) recorded in 2 nm HZO junction at 5 kHz and $V_{max} = 4$ *V with PUND after* $N_c = 10^4$ *training cycles. (b) P(V) loop obtained by integrating the current in (a). (c) Reading I(V) curves collected after pre-polarizing with* $V_w = +5$ *V (purple symbols) and* $V_w = -5$ *V (green symbols). Inset: logarithm scale of current (units in the main panel). (d) Resistance dependence on writing voltage amplitude in junction after* 10^4 *cycles. The junction is the same as in (a, b). Five sequential loops are shown for each* V_{max}*. Dashed vertical lines in (b) and (d) indicate the coercive voltages (*V_c^+*,* V_c^-*).* *118*
Figure 5. 8. (a) Endurance of OFF/ON resistive states obtained by applying 300 alternated writing pulses with amplitude $V_w = \pm 8$ *V and duration* $\tau_w = 300$ *μs. The junction has been previously trained by* $N_c = 10^4$ *cycles. (b) Retention of R states after writing pulse with an amplitude as indicated and* $\tau_w = 300$ *μs was applied to 2 nm HZO device. Junction in (b) is different from the one measured in (a). However, both have been cycled* $N_c = 10^4$ *previously.* *120*
Figure 5. 9. (a) Pulse train with $N_p = 12$ *positive writing pulses followed by* $N_p = 12$ *negative and (b) resistance dependence on the number of pulses for a 2 nm HZO tunnel junction. Each symbol represents the amplitude and duration of the writing pulses and is indicated in the label. (c) Voltage pulse sequence applied to the junction for repetition of measurement in (a) for eight potentiation/depression cycles and (d) corresponding resistance dependence on the pulse number. Symbol colors are the same as the label in (a).* *121*
Figure 5. 10. (a) Sketch of the pre- and post-neuron and synapse connecting them. Electrical impulse (b) Sketch of the electrical arrangement to characterize spike-timing-dependent plasticity of 2 nm HZO junction. (c) Pre- and post-synaptic voltage waveforms (spikes) applied on the platinum top electrode while the bottom electrode remains grounded. The duration of each pulse is 50 μs. (d) Modulation of conductance ΔG *in the function of the* Δt*.* *124*
Figure 5. 11. I(V) and P(V) loops recorded at 5 kHz with PUND in HZO ferroelectric tunnel junction with (a) 3 and (b) 5 nm. These loops were obtained after training each junction with $N_c = 2.10^3$ *and 8 cycles for 3 and 5 nm, respectively. Resistance dependence on* V_w *was obtained before cycling in HZO with (c) 3 and (d) 5 nm thickness. Resistance loops collected for (e) 3 and (f) 5 nm HZO capacitors after training. All R(*V_w*) data was obtained by applying writing pulses with 300 μs duration.* *126*
Figure 5. 12. ON and OFF states dependence on HZO thickness collected in pristine and cycled junctions as indicated. *127*

Figure A5. 1. Zoom around o-HZO (111) peak of the integrated scans in Figure 5.2 for 2, 3, and 5 nm sample. Data shows an absence of m-HZO peak, indicated by the black vertical dashed line. The narrow peak at ≈ 40º is associated with the Pt (111) reflection due to Pt electrodes. 128
Figure A5. 2. XRD 2θ scan in HZO films with 2, 3 and 5 nm in (a) 20º < 2θ < 50º and (b) 24º < 2θ < 36º ranges. 129
Figure A5. 3. PFM (a) amplitude and (b) phase images collected on HZO (2 nm) sample in the pristine state. After the region was field-cycled three times, the measurement was repeated by poling with ± 6 V and acquiring PFM (c) amplitude and (d) phase. 129
Figure A5. 4. (a) Derivative of polarization curve from Figure 5.7(b) with the voltage (dP/dV) and (b) Derivative of resistance loops with writing voltage amplitude (dR/dV_w) from Figure 5.7(d). Vertical dashed lines show coincidence of maxima peaks, suggesting a common origin. 130
Figure A5. 5. Current-voltage curve for (a, c) negative-positive-negative voltage excursion and (b, d) for positive-negative-positive. Identical curves discard resistive switching mediated by filament formation mechanism, which would rise a hysteresis with different direction (counter-clockwise or clockwise) 131
Figure A5. 6. PFM amplitude and phase loops collected on N_c = 100 cycled HZO (3 nm) sample on (a) film surface and on (b) platinum top electrode. (c) I(V) and P(V) loops recorded at 5 kHz with PUND in a previously $N_c = 10^4$ cycled electrode of the same sample. 132
Figure A5. 7. PFM (a) amplitude and (b) phase images collected on HZO (3 nm) sample in the pristine state. After cycling three times, the (c) amplitude and (d) phase were measured again. No visible difference can be seen in the images. 133
Figure A5. 8. Current density measured in (a) pristine and (b) cycled junction for 2, 3, and 5 nm thick HZO tunnel barriers. 134

Figure A. 1. Sketch of basic procedures in optical lithography. (a) After surface cleaning, the wafer is ready for lithography. (b) The photoresist is deposited on the surface, and the sample is soft bake on a hot plate. (c) Exposition to UV light through a mask, which defines the pattern to be transferred. (d) The sample is immersed in solvent for removal of regions that were exposed to UV light. (e) Argon ion beam etching removes material from regions unprotected by the photoresist. (f) A layer of metal is deposited on the sample, covering the regions unprotected. (g) The sample is immersed in acetone for lift-off, i.e., complete removal of photoresist. (h) Final patterned sample. 139
Figure A. 2. Alignment marks are used to align the first lithography pattern with possible sequential steps. They are located at the edges of the substrate. Image obtained after photoresist was developed. Bright color corresponds to the color of the substrate, and dark color is the color of the resist that was not removed. 140
Figure A. 3. MESA structure patterning. (a) Platinum 20 nm thick continuous layer deposition in samples 1 – 7 by sputtering. (b) Top view of Mask 1 image. (c) After photoresist deposition, the sample was exposed to radiation using Mask 1, and resist was developed. (d) Argon ion beam

etching of sample for removal of material not protected by resist. (e) The final structure was obtained after resist lift-off. (f) Top view optical microscopy from MESA structure after step (e). *143*
Figure A. 4. FTJ patterning. (a) Top view image of Mask 2. (b) Resist deposition and image reversal steps to ensure region exposed to UV radiation remains on the sample. (c) Argon ion beam etching to remove platinum layer not covered by the resist. (d) Sample structure after etching. (e) Deposition of SiO_2 layer to sustain FTJ pillar and insulate the top and bottom electrodes electrically. (f) Sample after resist lift-off in acetone. Inset: Top view optical microscopy from the sample at this stage indicating where the FTJ pillar is located.. *145*
Figure A. 5. Contact deposition. (a) The photoresist was deposited, and Mask 3 (inset) was drawn with the laser writer. The sample was developed, and the region exposed to UV is removed. (b) Deposition of chromium and gold, respectively, fills the gaps in the resist and pattern macroscopic electrical contacts. (d) Side view of the sample indicating support of Au/Cr layer by SiO_2 film. (e) Side view showing the location of FTJ and cross-section of the sample. (f) Top view optical microscopy of junction B9 illustrating where access to top and bottom electrodes are located.146
Figure A. 6. Optical microscopy image of two junctions from sample BTO (3nm). (a) Junction L2 has the SiO_2 well adhered, and the only path where the current will flow is through the pillar. (b) On the other hand, in junction G1, the SiO_2 around the pillar was not well adhered to the surface, and it was removed during the lift-off process. When a top electrode is deposited, a short circuit between the top Au electrode and the LSMO area is exposed. *148*
Figure A. 7. (a) Sketch of the electrical arrangement used to characterize the ferroelectric tunnel junctions patterned electrically. (b) Voltage pulse applied at the top electrode in order to measure the conductivity of devices. (c) Example of I(V) curve collected while pulse in (b) is applied to junction H11 from sample 1. Vertical dashed line indicates reading voltage for calculation of current density. Inset: the brightest spot in the center is the junction square pillar with side = 4.5 μm. (d) Dependence on current density on the area from all junctions in sample 1. The blue star represents current density measured in the sample with top electrode patterned with a shadow mask, as described in the Experimental Methods chapter. Blue area indicates a range of current densities observed in FTJ with a similar structure published in the literature........................... *149*
Figure A. 8. Current density dependence on the area for ferroelectric tunnel junction with (a) 3 nm (sample 2), (b) 4 nm (sample 3), (c) 5 nm (sample 4) thick BTO films, and (d) 4 nm BTO covered by Pt grown in situ (sample 8) patterned with optical lithography. Inset in (a) shows optical microscopy image for junction K2 and current dependence on the area for the BTO (3 nm) sample. Inset in (c) shows an optical microscopy image of junction F6...... ***Error! Bookmark not defined.***
Figure A. 9. Current-voltage curves collected in the indicated junctions from sample 1 (2 nm BTO). Junctions show (a) ohmic conduction or (b) sigmoidal I(V) typical from tunnel junctions........ 152
Figure A. 10. (a) I(V) curves collected at 1 Hz in junction G12 (area = 100 μm^2) from sample 1 (2 nm BTO). Vertical dashed lines indicate voltage where the current has a change in the slope. Inset shows zoom for positive voltages for clearer visualization of a second I(V) curve (blue curve). Units are indicated in the main graph. (b) $R(V_w)$ loop obtained by applying 1 ms pulses. Inset shows an

optical microscopy image of junction G12. (c) I(V) curve collected at 1 Hz in junction D11 (area = 77 μm^2) from sample 3 (4 nm BTO). Inset shows an optical microscopy image of junction D11. (d) R(V_w) loop obtained by applying 1 ms pulses..154
Figure A. 11. Current density dependence on the area for samples (a) 5 (b) 6, (c) 9 and (d) 7. Inset in (a) and (d) show optical microscopy images from junctions L12 and D9, respectively, with an area of ≈ 100 μm^2..155
Figure A. 12. Current-voltage curves collected in sample 7 /6 nm HZO) tunnel junctions with different areas. The curves' shape indicates a clear difference between an (a) ohmic conduction and (b) exponential-like typical from tunnel barriers....156

List of Tables

*Table 2. 1. Deposition parameters for oxides. The AlO_x layer is amorphous, and the gas inside the chamber was argon, as indicated with an *.* 36

Table 3. 1. Parameters extracted from fitting shown in Figure 3.3(c) are effective thickness (t_{eff}), barrier height at interfaces HZO/LSMO (ϕ_{LSMO}), and Pt/HZO (ϕ_{Pt}). Based on these values, the average barrier height (ϕ_{mean}) and the difference between heights ($\Delta\phi$) are calculated. Error bars represent the fitted parameters' dispersion from I(V) data collected after three sequential writing steps with $V_w = \pm 4.5$ V (Appendix 5). 75
Table 3. 2. Parameters extracted fitting data in Figure A2 using the Brinkman model. 84

Table 5. 1. Barrier parameters extracted from fittings are shown in Figure 5.6. The effective thickness (t_{eff}) was fixed at 3.15 nm, while the barrier height for both interfaces (ϕ_{LSMO} and ϕ_{Pt}) and parallel resistance (R) were fitted. 118
Table 5. 2.Non-linearity for potentiation (τ_p) and depression (τ_d) extracted from fittings in Figure 5.9(d). 122

Figure A4. 1. ER(V_w) data for (a) HZO, (b) HZO/STO1, and (c) HZO/STO2 samples. The number of junctions measured in each sample is indicated in the corresponding graph. 106
Figure A4. 2. Topography images from AFM collected on the surface of (a) HZO, (b) HZO/STO2, and (c) HZO/AlO2 samples. The diagonal line in (b) is mechanical damage caused in the surface of the film due to manual manipulation of the sample. 106

Table A. 1. The initial structure of samples deposited in ICMAB and to be patterned using optical lithography in Polifab. 138
Table A. 2. The number of junctions in each sample that were successfully patterned using the methodology described in section II. 147
Table A. 3. Current density values extracted from BTO tunnel junctions in the indicated references. 151
Table A. 4. Current density collected in tunnel junctions with different HZO thickness patterned with standard shadow mask technique. 157

List of Abbreviations

HZO	$Hf_{0.5}Zr_{0.5}O_2$
IoT	Internet of things
DRAM	Dynamic Random Acess Memory
ReRAM	Resistive Random Memory
STDP	Spike-timing-dependent plasticity
LRS	Low Resistive State
HRS	High Resistive State
MIM	Metal-insulator-metal
MIS	Metal-insulator-semiconductor
RS	Resistive Switching
VCM	Valence Change Memory
sDB	Soft-dielectric Breakdown
ECM	Electrochemical Memory
PCM	Phase Change Memory
STT	Spin-transfer-torque
SBT	$SrBi_2Ta_2O_9$
BLT	$Bi_{4-x}La_xTi_3O_{12}$
FeRAM	Ferroelectric Random Acess Memroy
FTJ	Ferroelectric Tunnel Junction
TER, ER	Tunneling Electroresistance
FE	Ferroelectric
PZT	$PbZr_xTi_{1-x}O_3$
LSMO	$La_{2/3}Sr_{1/3}MnO_3$
PFM	Piezo force microscopy
Co	Cobalt
DT	Direct tunneling
FNT	Fowler-Nordheim tunneling
TI	Thermionic injection

WKB	Wentzel-Kramers-Brillouin
YSZ	Yttria-stabilized Zirconia
C-AFM	Conductive atomic force microscopy
GB	Grain boundary
GI-XRD	Grazing Incidence X-ray diffraction
TEM	Transmission Electron Microscopy
FeFET	Ferroelectric Field Transistor
o-HZO	Orthorhombic phase $Hf_{0.5}Zr_{0.5}O_2$
m-HZO	Monoclinic phase $Hf_{0.5}Zr_{0.5}O_2$
ALD	Atomic layer deposition
LAO	$LaAlO_3$
STO	$SrTIO_3$
XRD	X-ray Diffraction
STEM	Scanning Transmission Electron Microscopy
FORC	First-order Reversal Curve
PLD	Pulsed Laser Deposition
AFM	Atomic Force Microscopy
LSAT	$(LaAlO_3)_{0.3}(Sr_2TaAlO_6)_{0.7}$
GSO	$GdScO_3$
TSO	$TbScO_3$
PVD	Physical Vapor Deposition
XRR	X-ray Reflection
Pt	Platinum
DLCC	Dynamic Leakage Current Compensation
DHM	Dynamic Hysteresis Mode
PUND	Positive-Up-Negative-Down
HAADF	High Angle Annular Dark-Field
Z	Atomic Number
EELS	Electron Energy-Loss Spectroscopy
ELNES	Energy-Loss Near-Edge Structure

ADF	Annular Dark Field
CF	Conductive filament
UV	Ultraviolet radiation
CD	Critical dimension

List of Acronyms

TER, ER	Tunneling electroresistance
G	Conductance
R	Resistance
P	Polarization
E	Electric field
P_R	Remnant polarization
P_s	Saturated polarization
E_C	Coercive field
σ_S	Surface charges
λ_{eff}	Screening length
φ	Electrostatic Potential
E_d	Depolarizing field
V	Voltage
J	Current density
ϕ	Barrier height
E_F	Fermi Energy
W_i	Work function
χ	Electron affinity
$I(V)$	Current-voltage curve
$P(V)$	Polarization-voltage curve
P_{O2}	oxygen partial pressure
V_W	Writing voltage amplitude
τ_D	Delay time
τ_W	Writing time duration
V_R	Reading voltage
V_c	Coercive Voltage
A	Area
D	Electrical displacement

ϵ_0	vacuum permittivity
ε_{stat}	static relative permittivity
ϵ_r	Relative permittivity
a_{LSMO}	LSMO lattice parameter
P_{total}	Total polarization
P_{linear}	Linear polarization
P_{FE}	Ferroelectric spontaneous polarization
I_{DE}	Displacement current
$I_{leakage}$	Leakage current
I_{FE}	Ferroelectric switching current
R_s	Series resistance
τ_{RC}	Time constant
C	Capacitance
v_0	Frequency
N_p	Number of pulses
N_c	Number of cycles
ΔG	Conductance variation
R_0	Initial resistance
d_{33}	piezoelectric coefficient
2θ	Scattering angle
λ	X-ray wavelength
V_{GB}	Transition voltage from Region I to II
t_{eff}	Effective thickness
d	Thickness of barrier
E_{imp}	Imprint field
t_{pre}	Trigger time pre-synaptic pulse
t_{post}	Trigger time post-synaptic pulse
Δt	Time difference

List of Publications

[1] Qian, M., Fina, I., Sulzbach, M. C., Sánchez, F. & Fontcuberta, J. Synergetic Electronic and Ionic Contributions to Electroresistance in Ferroelectric Capacitors. *Adv. Electron. Mater.* **5**, 1800646 (2019).

[2] Sulzbach, M. C. *et al.* Unraveling Ferroelectric Polarization and Ionic Contributions to Electroresistance in Epitaxial Hf0.5Zr0.5O2 Tunnel Junctions. *Adv. Electron. Mater.* **6**, 1900852 (2020).

[3] Sulzbach, M. C. *et al.* Blocking of Conducting Channels Widens Window for Ferroelectric Resistive Switching in Interface-Engineered Hf0.5Zr0.5O2 Tunnel Devices. *Adv. Funct. Mater.* **2002638**, 1–10 (2020).

[4] M. C. Sulzbach, H. Tan, S. Estandía, J. Gàzquez, F. Sánchez, I. Fina, J. Fontcuberta, Ferroelectric and resistive switching in epitaxial 2 nm $Hf_{0.5}Zr_{0.5}O_2$ tunnel junctions, to be submitted, 2021.

Author contributions

Milena Cervo Sulzbach performed the electrical and ferroelectric characterization measurements and analyzed the data. Dr. Ignasi Fina prepared the experimental setup, software for electrical and dielectric measurements, and script for data fitting and analysis. Dr. Jike Lyu optimized the HZO pulsed laser deposition process. Huan Tan collected the PFM and AFM images. Saúl Estandía and Dr. Jaume Gázquez performed STEM and EELS experiments and the corresponding analysis. Mengdi Qian and Raul Solanas fabricated the samples at the PLD facilities under the supervision of Dr. Florencio Sánchez. Anna Crespi collected the XRD 2θ-χ data. Joan. B. Esquius and Javier Campos collected the XRD θ-2θ scans. Dr. Nico Dix analyzed the XRD spectra.

Milena Cervo Sulzbach, Dr. Ignasi Fina, and Prof. Josep Fontcuberta wrote the published and submitted manuscripts. Huan Tan, Xiao Long, Saúl Estandía, Dr. Jaume Gázquez, Dr. Florencio Sánchez, Dr. Nico Dix, Dr. Matthew F. Chisholm co-wrote the paper. All authors discussed the results and commented on the manuscript.